1-1-2011

The Role of Schwann Cell Mitochondrial Metabolism in Schwann Cell Biology and Axonal Survival

Andreu Viader
Washington University in St. Louis

WASHINGTON UNIVERSITY IN ST. LOUIS

Division of Biology and Biomedical Sciences

Neurosciences

Dissertation Examination Committee:
Jeffrey Milbrandt, Chair
Peter A. Crawford
Aaron DiAntonio
Timothy M. Miller
Rakesh Nagarajan
Robert E. Schmidt

The Role of Schwann Cell Mitochondrial Metabolism in Schwann Cell Biology and Axonal Survival

By

Andreu Viader

A dissertation presented to the
Graduate School of Arts and Sciences
of Washington University in
partial fulfillment of the
requirements for the degree
of Doctor of Philosophy

December 2011

Saint Louis, Missouri

ABSTRACT OF THE DISSERTATION

The Role of Schwann Cell Mitochondrial Metabolism in Schwann Cell Biology and Axonal Survival

by

Andreu Viader

Mitochondrial dysfunction has emerged as a common cause of peripheral neuropathies. While the role of neuronal and axonal mitochondria in peripheral nerve disease is well appreciated, whether Schwann cell (SC) mitochondrial deficits contribute to peripheral neuropathies is unclear. Greater insight into the biology and pathology of SC mitochondrial metabolism could be relevant to the treatment of peripheral neuropathies, particularly because SCs critically support axonal stability and function as well as promote peripheral nerve regeneration. The present thesis investigates the contribution of SC mitochondrial deficits to disease progression in peripheral neuropathies as well as the gene regulatory network that drives the SC regenerative response after injury and in disease states.

We describe the generation and characterization of the first mouse model useful in directly interrogating the contribution of SC mitochondrial dysfunction to peripheral neuropathy. These mice (Tfam-SCKOs) were produced through the tissue-specific deletion of the mitochondrial transcription factor A gene (*Tfam*), which is required for mtDNA transcription and replication. Interestingly, induction of SC-specific mitochondrial dysfunction did not affect SC survival; instead, these deficits resulted in a severe, progressive peripheral neuropathy characterized by extensive axonal degeneration

that recapitulated critical features of human neuropathy. Mechanistically, we demonstrated that SC mitochondrial dysfunction activates a maladaptive integrated stress response and causes a shift in lipid metabolism away from new lipid biosynthesis towards increased lipid oxidation. These alterations in lipid metabolism caused the early depletion of key myelin lipid components as well as a dramatic accumulation of acylcarnitine lipid intermediates. Importantly, release of acylcarnitines from SCs was toxic to axons and induced their degeneration. Our results show that normal mitochondrial function in SCs is essential for maintenance of axonal survival and normal peripheral nerve function, suggesting that SC mitochondrial dysfunction contributes to human peripheral neuropathies. Moreover, our work identifies alterations in SC lipid metabolism and the accumulation of toxic lipid intermediates as novel mechanisms driving some of the pathology in peripheral neuropathies associated with mitochondrial dysfunction.

Tfam-SCKO mice showed a severe deficiency in their ability to remyelinate peripheral nerve axons after injury. To gain insight into the highly orchestrated process of SC-mediated support of axonal regeneration, we also investigated the transcriptional and post-transcriptional gene regulatory program that drives the SC regenerative response. We profiled the expression of SC microRNAs (miRNAs) after peripheral nerve lesions as well as characterized the injury response of SCs with disrupted miRNA processing and showed that SC miRNAs modulated the injury response largely by targeting positive regulators of SC dedifferentiation/proliferation. SC miRNAs cooperated with transcriptional regulators to promote rapid and robust transitions between the distinct differentiation states necessary to support nerve regeneration. Moreover, we identified miR-34a and miR-140 as regulators of SC proliferation and myelination. We then used a

novel computational approach to infer the gene regulatory network involved in this SC injury response and gain insight on cooperative regulation of this process by transcription factors and miRNAs.

Together, the results described in the present thesis represent a significant increase in our understanding of how mitochondrial abnormalities specifically in SCs contribute to clinical impairment in patients with peripheral neuropathy. Moreover, the mechanistic characterization of lipid metabolism abnormalities in SCs following mitochondrial dysfunction elucidates potentially important therapeutic targets. Finally, our analysis of the transcriptional and post-transcriptional gene regulatory network involved in the SC regenerative response also provides valuable insight that could be harnessed to help restore normal nerve function in patients with peripheral neuropathy.

ACKNOWLEDGEMENTS

This dissertation is the result of a number of years of work and would not have been possible without many people that helped and supported me along the way. First I would like to thank my advisor Dr. Jeffrey Milbrandt. Over the past five years Jeff has provided me with the guidance, the means, and the freedom to pursue exciting projects. Jeff has been instrumental to my scientific development and I could not have asked for a better mentor.

I am also grateful to my thesis committee members Dr. Robert Schmidt, Dr. Robert Baloh, Dr. Aaron DiAntonio, Dr. Rakesh Nagarajan, Dr. Timothy Miller and Dr. Peter Crawford for their time, advice, and contribution to my progress. Much of this work would not have been possible without the help of some fantastic collaborators including Dr. Judy Golden, Dr. Kui Yang, Dr. Richard Gross, Elizabeth Jin-Wright, Dr. Robert Heuckeroth, Daniel Hunter, and Dr. Dennis Dietzen. Dr. Li-Wei Chang and Dr. Michael Kiebish were particularly important colleagues and great friends both in and out of the lab.

I would also like to thank all of the current and past members of the Milbrandt lab for their support and friendship. I especially thank Dr. Jason Gustin for welcoming me into the lab and teaching me the basics of studying Schwann cells and peripheral nerves; Dr. Yo Sasaki, Dr. Jufang Chang, Dr. Biplab Dasgupta, Dr. Craig Press, Dr. Bin Zhang, Dr. Albert Misko and Dr. Vohra Bhupinder for invaluable discussions about new experiments and results; Amy Strickland, Timothy Farhner, Nina Pachenco, Tasha Crawford, Kelli Simburger, Amber Neilson, Anita Soteres and Mary Akin for helping

with a number of experiments and for keeping in motion all the pieces that it takes to carry out a dissertation project.

I owe a great deal of gratitude to my parents, Emilio and Angels, and my sister Neus who have always been there for me in every way possible and have always given me their unconditional love. I would also like to acknowledge the tremendous support and encouragement I have received from my US/St Louis family and friends, especially Maureen and Jaime, who welcomed me into their family with arms wide open, and Justin and Maia, who made St. Louis feel a little more like a home away from home.

Finally, I must thank my wife Meghan who has been the perfect travel companion in this journey. She has been extremely understanding of all the long hours spent in the lab, while keeping me grounded and showing me the importance of life outside science. I could not have done this without her and I look forward to a life full of adventures together. This work is dedicated to her.

TABLE OF CONTENTS

LIST OF FIGURES AND TABLES

Chapter 2

Chapter 3

Chapter 4

Chapter 5

Chapter 6

CHAPTER 1

Introduction: Peripheral Neuropathy and the Role of Schwann Cell Metabolism in the Biology and Pathology of Peripheral Nerves

Peripheral Neuropathies and their clinical impact

Peripheral neuropathy is a general term used to describe any disorder characterized by peripheral nerve abnormalities. These nerve abnormalities include electrophysiological deficits such as reduced nerve conduction velocity as well as structural changes like axonal degeneration or demyelination. Structural and functional nerve abnormalities in peripheral neuropathies cause the clinical impairment observed in individuals afflicted with these diseases and can lead to incapacitating pain, sensory loss, and debilitating muscle weakness (England and Asbury, 2004). With an overall prevalence of 2400 per 100 000 (2.4%), rising to 8000 per 100 000 (8%) in people older than 55 years (Hughes, 2002), peripheral neuropathies are a common cause of substantial morbidity. At the same time these diseases constitute a significant economic and societal burden. For example, the total annual health care costs in the US for diabetic neuropathy, the most common form of peripheral nerve disease in developed countries, were estimated to be between $4.6 and $13.7 billion in 2001 (Gordois et al., 2003). It is therefore imperative to develop new therapeutic interventions to effectively treat patients with peripheral neuropathy. Discovery of new therapies could be greatly facilitated by an increased understanding of the underlying pathophysiological mechanisms of peripheral nerve disease, which still remain incompletely understood.

Mitochondrial dysfunction as a common element in the diverse etiology of peripheral neuropathies

The term peripheral neuropathy encompasses a myriad of forms of peripheral nerve disease with very diverse etiologies. In the developed world, the most common

cause of peripheral neuropathy is diabetes mellitus (Hughes, 2002). Given the rising prevalence of diabetes worldwide due to the epidemic in obesity, the incidence of diabetic peripheral neuropathy is also expected to rise (Fernyhough et al., 2010). In the developing world, leprosy continues to be a major cause of neuropathy. A range of metabolic disorders, infectious agents, vasculitis, toxins, and drugs are other common systemic causes of peripheral neuropathy. Finally, immune abnormalities and genetic mutations are also responsible for a substantial portion of chronic neuropathies (Hughes, 2002).

Despite this apparent etiological diversity, mitochondrial derangements have emerged as a common cause of many types of peripheral neuropathy. Ultrastructural morphological abnormalities of mitochondria, which are commonly associated with organelle dysfunction, have been reported in the nerves of patients with diabetic neuropathy as well as in animal models of the disease (Fernyhough et al., 2010; Kalichman et al., 1998). Dorsal root ganglion neurons in animal models of diabetes also show decreased mitochondria respiratory chain enzyme activities and overall mitochondrial respiration (Chowdhury et al., 2010). Similarly, metabolic and morphological mitochondrial abnormalities are also present in the nerves of patients and animal models of neuropathy associated with HIV/AIDS as well as with antiretroviral or chemotherapeutic treatment (Flatters and Bennett, 2006; Lehmann et al., 2011; Lewis and Dalakas, 1995). Moreover, the recent identification of disease-causing mutations that affect mitochondrial proteins and function in patients with inherited forms of peripheral neuropathy (known as Charcot-Marie-Tooth disease, CMT) has further confirmed central role of mitochondrial derangements in the pathophysiology of peripheral nerve disease

(Niemann et al., 2006). The need to elucidate the manner in which mitochondrial dysfunction underlies progression of peripheral nerve disease is thus well appreciated.

To date much effort has been devoted to elucidating the role of neuronal and axonal mitochondria in peripheral neuropathies (Baloh, 2008). A growing body of evidence, however, has shown that Schwann cells (SCs), the main glial cell type in the peripheral nervous system, are essential to supporting axonal survival and peripheral nerve function (Chen et al., 2003; Meyer zu Horste et al., 2007; Reddy et al., 2003). These cells are also critical for nerve regeneration to occur after injury and during disease processes (Geuna et al., 2009). Moreover, glia are increasingly recognized as key contributors to the pathophysiology of neurodegenerative diseases traditionally thought to be neuron autonomous (Ilieva et al., 2009). The development of effective therapies for treatment of peripheral neuropathies will therefore need to address the contribution of SC mitochondrial dysfunction to disease progression.

SC support of axonal stability and peripheral nerve function

SCs are the main glial cell type in the peripheral nervous system (PNS) and they cover most of the surface of all axons in peripheral nerves. SCs are best known for their role in peripheral nerve myelinogenesis, during which individual SCs wrap around single axons, establish the boundaries for the formation of the nodes of Ranvier, and deposit the myelin sheath (Sherman and Brophy, 2005). SCs provide in this way the insulation and clustering of ion channels required for rapid, saltatory transmission of action potentials. Of the four types of SCs found in the mature nervous system, however, only myelinating SCs (MSCs) are involved in the formation of the myelin sheath. The majority of SCs in

the PNS are in intimate contact with neurons but do not form myelin (Corfas et al., 2004). This suggests that the role of SCs in the PNS extends beyond the assembly and maintenance of myelin.

A number of studies have now established a critical role for SCs in the preservation of axonal function and survival. Chen *et al.*(Chen et al., 2003) showed that disruption of ErbB receptor-mediated communication between axons and non-myelinating SCs (NMSCs) causes degeneration of unmyelinated axons and progressive sensory neuropathy. Similarly, perisynaptic SCs (PSCs), a second type of non myelin-forming SCs, are essential for the long-term survival of axon terminals at the neuromuscular junction (Reddy et al., 2003). MSCs are also vital for the maintenance of axonal integrity. Axonal degeneration ensues when the interactions between MSCs and axons are perturbed, as is presumably the case in axonopathies caused by mutations in the MSC-specific myelin protein zero (P0) (Bienfait et al., 2006; Shy, 2006), as well as in virtually all demyelinating neuropathies (Shy et al., 2002). In these situations, damage to axons is not caused by the loss of myelin itself since axonal degeneration and demyelination can be pharmacologically uncoupled (Meyer zu Horste et al., 2007). Long-term support of axonal integrity is, therefore, a primary function of all SCs separate from the role of some SCs in the formation and maintenance of myelin.

The mechanisms and cellular machinery underlying SC preservation of axons still remain largely unknown. It is currently believed that this glial support requires axonal engulfment and a molecular apparatus that includes some myelin-related components (Nave and Trapp, 2008). This notion stems from the observation that in the central nervous system (CNS), where oligodendrocytes (OLs) also preserve axonal integrity

independent of myelin (Griffiths et al., 1998; Lappe-Siefke et al., 2003), mutations in some myelin proteins cause axonal loss (Griffiths et al., 1998) while others cause severe dysmyelination without signs of axonal degeneration (Griffiths et al., 1998; Inoue et al., 1981; Rosenbluth, 1980). It is not clear, however, whether the same molecular machinery is at work in the PNS and how it may apply to MSCs and NMSCs.

Trophic support of axons through neurotrophic factors has also been hypothesized as a potential mechanism behind glia-mediated axonal maintenance. While the role of glia-derived neurotrophins during development, myelinogenesis, and remyelination has been described in detail (Rosenberg et al., 2006), there is little experimental evidence of continuous glial trophic support of mature axons. Further work is necessary before a role for SC-derived neurotrophins in axonal preservation can be asserted.

Metabolic support of axons by ensheathing cells is also a likely but poorly understood mechanism of axonal preservation. For example, SCs may support axons through the transfer of metabolites or by helping axons eliminate certain toxic species, as is the case between CNS neurons and astrocytes (Benarroch, 2005; Magistretti, 2006). This type of metabolic support by axon ensheathing glia has not been well analyzed, but may be particularly relevant in the context of neuropathies associated with mitochondrial dysfunction. Disruption of the putative SC metabolic support of axons following abnormalities in SC mitochondrial metabolism could potentially drive some of the pathology of peripheral neuropathies.

SC regenerative response after peripheral nerve injury and in disease states

Besides being essential to support axonal survival and normal peripheral nerve function under physiological conditions, SCs are also critical for nerve regeneration to occur during pathological processes. In the peripheral nervous system, SCs surrounding damaged axons undergo an injury response that enables the long distance regeneration of these axons. SCs have the striking ability to dedifferentiate and revert back to an immature-like state following axonal loss (Jessen and Mirsky, 2008). After a transient phase of proliferation, dedifferentiated SCs help support axonal regeneration by clearing myelin debris, forming tubular structures known as bands of Bungner, and upregulating the synthesis of a number of neurotrophic factors. As peripheral axons regenerate, SCs re-differentiate to form mature Remak bundles or new myelin sheaths, helping to restore, in this way, peripheral nerve function (Geuna et al., 2009). Greater insight into this highly orchestrated process of SC-mediated support of axonal regeneration could be harnessed to improve the treatment of peripheral and central neurodegenerative diseases characterized by axonopathy, including diabetic neuropathy (Coleman, 2005).

Existing evidence of the contribution of SC-specific mitochondrial derangements to the pathology of peripheral neuropathies

As described above, SCs have a primary role in supporting axonal function and survival (Chen et al., 2003; Meyer zu Horste et al., 2007; Reddy et al., 2003) and in enabling peripheral nerve repair in disease processes (Geuna et al., 2009). Given this critical involvement of SCs in the maintenance of peripheral nerves, mitochondrial dysfunction specifically in these glia is likely to cause some of the pathophysiological

changes that lead to clinical impairment in people with peripheral neuropathies. In fact, a growing body of literature implicates glial dysfunction in a number of neurodegenerative diseases traditionally thought to be neuron cell autonomous. Expression of disease-causing mutant proteins specifically in glial cells has been shown to alter disease onset and progression in transgenic mouse models of amyotrophic lateral sclerosis (Boillee et al., 2006; Wang et al., 2009; Yamanaka et al., 2008) and Parkinson's disease (Yazawa et al., 2005) among others (For review see Ilieva et al., 2009). The contribution of SC mitochondrial abnormalities to the pathology observed in peripheral nerve diseases, however, has remained largely unexplored.

Attempts to address how SC mitochondrial deficits may play a role in peripheral neuropathy have been limited by the fact that the mechanisms that disrupt mitochondrial function in neuropathic nerves presumably affect all cells and not just SCs. Moreover, neuropathies associated with mitochondrial dysfunction can display a range of presentation that make it difficult to establish what cell type is primarily involved. This is particularly clear in the case of inherited neuropathies caused by mutations in ubiquitously expressed mitochondrial proteins, such as ganglioside-induced differentiation associated protein 1 (GDAP1). GDAP1 is a protein that localizes to the outer mitochondrial membrane and regulates mitochondrial fission (Niemann et al., 2005). This process is essential to normal mitochondrial function because it regulates the number, morphology, and localization of these organelles, as well as their ability to exchange intraorganelle content and to carry out apoptosis (Detmer and Chan, 2007). GDAP1 mutations that lead to a reduction or loss of mitochondrial fission have now been identified in CMT patients. These patients can suffer from demyelinating, intermediate or

axonal forms of CMT (Niemann et al., 2005). Given that GDAP1 is expressed both in SCs and neurons, the degree to which SC mitochondrial dysfunction contributes to the diverse pathology observed in these CMT patients remains to be established.

Evidence from peripheral neuropathy-prone mitochondriopathies, however, first suggested that mitochondrial dysfunction specifically in SCs may be a major driving force in the development of both myelin and axonal degeneration. Studies reviewing the nerve pathology in mitochondrial disorder patients with clinically apparent signs of peripheral neuropathy found that most mitochondrial abnormalities were localized to SCs (Bouillot et al., 2002; Schroder, 1993). Enlarged mitochondria with an amorphous matrix, distorted cristae, or containing paracrystalline material were predominantly found in SCs, particularly those surrounding unmyelinated axons. Similar observations have been reported in patients suffering from polyneuropathies associated with diabetes and HIV/AIDS (Kalichman et al., 1998; Schroder, 1993). SC-mediated nerve regenerative plasticity is also severely compromised in diabetic neuropathy (Kennedy and Zochodne, 2005), further highlighting the potential importance of SC-specific metabolic abnormalities in the context of peripheral nerve disease. Therefore, the generation of novel models of peripheral neuropathy secondary to mitochondrial dysfunction that allow the examination of pathological processes specifically in SCs could greatly aid the development of new therapeutic strategies.

The polyol pathway as an example of SC metabolic abnormalities that drive some of the pathology in peripheral neuropathies

The notion that understanding how SC mitochondrial dysfunction contributes to peripheral neuropathies could be therapeutically relevant is supported by earlier work examining the polyol pathway in diabetic neuropathy. This pathway represents an example of a metabolic abnormality that primarily affects SCs yet causes some of the pathology present in diabetic neuropathy. The polyol pathway is an alternative catabolic pathway that converts glucose to sorbitol. This pathway is normally not very active because aldose reductase, the first enzyme in the pathway, has a lower affinity for glucose than the glycolytic enzyme hexokinase. In normal nerves, therefore, most glucose is converted to glucose-6-phosphate instead of sorbitol. Increased intracellular glucose in diabetic peripheral nerves, however, saturates hexokinase and increases the flux through the polyol pathway. A high "flux" rate of glucose through the polyol pathway is thought to deplete cofactors such as NADPH and NAD+, thus causing peripheral nerve pathology. Appreciable increases in intracellular sorbitol concentrations may also lead to some tissue toxicity through an increased osmotic effect (for review see Tomlinson and Gardiner, 2008).

Interestingly, aldose reductase was found to be mainly expressed in SCs (Ludvigson and Sorenson, 1980). The pathology present in diabetic nerves secondary to increased activity of the sorbitol pathway may therefore primarily reflect abnormal metabolism in SCs. Overexpression of aldose reductase specifically in SCs was in fact shown to worsen pathophysiolgocial alterations present in a mouse model of diabetes (Song et al., 2003). Aldose reductase inhibitors have been successfully used to treat

animal models of diabetic neuropathy and somewhat promising results have been achieved in human clinical trials (Tomlinson and Gardiner, 2008). Importantly these results emphasize the potential of targeting metabolic abnormalities that may primarily affect SCs as a way to treat peripheral neuropathies.

Thesis organization and significance

Mitochondrial dysfunction has emerged as a common cause of peripheral neuropathies, a heterogeneous group of disorders characterized by peripheral nerve abnormalities and associated with substantial morbidity (Hughes, 2002). The need to elucidate the manner in which mitochondrial dysfunction underlies progression of peripheral nerve disease is thus well appreciated; to date much effort has been devoted to clarifying the role played by neuronal/axonal mitochondria (Baloh, 2008). The contribution of SC-specific mitochondrial deficits to the pathophysiology of peripheral neuropathy, however, has remained largely unexplored. Greater insight into the biology and pathology of SC mitochondrial metabolism could be relevant to the treatment of peripheral neuropathies, particularly because SCs critically support axonal stability and function as well as peripheral nerve regeneration (Chen et al., 2003; Meyer zu Horste et al., 2007; Reddy et al., 2003). The present thesis addresses the contribution of mitochondrial deficits specifically in SCs to disease progression in peripheral nerve disease. We also explore the gene regulatory network that is important for peripheral nerve regeneration after injury and in disease states.

In the first part of the thesis (Chapter 2) we describe the generation and characterization of the first mouse model useful in directly interrogating the contribution

of SC mitochondrial dysfunction to peripheral neuropathy (Viader et al., 2011a). These mice, Tfam-SCKOs, were produced through the tissue-specific deletion of the mitochondrial transcription factor A gene (*Tfam*), which is required for mtDNA transcription and replication and when excised induces progressive defects in the mitochondrial electron transport chain (Larsson et al., 1998). Interestingly, induction of SC-specific mitochondrial dysfunction did not affect SC survival; instead, these deficits resulted in a severe, progressive peripheral neuropathy characterized by extensive axonal degeneration that recapitulated critical features of human neuropathy. These results showed that mitochondrial function in SCs is essential for maintenance of axonal survival and normal peripheral nerve function, suggesting that SC mitochondrial dysfunction contributes to human peripheral neuropathies.

Having established the relevance of the characterization Tfam-SCKO mice to understanding and potentially treating peripheral neuropathies, we next focused on discovering the mechanisms underlying the nerve pathology in these mice. In Chapter 3 (manuscript in preparation), we show that SC mitochondrial dysfunction activates a maladaptive integrated stress response and causes a shift in lipid metabolism away from new lipid biosynthesis towards increased lipid oxidation. These alterations in lipid metabolism caused the early depletion of key myelin lipid components that likely account for the severe demyelination that characterizes the late pathology in Tfam-SCKO mice. Moreover, increased lipid oxidation resulted in a dramatic accumulation of acylcarnitine lipid intermediates, particularly as mitochondrial dysfunction worsened. Importantly, we found that these lipid intermediates could be released from SCs and were toxic to axons, inducing them to degenerate. Our results identify alterations in SC lipid metabolism and

accumulation of toxic lipid intermediates as a novel mechanism driving some of the pathology of peripheral neuropathies associated with mitochondrial dysfunction.

During our investigation of mice lacking Tfam-specifically in SCs, we inadvertently deleted Tfam from enteric neurons and glia and generated mice with disrupted mitochondrial metabolism in the enteric nervous system (Tfam-ENSKOs; Viader et al., 2011b). This was of interest because mitochondrial dysfunction is a central mediator of disease progression in diverse neurodegenerative diseases that often present with prominent gastrointestinal abnormalities. Given the lack of animal models to study the role of mitochondrial deficits in ENS neurodegeneration and gastrointestinal dysfunction, we carried out a phenotypic characterization of the Tfam-ENSKO mice. Interestingly, these mice showed that mitochondrial defects differentially affected specific subpopulations of enteric neurons and regions of the gastrointestinal tract. This regional and subtype-specific variability in susceptibility to mitochondrial defects resulted in an imbalance of inhibitory and excitatory neurons that caused a severe gastrointestinal pseudo-obstruction phenotype in Tfam-ENSKO mice. Mitochondrial dysfunction, therefore, is likely to be an important driving force of neurodegeneration in the ENS and contribute to gastrointestinal symptoms in people with neurodegenerative disorders.

Tfam-SCKO mice showed a severe deficiency in their ability to remyelinate peripheral nerve axons after injury. To gain insight into the highly orchestrated process of SC-mediated support of axonal regeneration, the last part of this thesis investigates the transcriptional and post-transcriptional gene regulatory program that drives the SC regenerative response (Chapter 5, Viader et al., 2011c; Chapter 6, Chang et al., 2011).

Since at the time we started this work it was unclear whether injury-induced changes in SCs were orchestrated post-transcriptionally by microRNAs (miRNAs), we initially profiled the expression of SC miRNAs after peripheral nerve lesions and characterized the injury response of SCs with disrupted miRNA processing. We found that SC miRNAs modulated the injury response largely by targeting positive regulators of SC dedifferentiation/proliferation. SC miRNAs cooperated with transcriptional controls to promote rapid and robust transitions between the distinct differentiation states necessary to support nerve regeneration. Moreover, we identified miR-34a and miR-140 as regulators of SC proliferation and myelination. Having identified miRNAs as important modulators of the SC regenerative response, we used a novel computational approach to infer the integrated transcription factor (TF) and miRNA regulatory network involved in this SC process. Further analysis of regulatory network motifs in this SC injury response network provided insight on cooperative regulation of this process by TFs and miRNAs.

Together, the results described in the present thesis represent a significant increase in our understanding of how mitochondrial abnormalities specifically in SCs contribute to the disease progression and clinical impairment in patients afflicted with peripheral neuropathy. Furthermore, the mechanistic characterization of the lipid metabolism abnormalities that occur in SCs following mitochondrial dysfunction provides new potentially important therapeutic targets. Finally, our analysis of the transcriptional and posttranscriptional regulatory networks involved in the SC regenerative response also give new valuable insight that could be harnessed to restore normal nerve function in patients with peripheral neuropathy.

References

Baloh, R.H. (2008). Mitochondrial dynamics and peripheral neuropathy. Neuroscientist 14, 12-18.

Benarroch, E.E. (2005). Neuron-astrocyte interactions: partnership for normal function and disease in the central nervous system. Mayo Clin. Proc. 80, 1326-1338.

Bienfait, H.M., Faber, C.G., Baas, F., Gabreels-Festen, A.A., Koelman, J.H., Hoogendijk, J.E., Verschuuren, J.J., Wokke, J.H., and de Visser, M. (2006). Late onset axonal Charcot-Marie-Tooth phenotype caused by a novel myelin protein zero mutation. J. Neurol. Neurosurg. Psychiatry. 77, 534-537.

Boillee, S., Yamanaka, K., Lobsiger, C.S., Copeland, N.G., Jenkins, N.A., Kassiotis, G., Kollias, G., and Cleveland, D.W. (2006). Onset and progression in inherited ALS determined by motor neurons and microglia. Science 312, 1389-1392.

Bouillot, S., Martin-Negrier, M.L., Vital, A., Ferrer, X., Lagueny, A., Vincent, D., Coquet, M., Orgogozo, J.M., Bloch, B., and Vita, C. (2002). Peripheral neuropathy associated with mitochondrial disorders: 8 cases and review of the literature. J. Peripher. Nerv. Syst. 7, 213-220.

Chang, L.W., Viader, A., Payton, J.E., Varghese, N., Milbrandt, J., Nagarajan, R.. (2011). An integrated approach to infer transcription factor and microRNA regulatory networks. Nucleic Acid Res. Submitted.

Chen, S., Rio, C., Ji, R.R., Dikkes, P., Coggeshall, R.E., Woolf, C.J., and Corfas, G. (2003). Disruption of ErbB receptor signaling in adult non-myelinating Schwann cells causes progressive sensory loss. Nat. Neurosci. 6, 1186-1193.

Chowdhury, S.K., Zherebitskaya, E., Smith, D.R., Akude, E., Chattopadhyay, S., Jolivalt, C.G., Calcutt, N.A., and Fernyhough, P. (2010). Mitochondrial respiratory chain dysfunction in dorsal root ganglia of streptozotocin-induced diabetic rats and its correction by insulin treatment. Diabetes 59, 1082-1091.

Coleman, M. (2005). Axon degeneration mechanisms: commonality amid diversity. Nat. Rev. Neurosci. 6, 889-898.

Corfas, G., Velardez, M.O., Ko, C.P., Ratner, N., and Peles, E. (2004). Mechanisms and roles of axon-Schwann cell interactions. J. Neurosci. 24, 9250-9260.

Detmer, S.A., and Chan, D.C. (2007). Functions and dysfunctions of mitochondrial dynamics. Nat. Rev. Mol. Cell Biol. 8, 870-879.

England, J.D., and Asbury, A.K. (2004). Peripheral neuropathy. Lancet 363, 2151-2161.

Fernyhough, P., Roy Chowdhury, S.K., and Schmidt, R.E. (2010). Mitochondrial stress and the pathogenesis of diabetic neuropathy. Expert Rev. Endocrinol. Metab. 5, 39-49.

Flatters, S.J., and Bennett, G.J. (2006). Studies of peripheral sensory nerves in paclitaxel-induced painful peripheral neuropathy: evidence for mitochondrial dysfunction. Pain 122, 245-257.

Geuna, S., Raimondo, S., Ronchi, G., Di Scipio, F., Tos, P., Czaja, K., and Fornaro, M. (2009). Chapter 3: Histology of the peripheral nerve and changes occurring during nerve regeneration. Int. Rev. Neurobiol. 87, 27-46.

Gordois, A., Scuffham, P., Shearer, A., Oglesby, A., and Tobian, J.A. (2003). The health care costs of diabetic peripheral neuropathy in the US. Diabetes Care 26, 1790-1795.

Griffiths, I., Klugmann, M., Anderson, T., Yool, D., Thomson, C., Schwab, M.H., Schneider, A., Zimmermann, F., McCulloch, M., Nadon, N., and Nave, K.A. (1998). Axonal swellings and degeneration in mice lacking the major proteolipid of myelin. Science 280, 1610-1613.

Hughes, R.A. (2002). Peripheral neuropathy. BMJ 324, 466-469.

Ilieva, H., Polymenidou, M., and Cleveland, D.W. (2009). Non-cell autonomous toxicity in neurodegenerative disorders: ALS and beyond. J. Cell Biol. 187, 761-772.

Inoue, Y., Nakamura, R., Mikoshiba, K., and Tsukada, Y. (1981). Fine structure of the central myelin sheath in the myelin deficient mutant Shiverer mouse, with special reference to the pattern of myelin formation by oligodendroglia. Brain Res. 219, 85-94.

Jessen, K.R., and Mirsky, R. (2008). Negative regulation of myelination: relevance for development, injury, and demyelinating disease. Glia 56, 1552-1565.

Kalichman, M.W., Powell, H.C., and Mizisin, A.P. (1998). Reactive, degenerative, and proliferative Schwann cell responses in experimental galactose and human diabetic neuropathy. Acta Neuropathol. 95, 47-56.

Kennedy, J.M., and Zochodne, D.W. (2005). Impaired peripheral nerve regeneration in diabetes mellitus. J. Peripher. Nerv. Syst. 10, 144-157.

Lappe-Siefke, C., Goebbels, S., Gravel, M., Nicksch, E., Lee, J., Braun, P.E., Griffiths, I.R., and Nave, K.A. (2003). Disruption of Cnp1 uncouples oligodendroglial functions in axonal support and myelination. Nat. Genet. 33, 366-374.

Larsson, N.G., Wang, J., Wilhelmsson, H., Oldfors, A., Rustin, P., Lewandoski, M., Barsh, G.S., and Clayton, D.A. (1998). Mitochondrial transcription factor A is necessary for mtDNA maintenance and embryogenesis in mice. Nat. Genet. 18, 231-236.

Lehmann, H.C., Chen, W., Borzan, J., Mankowski, J.L., and Hoke, A. (2011). Mitochondrial dysfunction in distal axons contributes to human immunodeficiency virus sensory neuropathy. Ann. Neurol. 69, 100-110.

Lewis, W., and Dalakas, M.C. (1995). Mitochondrial toxicity of antiviral drugs. Nat. Med. 1, 417-422.

Ludvigson, M.A., and Sorenson, R.L. (1980). Immunohistochemical localization of aldose reductase. I. Enzyme purification and antibody preparation--localization in peripheral nerve, artery, and testis. Diabetes 29, 438-449.

Magistretti, P.J. (2006). Neuron-glia metabolic coupling and plasticity. J. Exp. Biol. 209, 2304-2311.

Meyer zu Horste, G., Prukop, T., Liebetanz, D., Mobius, W., Nave, K.A., and Sereda, M.W. (2007). Antiprogesterone therapy uncouples axonal loss from demyelination in a transgenic rat model of CMT1A neuropathy. Ann. Neurol. 61, 61-72.

Nave, K.A., and Trapp, B.D. (2008). Axon-glial signaling and the glial support of axon function. Annu. Rev. Neurosci. 31, 535-561.

Niemann, A., Berger, P., and Suter, U. (2006). Pathomechanisms of mutant proteins in Charcot-Marie-Tooth disease. Neuromolecular Med. 8, 217-242.

Niemann, A., Ruegg, M., La Padula, V., Schenone, A., and Suter, U. (2005). Ganglioside-induced differentiation associated protein 1 is a regulator of the mitochondrial network: new implications for Charcot-Marie-Tooth disease. J. Cell Biol. 170, 1067-1078.

Reddy, L.V., Koirala, S., Sugiura, Y., Herrera, A.A., and Ko, C.P. (2003). Glial cells maintain synaptic structure and function and promote development of the neuromuscular junction in vivo. Neuron 40, 563-580.

Rosenberg, S.S., Ng, B.K., and Chan, J.R. (2006). The quest for remyelination: a new role for neurotrophins and their receptors. Brain Pathol. 16, 288-294.

Rosenbluth, J. (1980). Central myelin in the mouse mutant shiverer. J. Comp. Neurol. 194, 639-648.

Schroder, J.M. (1993). Neuropathy associated with mitochondrial disorders. Brain Pathol. 3, 177-190.

Sherman, D.L., and Brophy, P.J. (2005). Mechanisms of axon ensheathment and myelin growth. Nat. Rev. Neurosci. 6, 683-690.

Shy, M.E. (2006). Peripheral neuropathies caused by mutations in the myelin protein zero. J. Neurol. Sci. 242, 55-66.

Shy, M.E., Garbern, J.Y., and Kamholz, J. (2002). Hereditary motor and sensory neuropathies: a biological perspective. Lancet Neurol. 1, 110-118.

Song, Z., Fu, D.T., Chan, Y.S., Leung, S., Chung, S.S., and Chung, S.K. (2003). Transgenic mice overexpressing aldose reductase in Schwann cells show more severe nerve conduction velocity deficit and oxidative stress under hyperglycemic stress. Mol. Cell. Neurosci. 23, 638-647.

Tomlinson, D.R., and Gardiner, N.J. (2008). Glucose neurotoxicity. Nat. Rev. Neurosci. 9, 36-45.

Viader, A., Golden, J.P., Baloh, R.H., Schmidt, R.E., Hunter, D.A., and Milbrandt, J. (2011a). Schwann cell mitochondrial metabolism supports long-term axonal survival and peripheral nerve function. J. Neurosci. 31, 10128-10140.

Viader, A., Wright-Jin , E.C., Vohra, B.P., Heuckeroth, R.O., Milbrandt, J.(2011b). Differential regional and subtype-specific vulnerability of enteric neurons to mitochondrial dysfunction. PlosOne. In Press.

Viader, A., Chang, L.W., Fahrner, T., Nagarajan, R., Milbrandt, J.(2011c). microRNAs modulate Schwann Cell response to nerve injury by reinforcing transcriptional silencing of dedifferentiation-related genes. J. Neurosci. In Press.

Wang, L., Sharma, K., Grisotti, G., and Roos, R.P. (2009). The effect of mutant SOD1 dismutase activity on non-cell autonomous degeneration in familial amyotrophic lateral sclerosis. Neurobiol. Dis. 35, 234-240.

Yamanaka, K., Chun, S.J., Boillee, S., Fujimori-Tonou, N., Yamashita, H., Gutmann, D.H., Takahashi, R., Misawa, H., and Cleveland, D.W. (2008). Astrocytes as determinants of disease progression in inherited amyotrophic lateral sclerosis. Nat. Neurosci. 11, 251-253.

Yazawa, I., Giasson, B.I., Sasaki, R., Zhang, B., Joyce, S., Uryu, K., Trojanowski, J.Q., and Lee, V.M. (2005). Mouse model of multiple system atrophy alpha-synuclein expression in oligodendrocytes causes glial and neuronal degeneration. Neuron 45, 847-859.

CHAPTER 2:

Schwann Cell Mitochondrial Metabolism Supports Long-term Axonal Survival and Peripheral Nerve Function

Adapted from: Viader A, Golden JP, Baloh RH, Schmidt RE, Hunter DA, Milbrandt J. (2011). Schwann cell mitochondrial metabolism supports long-term axonal survival and peripheral nerve function. J Neurosci 31(28): 10128-10140.

Abstract

Mitochondrial dysfunction is a common cause of peripheral neuropathies. While the role of neuron and axonal mitochondria in peripheral nerve disease is well appreciated, whether Schwann cell (SC) mitochondrial deficits contribute to peripheral neuropathies is unclear. Here we examine how SC mitochondrial dysfunction affects axonal survival and contributes to the decline of peripheral nerve function by generating mice with SC-specific mitochondrial deficits. These mice (Tfam-SCKOs) were produced through the tissue-specific deletion of the mitochondrial transcription factor A gene (*Tfam*), which is essential for mitochondrial DNA (mtDNA) transcription and maintenance. Tfam-SCKOs were viable but, as they aged, they developed a progressive peripheral neuropathy characterized by nerve conduction abnormalities as well as extensive muscle denervation. Morphological examination of Tfam-SCKO nerves revealed early preferential loss of small unmyelinated fibers followed by prominent demyelination and degeneration of larger-caliber axons. Tfam-SCKOs displayed sensory and motor deficits consistent with this pathology. Remarkably, the severe mtDNA depletion and respiratory chain abnormalities in Tfam-SCKO mice did not affect SC proliferation or survival. Mitochondrial function in SCs is therefore essential for maintenance of axonal survival and normal peripheral nerve function, suggesting that SC mitochondrial dysfunction contributes to human peripheral neuropathies.

Introduction

Peripheral neuropathies are a heterogeneous group of disorders characterized by peripheral nerve abnormalities. With an incidence of up to 8% in elderly populations, peripheral neuropathies are a common cause of substantial morbidity and constitute a significant economic and societal burden (Hughes, 2002). The etiology for these diseases is varied, ranging from vascular and metabolic irregularities to genetic mutations. Despite this apparent diversity, mitochondrial derangements have emerged as a common cause of many types of peripheral neuropathy. A number of mutations that affect mitochondrial function are now thought to be responsible for several forms of inherited neuropathies (Niemann et al., 2006). Similarly, diabetic neuropathy, the most prevalent form of peripheral nerve disease, is also associated with abnormalities in mitochondrial morphology and metabolism (Fernyhough et al., 2003). With the hope of developing new therapies, therefore, much effort is being devoted to understanding how mitochondrial deficiencies influence nerve function.

In recent years, significant progress has been made in elucidating the role of axonal mitochondria in peripheral neuropathies (Baloh, 2008). Peripheral nerve axons, however, do not function in isolation. SCs, the main glial cell type in the PNS, are intimately associated with all peripheral nerve axons and are essential for their long-term preservation and survival (Chen et al., 2003; Reddy et al., 2003; Meyer zu Horste et al., 2007). Mitochondrial dysfunction in SCs is thus likely to participate in the disease progression in peripheral neuropathies. In fact, pathological mitochondria in neuropathic nerves are often localized to SCs (Schroder, 1993; Kalichman et al., 1998). The

contribution of SC mitochondrial dysfunction to the pathology observed in peripheral nerve diseases, however, is poorly understood and remains largely unexplored.

With the goal of understanding whether SC mitochondrial abnormalities affect axonal survival and contribute to the decline of patients suffering from peripheral nerve diseases, we generated mice with impaired mitochondrial function exclusively in SCs. These Tfam-SCKO mice were generated through the tissue-specific deletion of the mitochondrial transcription factor A gene (*Tfam*), which is required for mtDNA transcription and replication (Larsson et al., 1998). Here we show that mitochondrial function in SCs is essential for maintenance of axonal survival and normal peripheral nerve function. Importantly, SC mitochondrial dysfunction alone recapitulated a number of critical features of human neuropathies. Remarkably, the severe mtDNA depletion and respiratory chain abnormalities in Tfam-SCKO mice did not affect SC survival. SC mitochondrial dysfunction, therefore, is a likely contributor to the impairment of patients suffering from peripheral neuropathies.

Results

Schwann cell-specific disruption of the *Tfam* gene

To study how mitochondrial dysfunction affects SCs and their ability to support long-term axonal survival, we generated mice with disrupted mitochondria only in SCs (Tfam-SCKOs). For this purpose we used a previously developed mouse with *loxP*-flanked *Tfam* alleles ($Tfam^{loxP}$) (Larsson et al., 1998) (Fig. 1a). TFAM is a nuclearly-encoded mitochondrial protein that is essential for mtDNA maintenance, copy number regulation and transcription (Larsson et al., 1998; Ekstrand et al., 2004). Previous reports

have shown that the deletion of *Tfam* in *Tfam*^{loxP} homozygous mice that express *cre*-recombinase in a tissue of interest results in severe tissue-specific mtDNA depletion and mitochondrial respiratory chain deficiency (Larsson et al., 1998; Wang et al., 1999; Silva et al., 2000; Sorensen et al., 2001; Wredenberg et al., 2002). This makes the tissue-specific deletion of Tfam an effective way to induce mitochondrial dysfunction in a selected population of cells.

We mated *Tfam*^{loxP} mice to mice that express *cre*-recombinase under the control of the P_0 promoter (P_0-Cre) (Feltri et al., 1999). P_0-Cre mice are well-established to induce specific recombination of floxed genes in peripheral myelinating and non-myelinating SCs starting at E13.5-14.5, but not in any other central or peripheral neuron or glia (Feltri et al., 1999; Feltri et al., 2002). We confirmed this selectivity by crossing P_0-Cre mice with Cre-inducible Rosa26-YFP reporter animals. Indeed, YFP fluorescence was visible in most sciatic nerve SCs but not in axons or perineurial cells. Similarly, YFP could also be seen in most dorsal root ganglia SCs (satellite cells) but not in DRG neurons (Fig. 1b). In agreement with previous reports, therefore, P_0-Cre induced selective recombination in most peripheral SCs.

The observed P_0-Cre-mediated excision of Tfam in SCs was highly efficient. Analysis of Tfam mRNA and protein levels from Tfam-SCKO sciatic nerve extracts showed an 80% reduction compared to littermate controls (Fig. 1c and d). Considering that an estimated 15% of endoneurial cells are P_0-Cre negative fibroblast and macrophages (King RH, 2005) and that nerve extracts also contain some perineurial and endothelial cells, the actual excision rate of Tfam in SCs was probably near complete. Given the high selectivity and efficiency of the P_0-promoter driven expression of *cre*-

recombinase, we conclude that the mating of *Tfam*^{loxP} to P_0-Cre mice resulted in animals that lacked Tfam specifically in SCs.

SC mtDNA depletion and respiratory dysfunction in Tfam-SCKOs

To determine the functional effect of deleting *Tfam* in SCs, we next assessed mtDNA copy number and transcript level in Tfam-SCKO sciatic nerves. Consistent with the essential role of Tfam in the maintenance, replication and transcription of mtDNA (Larsson et al., 1998; Ekstrand et al., 2004), as well as with previous reports describing tissue-specific Tfam knock-out mice (Larsson et al., 1998; Wang et al., 1999; Silva et al., 2000; Sorensen et al., 2001; Wredenberg et al., 2002), total mtDNA content was found to be significantly reduced in Tfam-SCKO nerves compared to control animals (Fig. 2a). Similarly, transcripts of two different mitochondrially-encoded proteins (*mt-ND2* and *mt-Cox1*) were also severely depleted in the sciatic nerves of Tfam-SCKO animals (Fig. 2b). As expected, no differences in the transcript levels of nuclearly-encoded mitochondrial proteins were observed (Fig. 2b).

The mitochondrial genome encodes 13 subunits that are essential components of complexes I, III, IV and V of the electron transport chain. The depletion of mtDNA and mitochondrially-encoded transcripts following *Tfam* excision has been previously shown to induce severe respiratory chain deficiency (Larsson et al., 1998; Wang et al., 1999; Silva et al., 2000; Sorensen et al., 2001; Wredenberg et al., 2002). To examine the dysfunction of SC mitochondria in Tfam-SCKO mice we first assessed respiratory chain enzyme activities in the sciatic nerves of 2 month old animals. At this age, Tfam has already been efficiently excised in sciatic nerve SCs and mtDNA content and transcripts

have been severely depleted (See Fig. 1c and d and Fig. 2a and b). Mitochondria isolated from Tfam-SCKO sciatic nerves showed a 60% reduction in COX activity (complex IV), which contains critical mtDNA-encoded subunits (Fig. 2c). As expected, the activity of SDH (complex II), which is fully nuclearly encoded, showed no significant change in mitochondria isolated from Tfam-SCKO sciatic nerves (data not shown).

To further confirm the disruption of SC mitochondria in Tfam-SCKO mice, we next used high-resolution respirometry to measure mitochondrial respiration under different substrates in permeabilized 2 month old Tfam-SCKO sciatic nerves. Respiration induced by substrates delivering electrons to complex I (pyruvate+malate), was significantly impaired in Tfam-SCKO sciatic nerves compared to littermate controls. Similarly, respiration induced by the convergent transport of electrons entering at complexes I and II (using pyruvate+malate+succinate as substrates), which best corresponds to the mitochondrial substrate supply in vivo (Gnaiger, 2009), was also significantly reduced in Tfam-SCKO sciatic nerves compared to littermate controls. These reductions in mitochondrial respiration in Tfam-SCKO nerves are likely explained by defects in complexes I, III and IV as these complexes contain mtDNA-encoded subunits. Respiration induced by electrons entering at the level of complex II remained unchanged in Tfam-SCKO nerves, which is explained by the fact that complex II contains only nuclearly-encoded subunits (Fig. 2d).

It should be emphasized that while the functional deficits described above were measured from whole Tfam-SCKO sciatic nerves, they are a reflection of the mtDNA-depletion and mitochondrial dysfunction taking place specifically in SCs. The high specificity of the P_0-cre mediated excision of *Tfam* ensures this (Fig. 1b). Moreover,

COX enzymatic staining, which reflects respiratory chain activity in individual cells, showed reduced staining intensity in the cell bodies of SCs in Tfam-SCKO sciatic nerves (Fig. 2e). Finally, electron microscopy of Tfam-SCKO nerves revealed abundant abnormal, enlarged mitochondria, sometimes with distorted cristae, specifically in SC but not in axons (Fig. 2f). Together, our results confirm that by deleting *Tfam* specifically in SCs we were able to generate a mouse with disrupted mitochondrial metabolism only in peripheral glia.

Tfam-SCKOs develop a progressive degenerative peripheral neuropathy

Despite severe mtDNA and transcript depletion as well as respiratory chain dysfunction in their SCs, Tfam-SCKO animals were born at the expected Mendellian ratios and survived to at least 12 months of age (the longest a Tfam-SCKO was allowed to survive before it was sacrificed). Tfam-SCKO animals developed normally and were indistinguishable from their control littermates up to 3 months of age. Starting at 3-4 months of age, however, Tfam-SCKOs showed signs of muscle weakness and gait abnormality. Tfam-SCKOs exhibited abnormal limb clasping, mild tremors, impaired coordination and developed a characteristic "swimming-gait". These deficits progressively worsened so that by 8 months of age, most Tfam-SCKOs were often unable to support themselves on their hind legs (Fig. 3a). Such motor abnormalities are indicative of peripheral nerve disease and have been previously described in other mouse models of peripheral neuropathy (Le et al., 2005; Ryu et al., 2007; Baloh et al., 2009).

Reduced peripheral nerve conduction velocity is a hallmark and diagnostic marker of diabetic as well as other mitochondria-related neuropathies (Arezzo and Zotova,

2002). To further characterize the peripheral nerve deficits in Tfam-SCKOs we performed nerve conduction studies both on pre-symptomatic and symptomatic mice. Nerve conduction velocity was significantly reduced in Tfam-SCKO animals as early as 2 months of age and this deficit persisted over time (Fig. 3c). Moreover, Tfam-SCKO mice displayed marked temporal dispersion at 4 months of age (Fig. 3b and d). Both these findings are suggestive of a progressive demyelinating phenotype in Tfam-SCKO mice.

Interestingly, electromyography (EMG) of Tfam-SCKOs showed occasional fibrillation potentials and fasciculations at 2-3 months of age, which became prominent at 4 months and continued to worsen with increasing age (Fig. 3e and data not shown). These EMG findings reflect loss of muscle fiber innervation and spontaneous firing of motor units, and are often seen in human nerve diseases involving motor axon loss. Thus, our EMG results indicated a progressive axonal degeneration phenotype in Tfam-SCKO mice. This was confirmed by muscle histology, which revealed abundant denervated atrophic muscle fibers (Fig. 3f). SC-specific mitochondrial dysfunction caused, therefore, a progressive peripheral neuropathy characterized by both demyelination as well as axonal degeneration.

Tfam-SCKOs display early preferential loss of small unmyelinated fibers

To examine in detail the peripheral nerve abnormalities in Tfam-SCKOs we performed histological and electron microscopy analysis of Tfam-SCKO sciatic nerves at different ages. Tfam-SCKO nerves initially developed normally and for the first 2-3 weeks of life there were no obvious differences between Ctrl and Tfam-deficient nerves

(data not shown). As early as 1 month of age, however, Tfam-SCKO nerves started to display signs of pathology. Interestingly, we found that these early abnormalities preferentially affected, and were initially limited to, small-caliber unmyelinated fibers (C fibers) (Fig. 4a-e)

Small caliber fibers are normally associated with non-myelinating SCs, such that a single SC wraps around multiple axons to form a Remak bundle. The Remak bundle is delimited by a basement membrane and individual axons are kept separate from one another inside it by a thin extension of SC cytoplasm (Fig. 4e-1). At 1 month, the structure of Remak bundles in Tfam-SCKO nerves was clearly disrupted (Fig. 4d and e). Unmyelinated axons within a Remak bundle were often found touching one another and interspersed by pathological SC processes known as Bands of Bungner (Fig. 4e-2). Moreover, degeneration of unmyelinated axons was extensive and evidenced by free-floating, excess basement membrane surrounding empty spaces previously occupied by axon bundles (Fig. 4e-2, 3). Precise quantification of small fiber loss in the nerves of Tfam-SCKO mice, however, was not possible because of the difficulty of distinguishing abnormal unmyelinated axons from SC processes forming Bands of Bungner. Note that, at this age (1 month old), large-caliber myelinated fibers (A fibers) in Tfam-SCKO nerves appeared normal (Fig. 4a-c).

The unmyelinated fibers in Tfam-SCKO nerves quickly deteriorated and by 2 months of age most non-myelinating SCs were associated with unstructured, degenerating Remak bundles. These bundles contained few intact axons and were often filled with phagocytic vesicles and membranous debris, indicative of axonal degeneration (Fig. 4e-4). We confirmed the early degeneration of unmyelinated fibers observed in

Tfam-SCKO sciatic nerves by quantifying C fiber density in the epidermis. Somatic C fibers are primarily high-threshold nociceptors that terminate in the epidermis (Kennedy and Wendelschafer-Crabb, 1993). In neuropathies characterized by loss of small unmyelinated fibers, skin denervation is one of the initial signs of pathology and correlates with disease severity (Ebenezer et al., 2007). While we did not observe differences in epidermal fiber density at one month of age, we found a significant decrease in skin innervation in 2 month old Tfam-SCKO mice (Fig. 4f and g). This was again in contrast to large myelinated fibers, which at this age were just beginning to show initial signs of pathology (Fig. 5a). Overall numbers of dorsal root ganglion neurons in L3, whose axons project to the sciatic nerve, were comparable in 2 month old Tfam-SCKO and Ctrl mice (average total # of neurons Ctrl= 7048 +/- 186; Tfam-SCKO= 7381+/- 211.3; n=3 mice per genotype). Similarly, TUNEL and cleaved caspase 3 immunostaining of the dorsal root ganglion neurons whose axons project to the sciatic nerve (levels L3-L5) showed no signs of cell death in either 2 or 4 month old Tfam-SCKOs (data not shown). The degeneration of small unmyelinated fibers in the nerves of Tfam-SCKO mice was, therefore, a primary pathological event and was not secondary to neuronal death.

Together, our results show that Tfam-SCKO mice initially suffered early preferential loss of small unmyelinated fibers, suggesting that these fibers are most sensitive to SC mitochondrial dysfunction. The temporal progression of fiber loss in Tfam-SCKO nerves is particularly interesting because early preferential loss of small unmyelinated fibers has been reported in polyneuropathies associated with diabetes and HIV/AIDS (Kennedy et al., 1996; McArthur et al., 2005), diseases in which

mitochondrial dysfunction is known to occur (Fernyhough et al., 2003; Dalakas et al., 2001)

Loss of large caliber myelinated fibers in older Tfam-SCKOs

While Tfam-SCKOs suffered an early preferential loss of small unmyelinated fibers, these mice also developed deficits in large caliber myelinated axons as they aged. Toluidene blue stained plastic sections of 2 month old Tfam-SCKO sciatic nerves showed early signs of axonal degeneration (Fig. 5a). This observation was confirmed by electron microscopic examination, which revealed a few axons undergoing active demyelination and Wallerian degeneration (data not shown). Note, however, that at this age there was not a significant decrease in the number of myelinating profiles in Tfam-SCKO nerves (Fig. 5b).

Severe axonal loss became prominent in Tfam-SCKOs by 4 months (Fig. 5a-c). At this age, the number of myelinating profiles in Tfam-SCKO nerves was greatly reduced compared to control littermates (Fig. 5b). Degeneration of myelinated axons continued to progress as Tfam-SCKO mice aged and by 8 months of age the number of myelinating profiles in these animals was less than 40% that of control littermates (Fig. 5a, b and c-3). Electron micrographs confirmed the severity of the axonal degeneration in Tfam-SCKO nerves, revealing large portions of endoneurium completely devoid of axons (Fig. 5c). Similarly, numerous axons undergoing degeneration were also visible. Detailed morphometric analysis (Hunter et al., 2007) showed no differences in the size distribution of myelinated axons in Tfam-SCKO nerves compared to control littermates at different ages, indicating that myelinated fibers of all calibers were susceptible to degeneration

(Fig. 5d). As in the case of small unmyelinated fibers, the degeneration of myelinated fibers was not secondary to neuronal death since no TUNEL or cleaved caspase 3 positive motor neurons were observed in the spinal cords of either 2 or 4 month old Tfam-SCKOs (data not shown).

At 4 months demyelination was also widespread in Tfam-SCKO nerves. At this age, large caliber axons without any myelin were a prominent pathological feature (Fig. 5c). Examination of osmicated teased fibers from 4 month old Tfam-SCKO nerves confirmed the presence of segmental demyelination (Fig. 5e). Consistent with demyelination, SCs actively digesting myelin debris were present in Tfam-SCKO nerves at this age (Fig. 5c-4). Occasionally, axons surrounded by abnormally thin myelin were also observed. Thin myelin was, however, not characteristic, and in fact there was no difference in the overall g-ratio between Tfam-SCKO and control nerves at different ages (data not shown). Overall, these results show that extensive axonal degeneration and demyelination ensue when SC mitochondria are disrupted. Normal SC mitochondrial function is therefore essential for maintaining the interaction between myelinating SCs and axons.

Tfam-SCKOs have behavioral deficits consistent with early loss of unmyelinated fibers followed by extensive degeneration of myelinated axons

To determine the physiological effects and confirm the temporal progression of the pathology observed in Tfam-SCKO nerves, we carried out a battery of sensorimotor tests in 2 and 4 month old animals. Behavioral tests that primarily assess the function of small unmyelinated C fibers were expected to show deficits in both 2 and 4 month old

Tfam-SCKO mice. On the other hand, behavioral paradigms looking mainly at the function of large myelinated fibers were predicted to show differences only in 4 month old Tfam-SCKO mice.

Small unmyelinated C-fibers have a primary role in nociception. To examine the physiological effect of the early C-fiber loss observed in Tfam-SCKOs we assessed their sensitivity to a noxious heat stimulus. When a noxious radiant heat stimulus was applied to the hind paw (Hargreaves test), Tfam-SCKOs displayed a longer withdrawal latency than their control littermates. As expected, this reduced sensitivity to noxious heat stimuli was detectable in 2 month old animals and persisted as these mice aged (Fig. 6a).

We also tested innocuous mechanical sensitivity in 2 month old Tfam-SCKOs using the von Frey test. Innocuous mechanical sensitivity is another form of somatosensation but, unlike nociception, it is primarily mediated by myelinated fibers. Interestingly, 2 month old Tfam-SCKO animals showed no deficits in the von Frey test compared to wild type littermate controls (average withdrawal threshold Ctrl=0.86 g +/- 0.08g; Tfam-SCKO=1.0g +/- 0.05g; n=4 mice per genotype). The results from these somatosensory studies supported the pathological observations indicating early preferential loss of small unmyelinated fibers in Tfam-SCKO mice.

Given that the axons of motor neurons are large myelinated fibers, we next determined whether the pathology observed in Tfam-SCKO nerves caused any abnormalities in motor function. As predicted, no motor deficits were detected in 2 month old Tfam-SCKOs (Fig 6b and c). 4 month old Tfam-SCKO animals, however, spent significantly less time on an accelerating rotarod (Fig. 6d) as well as on an inverted screen (Fig. 6b), indicating abnormal coordination and muscle weakness. The results

from these motor studies are consistent with the observation that large-caliber axons are not affected in Tfam-SCKO mice until later in the disease. Together, our results confirm that Tfam-SCKO mice initially suffered early preferential loss of small unmyelinated fibers followed by extensive loss of large-caliber myelinated axons.

SC mitochondrial dysfunction does not compromise SC survival

To determine whether the axonal loss and demyelination observed in Tfam-SCKO animals was simply the result of SC death we assessed changes in SC numbers in the nerves of these animals. Remarkably, we found no differences in the number of SC nuclei between Tfam-SCKO sciatic nerve and littermate controls up to 8 months of age (Fig. 7a and b). Moreover, by crossing Tfam-SCKO mice to Cre-inducible Rosa26-YFP reporter animals we were able to confirm that, at all ages examined, Tfam-deficient SCs present in Tfam-SCKO nerves (identified by their excision-dependent YFP fluorescence) remained viable (Fig. 7a and c). These results indicate that the survival of Tfam-deficient SCs was not compromised despite severe mtDNA depletion and respiratory chain abnormalities.

Consistent with the viability of Tfam-SCKO SCs, we did not detect any differences in TUNEL staining, a marker of cell death, between Tfam-SCKO sciatic nerve and controls at different ages (Fig. 7a and d). Similarly, staining with an antibody that recognizes the proliferation marker phospho-histone 3 showed no changes in proliferation that could compensate for the potential loss of Tfam-deficient SCs in Tfam-SCKO nerves (data not shown). The pathology observed in Tfam-SCKOs, therefore, was not due to the loss of SCs. Together, our findings indicate that normal mitochondrial

function is not required for SC survival, but is essential for maintenance of axonal survival and normal peripheral nerve function.

Tfam deficient SCs support axonal regeneration but fail to remyelinate following injury

Schwann cells play a critical role in promoting axonal regeneration following peripheral nerve injury. Upon degeneration of peripheral axons, SCs in the distal stump undergo an orchestrated process that helps support axonal regeneration (Geuna et al., 2009). To determine whether disrupting mitochondrial function affects the ability SCs to support axonal regeneration, we studied the response of these cells after peripheral nerve crush injury in 2 month old Ctrl and Tfam-SCKO mice. At this age, the peripheral nerves of Tfam-SCKOs show modest pathology that is mainly limited to unmyelinated fibers yet mitochondrial function has already been severely disrupted (see above).

We first looked at the initial response of SCs to axonal degeneration by assessing changes in SC proliferation and in their ability to break down existing myelin. Within the first few days after losing contact with axons SCs de-differentiate and start to proliferate (Geuna et al., 2009). Immunostaining of nerves harvested 4 days after injury distal to the site of crush using a phopho-histone 3 antibody showed no impairment in the ability of Tfam-deficient SCs to proliferate following axonal loss (Fig. 8a and b). Nerve regeneration also depends on the ability of SCs to break down existing myelin and remove the resulting debris. This process starts immediately after injury and takes place over a period of 3-6 weeks (Geuna et al., 2009). We did not observe differences in the amount of myelin debris present in Ctrl and Tfam-SCKO nerves 3 weeks after injury,

suggesting that disruption of mitochondrial function in SCs does not interfere with their ability to break down and remove myelin following axonal degeneration (Fig. 8c).

We next studied the ability of Tfam-deficient SCs to support axonal regeneration by analyzing toluidene blue stained plastic sections of Tfam-SCKO and Ctrl nerves collected distal to the site of crush 3 weeks after injury. At this time, we found that substantial axonal regeneration and SC remyelination had already taken place in Ctrl nerves (Fig. 8d). In Tfam-SCKO nerves, however, we observed a striking decrease in the number of myelinated fibers (Fig. 8d). Interestingly, examination of Tfam-SKO nerves by electron microscopy revealed that this decrease in myelinated profiles was not due to the inability of Tfam-deficient SCs to support axonal re-growth. In fact, the total number of fibers (myelinated and unmyelinated) distal to the crush site was equivalent between Ctrl and Tfam-SCKO nerves 3 weeks after injury (Fig. 8e and f). Moreover, the majority of regenerated axons in Tfam-SCKO nerves 3 weeks after injury were associated with SCs in the typical 1 to 1 ratio (Fig. 8g1-4). Tfam-deficient SCs, however, failed to form mature myelin. Given that the proportion of axons of large enough caliber to induce myelination (larger than 1 μm in diameter) was not different between Ctrl and Tfam-SCKOs (Fig. 8h), the inability of Tfam-deficient SCs to myelinate is likely a direct consequence of their disrupted mitochondrial metabolism.

Regenerated Remak bundles were also absent in Tfam-SCKO nerves compared to Ctrl littermates 3 weeks after crush injury. Instead, we observed pathological bundles of unorganized unmyelinated axons interspersed by Bands of Bungner (Fig. 8g-5,6), similar to those present in 2 month old Tfam-SCKO mice prior to injury. We conclude that disrupting SC mitochondrial function does not affect the ability of these glia to de-

differentiate, proliferate or support axonal regeneration following injury. Normal SC mitochondrial metabolism, however, is essential for SCs to form mature myelin and Remak bundles, suggesting that the formation and maintenance of these mature structures poses a high metabolic challenge.

Discussion

In the present study we describe the generation and characterization of mice with disrupted mitochondrial function only in SCs. We found that the induction of SC-specific mitochondrial dysfunction did not affect the survival of these cells but resulted in a severe, progressive peripheral neuropathy characterized by extensive axonal degeneration. SC mitochondrial dysfunction, therefore, disrupts the axo-glial interactions required for the long-term support of axons and is a likely contributor to the clinical impairment of patients suffering from peripheral neuropathies.

Mitochondrial dysfunction is a common cause of peripheral neuropathies. An extensive body of literature has now addressed how neuronal/axonal mitochondria may contribute to the pathology observed in these diseases (Niemann et al., 2006; Baloh, 2008). The results described above show for the first time that disrupted mitochondrial function specifically in SCs can itself also cause axonal degeneration and peripheral nerve disease. These findings are consistent with observations in patients suffering from polyneuropathies associated with diabetes, HIV/AIDS, and mitochondrial disorders, in which most nerve mitochondrial abnormalities are localized to SCs (Schroder, 1993; Kalichman et al., 1998).

Moreover, the Tfam-SCKO mice generated in our study recapitulated a number of critical pathological features of human peripheral neuropathies. Disrupting mitochondrial metabolism specifically in SCs was sufficient to induce both axonal degeneration as well as demyelination. Tfam-SCKOs also displayed distal weakness and sensory deficits, two common problems in human patients. Finally, Tfam-SCKOs suffered preferential early loss of unmyelinated C fibers followed by the degeneration of large-caliber myelinated axons. This was of particular interest because preferential loss of small-caliber unmyelinated fibers is characteristic of peripheral and optic neuropathies associated with systemic diseases such as diabetes or with exposure to environmental toxins (Kennedy et al., 1996; McArthur et al., 2005; Sadun, 2002). Together, our results indicate that SC mitochondria are underappreciated contributors to the abnormalities observed in peripheral neuropathies. Furthermore, key pathological features commonly encountered in human peripheral nerve disease can potentially be explained by SC-specific mitochondrial dysfunction.

The findings described in the present paper are consistent with a growing body of literature that implicates glial dysfunction in a number of neurodegenerative diseases traditionally thought to be cell autonomous. This is best exemplified by amyotrophic lateral sclerosis (ALS), a disease characterized by premature death of motor neurons which is sometimes linked to dominant mutations in the antioxidant protein superoxide dismutase 1 (SOD1) (Rosen et al., 1993). While neuronal expression of mutant SOD1 in transgenic mouse models of ALS was found to be important for the initial timing of disease onset (Boillee et al., 2006; Yamanaka et al., 2008; Wang et al., 2009), expression in microglia cells (Boillee et al., 2006; Wang et al., 2009) and astrocytes (Yamanaka et

al., 2008) was found to significantly contribute to disease progression. Similarly, in a mouse model of Parkinson's disease, oligodendrocyte-specific overexpression of the disease-related protein α-synuclein resulted in neurodegeneration (Yazawa et al., 2005). A central role for glia in diseases such as Huntington's, spinocerebellar ataxia or Alzheimer's has also been reported (For review see Ilieva et al., 2009). The development of effective therapies for peripheral neuropathies and neurodegenerative disorders, therefore, will need to address the contribution of SCs and other glia to disease progression.

An unexpected finding of our work was that severe mtDNA depletion and respiratory chain abnormalities in the SCs of Tfam-SCKO mice did not affect their survival. This observation suggests that SCs have an adaptable energy metabolism and that their survival and ATP production are not fully dependent on mitochondrial function. Previous studies looking at the effect of Tfam deletion in a number of tissues have indeed reported cell-specific metabolic changes that take place following the *Tfam* deletion-induced disruption of the electron transport chain. For example, following the muscle-specific deletion of *Tfam*, myocytes increased their mitochondrial mass to compensate for any deficiencies in their respiratory chain (Wredenberg et al., 2002). Cardiomyocytes, on the other hand, were reported to switch to a primarily glycolytic metabolism in response to the heart-specific excision of *Tfam* (Hansson et al., 2004). Some of these adaptations likely account for the limited or largely delayed cell death observed in several tissue-specific Tfam KOs (Larsson et al., 1998; Wang et al., 1999; Silva et al., 2000; Sorensen et al., 2001; Wredenberg et al., 2002). Specific metabolic adaptations following Tfam

depletion-induced mitochondrial dysfunction may also explain why SC viability was not affected in Tfam-SCKO mice.

SCs have, in fact, been hypothesized to be largely glycolytic and rely on the non-oxidative catabolism of glucose to meet their energy needs (Pellerin and Magistretti, 2003). This idea is supported by the observation that in explant systems SCs take up a disproportionately large amount of glucose (Vega et al., 2003). The fact that disruption of mitochondrial energy metabolism in Tfam-SCKO mice did not affect SC survival provides indirect support for this hypothesis. Our current knowledge of the basic energy metabolism and requirements of SCs, however, is still very rudimentary. Future work aimed at understanding the metabolic changes that take place in SCs following *Tfam* deletion-induced respiratory chain deficiency should provide valuable insight into both the biology and pathology of SCs.

Following peripheral nerve injury, SCs undergo a process of de-differentiation, proliferation, and formation of tubular structures known as bands of Bungner, which together with their production of neurotrophic factors, helps support axonal regeneration (Geuna et al., 2009). Interestingly, we found that Tfam depletion-induced mitochondrial dysfunction did not interfere with the ability of SCs to perform these duties and support axonal re-growth. However, Tfam-deficient SCs failed to re-differentiate and form mature Remak bundles and myelin sheaths after having promoted axonal regeneration. The high metabolic challenge posed by the reconstruction of these mature structures, therefore, appears to require an undisturbed SC mitochondrial anaplerotic metabolism. Elucidation of deficiencies in the intermediate metabolism of Tfam-SCKOs could thus provide new targets whose manipulation may promote the remyelination and the

restoration of normal nerve function in patients suffering from mitochondrial-related peripheral neuropathies.

SCs have a primary role in supporting axonal function and survival (Chen et al., 2003; Reddy et al., 2003; Meyer zu Horste et al., 2007), yet the mechanisms and cellular machinery underlying SC preservation of axons still remain largely unknown. Others have hypothesized that glial support requires axonal ensheathment as well as some myelin-related proteins. Trophic support of axons through neurotrophic factors has also been postulated as a potential mechanism behind glia-mediated axonal maintenance. Metabolic support of axons by ensheathing cells is also a likely but poorly understood mechanism of axonal preservation (Nave and Trapp, 2008). For example, SCs may support axons through the transfer of metabolites or by helping axons eliminate certain toxic species, as is the case between CNS neurons and astrocytes (Benarroch, 2005). Our results show that SC mitochondria are essential for the SC-mediated support of axonal function and survival. Given the central role of mitochondria in cellular energy and anaplerotic metabolism, we speculate that the axonal degeneration in Tfam-SCKOs reflects a disruption of SC-mediated metabolic support of axons. The preferential loss of small unmyelinated fibers early in the Tfam-SCKO disease process would then reflect a greater dependence of these fibers on SC metabolic support. Consistent with this hypothesis, unmyelinated axons have been found to be more energetically demanding than myelinated axons and are estimated to consume 2.5-10 fold more energy per action potential generated (Wang et al., 2008).

In summary, Tfam-SCKOs are, to our knowledge, the first SC-specific metabolic mutant that recapitulates some of the pathology of human peripheral neuropathies. These

mice demonstrate that SC-specific mitochondrial dysfunction can be sufficient to cause both demyelination and axonal degeneration. Our study also provides evidence that SC mitochondria help maintain the axo-glial interactions required for the long-term support of axons. A greater understanding of SC mitochondria and how to prevent their dysfunction is, therefore, relevant to the treatment of patients suffering from peripheral neuropathies.

Materials and Methods

Matings of transgenic animals: All animal experiments were carried out in compliance with institutional animal protocols. Tfam$^{loxP/loxP}$ mice in a pure C57Bl6 background (Larsson et al., 1998) were crossed to P_0-Cre mice also in a pure C57Bl6 background (Feltri et al., 1999). Compound heterozytoges (P_0-Cre $^{+/-}$, *Tfam*$^{+/loxP}$) were then backcrossed to homozygous Tfam$^{loxP/loxP}$ to generate the Tfam-SCKO mice (P_0-Cre $^{+/-}$, *Tfam*$^{loxP/loxP}$) and their Ctrl littermates (P_0-Cre $^{-/-}$, *Tfam*$^{loxP/loxP}$). Tfam$^{loxP/loxP}$ mice were also crossed to homozygosity to Rosa26-YFP reporter mice. Tfam$^{loxP/loxP}$/Rosa26-YFP$^{+/+}$ were then crossed to P_0-Cre mice using an analogous breeding scheme. Tfam$^{loxP/loxP}$ genotyping was carried out as previously described (Larsson et al., 1998).

Immunohistochemistry and cell quantification: The following primary and secondary antibodies were used: rabbit anti-GFP (1:1000, Invitrogen), chicken anti-GFP (1:1000, Aves), rabbit anti-βIII tubulin (1:1000, Covance), rabbit anti-phospho histone 3 (1:200, Millipore), rabbit anti-Kv1.1 (1:100, Abcam), rabbit anti-Nav1.6 (1:100, Millipore), mouse anti-Caspr (1:1000, gift from Dr. Elior Peles, Weizmann Institute of Science,

Rehovot, Israel), anti-rabbit Cy3 (1:500, Jackson ImmunoResearch Laboratories), streptavidin conjugated Cy3 (1:500, Jackson ImmunoResearch Laboratories), anti-rabbit Alexa 488 (1:500, Jackson ImmunoResearch Laboratories), and anti-chicken Alexa 488 (1:500, Jackson ImmunoResearch Laboratories).

For immunohistochemical analysis of sciatic nerves, nerves were dissected, immersion fixed in 4% paraformaldehyde for 2 h, rinsed with PBS, and cryoprotected in 30% sucrose. Sciatic nerves were then embedded in Tissue-Tek OCT Compound (Sakura Finetek) and sectioned at 6 μm. For analysis of DRGs, mice were transcardially perfused with 4% paraformaldehyde. The entire spinal cord was then dissected, post-fixed in PFA overnight, rinsed in PBS and cryoprotected in 30% sucrose. After cryoprotection DRGs were dissected, embedded in Tissue-Tek OCT Compound, and sectioned at 6 μm. For analysis of foot pads, foot pad skin was removed from the plantar surface of the hindpaw, immersion fixed in Zamboni's fixative for 2 h, rinsed with PBS, and cryoprotected in 30% sucrose. Skin was sectioned at 30 μm in a plane perpendicular to the skin surface. For analysis of teased nerve fibers, mouse sciatic nerves were dissected and incubated in 4% paraformaldehyde in PBS for 30 min at room temperature. The nerves were washed three times in PBS for 5 min and de-sheathed, and bundles of nerve were dissected with fine needles in PBS on Fisherbrand Superfrost/Plus microscope slides. Slides were air dried for at least 2hrs at room temperature and stored at -20°C until staining.

All frozen sections were immunostained by post-fixing in ice-cold acetone at -20°C for 10 min and blocking in 10% horse serum (DRG and foot pads) or 5% fish skin gelatin (sciatic nerve and teased fibers) in PBS-0.2% Triton for 1 h at room temperature. Sections were then incubated with primary antibody diluted in blocking buffer overnight

at 4°C. Secondary antibody incubation was performed at room temperature for 1 h also in blocking buffer. TUNEL staining was performed as previously described (Grinspan et al., 1996). After all stainings, sections were mounted with Vectashield Mounting Medium with DAPI (Vector Laboratories) for microscopic visualization. Images were captured using an upright microscope equipped for epifluorescence microscopy (Nikon 80i; CoolSnapES camera) and were processed using MetaMorph, Image-J and Gimp software using global adjustments in brightness and contrast.

All cell number quantifications were carried out by counting the cells of interest in 4 randomly selected regions in longitudinal nerve sections from each animal assessed (at least 3 mice per genotype at each age) at a 20x magnification. Epidermal innervation density was quantified by tracing the dermal–epidermal border and determining the number of fibers that crossed this borders as previously described (Golden et al., 2010).

Western Blotting: Sciatic nerves were isolated, desheathed in PBS, and immediately frozen in liquid nitrogen. Lysates were prepared by homogenizing the tissue by sonication in a buffer containing 150 mM sodium chloride, 50 mM Hepes, 1% NP-40, 1mM EDTA, 1mM sodium fluoride, 1mM sodium orthovanodate, and complete protease inhibitor cocktail (Roche Applied Science). The lysates were clarified by centrifugation at 14,000 rpm for 10 min and quantified using the MicroBCAProtein Assay kit (Pierce). For Western blotting, the proteins were separated by SDS-PAGE and transferred to a PVDF membrane (Millipore). Membranes were blocked in 5% milk in 0.5% TBS-Tween and incubated overnight with the appropriate primary antibody. Following incubation with secondary antibodies conjugated to HRP (GE Healthcare), membranes were

developed with SuperSignal West Dura substrate (Pierce). The primary antibodies used were rabbit anti-Tfam (1:4000, Dr. Nils-Goran Larsson), mouse anti-Porin 31HL (ab2) (1:200, Calbiochem) and mouse anti-tubulin (1:1000, Sigma). The secondary antibodies used were anti-mouse and anti-rabbit HRP (1:5000; Jackson ImmunoResearch Laboratories).

RNA and DNA preparation and quantitative real-time PCR: Sciatic nerves were harvested from Tfam-SCKO mice at different ages and immediately frozen in liquid nitrogen. For RNA isolation, tissue was homogenized in Trizol reagent (Invitrogen) and total RNA prepared according to the manufacturer's protocol. For DNA isolation, tissue was digested and DNA isolated using DNeasy Blood and Tissue Kit (Qiagen) according to the manufacturer's protocol. DNA and RNA concentration were quantified using an ND-1000 spectrophotometer (Nanodrop Technologies).

For RNA qRT-PCR cDNA was reverse transcribed from total RNA using M-MLV reverse transcriptase (Invitrogen). qRT-PCR was performed using a SYBR green-based detection system on a 7700 Sequence Detector instrument (Applied Biosystems) as described previously (Nagarajan et al., 2001). Glyceraldehyde-3-phosphate dehydrogenase expression was used to normalize samples and obtain relative expression values that were used to calculate fold changes. mtDNA content was also quantified by qRT-PCR using a SYBR green-based detection system on a 7700 Sequence Detector instrument (Applied Biosystems) in a similar way as described previously (Nagarajan et al., 2001). Instead of cDNA, however, 15ng of total DNA were used per reaction. Primers that recognized a region unique to the mitochondrial genome were used to determine the

mtDNA content relative to a serial dilutions standard curve. mtDNA content values were normalized to nuclear DNA content as determined by a set of primers directed to the genomic locus of Smrt1. DNA and RNA qRT-PCR primer sequences were as follows (5'-3'): Tfam: F, CAGGAGGCAAAGGATGATTC; R, ATGTCTCCGGATCGTTTCAC; GAPDH: F, TGCCCCCATGTTTGTGATG; R, TGTGGTCATGAGCCCTTCC; mt-ND2: F, CGCCCCATTCCACTTCTGATTACC; R, TTAAGTCCTCCTCATGCCCCTATG. mt-Cox1: F, GAACCCTCTATCTACTATTCGG; R, CAAGTCAGTTTCCAAAGCCT. SDHB: F, TGTAGAGAAGGCATCTGTGG ; R, CGTAGAAGTTACTCAAATCAGGG. mtDNA: F, AAGTCGTAACAAGGTAAGCA; R, ATATTTGTGTAGGGCTAGGG. Nuc.DNA: F, GGGTATATTTTTGATACCTTCAATGAGTTA; R, TCTGAAACAGTAGGTAGAGACCAAAGC

Mitochondrial isolation, respiratory enzyme activity measurements, and respirometry: For mitochondrial isolation, 4 sciatic nerves were dissected, desheathed, mechanically dissociated, digested with collagenase for 20 min and pooled together in 2 ml of homogenization buffer (HM) containing 0.22 M mannitol, 70 mM sucrose, 10 mM Tris-HCl, 0.5 mM EDTA, 1mM EGTA and 0.5% delipidated BSA. Nerves were homogenized for about 2 minutes (12 strokes) using a Teflon-glass homogenizer turning at 200 rpm. The homogenate was then centrifuged at 800xg for 10 min. The clarified supernatant was centrifuged at 8,000xg for 10 min and the pellet was resuspended in 1ml of HM buffer without BSA and spun once more at 7,500xg. The resulting pellet was resuspended in 250 μl of HM buffer without BSA. The protein concentration of the

resuspended mitochondrial fractions was determined using a MicroBCAProtein Assay kit (Pierce). Five micrograms of protein from these mitochondrial preps were used to measure complex II and complex IV activity spectrophotometrically as previously described (Birch-Machin and Turnbull, 2001).

For high resolution respirometry 2 sciatic nerves were dissected, briefly digested with collagenase for 10 min, then desheathed and fluffed using a pair of fine forceps. At this point, nerve respiration was measured in a 2-ml chamber using and OROBOROS Oxygraph 2k (Oroboros) as previously described (Mancuso et al., 2010).

Surgical procedure: Mice were anesthetized by intraperitoneal injection of 2-2-2 tribromoethanol at a dose of 500 mg/kg. The sciatic nerve was exposed at the hip and a reproducible crush injury was created by using #5 jeweler's forceps for 30 sec. The site of injury was marked with a single 10-0 nylon epineural suture. Nerve lesions were produced on the right side and the contralateral nerve was left intact and served as the uninjured control. At the appropriate time nerves were harvested and processed for histology.

Nerve light and electron microscopy and morphometry: Sciatic nerves from Ctrl and Tfam-SCKO mice at different ages were dissected and placed in 3% glutaraldehyde overnight. After washing with phosphate buffer, nerves were postfixed in 1% osmium tetraoxide in phosphate buffer overnight at 4°C. Specimens were then dehydrated in graded alcohols and embedded in 100% epoxy (Araldite 502). One-micrometer-thick plastic embedded sections were prepared and stained with toluidene blue for light

microscopy. For electron microscopy, thin sections were prepared, stained with uranyl acetate and lead citrate, and photographed with a JEOL (Akishima) 1200 electron microscope. All nerves underwent qualitative assessment of neural architecture followed by detailed histomorphometric analysis carried out as previously described (Hunter et al., 2007).

Nerve electrophysiology and electromyography: Electrophysiology and electromyography were performed on mice at 2, 4 and 8 months of age using a Viking Quest electromyography machine (Nicolet) as previously described (Baloh et al., 2009). Briefly mice were anesthetized with avertin, and placed on a heating pad. For nerve electrophysiology subcutaneous platinum subdermal EEG electrodes 0.4 mm diameter, 12 mm length (Viasys) were used. Stimulating electrodes were placed just above the left ankle and the left sciatic notch for nerve stimulation. Recording electrodes were placed in the footpad. Evoked CMAPs were obtained using supramaximal stimulation, and distance between the two sites of stimulating electrodes was used to calculate conduction velocity. For EMG recordings a 27-gauge, Teflon-coated, monopolar needle electrode with a 70 × 500 μm recording surface (PRO-37SAF; Electrode Store) was used. A 29-gauge reference needle electrode (GRD-SAF; Electrode Store) was inserted subcutaneous in close approximation to the recording electrode. A subdermal ground electrode was placed on the back. The recording electrode was inserted into the tibialis anterior (TA) or gastrocnemius/soleus muscles, and spontaneous electrical activity was recorded for 90 s.

Muscle histology: Gastrocnemius muscles were dissected fresh, immediately frozen in isopentane cooled in liquid nitrogen. Cryostat sections of gastrocnemius muscle were cut at 10 μm onto slides and stained with hematoxylin and eosin.

Nerve Cytochrome oxidase staining: Sciatic nerves were dissected fresh, placed in Tissue-Tek OCT Compound, and immediately frozen in isopentane cooled in liquid nitrogen. Tissue was then sectioned at 6 μm. Sections were placed in an incubating solution containing sucrose (100mg/ml), 3,3'-diaminobenzidine tetrahydrochloride 2 (DAB, 0.6 mg/ml), sodium phosphate buffer (final concentration 0.05 M), catalase 3 (2.6 μg/ml), and cytochrome c (1.6 mg/ml) for 60 minutes at room temperature. After incubation, sections were washed 3 times with deionized water, dehydrated in a series of ascending alcohols and cleared with xylene, and mounted using permount.

Behavioral testing: Behavior testing was performed using male and female Tfam-SCKO mice and littermate controls at 2 and 4 months of age. The experimenter was blind to the genotypes of the mice during data acquisition. Noxious heat sensitivity (Hargreaves test) was determined as previously described (Golden et al., 2010). Briefly, the thermal threshold was determined by measuring the withdrawal latency to a radiant heat source applied to the plantar surface of the hindpaw in 5 separate trials for each hindpaw with a 15 min interval between trials. The withdrawal threshold was determined by averaging the withdrawal latency obtained in each of the trials. Mechanical sensitivity was determined using the von Frey test. Beginning with the smallest filament and continuing from smallest to largest, calibrated von Frey filaments were pressed to the plantar surface

of the hindpaw until the filament just bent. The withdrawal threshold is defined as the force that produces a withdrawal response in 3 of 5 consecutive applications within one trial. The threshold was determined in 3 trials per hindpaw with a 15 min interval between trials. An accelerating rotarod was used to evaluate motor coordination and balance. Five consecutive acceleration trials were performed with a 5 min interval between trials as described previously (Montana et al., 2009). Muscle strength was measured using an inverted screen test as previously described (Golden et al., 2010).

Osmicated teased sciatic nerve fibers: Sciatic nerves were dissected and immersion fixed in 3% glutaraldehyde overnight. After washing with 0.1M phosphate buffer nerves were incubated in 1% osmium tetraoxide plus 1.5% potassium ferricyanide in 0.5 M phosphate buffer for 1 h. Nerves were washed in PBS followed by incubation in 33, 66, and 100% glycerol/PBS for 6 h each. Nerves were then treated with 0.6% sudan black dissolved in 70% ethanol at 25 ℃ for 30 minutes, rinsed with 70% ethanol and with water and then placed back in 100% glycerol. Nerves were teased in 100% glycerol and coverslipped for imaging.

Statistical analysis: All values are expressed as mean ± SEM. If not stated otherwise, *p* values were determined by unpaired, two-tailed Student's *t* test. All statistical analyses were performed using Microsoft Excel 2007.

Acknowledgements

We thank Michael A. Kiebish for providing valuable technical advice and helpful discussions; Amy Strickland and Nina Panchenko for experimental assistance; Nils-Goran Larsson for the *Tfam*^{loxP} mice and comments on the manuscript; Lawrence Wrabetz and Albee Messing for the P_0-Cre mice; members of the Milbrandt laboratory for their comments on the manuscript and helpful discussions. This work was supported by NIH Neuroscience Blueprint Center Core Grant P30 NS057105 to Washington University, the HOPE Center for Neurological Disorders, National Institutes of Health Grants NS040745 (J.M.), AG13730 (J.M.), NS055980 (R.H.B), DK19645 (R.E.S), R21NS059566 (J.P.G.) and Muscular Dystrophy Association grants 10040 (J.M.), and 135428 (R.H.B.).

References

Arezzo J.C., Zotova E. (2002). Electrophysiologic measures of diabetic neuropathy: Mechanism and meaning. Int Rev Neurobiol, 50:229-255.

Baloh R.H. (2008) Mitochondrial dynamics and peripheral neuropathy. Neuroscientist, 14:12-18.

Baloh R.H., Strickland A., Ryu E., Le N., Fahrner T., Yang M., Nagarajan R., Milbrandt J. (2009). Congenital hypomyelinating neuropathy with lethal conduction failure in mice carrying the Egr2 I268N mutation. J Neurosci, 29:2312-2321.

Benarroch E.E. (2005) Neuron-astrocyte interactions: Partnership for normal function and disease in the central nervous system. Mayo Clin Proc, 80:1326-1338.

Birch-Machin M.A., Turnbull D.M. (2001) Assaying mitochondrial respiratory complex activity in mitochondria isolated from human cells and tissues. Methods Cell Biol, 65:97-117.

Boillee S., Yamanaka K., Lobsiger C.S., Copeland N.G., Jenkins N.A., Kassiotis G., Kollias G., Cleveland D.W. (2006) Onset and progression in inherited ALS determined by motor neurons and microglia. Science, 312:1389-1392.

Chen S., Rio C., Ji R.R., Dikkes P., Coggeshall R.E., Woolf C.J., Corfas G. (2003). Disruption of ErbB receptor signaling in adult non-myelinating schwann cells causes progressive sensory loss. Nat Neurosci, 6:1186-1193.

Dalakas M.C., Semino-Mora C., Leon-Monzon M. (2001). Mitochondrial alterations with mitochondrial DNA depletion in the nerves of AIDS patients with peripheral neuropathy induced by 2'3'-dideoxycytidine (ddC). Lab Invest, 81:1537-1544.

Ebenezer G.J., Hauer P., Gibbons C., McArthur J.C., Polydefkis M .(2007). Assessment of epidermal nerve fibers: A new diagnostic and predictive tool for peripheral neuropathies. J Neuropathol Exp Neurol, 66:1059-1073.

Ekstrand M.I., Falkenberg M., Rantanen A., Park C.B., Gaspari M., Hultenby K., Rustin P., Gustafsson C.M., Larsson N.G. (2004) Mitochondrial transcription factor A regulates mtDNA copy number in mammals. Hum Mol Genet, 13:935-944.

Feltri M.L., D'Antonio M., Previtali S., Fasolini M., Messing A., Wrabetz L. (1999) P0-cre transgenic mice for inactivation of adhesion molecules in schwann cells. Ann N Y Acad Sci, 883:116-123.

Feltri M.L., Graus Porta D., Previtali S.C., Nodari A., Migliavacca B., Cassetti A., Littlewood-Evans A., Reichardt L.F., Messing A., Quattrini A., Mueller U., Wrabetz L. (2002). Conditional disruption of beta 1 integrin in schwann cells impedes interactions with axons. J Cell Biol, 156:199-209.

Fernyhough P., Huang T.J., Verkhratsky A. (2003). Mechanism of mitochondrial dysfunction in diabetic sensory neuropathy. J Peripher Nerv Syst, 8:227-235.

Geuna S., Raimondo S., Ronchi G., Di Scipio F., Tos P., Czaja K., Fornaro M. (2009). Chapter 3: Histology of the peripheral nerve and changes occurring during nerve regeneration. Int Rev Neurobiol, 87:27-46.

Gnaiger E. (2009) Capacity of oxidative phosphorylation in human skeletal muscle: New perspectives of mitochondrial physiology. Int J Biochem Cell Biol, 41:1837-1845.

Golden J.P., Hoshi M., Nassar M.A., Enomoto H., Wood J.N., Milbrandt J., Gereau R.W.,4th, Johnson E.M.,Jr, Jain S. (2010) RET signaling is required for survival and normal function of nonpeptidergic nociceptors. J Neurosci, 30:3983-3994.

Grinspan J.B., Marchionni M.A., Reeves M., Coulaloglou M., Scherer S.S. (1996). Axonal interactions regulate schwann cell apoptosis in developing peripheral nerve: Neuregulin receptors and the role of neuregulins. J Neurosci, 16:6107-6118.

Hansson A., Hance N., Dufour E., Rantanen A., Hultenby K., Clayton D.A., Wibom R., Larsson N.G. (2004). A switch in metabolism precedes increased mitochondrial biogenesis in respiratory chain-deficient mouse hearts. Proc Natl Acad Sci U S A, 101:3136-3141.

Hughes R.A. (2002) Peripheral neuropathy. BMJ, 324:466-469.

Hunter D.A., Moradzadeh A., Whitlock E.L., Brenner M.J., Myckatyn T.M., Wei C.H., Tung T.H., Mackinnon S.E. (2007). Binary imaging analysis for comprehensive quantitative histomorphometry of peripheral nerve. J Neurosci Methods, 166:116-124.

Ilieva H., Polymenidou M., Cleveland D.W. (2009). Non-cell autonomous toxicity in neurodegenerative disorders: ALS and beyond. J Cell Biol, 187:761-772.

Kalichman M.W., Powell H.C., Mizisin A.P. (1998). Reactive, degenerative, and proliferative schwann cell responses in experimental galactose and human diabetic neuropathy. Acta Neuropathol, 95:47-56.

Kennedy W.R., Wendelschafer-Crabb G. (1993). The innervation of human epidermis. J Neurol Sci, 115:184-190.

Kennedy W.R., Wendelschafer-Crabb G., Johnson T. (1996). Quantitation of epidermal nerves in diabetic neuropathy. Neurology, 47:1042-1048.

King R.H. (2005) Nerve trunks and spinal roots. In: Peripheral neuropathy.(Dyck PJ TP, ed), pp35. Philadelphia: Elsevier Saunders.

Larsson N.G., Wang J., Wilhelmsson H., Oldfors A., Rustin P., Lewandoski M., Barsh G.S., Clayton D.A. (1998). Mitochondrial transcription factor A is necessary for mtDNA maintenance and embryogenesis in mice. Nat Genet, 18:231-236.

Le N., Nagarajan R., Wang J.Y., Svaren J., LaPash C., Araki T., Schmidt R.E., Milbrandt J. (2005). Nab proteins are essential for peripheral nervous system myelination. Nat Neurosci, 8:932-940.

Mancuso D.J., Sims H.F., Yang K., Kiebish M.A., Su X., Jenkins C.M., Guan S., Moon S.H., Pietka T., Nassir F., Schappe T., Moore K., Han X., Abumrad N.A., Gross R.W. (2010). Genetic ablation of calcium-independent phospholipase A2{gamma} prevents obesity and insulin resistance during high fat feeding by mitochondrial uncoupling and increased adipocyte fatty acid oxidation. J Biol Chem .

McArthur J.C., Brew B.J., Nath A. (2005). Neurological complications of HIV infection. Lancet Neurol, 4:543-555.

Meyer zu Horste G., Prukop T., Liebetanz D., Mobius W., Nave K.A., Sereda M.W. (2007). Antiprogesterone therapy uncouples axonal loss from demyelination in a transgenic rat model of CMT1A neuropathy. Ann Neurol, 61:61-72.

Montana M.C., Cavallone L.F., Stubbert K.K., Stefanescu A.D., Kharasch E.D., Gereau R.W.,4th. (2009). The metabotropic glutamate receptor subtype 5 antagonist fenobam is analgesic and has improved in vivo selectivity compared with the prototypical antagonist 2-methyl-6-(phenylethynyl)-pyridine. J Pharmacol Exp Ther, 330:834-843.

Nagarajan R., Svaren J., Le N., Araki T., Watson M., Milbrandt J. (2001). EGR2 mutations in inherited neuropathies dominant-negatively inhibit myelin gene expression. Neuron, 30:355-368.

Nave K.A., Trapp B.D. (2008). Axon-glial signaling and the glial support of axon function. Annu Rev Neurosci, 31:535-561.

Niemann A., Berger P., Suter U. (2006). Pathomechanisms of mutant proteins in charcot-marie-tooth disease. Neuromolecular Med, 8:217-242.

Pellerin L., Magistretti P.J. (2003). How to balance the brain energy budget while spending glucose differently. J Physiol, 546:325.

Reddy L.V., Koirala S., Sugiura Y., Herrera A.A., Ko C.P. (2003). Glial cells maintain synaptic structure and function and promote development of the neuromuscular junction in vivo. Neuron, 40:563-580.

Rosen D.R., Siddique T., Patterson D., Figlewicz D.A., Sapp P., Hentati A., Donaldson D., Goto J., O'Regan J.P., Deng H.X. (1993). Mutations in Cu/Zn superoxide dismutase gene are associated with familial amyotrophic lateral sclerosis. Nature, 362:59-62.

Ryu E.J., Wang J.Y., Le N., Baloh R.H., Gustin J.A., Schmidt R.E., Milbrandt J. (2007). Misexpression of Pou3f1 results in peripheral nerve hypomyelination and axonal loss. J Neurosci, 27:11552-11559.

Sadun A.A. (2002). Metabolic optic neuropathies. Semin Ophthalmol, 17:29-32.

Schroder J.M. (1993). Neuropathy associated with mitochondrial disorders. Brain Pathol, 3:177-190.

Silva J.P., Kohler M., Graff C., Oldfors A., Magnuson M.A., Berggren P.O., Larsson N.G. (2000). Impaired insulin secretion and beta-cell loss in tissue-specific knockout mice with mitochondrial diabetes. Nat Genet, 26:336-340.

Sorensen L., Ekstrand M., Silva J.P., Lindqvist E., Xu B., Rustin P., Olson L., Larsson N.G. (2001) Late-onset corticohippocampal neurodepletion attributable to catastrophic failure of oxidative phosphorylation in MILON mice. J Neurosci, 21:8082-8090.

Vega C., Martiel J.L., Drouhault D., Burckhart M.F., Coles J.A. (2003). Uptake of locally applied deoxyglucose, glucose and lactate by axons and schwann cells of rat vagus nerve. J Physiol, 546:551-564.

Wang J., Wilhelmsson H., Graff C., Li H., Oldfors A., Rustin P., Bruning J.C., Kahn C.R., Clayton D.A., Barsh G.S., Thoren P., Larsson N.G. (1999). Dilated cardiomyopathy and atrioventricular conduction blocks induced by heart-specific inactivation of mitochondrial DNA gene expression. Nat Genet, 21:133-137.

Wang L., Sharma K., Grisotti G., Roos R.P. (2009). The effect of mutant SOD1 dismutase activity on non-cell autonomous degeneration in familial amyotrophic lateral sclerosis. Neurobiol Dis, 35:234-240.

Wang S.S., Shultz J.R., Burish M.J., Harrison K.H., Hof P.R., Towns L.C., Wagers M.W., Wyatt K.D. (2008) Functional trade-offs in white matter axonal scaling. J Neurosci, 28:4047-4056.

Wredenberg A., Wibom R., Wilhelmsson H., Graff C., Wiener H.H., Burden S.J., Oldfors A., Westerblad H., Larsson N.G. (2002). Increased mitochondrial mass in mitochondrial myopathy mice. Proc Natl Acad Sci U S A, 99:15066-15071.

Yamanaka K., Chun S.J., Boillee S., Fujimori-Tonou N., Yamashita H., Gutmann D.H., Takahashi R., Misawa H., Cleveland D.W. (2008). Astrocytes as determinants of disease progression in inherited amyotrophic lateral sclerosis. Nat Neurosci, 11:251-253.

Yazawa I., Giasson B.I., Sasaki R., Zhang B., Joyce S., Uryu K., Trojanowski J.Q., Lee V.M. (2005). Mouse model of multiple system atrophy alpha-synuclein expression in oligodendrocytes causes glial and neuronal degeneration. Neuron, 45:847-859.

Figures

Figure 1: P_0-Cre deletes *Tfam* from SCs specifically and efficiently in Tfam-SCKO mice. ***a)*** Diagram of the targeted *Tfam* locus in $Tfam^{loxP}$ mice. When $Tfam^{loxP}$ mice are crossed with mice that express Cre recombinase under the control of the P_0 promoter, exons 6 and 7 of *Tfam* are excised to produce $Tfam^{-}$ mice. ***b)*** YFP fluorescence in SCs (arrowheads) of longitudinal sciatic nerve sections (ScN), as well as satellite SCs (arrowheads) in DRGs (DRG) of Rosa26-YFP/P_0-Cre mice. P_0-Cre induces recombination specifically in SCs and excision-dependent YFP fluorescence is localized to regions of SC cytoplasm but not to axons (Tuj1 and stars; note non-overlapping Tuj1 and YFP staining) or DRG neuron cell bodies (stars). Scale Bars: top and bottom panels 100 μm, middle magnified panel 50 μm. ***c)*** qRT-PCR results showing efficient depletion of Tfam mRNA in Tfam-SCKO sciatic nerves. Tfam mRNA levels in the sciatic nerve of 1 month old Tfam-SCKOs were decreased by 60% ($p=0.001$, two-tailed Student's t-test) compared to Ctrl littermates. By 2 months of age Tfam mRNA levels were reduced by 85% ($p=0.002$, two-tailed Student's t-test) compared to Ctrl littermates. Reported values are normalized to GAPDH; error bars, SEM; n=2 pools of 3 mice run in 3 independent experiments. ***d)*** Western blot showing efficient depletion of Tfam protein in the sciatic nerves of Tfam-SCKO mice compared to Ctrl littermates by 2 months of age.

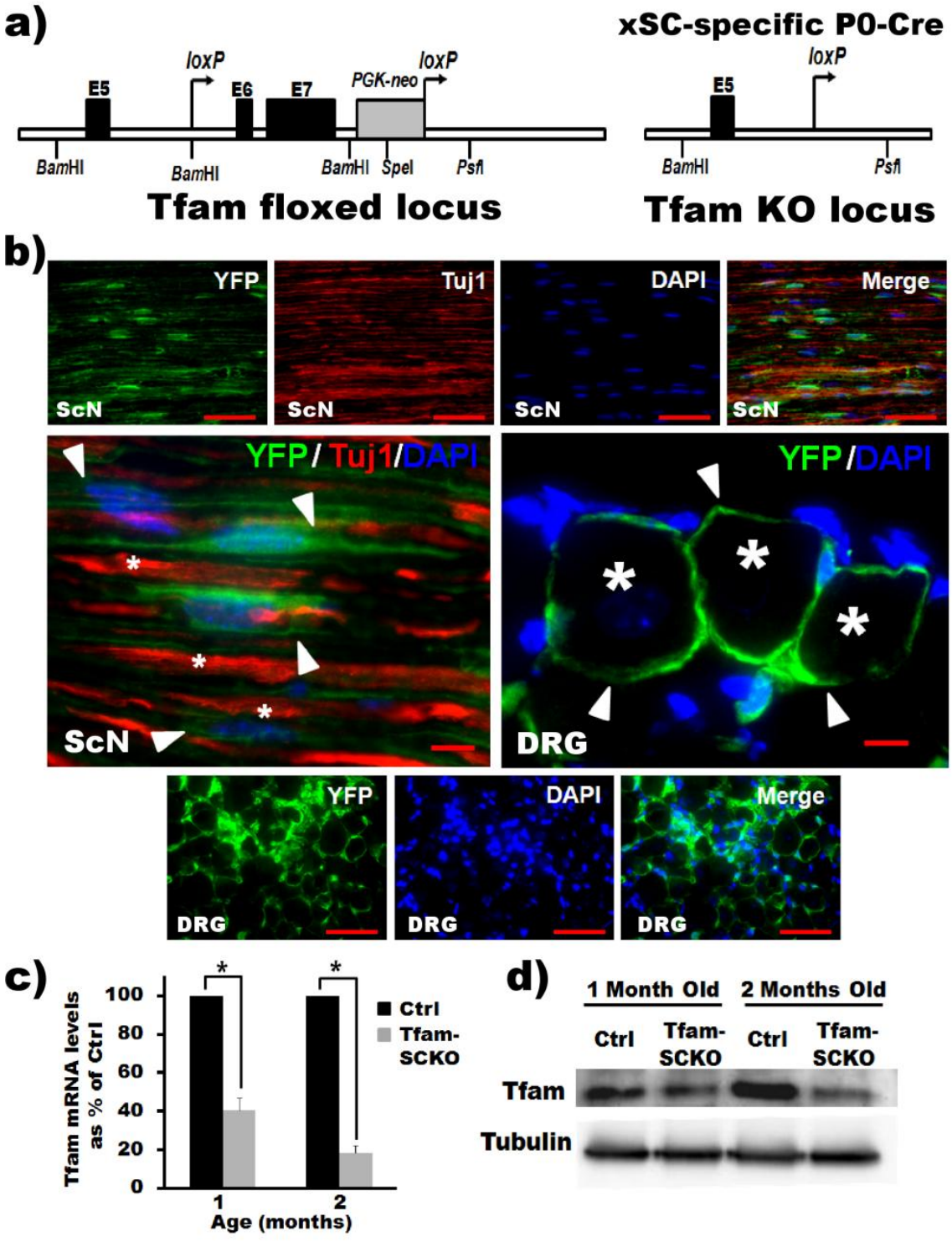
a)
xSC-specific P0-Cre
loxP
E5
E6
E7
PGK-neo
loxP
BamHI
BamHI
BamHI
SpeI
PsfI
Tfam floxed locus
loxP
E5
BamHI
PsfI
Tfam KO locus
b)
YFP
Tuj1
DAPI
Merge
ScN
YFP / Tuj1/DAPI
YFP/DAPI
DRG
c)
Tfam mRNA levels as % of Ctrl
100
80
60
40
20
0
Ctrl
Tfam-SCKO
1
2
Age (months)
d)
1 Month Old
2 Months Old
Ctrl
Tfam-SCKO
Ctrl
Tfam-SCKO
Tfam
Tubulin

Figure 2: SC-specific excision of *Tfam* induces mtDNA and transcript depletion and respiratory dysfunction in Tfam-SCKOs. ***a)*** qRT-PCR results showing depletion of mtDNA content in the sciatic nerves of Tfam-SCKO mice compared to littermate Ctrls. mtDNA content was significantly reduced by 50% ($p=0.01$, two-tailed Student's t-test) in 2 month old Tfam-SCKO sciatic nerves compared to Ctrl nerves. Reported values are normalized to nuclear DNA content; error bars, SEM; n=3 mice per genotype run in 2 independent experiments. ***b)*** qRT-PCR results showing depletion of mitochondrially-encoded electron transport chain subunit transcripts (mt-ND2 and mt-Cox1) in Tfam-SCKO sciatic nerves. mRNA levels of these subunits were decreased 85% ($p=0.02$, two-tailed Student's t-test) in 2 month old Tfam-SCKO sciatic nerves compared to Ctrl littermates. In contrast, transcripts of nuclearly-encoded electron transport chain subunits (nuclear SDHB) are not depleted in Tfam-SCKO sciatic nerves. Reported values are normalized to GAPDH; error bars, SEM; n=2 pools of 3 mice run in 3 independent experiments. ***c)*** Respiratory chain enzyme activity measured from mitochondria isolated from the sciatic nerves of 2 month old Tfam-SCKO nerves and Ctrl littermates. COX activity (complex IV), which contains critical mtDNA-encoded subunits, is reduced 65% ($p<0.01$, two-tailed Student's t-test) in Tfam-SCKO mice. Error bars, SEM; n=3 pools of 2 mice per genotype. ***d)*** Mitochondrial respiration in 2 month old Tfam-SCKO and littermate Ctrl permeabilized sciatic nerves measured using high resolution respirometry. Respiration induced by substrates delivering electrons to complex I (pyruvate+malate) is reduced by 35% ($p=0.04$, two-tailed Student's t-test) in Tfam-SCKO sciatic nerves compared to littermate controls. Respiration induced by the convergent transport of electrons entering at complexes I and II (using pyruvate+malate+succinate as substrates)

is decreased by 25% (p=0.04, two-tailed Student's t-test) in Tfam-SCKO sciatic nerves compared to littermate Ctrls. Respiration induced by substrates delivering electrons to complex II alone (succinate), which is fully nuclearly-encoded, was not significantly changed in Tfam-SCKO nerves compared to littermate Ctrls. Error bars, SEM; n=5 mice per genotype. ***e)*** COX enzymatic staining of 4 month old Ctrl and Tfam-SCKO sciatic nerves. The intense COX staining that localizes to SCs in Ctrl nerves (arrowheads) is largely lost in Tfam-SCKO nerves, indicating mitochondrial dysfunction specifically in this cell type. ***f)*** Electron micrographs of Tfam-SCKO sciatic nerves show abundant abnormal enlarged mitochondria (arrowheads), often with distorted cristae. Aberrant mitochondria are mainly found in SCs, while axonal mitochondria show no morphological abnormalities (arrows). Pathological mitochondria are visible as early as 1 month in Tfam-SCKO nerves (top 3 panels) and become more abundant as these mice age (bottom panels from 4 month old mice). Scale bars: 500 nm

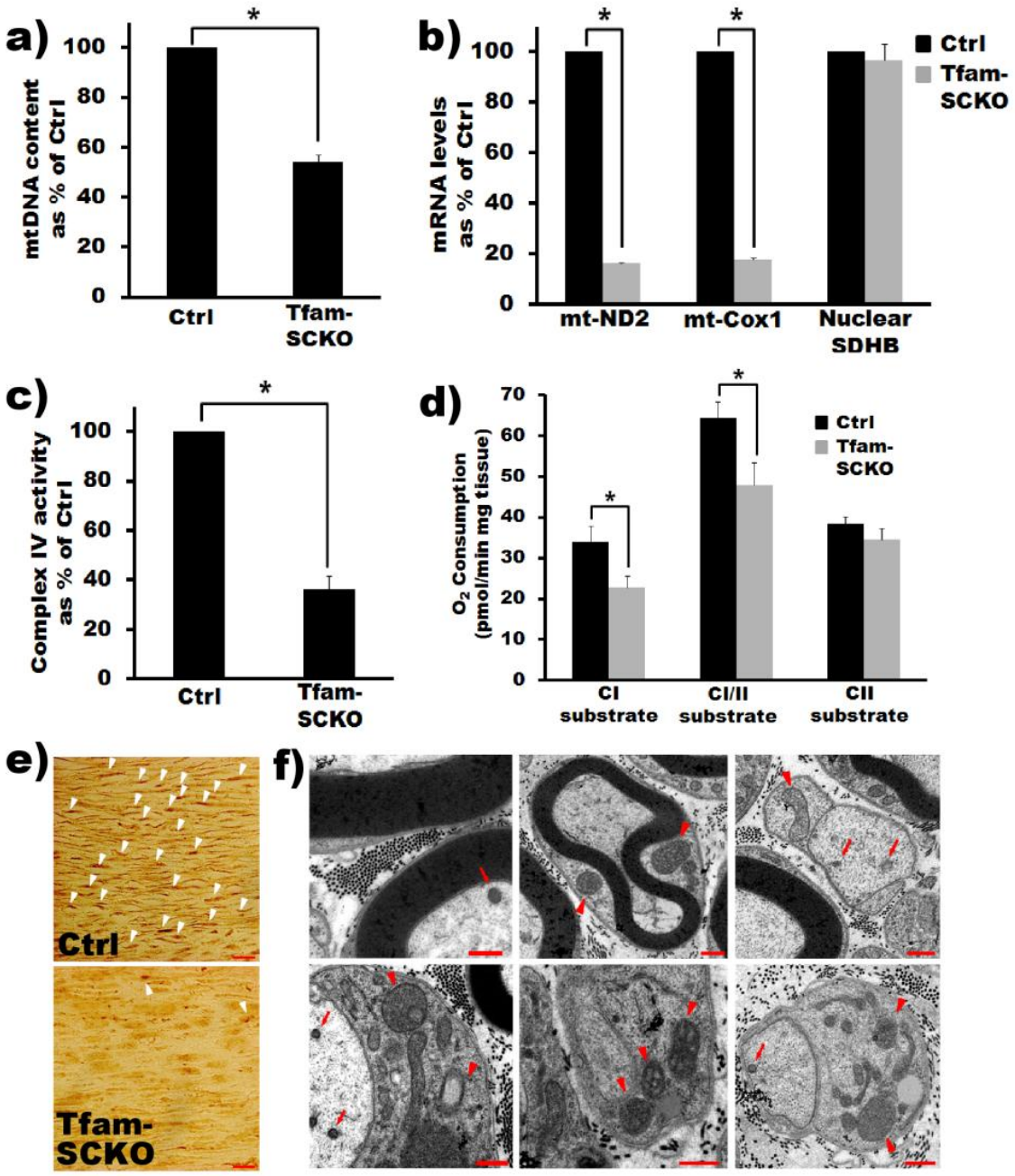
a)
mtDNA content as % of Ctrl
100
80
60
40
20
0
*
Ctrl
Tfam-SCKO
b)
mRNA levels as % of Ctrl
100
80
60
40
20
0
*
*
Ctrl
Tfam-SCKO
mt-ND2
mt-Cox1
Nuclear SDHB
c)
Complex IV activity as % of Ctrl
100
80
60
40
20
0
*
Ctrl
Tfam-SCKO
d)
O2 Consumption (pmol/min mg tissue)
70
60
50
40
30
20
10
0
*
*
Ctrl
Tfam-SCKO
CI substrate
CI/II substrate
CII substrate
e)
Ctrl
Tfam-SCKO
f)

Figure 3: Tfam-SCKOs develop a progressive degenerative peripheral neuropathy. ***a)*** Photograph of end-stage Tfam-SCKO mouse (≈8 months old). At this stage Tfam-SCKOs display a characteristic "swimming-gait" and are unable to support themselves on their hind legs. ***b)*** Typical nerve conduction trace from a 4 month old Tfam-SCKO mouse showing marked temporal dispersion. Scale bars 1ms and 1 mV. ***c, d)*** Electrophysiological studies of Tfam-SCKO mice show that, as early as 2 months of age, these mice have significantly reduced nerve conduction velocity (*c,* $p<0.001$, two-tailed Student's t-test) compared to littermate Ctrls. This deficit persists in 4 month old animals (*c,* $p<0.001$, two-tailed Student's t-test), which also have severe temporal dispersion as shown by an increased response duration *(d,* $p <0.001$, two-tailed Student's t-test). These findings indicate segmental demyelination. Error bars, SEM. N=4 mice per genotype at each age. ***e)*** Typical electromyography traces from a 4 month old Tfam-SCKO mouse showing fibrillation (arrowheads) and fasciculations (arrows), common findings in diseases involving motor axon loss, indicative of muscle fiber denervation and motor unit degeneration/regeneration. These findings were never present in Ctrl littermates. Scale bars 50 ms, 500 μV ***f)*** Hematoxylin and eosin stain of the gastrocnemius muscle from a Ctrl and a Tfam-SCKO mouse showing scattered and grouped muscle fiber atrophy (arrowheads). This is characteristic of motor axon degeneration. Scale bar 50 μm.

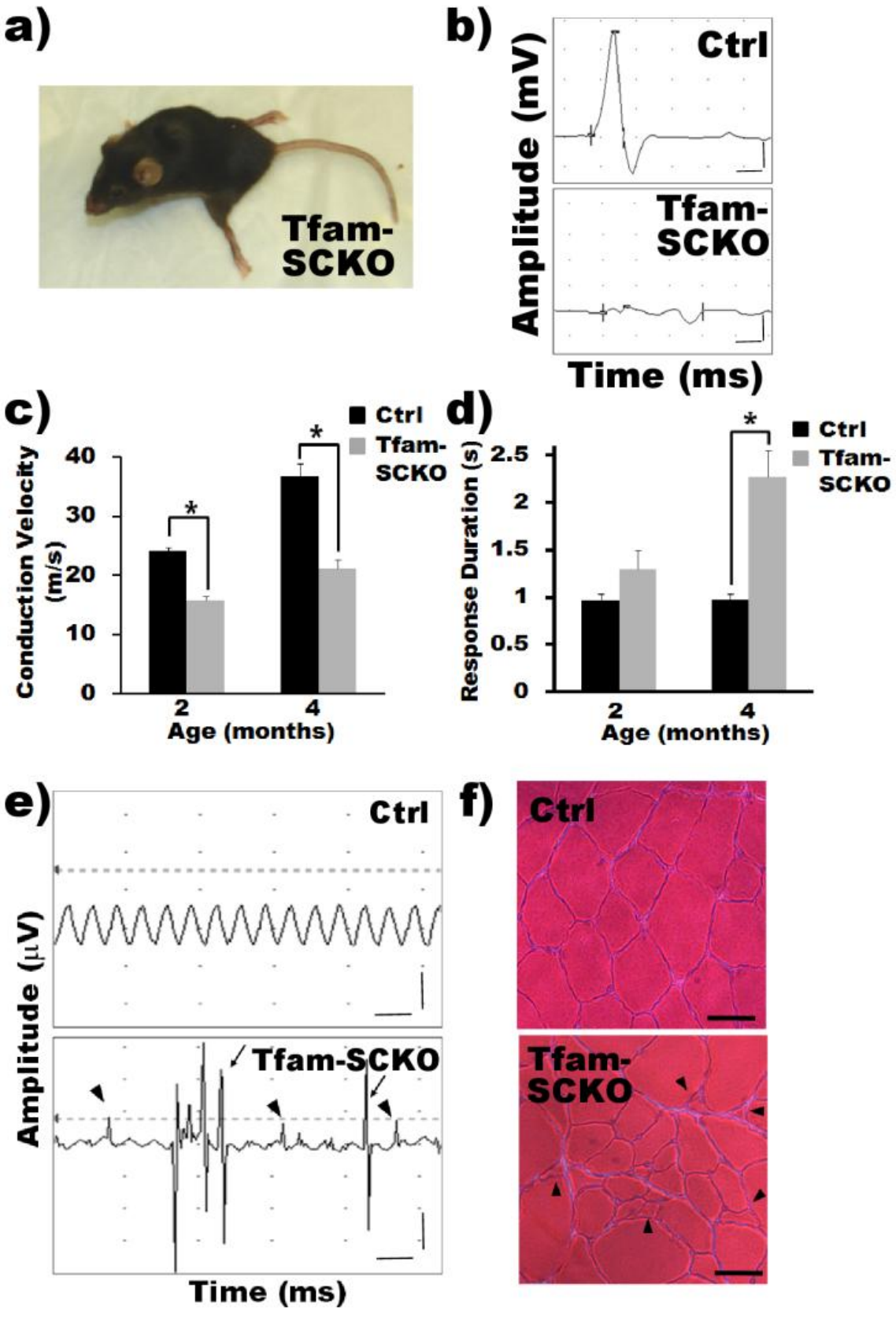
a)
Tfam-SCKO
b)
Ctrl
Amplitude (mV)
Tfam-SCKO
Time (ms)
c)
Ctrl
Tfam-SCKO
Conduction Velocity (m/s)
40
30
20
10
0
*
*
2
4
Age (months)
d)
Ctrl
Tfam-SCKO
Response Duration (s)
2.5
2
1.5
1
0.5
0
*
2
4
Age (months)
e)
Ctrl
Amplitude (μV)
Tfam-SCKO
Time (ms)
f)
Ctrl
Tfam-SCKO

Figure 4: Tfam-SCKOs display early preferential loss of small unmyelinated fibers. ***a-c)*** Toluidene blue stained plastic sections of 1 month old Tfam-SCKO sciatic nerve and littermate Ctrls *(a)* show that at this age there are no differences in the number of myelinated fibers *(b)* or the extent of myelination (g-ratio, axon area/fiber area) *(c)*. Scale bar 25 μm. Error bars, SEM. n=4 mice per genotype. ***d)*** Electron micrographs of 1 month old Ctrl and Tfam-SCKO sciatic nerves show that while large myelinated fibers are mostly normal in Tfam-SCKO mice at this age (arrows), the structure of Remak bundles (arrowheads) is largely abnormal. Scale bar 2 μm. ***e 1-4)*** Compared to Ctrl littermates (1), unmyelinated axons in Tfam-SCKO Remak bundles are found touching one another (2, 4, stars) and interspersed by pathological SC processes known as Bands of Bungner (2, arrowheads). Free-floating excess basement membrane (2, 3, arrows) enclosing SC cytoplasm (3**,** star) with few or no axons left, indicative of extensive degeneration of unmyelinated axons, is also visible. By 2 months of age most non-myelinating SCs are associated with unstructured, degenerating Remak bundles, containing abnormal axons (4, star) and filled with phagocytic vesicles and membranous debris (4, arrowhead). Scale bar 500 nm. ***f)*** Representative photographs of epidermal fiber innervation (arrowheads) in the foot pads of 2 month old Tfam-SCKO and littermate Ctrl mice. Scale bar, 10 μm ***g)*** Quantification of fiber density in the epidermis shows a 30% decrease in Tfam-SCKO by 2 months of age ($p=0.02$, two-tailed Student's t-test), indicating early degeneration of small unmyelinated C-fibers. Results reported are normalized to per unit area. Error bars, SEM; n=3 mice per genotype at each age.

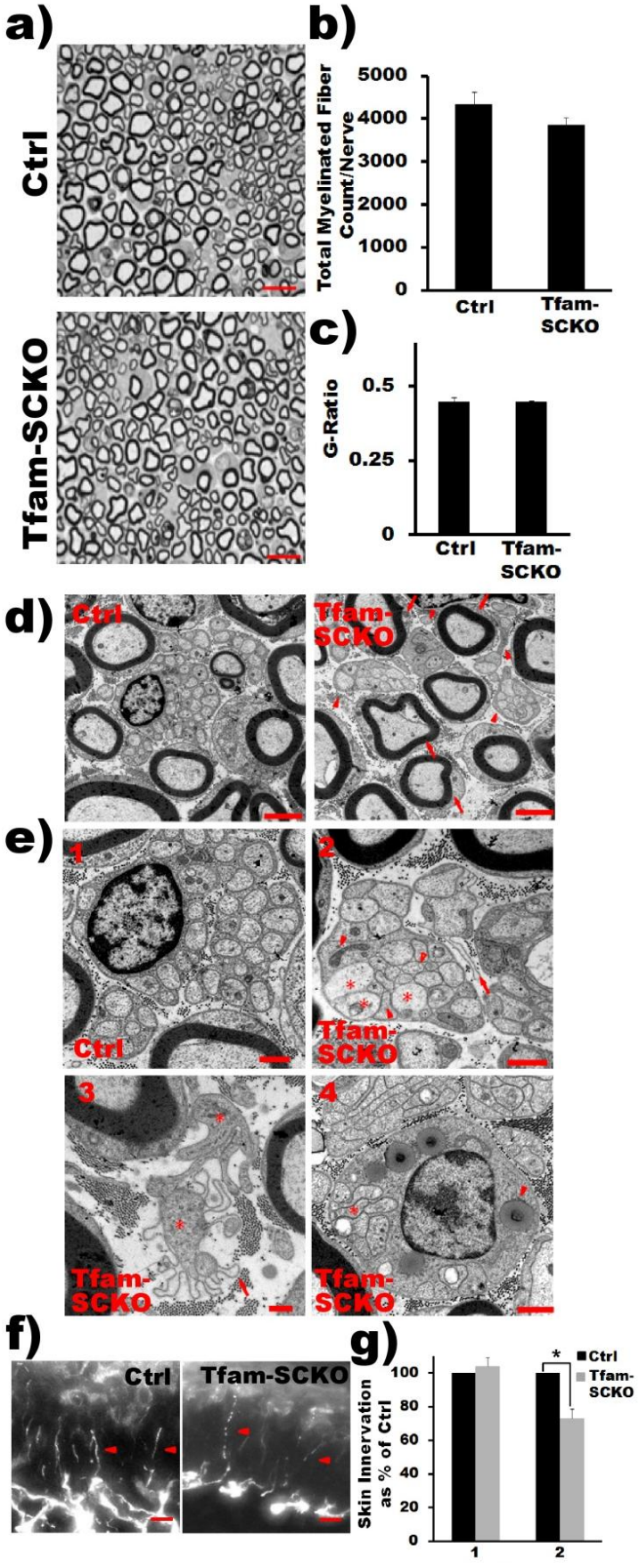
a)
b)
Ctrl
Tfam-SCKO
Total Myelinated Fiber Count/Nerve
5000
4000
3000
2000
1000
0
Ctrl
Tfam-SCKO
c)
G-Ratio
0.5
0.25
0
Ctrl
Tfam-SCKO
d)
Ctrl
Tfam-SCKO
e)
1
2
Ctrl
Tfam-SCKO
3
4
Tfam-SCKO
Tfam-SCKO
f)
Ctrl
Tfam-SCKO
g)
*
Ctrl
Tfam-SCKO
Skin Innervation as % of Ctrl
100
80
60
40
20
0
1
2

Figure 5: Degeneration of large caliber myelinated fibers in older Tfam-SCKOs. ***a, b)*** Toluidene blue stained plastic sections of Tfam-SCKO sciatic nerves and littermate Ctrls at different ages *(a)* and quantification of total number of myelinated profiles per nerve *(b)*. At 2 months, some initial signs of axonal degeneration are apparent (arrowhead) in Tfam-SCKO nerves, but at this age there are no differences in the number of myelinated fibers *(b)*. By 4 months there is prominent axonal degeneration, as shown by a significant decrease ($p>0.001$, two-tailed Student's t-test) in the total number of myelinated profiles in Tfam-SCKO nerves. Axonal degeneration worsens by 8 months of age ($p>0.001$, two-tailed Student's t-test). Scale bar 25 μm. Error bars, SEM. n=4 mice per genotype at each age. ***c 1-4)*** Electron micrographs of Tfam-SCKO nerves at different ages confirm that large myelinated fiber degeneration becomes prominent by 4 months of age (*2)* and worsens by 8 months (3*)*, as shown by large portions of endoneurium completely devoid of axons (stars). By 4 months of age actively demyelinating and degenerating axons filled with membranous debris (arrowheads) are also common in Tfam-SCKO nerves (4*)*.By this age segmental demyelination as shown by large caliber axons without myelin is also prominent (*2-4*, arrows). This type of pathology is not visible in Ctrl nerves (*1)*. Scale bar, 2 μm. ***d)*** Fiber size distribution analysis in Tfam-SCKO and Ctrl littermate nerves at different ages. No differences in fiber size distribution are evident despite severe axonal degeneration, indicating that myelinated fibers of all calibers are susceptible to degeneration. Error bars, SEM. n=4 mice per group at each age ***e)*** Osmicated teased fibers from 4 month old Tfam-SCKO nerves confirm the presence of segmental demyelination. Scale bar 25 μm.

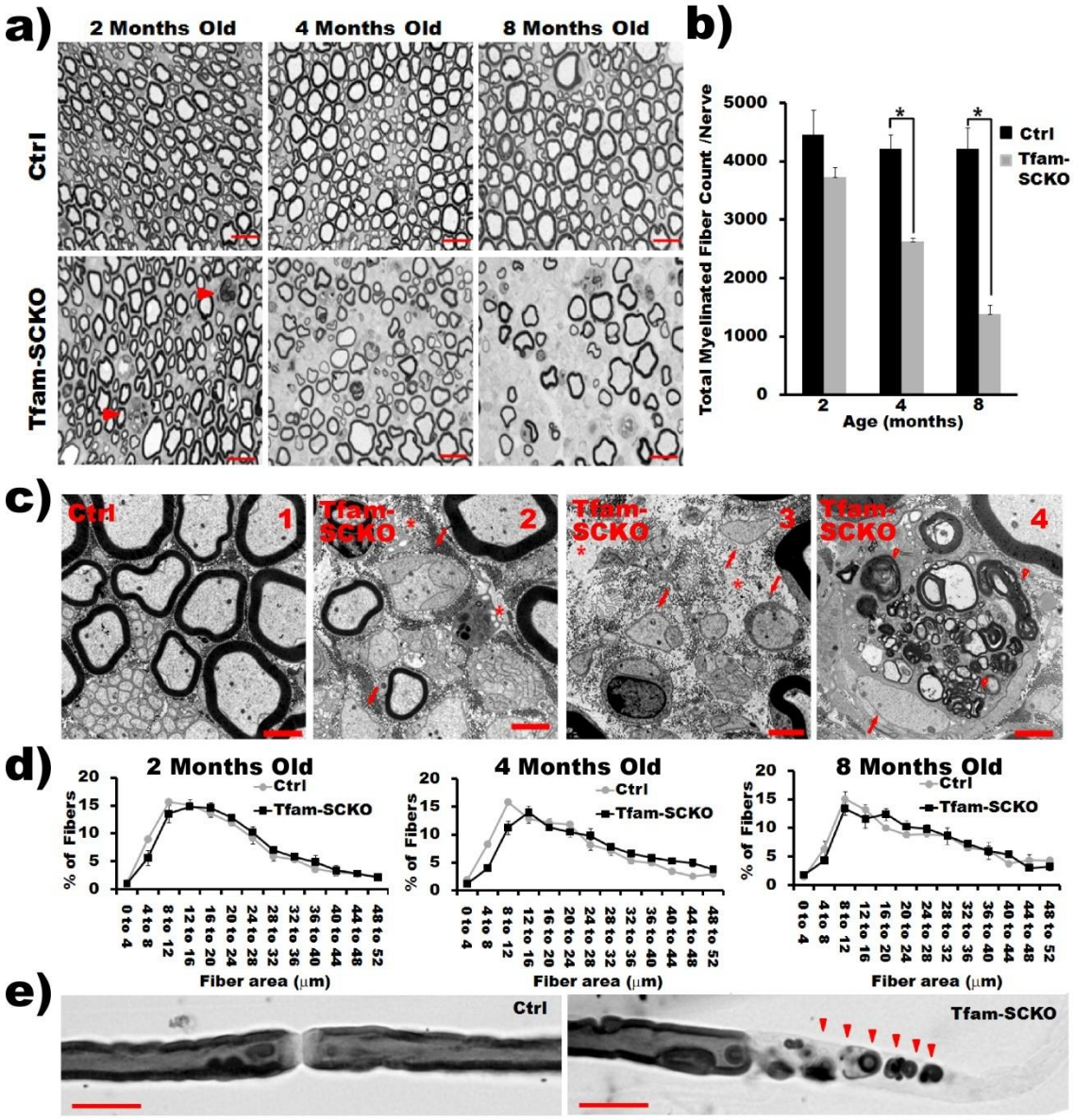
a)
2 Months Old
4 Months Old
8 Months Old
Ctrl
Tfam-SCKO
b)
Total Myelinated Fiber Count /Nerve
5000
4000
3000
2000
1000
0
2
4
8
Age (months)
Ctrl
Tfam-SCKO
c)
Ctrl
1
Tfam-SCKO
2
Tfam-SCKO
3
Tfam-SCKO
4
d)
2 Months Old
4 Months Old
8 Months Old
Ctrl
Tfam-SCKO
% of Fibers
Fiber area (µm)
0 to 4
4 to 8
8 to 12
12 to 16
16 to 20
20 to 24
24 to 28
28 to 32
32 to 36
36 to 40
40 to 44
44 to 48
48 to 52
e)
Ctrl
Tfam-SCKO

Figure 6: Tfam-SCKOs have behavioral deficits consistent with early loss of unmyelinated fibers followed by extensive degeneration of myelinated axons *a)* 2 month old Tfam-SCKOs are less sensitive to an applied noxious heat stimulus than Ctrl littermates ($p<0.01$, two-tailed Student's t-test), as shown by an increased withdrawal latency, which indicates loss of unmyelinated C-fiber nociceptors. This deficiency persists in 4 month old Tfam-SCKO mice ($p<0.01$, two-tailed Student's t-test). ***b-d)*** At 2 months of age, consistent with the early preservation of large myelinated motor axons, Tfam-SCKOs do not display significant motor deficits as shown by the inverted screen test *(b)* or accelerating rotarod *(c)*. 4 month old Tfam-SCKOSs, however, spend significantly less time on an inverted screen ($p<0.01$, two-tailed Student's t-test) *(b)* and accelerating rotarod ($p<0.01$, two-tailed Student's t-test) *(d)*, motor deficits that indicate the loss of large myelinated fibers by this age. Error bars, SEM. N=4 mice per genotype at each age.

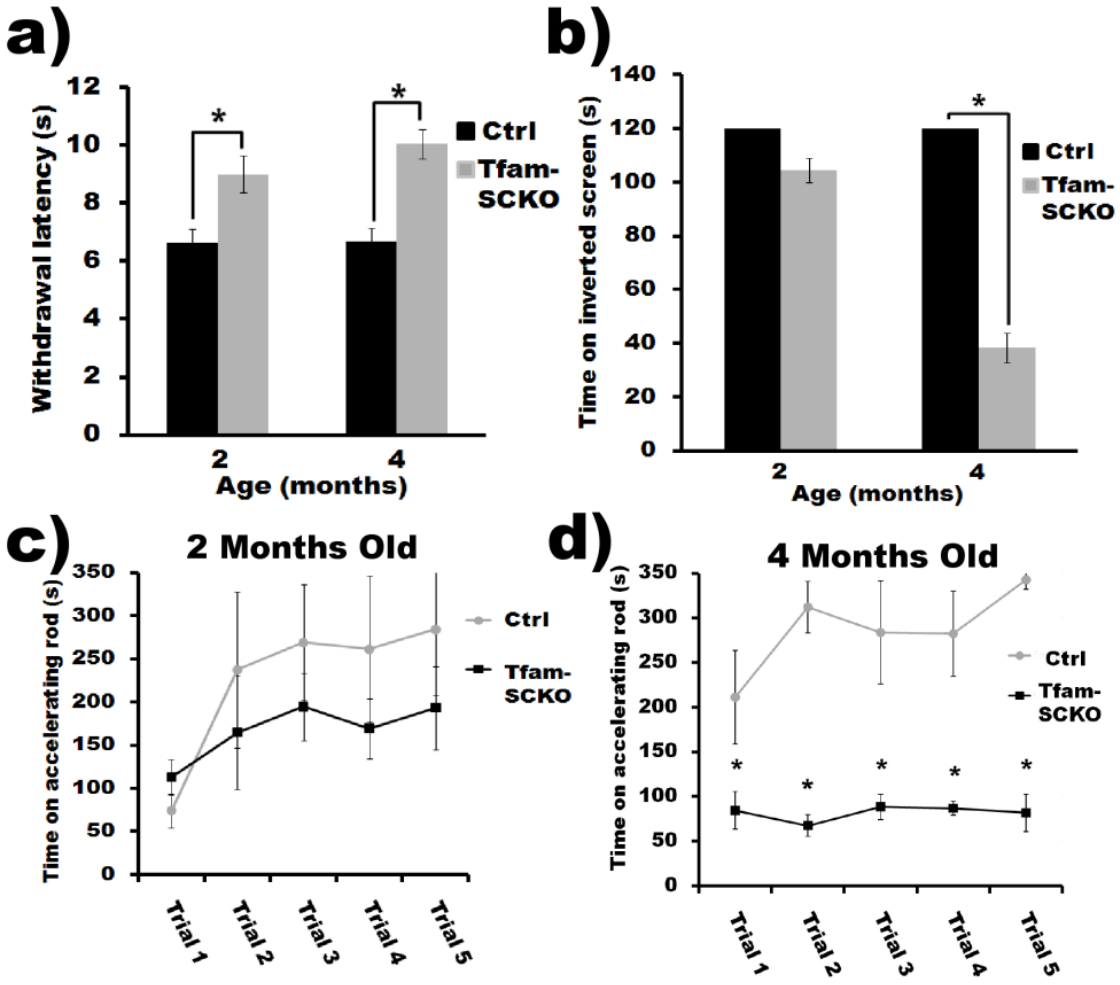
a)
Withdrawal latency (s)
12
10
8
6
4
2
0
*
*
Ctrl
Tfam-SCKO
2
4
Age (months)
b)
Time on inverted screen (s)
140
120
100
80
60
40
20
0
*
Ctrl
Tfam-SCKO
2
4
Age (months)
c)
2 Months Old
Time on accelerating rod (s)
350
300
250
200
150
100
50
0
Ctrl
Tfam-SCKO
Trial 1
Trial 2
Trial 3
Trial 4
Trial 5
d)
4 Months Old
Time on accelerating rod (s)
350
300
250
200
150
100
50
0
Ctrl
Tfam-SCKO
*
*
*
*
*
Trial 1
Trial 2
Trial 3
Trial 4
Trial 5

Figure 7: SC mitochondrial dysfunction does not compromise SC survival. ***a, b)*** Nuclear staining *(a Dapi)* and quantification *(b)* shows that there is no difference in the number of SC nuclei between Tfam-SCKO and Ctrl sciatic nerves at different ages. ***a, c)*** Quantification of Rosa-YFP immunofluorescence *(a YFP/DAPI, c)* in Tfam-SCKO/Rosa-YFP nerves at different ages shows that the majority of SCs are Tfam-deficient at all ages. ***a, d)*** Quantification of TUNEL immunohistochemistry *(a Tunel/DAPI, d)* of Tfam-SCKO and Ctrl littermate shows no differences in the number of TUNEL positive cells at different ages, indicating that SCs are able to survive despite the disruption in their mitochondria. Scale bar 100 μm. Error bars, SEM. n=3 mice per genotype at each age.

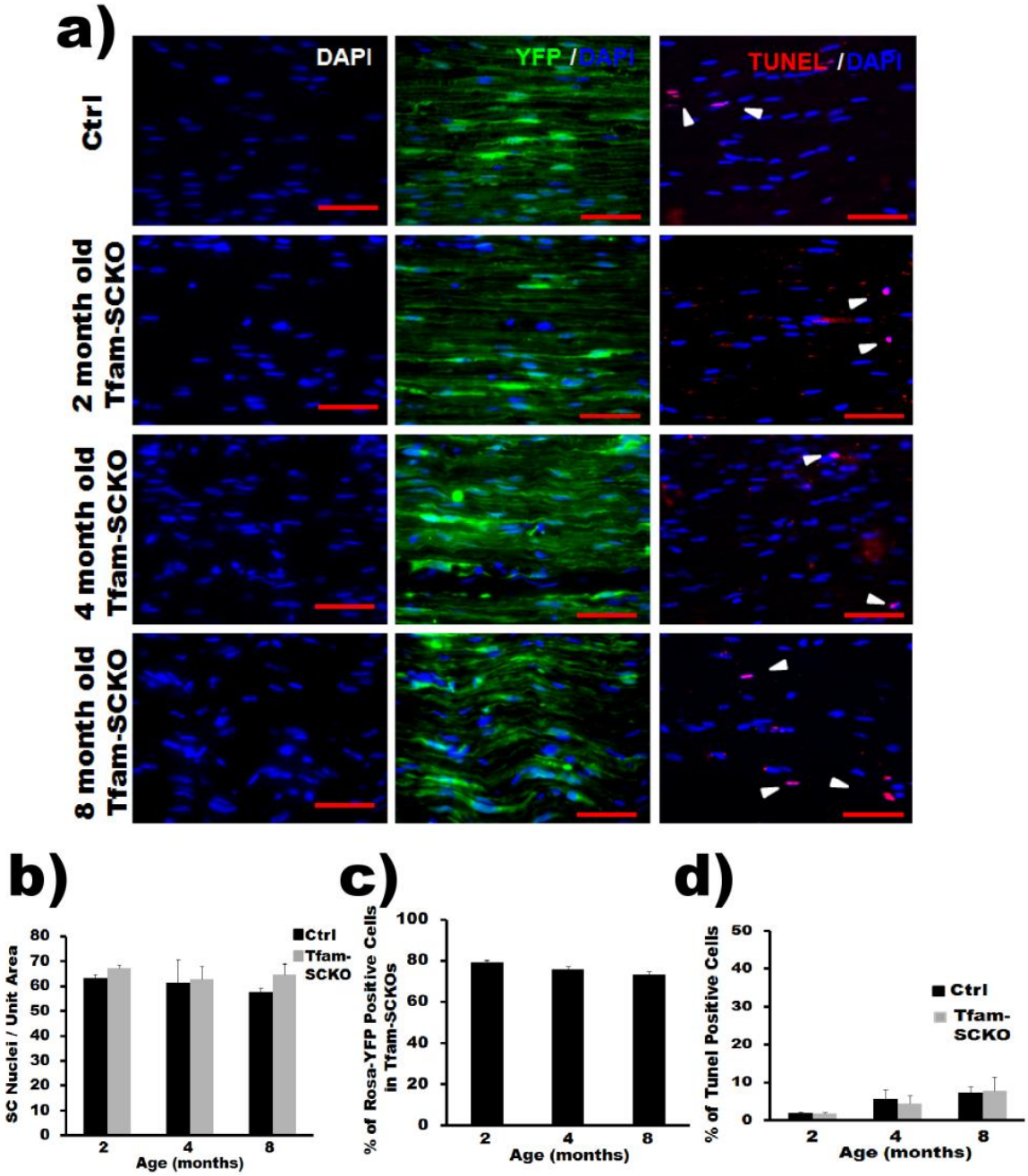
a)
DAPI
YFP / DAPI
TUNEL / DAPI
Ctrl
2 month old Tfam-SCKO
4 month old Tfam-SCKO
8 month old Tfam-SCKO
b)
SC Nuclei / Unit Area
Ctrl
Tfam-SCKO
Age (months)
c)
% of Rosa-YFP Positive Cells in Tfam-SCKOs
Age (months)
d)
% of Tunel Positive Cells
Ctrl
Tfam-SCKO
Age (months)

Figure 8: ***Tfam-deficient SCs support axonal regeneration but fail to remyelinate following injury. a, b)*** Phospho-histone 3 (PH3) immunostaining *(a)* and quantification *(b)* shows that there is no difference in the number of proliferating SCs (arrowheads) between Tfam-SCKO and Ctrl sciatic nerves 4 days after crush injury. Scale bar 100 μm. Error bars, SEM. n=at least 3 mice per genotype. ***c)*** Quantification of the amount of myelin debris present in Ctrl and Tfam-SCKO nerves 3 weeks after crush injury shows no impairment in the ability of Tfam-deficient SCs to break down existing myelin. Error bars, SEM. n=3 mice per genotype. ***d)*** Quantification of the number of myelinated profiles in Ctrl and Tfam-SCKO nerves 3 weeks after crush distal to the site of injury shows a significant decrease ($p<0.001$, two-tailed Student's t-test) in the number of myelinated profiles formed by Tfam-deficient SCs following injury. Error bars, SEM. n=3 mice per genotype. ***e)*** Electron micrographs of Ctrl and Tfam-SCKO nerves 3 weeks after crush depicting the inability of Tfam-deficient SCs to form mature myelin even though they are capable of supporting axonal regeneration. Scale bar, 2 μm. ***f)*** Quantification of the total number of fibers (myelinated and unmyelinated) distal to the site of injury 3 weeks after crush shows no differences between Tfam-SCKO and Ctrl nerves, confirming that Tfam-deficient SCs are able to support axonal regeneration. Error bars, SEM. n=3 mice per genotype ***g)*** Electron micrographs of Ctrl (1) and Tfam-SCKO (2-4) large caliber fibers distal to the site of injury 3 weeks after crush showing that while Tfam-deficient SCs are capable of ensheathing axons and forming 1 to 1 associations with them (arrowheads, axons; arrows, SCs) they are not able to form mature myelin. Regenerating Remak bundles are present in Ctrl nerves (5) but are absent in Tfam-SCKO nerves (6; arrowheads, axons; arrows, SCs). ***h)*** Proportion of axons larger than 1 μm is

similar between Tfam-SCKO and Ctrl nerves following injury and cannot explain the absence of myelin in Tfam-SCKO nerves.

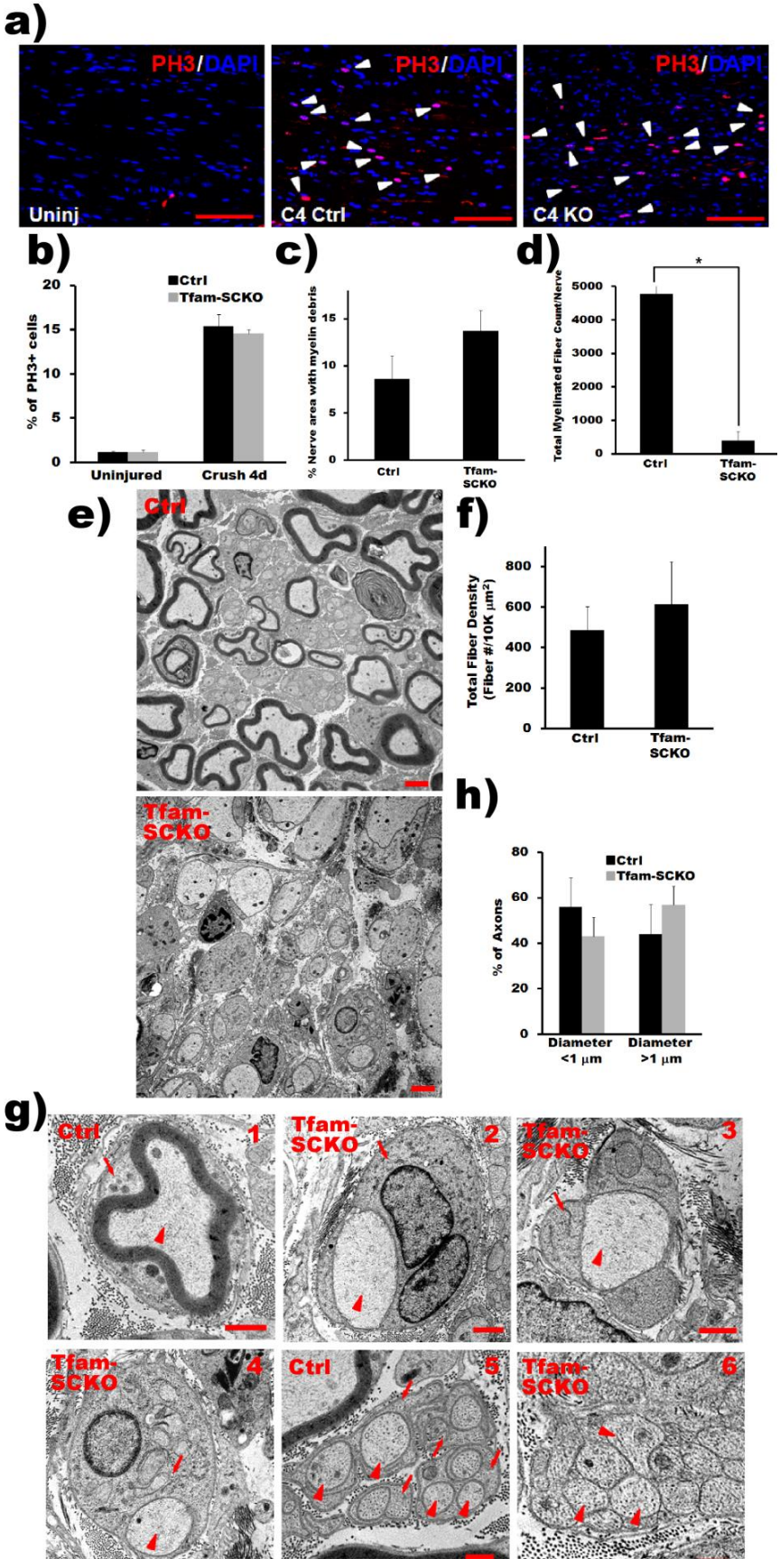
a)
PH3/DAPI
Uninj
C4 Ctrl
C4 KO
b)
Ctrl
Tfam-SCKO
% of PH3+ cells
Uninjured
Crush 4d
c)
% Nerve area with myelin debris
Ctrl
Tfam-SCKO
d)
Total Myelinated Fiber Count/Nerve
Ctrl
Tfam-SCKO
e)
Ctrl
Tfam-SCKO
f)
Total Fiber Density (Fiber #/10K μm²)
Ctrl
Tfam-SCKO
h)
Ctrl
Tfam-SCKO
% of Axons
Diameter <1 μm
Diameter >1 μm
g)
Ctrl
Tfam-SCKO
1
2
3
4
5
6

Supplementary Figure 1: Tfam-SCKOs initially develop and myelinate normally. ***a-c)*** Toluidene blue stained plastic sections of 2 week old Tfam-SCKO sciatic nerve and littermate Ctrls *(a)* show that at this age there are no differences in the number of myelinated fibers *(b)* or extent of myelination *(c)* (g-ratio, axon area/fiber area). Scale bar 25 μm. Error Bars, SEM. n= 3 mice per genotype ***d,e)*** Electron micrographs from 2 week old Tfam-SCKO sciatic nerve and littermate Ctrls confirm that myelin *(d)* as well as nodes of Ranvier initially develop normally. N, node; Mv, microvilli; Pn, paranode; arrowheads, paranodal loops. Scale bar 2 μm *(d)* and 500 nm (magnified panels)*(e).* ***f)*** Immunostaining of teased nerve fibers from 3 week old Tfam-SCKO and Ctrl mice with antibodies against nodal (Nav1.6), paranodal (Caspr) and juxtaparanodal (Kv1.1) markers confirm that nodal architecture initially develops normally in these mice. Scale bar 50 μm.

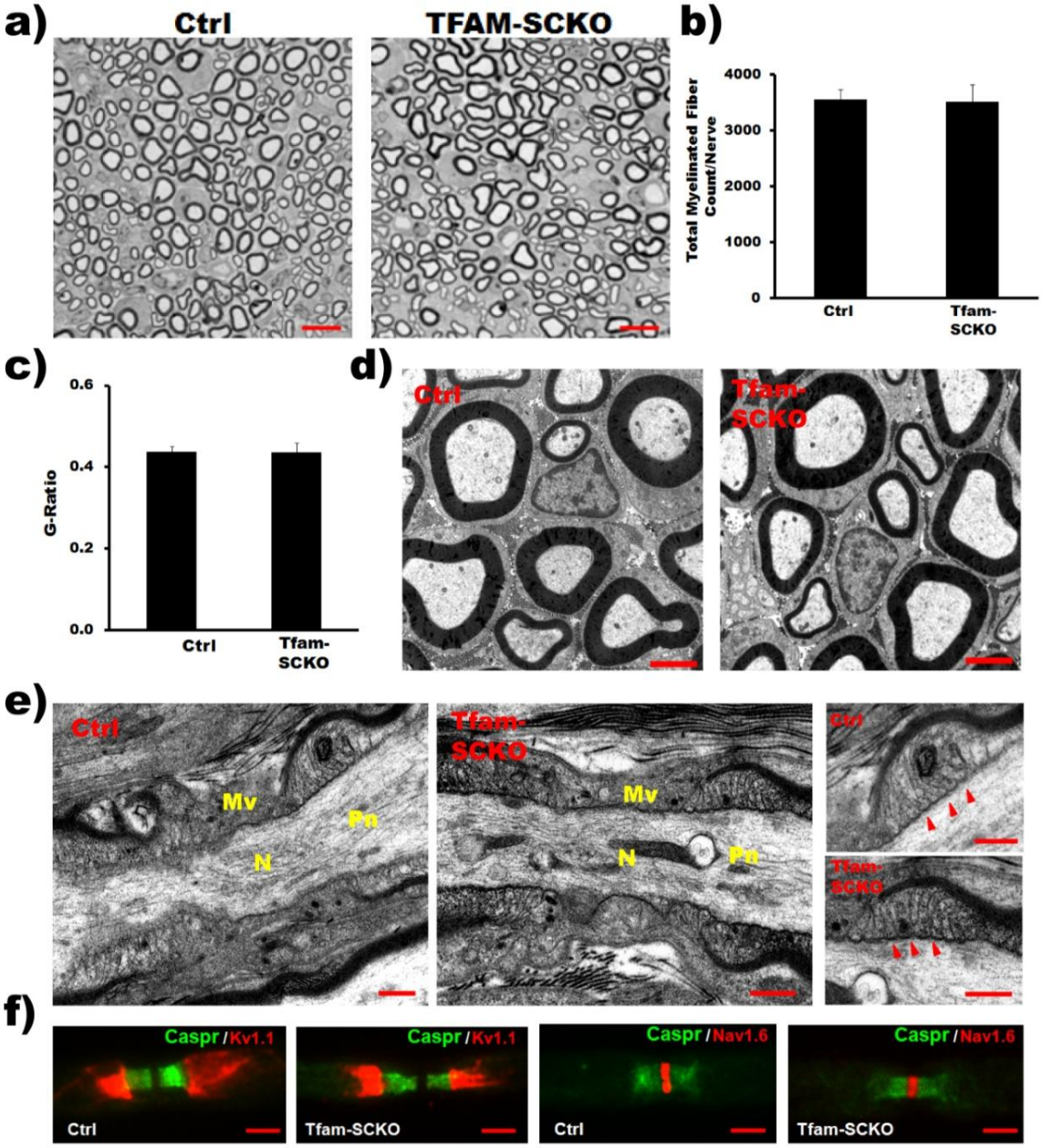
a)
Ctrl
TFAM-SCKO
b)
Total Myelinated Fiber Count/Nerve
4000
3000
2000
1000
0
Ctrl
Tfam-SCKO
c)
G-Ratio
0.6
0.4
0.2
0.0
Ctrl
Tfam-SCKO
d)
Ctrl
Tfam-SCKO
e)
Ctrl
Mv
Pn
N
Tfam-SCKO
Mv
N
Pn
Ctrl
Tfam-SCKO
f)
Caspr / Kv1.1
Ctrl
Caspr / Kv1.1
Tfam-SCKO
Caspr / Nav1.6
Ctrl
Caspr / Nav1.6
Tfam-SCKO

CHAPTER 3:

Mitochondrial Dysfunction-induced Abnormalities in Schwann Cell Lipid Metabolism Lead to Axonal Degeneration and Peripheral Neuropathy

Adapted from: Viader A, Sasaki Y, Yang K, Gross RW, Milbrandt J. (2011). Mitochondrial dysfunction-induced abnormalities in Schwann cell lipid metabolism lead to axonal degeneration and peripheral neuropathy. Submitted.

Abstract

Mitochondrial dysfunction is a common cause of peripheral neuropathy. Much effort has been devoted to examining the role played by neuronal/axonal mitochondria, but how mitochondrial deficits in peripheral nerve glia (Schwann cells, SCs) contribute to peripheral nerve diseases remains unclear. Here, we investigate a mouse model of peripheral neuropathy secondary to SC mitochondrial dysfunction (Tfam-SCKOs). We show that disruption of SC mitochondria activates a maladaptive integrated stress response and causes a shift in lipid metabolism away from fatty acid synthesis toward oxidation. These alterations in SC lipid metabolism result in depletion of important myelin lipid components as well as in extensive accumulation of acylcarnitines, an intermediate of fatty acid β-oxidation. Importantly, we show that acylcarnitines are released from SCs and induce axonal degeneration. Altered SC lipid metabolism accompanied by toxic accumulation of lipid intermediates is thus an underlying pathological mechanism in mitochondria-related peripheral neuropathies.

Introduction

Mitochondrial metabolic irregularities are a common culprit in diverse neurodegenerative diseases and are key pathological contributors to peripheral neuropathy. Mitochondrial dysfunction is thought to be largely responsible for the peripheral nerve deficits that afflict up to 50% of all people with diabetes and can lead to incapacitating pain, sensory loss, and debilitating muscle weakness [1]. Similarly, a number of mutations in mitochondrial proteins have now been identified as the cause of several forms of inherited neuropathies known as Charcot Marie Tooth (CMT) [2]. The need to elucidate the manner in which mitochondrial dysfunction underlies progression of peripheral nerve disease is thus well appreciated; to date much effort has been devoted to clarifying the role played by neuronal/axonal mitochondria [3].

Glial cells, the main non-neuronal cell component of the nervous system, are involved in virtually every aspect of nervous system function [4]. Moreover, glia are increasingly recognized to influence neurodegenerative diseases traditionally thought to be neuron autonomous (e.g. amyotrophic lateral sclerosis) [5]. Schwann cells (SCs), the glial cells in the peripheral nervous system (PNS), intimately associate with all peripheral nerve axons to support their long-term preservation and function [6-8]. Moreover, SCs are also essential for peripheral nerve repair after axonal damage [9]. Interestingly, SCs from nerves of patients with neuropathy often present with abnormal mitochondria [10, 11]. Given this critical involvement of SCs in the maintenance of peripheral nerves and the role of mitochondria in cell energy and anaplerotic metabolism, mitochondrial dysfunction in these glia is likely to contribute to disease progression of peripheral neuropathies.

With the goal of understanding whether SC mitochondrial abnormalities affect axonal survival and peripheral nerve function we recently generated mice (Tfam-SCKOs) with disrupted mitochondrial metabolism exclusively in SCs [12]. Using this novel model of peripheral neuropathy, the present work demonstrates that SC mitochondrial dysfunction activates a maladaptive integrated stress response and causes a shift in lipid metabolism away from new lipid synthesis towards increased fatty acid oxidation. This metabolic alteration results in early depletion of myelin lipid components as well as a large accumulation of acylcarnitine lipid intermediates. Importantly, we show that acylcarnitines are released from SCs and induce axonal degeneration. Altered SC lipid metabolism accompanied by the toxic accumulation of lipid intermediates is thus an underlying mechanism of axonal degeneration and demyelination in peripheral neuropathies and constitutes a potentially important therapeutic target.

Results

Energy depletion does not drive nerve pathology in Tfam-SCKO mice

To directly interrogate the contribution of SC mitochondrial dysfunction to peripheral neuropathy, we recently generated mice (Tfam-SCKOs) with impaired mitochondrial function exclusively in SCs [12]. These mice were produced through the tissue-specific deletion of the mitochondrial transcription factor A gene (*Tfam*), which is required for mtDNA transcription and replication and when excised induces progressive defects in the mitochondrial electron transport chain [13]. Interestingly, induction of SC-specific mitochondrial dysfunction did not affect SC survival; instead, these deficits resulted in a severe, progressive peripheral neuropathy characterized by extensive axonal

degeneration that recapitulated critical features of human neuropathy. Tfam-SCKO nerves displayed early morphological abnormalities and preferential loss of small unmyelinated C fibers (starting at 1-2 months of age, Fig. 1a) followed by the degeneration of large-caliber myelinated axons (starting at 3-4 months of age, Fig 1b and c) [12]. Extensive demyelination was apparent at late stages of the disease (Fig 1b). Consistent with this nerve pathology, Tfam-SCKO mice developed progressive distal weakness and sensory deficits [12], common symptoms in patients with peripheral neuropathy.

Having established the utility of the Tfam-SCKO mouse model in understanding and potentially treating peripheral neuropathies, we explored causal mechanisms of the nerve pathology in these mice. We focused on identifying processes that drive disease progression in 2 month old Tfam-SCKOs, an age when SC mitochondrial function is already disrupted yet Tfam-SCKO nerves display only limited, early pathological changes (Fig 1c) [12]. All experiments described below were carried out on mice this age. We first determined the energy status of Ctrl and Tfam-deficient SCs, because clinical deficits in diseases associated with mitochondrial dysfunction are often assumed to be directly related to depletion of cellular energy levels. Surprisingly, HPLC measurement of nerve adenylate pools and determination of the Adenylate Energy Charge (EC), an index used to measure cellular energy status (see methods) [14], revealed only a very slight energy reduction (≈8%) in Tfam-SCKO nerves (EC Ctrl=0.812 +/- 0.009; EC Tfam-SCKO=0.747 +/-0.008; $p<0.001$; Fig. 1d). Increased mitochondrial content and glycolysis in Tfam-deficient SCs (Supplementary Fig.1), two metabolic adaptations that often follow mitochondrial deficits [15, 16], likely account for this relative preservation of

energy levels in Tfam-SCKO nerves. When we assessed the activation status (phosphorylation at Thr172) of the cellular energy sensor AMP-activated protein kinase (AMPK) [17], we observed no differences between Ctrl and Tfam-SCKO nerves (Fig. 1e and f). This indicates that Tfam-deficient SCs do not experience a significant energy depletion to an extent that is likely responsible for the pathology observed in the nerves of these mice.

Mitochondrial dysfunction activates a maladaptive stress response and shifts the balance of lipid metabolism in SCs

In an attempt to identify other potential disease-causing processes, we carried out gene expression profiling of 2 month old Ctrl and Tfam-SCKO nerves. This analysis uncovered the upregulation of a number of genes activated by the integrated stress response (ISR), including *Chop10, Asns,* and *Trib3,* in SCs with disrupted mitochondrial metabolism (data not shown). The ISR is an evolutionarily conserved, "stress"-activated, gene expression program controlled by the phosphorylation of translation initiation factor 2α (eIF2α) [18]. Importantly, previous studies examining neuropathy models induced by mutations in structural myelin proteins have shown that activation of the ISR by endoplasmic reticulum (ER) accumulation of the mutant proteins is particularly maladaptive to SCs [19]. Thus, we first used qRT-PCR to confirm the activation of ISR in Tfam-SCKOs nerves and verified the upregulation of ISR target genes (Fig 2a). Moreover, Western blot analysis showed hyper-phosphorylation of eIF2α in Tfam-SCKO nerves compared to Ctrl (Fig. 2b), further establishing the activation of ISR following SC mitochondrial dysfunction.

To ensure that ISR activation in Tfam-SCKO nerves was a primary effect of mitochondrial defects in Tfam-deficient SCs, we treated SCs *in vitro* with mitochondrial inhibitors (e.g. FCCP, antimycin, oligomycin) and examined the effect on the activity of the pathway. Application of mitochondrial inhibitors on SCs *in vitro* also increased phosphorylation of eIF2α (Fig. 2c) and induced ISR target genes (Fig. 2d). These results suggest that the activation of the ISR in Tfam-SCKO nerves was a consequence of SC mitochondrial deficits. Note, however, that unlike previous reports on other mouse models of neuropathy [19], activation of the ISR in Tfam-SCKOs was not associated with ER stress or an unfolded protein response (UPR). Levels of activated PERK (as determined by its phosphorylation), the main ER-stress sensor known to induce ISR [18], were not elevated in Tfam-SCKO nerves (Fig. 2e). Similarly, IRE-1, a second ER stress sensor normally activated by the UPR [18], was not engaged either in Tfam-SCKO nerves or in cultured SCs treated with mitochondrial inhibitors (as determined by splicing of the IRE-1 target Xbp-1; Fig. 2f). Therefore, SC mitochondrial electron transport chain deficits activate ISR through a process that is distinct from ER-stress. Maladaptive activation of the ISR in SCs by a variety of stressors may thus be a central pathological mechanism common to different forms of peripheral neuropathy.

The downstream cellular processes initiated by the ISR that are maladaptive to SCs are unclear. Recent reports have linked activation of this pathway to a decrease in expression of lipid biosynthesis genes [20] as well as alterations in intermediate lipid metabolism [21]. Moreover, increased expression of the ISR target gene *Trib3,* which we found to be highly upregulated in Tfam-SCKO nerves, shifts the balance of fatty acid metabolism away from lipogenesis and toward oxidation in muscle and fat cells [22]. Given

the central role of lipids in the normal biology of SCs (e.g. myelin formation) (Chrast et al., 2010) and the importance of mitochondria to lipid metabolic reactions (e.g. as a source of intermediates), we hypothesized that nerve deficits in neuropathies modeled by Tfam-SCKO mice might be largely caused by alterations in SC lipid metabolism secondary to mitochondrial derangements. Consistent with this idea we found that differentially expressed genes in Tfam-SCKO vs. Ctrl nerves were enriched for targets involved in lipid metabolism. Lipid-related metabolic pathways were in fact over-represented among differentially expressed genes in Tfam-SCKO nerves (Fig. 3a). qRT-PCR confirmed that a number of genes critically involved in lipid synthesis were downregulated in Tfam-deficient SCs following mitochondrial dysfunction, including fatty acid synthetase (FASN) and HMG-CoA reductase (HMGCR) (Fig. 3b). Moreover, we found that Acetyl-coA carboxylase (ACC) phosphorylation, which inhibits the activity of this enzyme (Fig. 3c), was increased 3-fold in Tfam-SCKO nerves compared to Ctrls (Fig. 3d and e). ACC supplies malonyl-coA required for lipid biosynthesis and as such critically regulates the balance between lipid synthesis vs. oxidation (Fig. 3c) [23]. Increased phosphorylation of ACC in Tfam-SCKO nerves and decreased expression of lipid synthetic genes is consistent with a shift in lipid metabolism away from new lipid synthesis and towards increased lipid oxidation. Together, these results show that mitochondrial dysfunction in SCs activates a maladaptive stress response and remodels SC lipid metabolism.

SC mitochondrial dysfunction causes depletion of myelin lipids and accumulation of fatty acid oxidation intermediates

The signs of altered lipid metabolism in SCs with disrupted mitochondria prompted us to examine in more detail the implications of these changes for the pathology observed in Tfam-SCKO nerves. To this end, we analyzed the lipid composition of 2 month old Ctrl and Tfam-SCKO nerves using multidimensional mass spectrometry-based shotgun lipidomics. This method provides a comprehensive description of alterations in cellular lipids by identifying and quantifying individual lipid molecular species in a high-throughput fashion from a database of over 36,000 potential lipid molecular species [24]. Among all the different lipid classes examined, cerebrosides and sulfatides were the only lipid classes showing a depletion in 2 month old Tfam-SCKO nerves compared to Ctrls, with a 30% and a 40% reduction respectively (Fig. 4a and b, Supplementary Fig. 2a). In peripheral nerves, cerebrosides and sulfatides are almost exclusively produced by SCs and are particularly enriched in myelin; together they represent almost 30% of all lipid content in peripheral myelin [25]. The depletion of these two important myelin glycosphingolipids from Tfam-SCKO nerves is in agreement with our observations suggesting that mitochondrial dysfunction in SCs results in a metabolic shift away from lipid biosynthesis. Moreover, sulfatide and cerebroside depletion disrupts saltatory conduction of action potentials by increasing myelin fluidity and interfering with the maintenance of SC-axon contacts [26-28]. The reduction of myelin lipid components induced by mitochondrial dysfunction may underlie the prominent demyelinating phenotype apparent in late stages of the disease in Tfam-SCKO mice (Fig. 1b and d) [12]. This is supported by the observation that depletion of sulfatides and cerebrosides preceded the extensive demyelination or reduction in expression of myelin proteins in Tfam-SCKO nerves (Fig.1b and c, Fig. 4c) [12].

The most prominent alteration in lipid composition in 2 month old Tfam-SCKO nerves was a 25-fold increase in acylcarnitine species (Fig. 5a). This dramatic increase affected most long-chain acylcarnitines with some species being hundreds of times higher in Tfam-SCKO nerves compared to Ctrls (Fig. 5b, Supplementary Fig. 2b). Acylcarnitines are intermediates in the transport of fatty acyl groups across the mitochondrial membrane required for them to undergo mitochondria fatty acid β-oxidation, an important source of cellular energy and anabolic metabolites [29]. Fatty acids longer than 10 carbon atoms are converted to acylcarnitines to be shuttled into the mitochondrial matrix, the site of β-oxidation, where they are oxidized through repeated cycles of four enzymatic reactions that catalyze this process (Fig. 5c) [29]. Increased acylcarnitine levels in Tfam-SCKO nerves, therefore, support our previous observations suggesting a shift away from lipid synthesis toward oxidation following SC mitochondrial deficits (Fig. 3). The severity of the acylcarnitine accumulation in Tfam-deficient SCs, however, likely indicates that the increased shunting of lipids toward β-oxidation was accompanied by a decrease in the ability of SCs to oxidize them. The large presence of hydroxy-acylcarnitines (Fig. 5d) and reduced NAD^+/NADH ratio in Tfam-SCKO nerves (Fig. 5e), likely related to the inability of Tfam-deficient SCs to re-oxidize NADH as mitochondrial dysfunction worsened, suggests the inhibition of the rate determining step in β-oxidation of fatty acids that is catalyzed by 3-hydroxyacyl CoA dehydrogenase. This step normally converts β-hydroxy-acyl-CoA to keto-acyl-CoA (Fig. 5c); inhibition of this NAD^+-dependent step of β-oxidation (by a decreased NAD^+/NADH ratio) leads to accumulation of the transient intermediate 3-hydroxy acyl CoA, which can then be converted to hydroxy-acylcarnitines (Fig. 5c) [30, 31].

The accumulation of acylcarnitine β-oxidation intermediates can be toxic and has been observed to exacerbate pathological states [32]. We hypothesized therefore that accumulation of acylcarnitines in Tfam-SCKO nerves may contribute to the neuropathy present in these mice. In fact, genetic diseases that inhibit fatty acid β-oxidation and lead to a significant accumulation of acylcarnitines often present with severe forms of peripheral neuropathy [33, 34]. Together, these results suggest that depletion of myelin lipid components and accumulation of toxic lipid intermediates in SCs with dysfunctional mitochondria are underlying pathological mechanisms in peripheral neuropathies.

Acylcarnitines can be released from SCs and cause axonal toxicity

Given the dramatic increase in acylcarnitine concentration in Tfam-SCKO nerves we examined the possibility that acylcarnitines cause the axonal degeneration observed in Tfam-SCKO mice. This amphiphilic metabolite adversely alters the properties of membranes and ion channels with devastating effects. In the heart, for example, acylcarnitine-mediated disruption of ion homeostasis can predispose the myocardium to lethal ventricular tachyarrhythmias and sudden death during ischemic episodes [35-37]. Given the ability of acylcarnitines to cross the plasma membrane [29] and the intimate association between SCs and axons in peripheral nerves, we hypothesized that release of acylcarnitines from SCs onto the surrounding axons could alter axonal membrane properties and ion homeostasis and contribute to the severe axon degeneration phenotype in Tfam-SCKO nerves as well as in neuropathies that present with prominent axonal loss.

To test this hypothesis we first examined whether long-chain acylcarnitines are released from SCs onto surrounding axons. Two-month old Ctrl and Tfam-SCKO nerves

were cultured as explants for 2.5 days. At the end of this time, we measured the amount of long-chain acylcarnitines released from the nerves into the culture media. While Ctrl nerves released very low levels of long-chain acylcarnitines into the surrounding media, Tfam-SCKO nerves secreted 35-fold more long-chain acylcarnitines (primarily C16 and C18; Fig. 6a). Remarkably, the buildup of long-chain acylcarnitines from a single Tfam-SCKO nerve in 100 μl of media reached up to ≈ 2 μM within 2.5 days. Tfam-deficient SCs therefore not only accumulate acylcarnitines following mitochondrial dysfunction, but also release them in significant quantities onto surrounding axons.

We next assessed the ability of acylcarnitines to disrupt axonal membrane properties and ion homeostasis. We specifically focused on the effect of acylcarnitines on axonal calcium levels (Ca^{2+}), since long-chain acylcarnitines have been previously shown to alter Ca^{2+} homeostasis in cardiac and skeletal muscle [37]. Ca^{2+} is also important for axonal integrity and function; intra-axonal Ca^{2+} elevation often leads to severe axon degeneration [38], and its homeostasis is disrupted in peripheral neuropathies [39]. Acute application of palmitoyl-carnitine, one of the most highly increased acylcarnitine species in Tfam-SCKO nerves, caused a significant elevation of intracellular Ca^{2+} in cultured dorsal root ganglion (DRG) neurons loaded with the calcium dye Fluo-4 (Fig. 6b and c). This rise in intracellular Ca^{2+} took place within minutes after exposure to acylcarnitine, was dose-dependent, and was specific to acylcarnitines; application of the corresponding free fatty acid at the same concentrations exerted no comparable effect (Fig. 6b and c). The acute influx of Ca^{2+} after addition of palmitoyl-carnitine also caused significant axonal blebbing (Fig. 6b and d), which when severe enough results in axonal degeneration.

Finally, we explored the long-term effect of chronic exposure to moderate levels of acylcarnitines on axonal stability as this more likely recapitulates the situation *in vivo*. For these experiments we applied 25 μM palmitoyl-carnitine onto DRG neurons daily for up to nine days; this concentration caused no immediate axonal degeneration when applied acutely and was close to the range of long-chain acylcarnitines released from a single Tfam-SCKO nerve cultured as an explant (Fig. 6a). Interestingly, axons were able to withstand exposure to 25 μM palmitoyl-carnitine for up to four days. After four days, however, prominent axonal blebbing started to develop and axonal degeneration followed soon thereafter and progressively worsened (Fig. 6e and f). Note, that 12.5 μM palmitoyl-carnitine applied chronically resulted in axons of unhealthy appearance that displayed morphological abnormalities, but no statistically significant increase in the degeneration index of these axons was observed within the time frame of our experiments (data not shown). Together, these results demonstrate that the long-chain acylcarnitines that accumulate in SCs following mitochondrial dysfunction can be released out of these glia onto the surrounding axons. Moreover, exposure of axons to long-chain acylcarnitines can disrupt axonal membrane properties and ion homeostasis, compromising axonal stability over time.

Discussion

In the present study we have found that a lipid metabolic shift away from synthesis towards oxidation is induced in SC following mitochondrial dysfunction. This metabolic shift is induced, at least in part, by the activation of a conserved stress response (the ISR), which is maladaptive in SCs. We demonstrate that this shift in lipid

metabolism results in the depletion of important lipid myelin components, which preceded overt demyelination and is therefore a likely driver of this process in mitochondria-related neuropathies. Finally, we propose a novel mechanism by which lipid abnormalities in SCs can exacerbate axonal loss in peripheral neuropathies through the release of toxic long-chain acylcarnitines (Fig. 7). Disruption of SC lipid metabolism homeostasis secondary to mitochondrial dysfunction is thus a critical underlying pathological mechanism in peripheral neuropathies.

Mitochondrial dysfunction is a common cause of peripheral neuropathies. We recently generated the first mouse model (Tfam-SCKOs) useful in directly interrogating the contribution of SC mitochondrial derangements to peripheral neuropathy, by disrupting mitochondria specifically in these glia [12]. Interestingly, SC mitochondrial deficits in Tfam-SCKO mice did not affect the survival of these glia but instead resulted in a severe, progressive peripheral neuropathy characterized by extensive axonal degeneration that recapitulated critical features of human neuropathy [12]. These results showed that normal mitochondrial function in SCs is essential for maintenance of the axo-glial interactions required for the long-term support of axons and normal peripheral nerve function. Importantly this work indicated that SC mitochondrial dysfunction may contribute to human peripheral neuropathies and that Tfam-SCKO mice, a new model of neuropathy secondary to SC mitochondrial dysfunction, could be useful in identifying causal pathophysiological mechanisms.

The examination of Tfam-SCKO mice described above uncovered the activation of the ISR in Tfam-deficient SCs secondary to mitochondrial dysfunction. The ISR is an evolutionarily conserved, "stress"-activated, gene expression program centered on

phosphorylation of eIF2α. Activation of this program is meant to promote a cellular stress-resistant state by global attenuation of protein synthesis, which reduces the ER load and diverts amino acids from energetically costly protein synthesis to other metabolic pathways [18]. Activation of this program in SCs, however, has previously been shown to be particularly maladaptive. In a study examining a model of CMT caused by mutations to myelin protein zero (P0), the authors found that accumulation of mutant P0 in the ER activated the ISR as part of an UPR [19]. Importantly, by blocking the induction of this pathway through the deletion of a key downstream mediator (Chop), the behavioral and pathological presentations of this disease model could be prevented [19]. These and other studies have led to the notion that UPR-mediated activation of the ISR in SCs contributes to the pathology in myelin-related neuropathies [40]. Activation of the ISR in Tfam-SCKO mice, however, was not associated with ER stress or an UPR. The maladaptive induction of the ISR in SCs may therefore be a central pathological mechanism common to different forms of peripheral neuropathy, including those associated with mutations to structural myelin proteins as well as metabolic abnormalities. Intriguingly, chemotherapeutic agents that cause neuropathy also activate the ISR in cultured cells [41], which highlights the fact that this maladaptive pathway in SCs could be operant in diverse forms of neuropathy.

The downstream cellular processes initiated by the ISR that are maladaptive to SCs are unclear. Activation of this pathway, however, has been linked to alterations in lipid metabolism that are characterized, overall, by a shift away from lipid synthesis and towards lipid oxidation [20-22]. The results described above are consistent with a decreased shunting of fatty acids towards new lipid synthesis and a concomitant increase in fatty

acid oxidation in the nerves of Tfam-SCKO mice. Lipids play a crucial role in the normal biology of SCs; they are required for myelin assembly and maintenance, regulate the differentiation status of these glia, and may also be important for SC-mediated metabolic support of axons [42]. The observed early shift in the lipid metabolism of Tfam-deficient SCs secondary to mitochondrial dysfunction is thus a likely cause of the phenotype in Tfam-SCKO mice. Given that abnormalities in peripheral nerve lipid composition are present in mitochondrial disorders [42, 43], our results suggests that alterations in SC lipid metabolism may be central pathological mechanisms of mitochondrial-related neuropathies.

The shift in lipid metabolism of Tfam-deficient SCs resulted in depletion (sulfatides and cerebrosides) as well as in accumulation (acylcarnitines) of specific lipid molecular species. Both of these lipid alterations in Tfam-SCKO nerves are likely to participate in the subsequent neuropathy phenotype of these mice. The depletion of cerebrosides and sulfatides from Tfam-deficient SCs, which together represent almost 30% of all myelin lipid content [25], likely underlie the prominent demyelinating phenotype apparent in late stages of disease in Tfam-SCKO mice [12]. Moreover, given the central role of sulfatides and cerebrosides in maintaining axon-glial contact [27, 28], depletion of these glycosphingolipids could also drive some of the axon loss in Tfam-SCKO nerves by disrupting the ability of SCs to properly associate with and support axons. This axonal degeneration is likely exacerbated by the accumulation of acylcarnitines in Tfam-SCKO nerves following mitochondrial dysfunction. Accordingly, long-chain acylcarnitines accumulating in SCs could be released onto surrounding axons where they could disrupt axon membrane properties and induce axon degeneration. These results are consistent

with presentations of peripheral neuropathy in patients with genetic defects in fatty acid β-oxidation that lead to a buildup of acylcarnitines [33, 34].

In summary, Tfam-SCKO mice, a novel model of neuropathy secondary to mitochondrial dysfunction, have enabled us to examine for the first time the mechanisms by which deficits in mitochondrial metabolism in SCs specifically contribute to peripheral nerve diseases. Our work demonstrates that mitochondrial deficits activate a maldaptive stress response in SCs and cause a shift in the lipid metabolism of these glia. We provide evidence that the resulting early depletion of important lipid myelin components as well as the accumulation and release of toxic lipid intermediates from SCs drive the pathology observed in Tfam-SCKO mice. New therapeutic strategies that prevent the depletion of lipids that support axo-glial interactions as well as the accumulation of fatty acid intermediates with marked axonal toxicity may be useful in treating patients with diabetic neuropathy and other mitochondria-related peripheral nerve disorders.

Acknowledgments

We thank Michael A. Kiebish for providing valuable technical advice and helpful discussions; Amy Strickland, Casey Spencer Workman, Kelli Simburger and Nina Panchenko for experimental assistance; Dennis Dietzen and the St Louis Children's Hospital Metabolic Genetics Section Core laboratory for help with acylcarnitine release measurements; Nils-Goran Larsson for the *Tfam*^{loxP} mice; Lawrence Wrabetz and Albee Messing for the P_0-Cre mice; members of the Milbrandt laboratory for their comments on the manuscript and helpful discussions. We thank the Genome Technology Access Center

(GTAC) in the Department of Genetics for help with genomic analysis. We also thank the Alvin J. Siteman Cancer Center at Washington University School of Medicine and Barnes-Jewish Hospital in St. Louis, Mo., for the use of the Biomedical Informatics Core (BMC), which provided the in silico analysis service, especially Nobish Varghese. Both GTAC and BMC are partially supported by NCI Cancer Center Support Grant #P30 CA91842 to the Siteman Cancer Center and by ICTS/CTSA Grant# UL1RR024992 from the National Center for Research Resources (NCRR), a component of the National Institutes of Health (NIH), and NIH Roadmap for Medical Research. This work was also supported by NIH Neuroscience Blueprint Center Core Grant P30 NS057105 to Washington University, the HOPE Center for Neurological Disorders, National Institutes of Health Grants NS040745 (J.M.), AG13730 (J.M.)., and PPG 2P01 HL057278 (R.W.G).

Methods

Matings of transgenic animals: All animal experiments were carried out in compliance with institutional animal protocols. Tfam-SCKO mice (P_0-Cre $^{+/-}$, *Tfam*$^{loxP/loxP}$) and Ctrl littermates (P_0-Cre $^{-/-}$, *Tfam*$^{loxP/loxP}$) were generated by crossing Tfam$^{loxP/loxP}$ mice [13] to P_0-Cre mice [44]. Mating and genotyping were carried out as previously described [12].

Nerve histology and morphometry: Sciatic nerves from Ctrl and Tfam-SCKO mice at different ages were dissected and placed in 3% glutaraldehyde overnight. After washing with phosphate buffer, nerves were postfixed in 1% osmium tetraoxide in phosphate buffer overnight at 4°C. Specimens were then dehydrated in graded alcohols and

embedded in 100% epoxy (Araldite 502). One-micrometer-thick plastic embedded sections were prepared and stained with toluidene blue for light microscopy. For electron microscopy, thin sections were prepared, stained with uranyl acetate and lead citrate, and photographed with a JEOL (Akishima) 1200 electron microscope. All nerves underwent qualitative assessment of neural architecture followed by detailed histomorphometric analysis carried out as previously described [45].

Metabolite measurements: For ATP, ADP, AMP, and lactate measurements sciatic nerves were excised from Ctrl and Tfam-SCKO mice, weighted, and metabolites extracted with 1M perchloric acid (10 to 1 volume : weight). Extracts were centrifuged and neutralized with 3 M potassium carbonate. For ATP, ADP and AMP determination, neutralized extracts were diluted 1:10 with potassium phosphate buffer and assayed by HPLC (Shimazu) using an LC-18T HPLC column (Supelco) at flow rate of 1 ml/min and the absorbance at 254 nm was recorded. Each elution peak was compared with standards for identification and quantification and levels were normalized to tissue weight. EC was defined as follows: EC=[ATP]+1/2[ADP])/([ATP]+[ADP]+[AMP]. Lactate levels were determined spectrophotometrically as previously described [46]. NAD+, NADH+ and the NAD+/NADH ratio was determined using a CycLex NAD+/NADH colorimetric assay kit (MBL International) according to the manufacturer's protocol.

Western Blotting: Sciatic nerves were isolated, desheathed in PBS, and immediately frozen in liquid nitrogen. Lysates were prepared by homogenizing the tissue by sonication in a buffer containing 150 mM sodium chloride, 50 mM Hepes, 1% NP-40, 1

mM EDTA, 1 mM sodium fluoride, 1mM sodium orthovanodate, and complete protease inhibitor cocktail (Roche Applied Science). The lysates were clarified by centrifugation at 14,000 rpm for 10 min and quantified using the MicroBCA Protein Assay kit (Pierce). For Western blotting, the proteins were separated by SDS-PAGE and transferred to a PVDF membrane (Millipore). Membranes were blocked in 5% milk in 0.5% TBS-Tween and incubated overnight with the appropriate primary antibody. Following incubation with secondary antibodies conjugated to HRP (GE Healthcare), membranes were developed with SuperSignal West Dura substrate (Pierce). The primary antibodies for p-AMPKα, AMPKα, p-ACC, ACC, and p-Perk were all raised in rabbit, used 1:1000 and purchased from Cell Signaling. We also used mouse anti-Porin (31HL, 1:1000, Calbiochem), mouse anti-β actin (1:1000, Sigma), mouse anti-myelin basic protein (SMI 94, 1:1000, Covance), and rabbit anti-myelin protein zero (1:1000, Sigma). The secondary antibodies used were anti-mouse and anti-rabbit HRP (1:5000; Jackson ImmunoResearch Laboratories). Optical density of the signals was determined using Image-J.

RNA preparation and quantitative real-time PCR: Total RNA was isolated after homogenization (for sciatic nerves) or lysis (for cultured SCs) in Qiazol lysis reagent (Qiagen) using a miRNeasy Minikit (Qiagen) according to the manufacturer's protocol. RNA concentration was quantified using an ND-1000 spectrophotometer (Nanodrop Technologies). mRNA was reverse transcribed from 100 ng of total RNA using qScript cDNA SuperMix (Quanta Biosciences). mRNA qRT-PCR was performed using a SYBR green-based detection system on a 7900 HT Sequence Detector instrument (Applied

Biosystems) as described previously [47]. GAPDH expression was used to normalize samples and obtain relative expression values that were used to calculate percent changes. The sequences of the qRT-PCR primers used are as follows (5'-3'; mouse unless specified): ATF4: F, GGCTATGGATGATGGCTTGG, R, AATTGGGTTCACTGTCTGAGG; ATF4 (rat): F, CTTAAGCCATGGCGCTCTTC, R, TTGCTGGTATCGAGGAATGTG ; Chop: F, AAGTGCATCTTCATACACCACC, R, TTGATTCTTCCTCTTCGTTTCCTG; Chop (rat): F, CTGAGGAGAGAGTGTTCCAG, R, GTGTGGTGGTGTATGAAGATG; ASNS: F, GCCCAAGTTCAGTATCCTCTC, R, TAAATACATGCCCACAGATGCC; mthfd2: F, AATTAAGCGAACAGGCATTCCA, R, AGGATCGTGTGCTTCTTCAG; Trib3: F, CACTTTAGCAGCGGAAGAGG, R, GTGTAGCTCGCATCTTGTCC; Trib3 (rat): F, TGTCTTCAGCAACTGTGAGAGGACGAA, R, GTAGGATGGCCGGGAGCTGAGTAT; Srebp1: F, CATGCCATGGGCAAGTACAC, R, TGTTGCCATGGAGATAGCATCT; FASN: F, GGGTGCTGACTACAACCTCTCC, R, TGCACAGACACCTTCCCGTC; HMGCR: F, TGGTGGGACCAACCTTCTAC, R, GCCATCACAGTGCCACATAC; Acly: F, AGGAAGTGCCACCTCCAACAGT, R, CGCTCATCACAGATGCTGGTCA; ACC2: F, GGGCTCCCTGGATGACAAC, R, TCTTCCGGGAGGAGTTCT; GAPDH: F, TGCCCCCATGTTTGTGATG, R, TGTGGTCATGAGCCCTTCC.

Xbp-1 splicing RT-PCR: *xbp-1 splicing in Ctrl and Tfam-SCKO nerves as well as in cultured SCs was determined from cDNA in a 25 μl* PCR reaction with a single 4 min 94ºC denaturation cycle followed by 35 cycles of 94ºC for 10 s, 63ºC for 30 s, and 72ºC

for 30 s followed by separation of the unsplice (254 bp) and spliced (229 bp) XBP-1 RT-PCR products on a 10 cm 2% agarose gel. Primers used were as follows (5'-3') F: GGCCTTGTGGTTGAGAACCAGGAG; R: GAATGCCCAAAAGGATATCAGACTC. Explanted nerves maintained in 10% fetal bovine serum (FBS) supplemented with 2 mM L-glutamine and 100 ng/ml of nerve growth factor in the presence of 10 μg/ml of tunicamycin served as a positive control for nerve samples.

Microarray and computational analysis*:* total RNA samples were prepared by isolating and pooling RNA from at least 3 different 2 month old Tfam-SCKO and Ctrl mice. Replicates were prepared entirely independently from two separate pools of at least three animals each, 2 replicates were used. Total RNA concentration and purity was obtained from an absorbance ratio at 260 nm and 280 nm. Total RNA quality was then determined by Agilent 2100 bioanalyzer (Agilent Technologies) according to manufacturer's recommendations. RNA transcripts were amplified by T7 linear amplification messageAmp TotalPrep amplification kit (ABI-Ambion) using 400 ng of each total RNA sample. The amplified RNA samples (aRNA) were then cleaned with RNA columns and quantified on a spectrophotometer, and RNA quality was determined by Agilent 2100 bioanalyzer (Agilent Technologies). 1500 ng of each aRNA were hybridized onto Illumina Mouse WG-6 v2.0 Expression Beadchips according to manufacturer's recommendations. Arrays were scanned on an Illumina BeadArray Reader. Images were quantitated by Illumina Beadscan, v3 and the resulting data was imported into Illumina GenomeStudio software, where on-slide spot replicates were averaged and individual spot probe was reported. This signal intensity data was background subtracted and

quantile normalized in Illumina genome Studio. Probes having detection p-value>0.05 in all samples were removed and a two class unpaired SAM analysis was performed. Differentially expressed genes with at least 2.0 fold differential regulation between Tfam-SCKO and Ctrl nerves at a false discovery rate (FDR) of 0.5% were selected for further analysis. Gene enrichment of metabolic pathway was examined using GeneGO (Genego Inc).

Tissue and mitochondria Complex IV determination: nerve mitochondria were isolated and maximum complex IV activity determined as previously described [12]. Tissue maximum Complex IV activity was determined using high resolution respirometry in an OROBOROS Oxygraph 2k (Oroboros) as previously described [12, 48].

Nerve sample lipid extract preparation for mass spectrometric analysis: lipid extraction of nerve samples was performed essentially as described previously [49]. Briefly, a protein assay on each nerve sample was performed by using BCA method with bovine albumin as standard. Lipid internal standards (approximately one for each lipid class) were added based on protein content of each nerve sample. The molecular species of internal standards (e.g., $^{13}C_4$-16:0 carnitine, N-Pentadecanoyl-psychosine (N15:0 Cerebroside), N-Hexadecanoyl-sulfatide (N16:0 sulfatide) were selected because they are either stable isotope labeled species or represent <0.1% of the endogenous cellular lipid mass as demonstrated by mass spectrometric analysis of the nerve lipid extract without addition of internal standards. A modified Bligh and Dyer procedure was used to extract lipids from each nerve sample as previously described [49] . Each lipid extract was

reconstituted in 200 μl /mg of protein (which was the measured protein content aforementioned) in chloroform/methanol (1:1, v/v). A portion of each lipid extract (e.g., 50 uL) was treated with LiOMe to hydrolyze phospholipids followed by washing with hexane as previously described [50]. The treated lipid samples were used for the analysis of the sphingolipidome of each nerve sample. The original and treated lipid extracts were flushed with nitrogen, capped and stored at -20°C until ESI/MS analysis, typically within one week.

Lipidomic analysis of nerve lipid extracts by multi-dimensional mass spectrometry-based shotgun lipidomics: a triple-quadrupole mass spectrometer (Thermo Fisher TSQ Quantum Ultra Plus) equipped with an automated nanospray apparatus (i.e., Nanomate HD, Advion Bioscience Ltd., Ithaca, NY) and Xcalibur system software were utilized in the study as previously described [49]. Briefly, each originally-prepared lipid extract was diluted to < 50 pmol/uL with chloroform/methanol/isopropanol 1:2:4 (v/v/v) prior to direct infusion through a nanospray apparatus linked to the mass spectrometer for the analyses of phospholipids, lyso-phopholipids, acyl-carnitine, non-esterified fatty acids and triacylglycerols with or without the presence of a small amount of LiOH [51]. Each LiOMe-treated lipid extract was properly diluted prior to infusion to the mass spectrometer for the analyses of sphingolipids (Jiang et al., 2007). Typically, a 2-min period and 2-5-min of signal averaging in the profile mode were employed for acquisition of each survey scan and each tandem MS scan, respectively. For tandem mass spectrometry, a collision gas pressure was set at 1.0 mTorr but the collisional energy was varied with the classes of lipids as previously described [51] . All the MS spectra and

tandem MS spectra were automatically acquired by a customized sequence subroutine operated under Xcalibur software. Each individual lipid species in a lipid class was identified using multi-dimensional mass spectrometry through building block analyses [52]. The identified species were quantified using a two-step approach as previously described [52].

Primary SC cultures and in vitro ISR induction: Primary rat SCs were cultured from sciatic nerves of postnatal day1 to day3 rat pups as previously described [47]. For SC *in vitro* ISR induction assays, SCs were initially seeded onto collagen coated 24-well plates (~75,000 cells/well) in 10% FBS-DMEM media supplemented with 2 μM forskolin and 20 μg/ml of bovine pituitary extract. 48 h later cells were switched to 1% FBS-DMEM media for 2 days to stop proliferation. At this point, SCs were treated with either vehicle, 5 μM FCCP, 2.5 μM oligomycin, 10 μM antimycin or 1 μM tunicamycin. RNA or protein were isolated 24 h later. Reported results are from duplicate wells from at least three independent assays.

Acyl-carnitine release measurements: To measure the ability of Tfam-deficient SCs to secrete long-chain acylcarnitines, nerves were explanted from Tfam-SCKO and Ctrl mice and maintained in 100 μl of 10% fetal bovine serum (FBS) supplemented with 2 mM L-glutamine and 100 ng/ml of nerve growth factor for 2.5 days. At this time, media was collected and immediately frozen in liquid nitrogen. Media was then analyzed for acylcarnitine species content (C2–C18 saturated, unsaturated, and hydroxylated) as butyl esters by direct flow injection and precursor ion scanning on an API 3200 LC-MS/MS

system (Applied Biosystems, Foster City, CA, USA). Quantitation was achieved using a cocktail of internal standards. Concentrations were normalized to tissue weight.

DRG neuron culture and Fluo-4 imaging: mouse DRG neurons were isolated from E12 embryos in DMEM (Sigma), dissociated by incubation in 0.25% trypsin, and resuspended (100 µl/embryo) in complete DRG medium: neurobasal medium (Invitrogen) containing 2% B27 supplement (Invitrogen), 50 ng/ml of nerve growth factor (Harlan Laboratories), 1 µM 5-fluoro-2′-deoxyuridine (Sigma), and 1 µM uridine (Sigma). Cells were then seeded onto either 24-well or 96-well cell cultures plates coated with poly-d-lysine (Sigma) and Laminin (Invitrogen) by spotting a single 0.5 µl (96-well) or 2 µl (24-well) droplet of the concentrated cell suspension, incubating for 15 min at 37 °C to allow neurons to adhere, then adding 100 µl (96-well) or 400 ul (24-well) of complete DRG media. All experiments were carried out 5-6 days after seeding. For calcium imaging experiments, neurons were incubated with the calcium indicator Fluo-4 AM (2 µM, Invitrogen) for 30 min at 37 °C, washed by replacing half the media twice, then incubated for another 30 min to allow complete de-esterification of intracellular AM esters. Baseline fluorescence and phase images were taken at this point. Neurons were then treated either with vehicle, palmitoyl-carnitine (Sigma), or palmitate (Sigma) at the appropriate concentrations. Phase and fluorescence images were acquired every 15 minutes for up to 6 hours using an Operetta imaging system equipped with an environmental chamber (Perkin Elmer). To examine the effect of chronic acylcarnitine exposure, DRG neurons were treated daily for up to nine days with vehicle or with palmitoyl-carnitine at the appropriate concentration.

Automated analysis and quantification of images: Axon degeneration, axonal calcium accumulation, and calcium containing vacuole formation were quantified using ImageJ as follows. For axon degeneration, bright field images of axons were binarized and fragmented axons were detected using particle analyzer. The ratio of fragmented axon area against the total axon area was expressed as degeneration index. Axonal calcium accumulation was quantified from the fluorescent images of axons loaded with Fluo-4 calcium sensitive dye as described above. The fluorescent intensity of the pixels over the axon area (as determined from accompanying bright field images) were summed and then normalized by the total axon area. Palmitoyl-carnitine treated axons tend to form vacuoles containing high concentration of Ca^{2+} which are recognized as spherical structures with higher Fluo-4 intensity than surrounding axons. The total area of these vacuoles was expressed as a Fluo-4 blebbing index. This index was determined by first calculating the total Fluo-4 positive axon area. Then the area of calcium containing vacuoles was quantified using binarized Fluo-4 images threshold such that only vacuoles but not the rest of axons were recognized by a particle analyzer. The total vacuole area detected was normalized against total Fluo-4 positive area to give Fluo-4 blebbing index.

Statistical analysis: All values are expressed as mean ± SEM. If not stated otherwise, *p* values were determined by unpaired, two-tailed Student's *t* test. All statistical analyses were performed using Microsoft Excel 2007.

References

1. Fernyhough, P., Roy Chowdhury, S. K. & Schmidt, R. E. Mitochondrial stress and the pathogenesis of diabetic neuropathy. *Expert Rev. Endocrinol. Metab.* 5, 39-49 (2010).

2. Niemann, A., Berger, P. & Suter, U. Pathomechanisms of mutant proteins in Charcot-Marie-Tooth disease. *Neuromolecular Med.* 8, 217-242 (2006).

3. Baloh, R. H. Mitochondrial dynamics and peripheral neuropathy. *Neuroscientist* 14, 12-18 (2008).

4. Barres, B. A. The mystery and magic of glia: a perspective on their roles in health and disease. *Neuron* 60, 430-440 (2008).

5. Ilieva, H., Polymenidou, M. & Cleveland, D. W. Non-cell autonomous toxicity in neurodegenerative disorders: ALS and beyond. *J. Cell Biol.* 187, 761-772 (2009).

6. Chen, S. *et al*. Disruption of ErbB receptor signaling in adult non-myelinating Schwann cells causes progressive sensory loss. *Nat. Neurosci.* 6, 1186-1193 (2003).

7. Reddy, L. V., Koirala, S., Sugiura, Y., Herrera, A. A. & Ko, C. P. Glial cells maintain synaptic structure and function and promote development of the neuromuscular junction in vivo. *Neuron* 40, 563-580 (2003).

8. Meyer zu Horste, G. *et al*. Antiprogesterone therapy uncouples axonal loss from demyelination in a transgenic rat model of CMT1A neuropathy. *Ann. Neurol.* 61, 61-72 (2007).

9. Geuna, S. *et al*. Chapter 3: Histology of the peripheral nerve and changes occurring during nerve regeneration. *Int. Rev. Neurobiol.* 87, 27-46 (2009).

10. Schroder, J. M. Neuropathy associated with mitochondrial disorders. *Brain Pathol.* 3, 177-190 (1993).

11. Kalichman, M. W., Powell, H. C. & Mizisin, A. P. Reactive, degenerative, and proliferative Schwann cell responses in experimental galactose and human diabetic neuropathy. *Acta Neuropathol.* 95, 47-56 (1998).

12. Viader, A. *et al*. Schwann cell mitochondrial metabolism supports long-term axonal survival and peripheral nerve function. *J. Neurosci.* 31, 10128-10140 (2011).

13. Larsson, N. G. *et al*. Mitochondrial transcription factor A is necessary for mtDNA maintenance and embryogenesis in mice. *Nat. Genet.* 18, 231-236 (1998).

14. Atkinson, D. E. The energy charge of the adenylate pool as a regulatory parameter. Interaction with feedback modifiers. *Biochemistry* 7, 4030-4034 (1968).

15. Chabi, B., Adhihetty, P. J., Ljubicic, V. & Hood, D. A. How is mitochondrial biogenesis affected in mitochondrial disease? *Med. Sci. Sports Exerc.* 37, 2102-2110 (2005).

16. Piao, L., Marsboom, G. & Archer, S. L. Mitochondrial metabolic adaptation in right ventricular hypertrophy and failure. *J. Mol. Med. (Berl)* 88, 1011-1020 (2010).

17. Hardie, D. G. Sensing of energy and nutrients by AMP-activated protein kinase. *Am. J. Clin. Nutr.* 93, 891S-6 (2011).

18. Ron, D. & Walter, P. Signal integration in the endoplasmic reticulum unfolded protein response. *Nat. Rev. Mol. Cell Biol.* 8, 519-529 (2007).

19. Pennuto, M. *et al*. Ablation of the UPR-mediator CHOP restores motor function and reduces demyelination in Charcot-Marie-Tooth 1B mice. *Neuron* 57, 393-405 (2008).

20. Harding, H. P. *et al*. Bioactive small molecules reveal antagonism between the integrated stress response and sterol-regulated gene expression. *Cell. Metab.* 2, 361-371 (2005).

21. Oyadomari, S., Harding, H. P., Zhang, Y., Oyadomari, M. & Ron, D. Dephosphorylation of translation initiation factor 2alpha enhances glucose tolerance and attenuates hepatosteatosis in mice. *Cell. Metab.* 7, 520-532 (2008).

22. Qi, L. *et al*. TRB3 links the E3 ubiquitin ligase COP1 to lipid metabolism. *Science* 312, 1763-1766 (2006).

23. Barber, M. C., Price, N. T. & Travers, M. T. Structure and regulation of acetyl-CoA carboxylase genes of metazoa. *Biochim. Biophys. Acta* 1733, 1-28 (2005).

24. Yang, K., Cheng, H., Gross, R. W. & Han, X. Automated lipid identification and quantification by multidimensional mass spectrometry-based shotgun lipidomics. *Anal. Chem.* 81, 4356-4368 (2009).

25. Garbay, B., Heape, A. M., Sargueil, F. & Cassagne, C. Myelin synthesis in the peripheral nervous system. *Prog. Neurobiol.* 61, 267-304 (2000).

26. Bosio, A., Binczek, E., Haupt, W. F. & Stoffel, W. Composition and biophysical properties of myelin lipid define the neurological defects in galactocerebroside- and sulfatide-deficient mice. *J. Neurochem.* 70, 308-315 (1998).

27. Dupree, J. L., Coetzee, T., Suzuki, K. & Popko, B. Myelin abnormalities in mice deficient in galactocerebroside and sulfatide. *J. Neurocytol.* 27, 649-659 (1998).

28. Hoshi, T. *et al*. Nodal protrusions, increased Schmidt-Lanterman incisures, and paranodal disorganization are characteristic features of sulfatide-deficient peripheral nerves. *Glia* 55, 584-594 (2007).

29. Houten, S. M. & Wanders, R. J. A general introduction to the biochemistry of mitochondrial fatty acid beta-oxidation. *J. Inherit. Metab. Dis.* 33, 469-477 (2010).

30. Su, X., Han, X., Mancuso, D. J., Abendschein, D. R. & Gross, R. W. Accumulation of long-chain acylcarnitine and 3-hydroxy acylcarnitine molecular species in diabetic myocardium: identification of alterations in mitochondrial fatty acid processing in diabetic myocardium by shotgun lipidomics. *Biochemistry* 44, 5234-5245 (2005).

31. Zammit, V. A., Corstorphine, C. G., Kolodziej, M. P. & Fraser, F. Lipid molecular order in liver mitochondrial outer membranes, and sensitivity of carnitine palmitoyltransferase I to malonyl-CoA. *Lipids* 33, 371-376 (1998).

32. Bonnet, D. *et al*. Metabolic and genetic investigations in childhood cardiomyopathies. *Arch. Mal. Coeur. Vaiss.* 92, 1509-1514 (1999).

33. Schaefer, J., Jackson, S., Dick, D. J. & Turnbull, D. M. Trifunctional enzyme deficiency: adult presentation of a usually fatal beta-oxidation defect. *Ann. Neurol.* 40, 597-602 (1996).

34. Tyni, T. & Pihko, H. Long-chain 3-hydroxyacyl-CoA dehydrogenase deficiency. *Acta Paediatr.* 88, 237-245 (1999).

35. Corr, P. B. *et al*. Electrophysiological effects of amphiphiles on canine purkinje fibers. Implications for dysrhythmia secondary to ischemia. *Circ. Res.* 49, 354-363 (1981).

36. DaTorre, S. D., Creer, M. H., Pogwizd, S. M. & Corr, P. B. Amphipathic lipid metabolites and their relation to arrhythmogenesis in the ischemic heart. *J. Mol. Cell. Cardiol.* 23 Suppl 1, 11-22 (1991).

37. Yamada, K. A., Kanter, E. M. & Newatia, A. Long-chain acylcarnitine induces Ca2+ efflux from the sarcoplasmic reticulum. *J. Cardiovasc. Pharmacol.* 36, 14-21 (2000).

38. George, E. B., Glass, J. D. & Griffin, J. W. Axotomy-induced axonal degeneration is mediated by calcium influx through ion-specific channels. *J. Neurosci.* 15, 6445-6452 (1995).

39. Fernyhough, P. & Calcutt, N. A. Abnormal calcium homeostasis in peripheral neuropathies. *Cell Calcium* 47, 130-139 (2010).

40. Lin, W. & Popko, B. Endoplasmic reticulum stress in disorders of myelinating cells. *Nat. Neurosci.* 12, 379-385 (2009).

41. Gately, D. P., Sharma, A., Christen, R. D. & Howell, S. B. Cisplatin and taxol activate different signal pathways regulating cellular injury-induced expression of GADD153. *Br. J. Cancer* 73, 18-23 (1996).

42. Chrast, R., Saher, G., Nave, K. A. & Verheijen, M. H. Lipid metabolism in myelinating glial cells: lessons from human inheriteddisorders and mouse models. *J. Lipid Res.* (2010).

43. Navarro, J. A. *et al*. Altered lipid metabolism in a Drosophila model of Friedreich's ataxia. *Hum. Mol. Genet.* 19, 2828-2840 (2010).

44. Feltri, M. L. *et al*. P0-Cre transgenic mice for inactivation of adhesion molecules in Schwann cells. *Ann. N. Y. Acad. Sci.* 883, 116-123 (1999).

45. Hunter, D. A. *et al*. Binary imaging analysis for comprehensive quantitative histomorphometry of peripheral nerve. *J. Neurosci. Methods* 166, 116-124 (2007).

46. Marbach, E. P. & Weil, M. H. Rapid enzymatic measurement of blood lactate and pyruvate. Use and significance of metaphosphoric acid as a common precipitant. *Clin. Chem.* 13, 314-325 (1967).

47. Nagarajan, R. *et al*. EGR2 mutations in inherited neuropathies dominant-negatively inhibit myelin gene expression. *Neuron* 30, 355-368 (2001).

48. Mancuso, D. J. *et al*. Genetic ablation of calcium-independent phospholipase A2{gamma} prevents obesity and insulin resistance during high fat feeding by mitochondrial uncoupling and increased adipocyte fatty acid oxidation. *J. Biol. Chem.* (2010).

49. Han, X., Yang, K. & Gross, R. W. Microfluidics-based electrospray ionization enhances the intrasource separation of lipid classes and extends identification of individual molecular species through multi-dimensional mass spectrometry: development of an automated high-throughput platform for shotgun lipidomics. *Rapid Commun. Mass Spectrom.* 22, 2115-2124 (2008).

50. Jiang, X., Cheng, H., Yang, K., Gross, R. W. & Han, X. Alkaline methanolysis of lipid extracts extends shotgun lipidomics analyses to the low-abundance regime of cellular sphingolipids. *Anal. Biochem.* 371, 135-145 (2007).

51. Han, X. & Gross, R. W. Shotgun lipidomics: electrospray ionization mass spectrometric analysis and quantitation of cellular lipidomes directly from crude extracts of biological samples. *Mass Spectrom. Rev.* 24, 367-412 (2005).

52. Yang, K., Cheng, H., Gross, R. W. & Han, X. Automated lipid identification and quantification by multidimensional mass spectrometry-based shotgun lipidomics. *Anal. Chem.* 81, 4356-4368 (2009).

Figures

Figure 1: SC mitochondrial dysfunction induces a progressive degenerative peripheral neuropathy that is not directly linked to energy depletion. ***a)*** Electron micrographs of 1 month old Ctrl and Tfam-SCKO sciatic nerve cross sections depicting early structural abnormalities of Remak bundles (SC surrounding multiple unmyelinated axons) and degeneration of unmyelinated axons (asterisk). A, axons; N, SC nucleus; C, SC cytoplasm. Scale bar 500 nm. ***b, c)*** Toluidene blue stained plastic sections of Tfam-SCKO and Ctrl sciatic nerve cross sections (b) and quantification of total number of myelinated profiles per nerve (c) at different ages show prominent, progressive degeneration of large-caliber myelinated axons and demyelination starting at 3-4 months of age. Arrowheads (b) indicate axons surrounded by unusually thin myelin, a sign of demyelination. Arrow (c) indicates the point in the progression of the pathology for all mice used in later experiments; note that at this age nerves display only limited, early pathological changes with minimal axon loss and demyelination. Error bars, SEM. n=4 mice per genotype at each age. *P<0.01 Scale bar 25 μm. ***d)*** Adenylate energy charge in Tfam-SCKO nerves shows only a slight decrease in the energy levels of Tfam-deficient SCs compared to Ctrl nerves. Error bars, SEM. n=8 mice per genotype. *P<0.01 ***e, f)*** Immunoblot analysis (e) and quantification of band intensity (f) reveals no increase in the phosphorylation (activation) of the energy sensor AMPK in Tfam-SCKO nerves, indicating that energy depletion is an unlikely driver of nerve pathology in these mice. Error bars, SEM. n=4 mice per genotype.

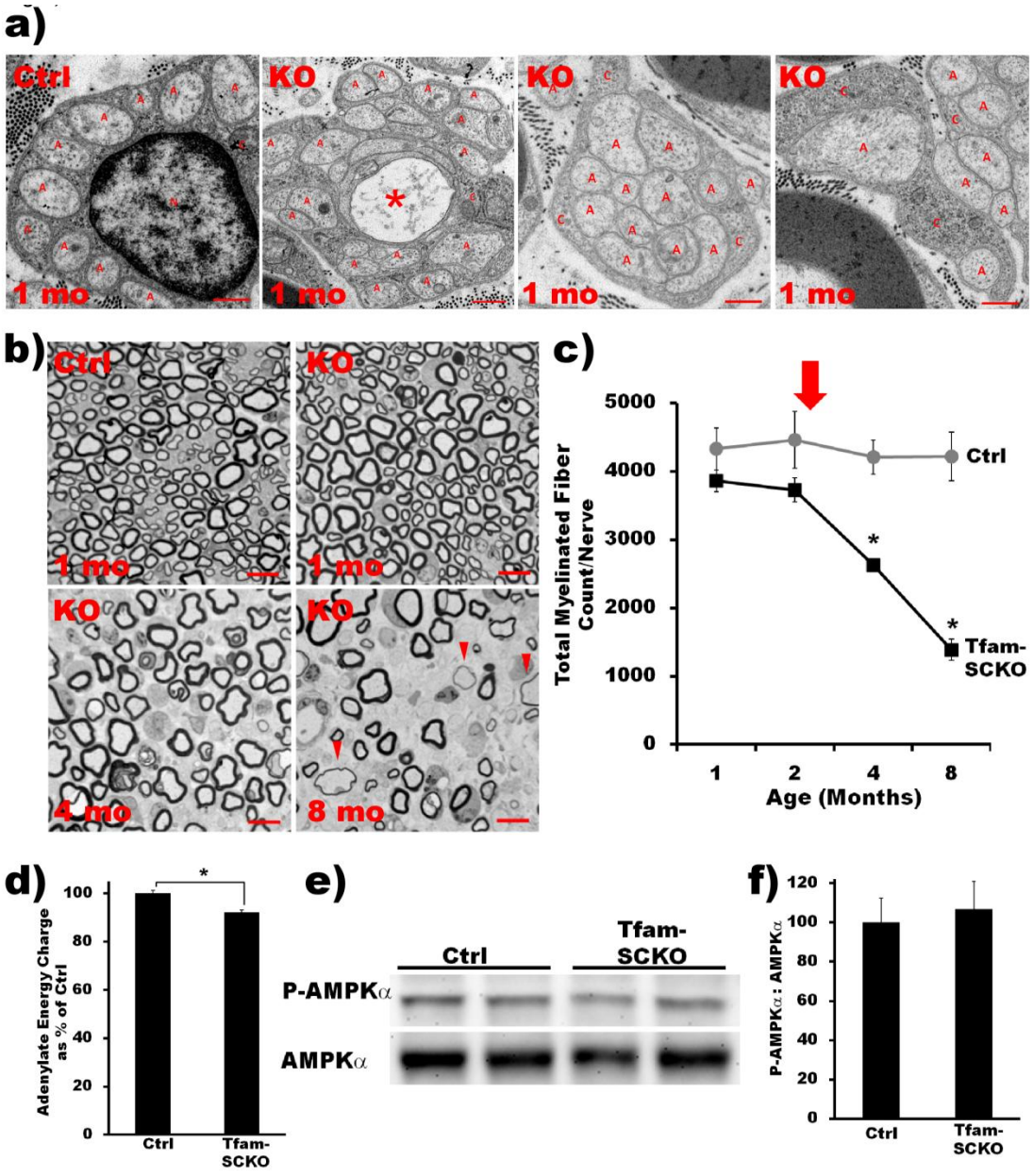
a)
Ctrl
KO
KO
KO
1 mo
1 mo
1 mo
1 mo
b)
Ctrl
KO
1 mo
1 mo
KO
KO
4 mo
8 mo
c)
Total Myelinated Fiber Count/Nerve
5000
4000
3000
2000
1000
0
1
2
4
8
Age (Months)
Ctrl
Tfam-SCKO
*
*
d)
Adenylate Energy Charge as % of Ctrl
100
80
60
40
20
0
*
Ctrl
Tfam-SCKO
e)
Ctrl
Tfam-SCKO
P-AMPKα
AMPKα
f)
P-AMPKα : AMPKα
120
100
80
60
40
20
0
Ctrl
Tfam-SCKO

Figure 2: SC mitochondrial dysfunction activates a maladaptive integrated stress response (ISR) independent of ER-stress. ***a)*** SC mitochondrial dysfunction upregulates the expression of ISR target genes in Tfam-SCKO nerves compared to Ctrl as measured by qRT-PCR. *ATF4,* activating transcription factor 4; *Chop,* DNA-damage inducible transcript 3; *ASNS,* asparagine synthetase; *MTHFD2,* methylenetetrahydrofolate dehydrogenase; *TRIB3,* tribbles homolog 3. Error bars, SEM. n=5 mice per genotype. *P<0.05 ***b)*** Immunoblot analysis shows increased phosphorylation of eIF2α in Tfam-SCKO vs. Ctrl nerves, confirming the activation of the ISR ***c)*** Immunoblot analysis shows that application of the mitochondrial inhibitor FCCP to cultured SCs increases phosphorylation of eIF2α, indicating that inhibition of the mitochondrial electron transport chain activates the ISR. ***d)*** Inhibition of mitochondrial respiration in cultured SCs with mitochondrial inhibitors upregulates the expression of ISR target genes as measured by qRT-PCR. Error bars, SEM. n=duplicate wells from 3 independent experiments. *P<0.05. ***e)*** Immunoblot analysis of the phosphorylation (activation) status of the ER-stress sensor Perk in Ctrl and Tfam-SCKO nerves shows no differences, indicating that ISR activation following SC mitochondrial deficits does not involve ER-stress. ***f)*** Gel showing the absence of Xbp-1 splicing downstream of the activation of the ER-stress sensor Ire-1 in Tfam-SCKO nerves, or SCs treated with mitochondrial inhibitors, confirms that ISR activation induced by mitochondrial derangement is independent of ER-Stress. Tunicamycin treatment of sciatic nerves cultured as explants or of SCs, serves as a positive control for ER-stress.

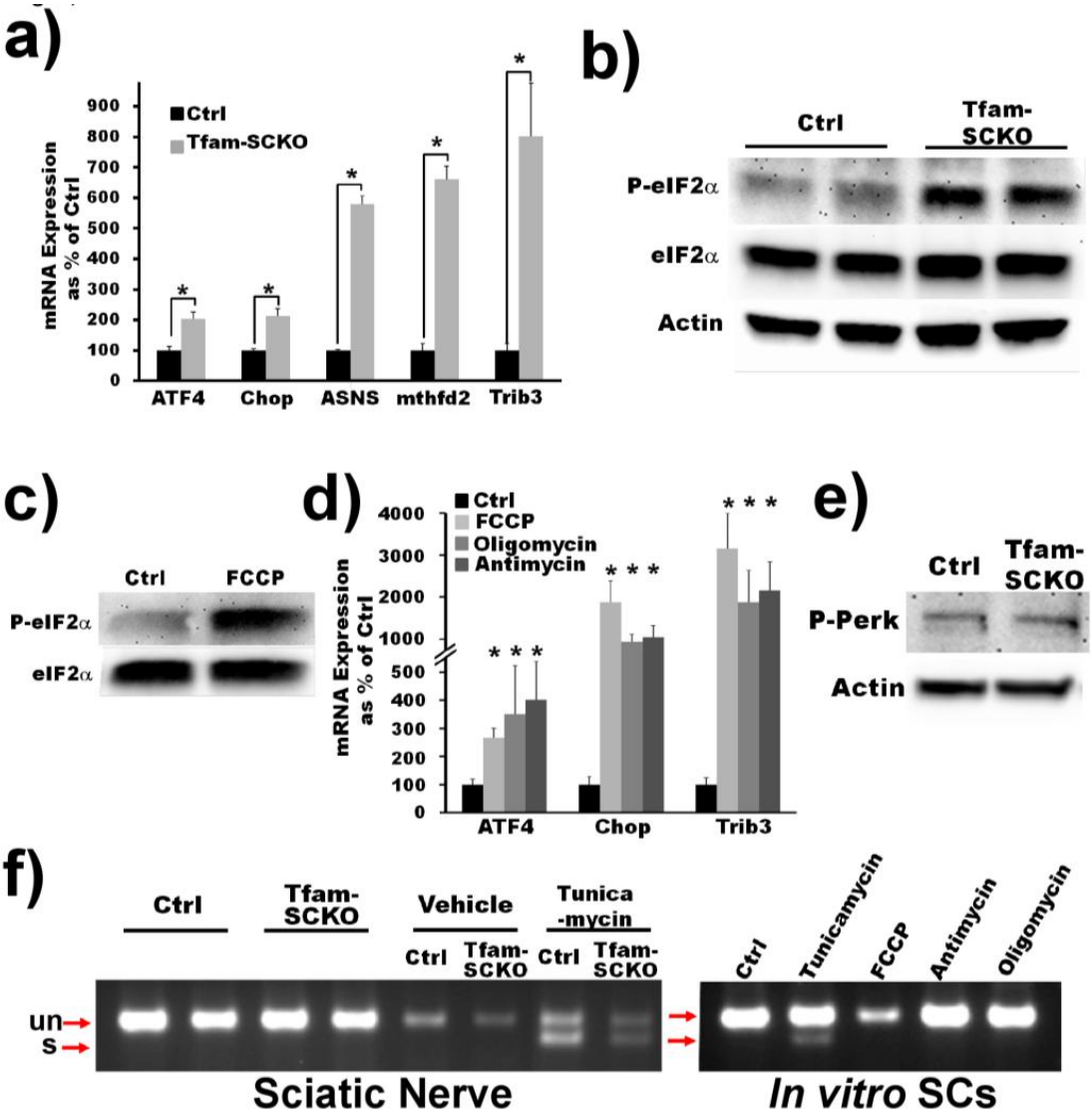
a)
mRNA Expression as % of Ctrl
Ctrl
Tfam-SCKO
ATF4
Chop
ASNS
mthfd2
Trib3
b)
Ctrl
Tfam-SCKO
P-eIF2α
eIF2α
Actin
c)
Ctrl
FCCP
P-eIF2α
eIF2α
d)
Ctrl
FCCP
Oligomycin
Antimycin
mRNA Expression as % of Ctrl
ATF4
Chop
Trib3
e)
Ctrl
Tfam-SCKO
P-Perk
Actin
f)
Ctrl
Tfam-SCKO
Vehicle
Tunica-mycin
Ctrl
Tfam-SCKO
Ctrl
Tfam-SCKO
uns
Sciatic Nerve
Ctrl
Tunicamycin
FCCP
Antimycin
Oligomycin
In vitro SCs

Figure 3: SC mitochondrial dysfunction causes a shift in lipid metabolism away from lipid biosynthesis and toward fatty acid oxidation. *a*) Differentially expressed mRNAs in Tfam-SCKO nerves as determined by microarray analysis are enriched for genes involved in lipid metabolism pathways. The 10 pathways with most significant enrichment among differentially expressed genes in Tfam-SCKO nerves are shown. ***b***) qRT-PCR analysis confirms that a number of lipid synthesis related enzymes are downregulated in Tfam-SCKO vs. Ctrl nerves. *SREBP1,* sterol regulatory element binding transcription factor 1; *FASN,* fatty acid synthase; *HMGCR,* 3-hydroxy-3-methylglutaryl-Coenzyme A reductase; *ACLY,* ATP citrate lyase; *ACC2,* acetyl-Coenzyme A carboxylase beta (primarily localized to mitochondria). Error bars, SEM. n=5 mice per genotype. *P<0.05. ***c)*** Diagram depicting the regulation by acetyl-coA carboxylase (ACC) of the balance between fatty acid synthesis vs. oxidation and how it is altered by ACC's phosphorylation status. ***d, e)*** Immunoblot analysis (d) and quantification of band intensity (e) show increased phospohorylation of ACC in Tfam-SCKO nerves compared to Ctrls. Phosphorylation inhibits this central regulator of the balance between lipid synthesis vs. oxidation, indicating (together with gene expression results) a shift in lipid metabolism away from new lipid synthesis and towards increased lipid oxidation in SC following mitochondrial dysfunction. Error bars, SEM. n=4 mice per genotype. *P<0.05.

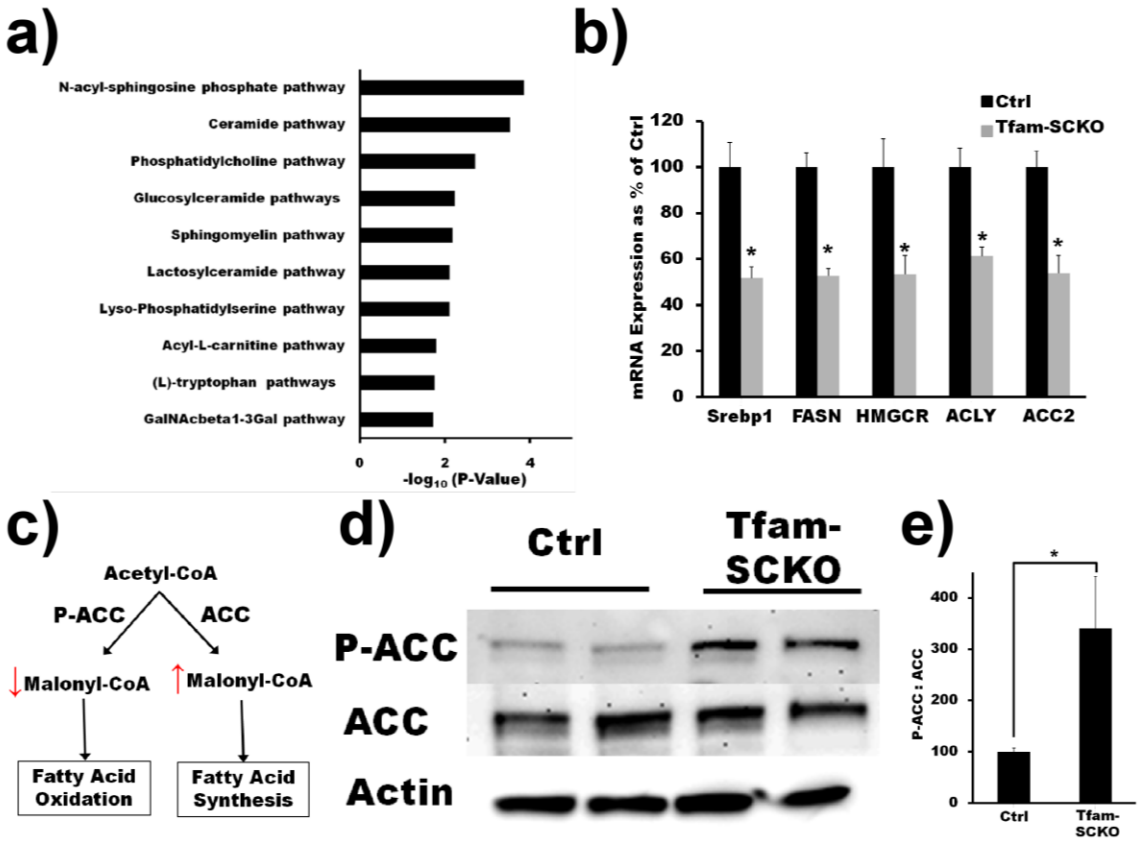
a)
N-acyl-sphingosine phosphate pathway
Ceramide pathway
Phosphatidylcholine pathway
Glucosylceramide pathways
Sphingomyelin pathway
Lactosylceramide pathway
Lyso-Phosphatidylserine pathway
Acyl-L-carnitine pathway
(L)-tryptophan pathways
GalNAcbeta1-3Gal pathway
0
2
4
-log10 (P-Value)
b)
Ctrl
Tfam-SCKO
mRNA Expression as % of Ctrl
120
100
80
60
40
20
0
Srebp1
FASN
HMGCR
ACLY
ACC2
c)
Acetyl-CoA
P-ACC
ACC
Malonyl-CoA
Malonyl-CoA
Fatty Acid Oxidation
Fatty Acid Synthesis
d)
Ctrl
Tfam-SCKO
P-ACC
ACC
Actin
e)
P-ACC : ACC
400
300
200
100
0
Ctrl
Tfam-SCKO

Figure 4: Abnormal lipid metabolism secondary to mitochondrial dysfunction results in depletion of myelin lipid components in Tfam-SCKO nerves. *a, b*) Lipidomic analysis revealed an early and significant depletion of two key myelin lipid components, cerebrosides (a) and sulfatides (b), in Tfam-SCKO vs. Ctrl nerves, likely accounting for the subsequent demyelination observed in these mice. Error bars, SEM. n=5 mice per genotype. *P<0.05. ***c*)** Immunoblot analysis reveals that sulfatide and cerebroside depletion precedes any decrease in expression of nerve myelin basic protein (MBP) and myelin protein zero (P0), making lipid depletion a potential driver of the later demyelination.

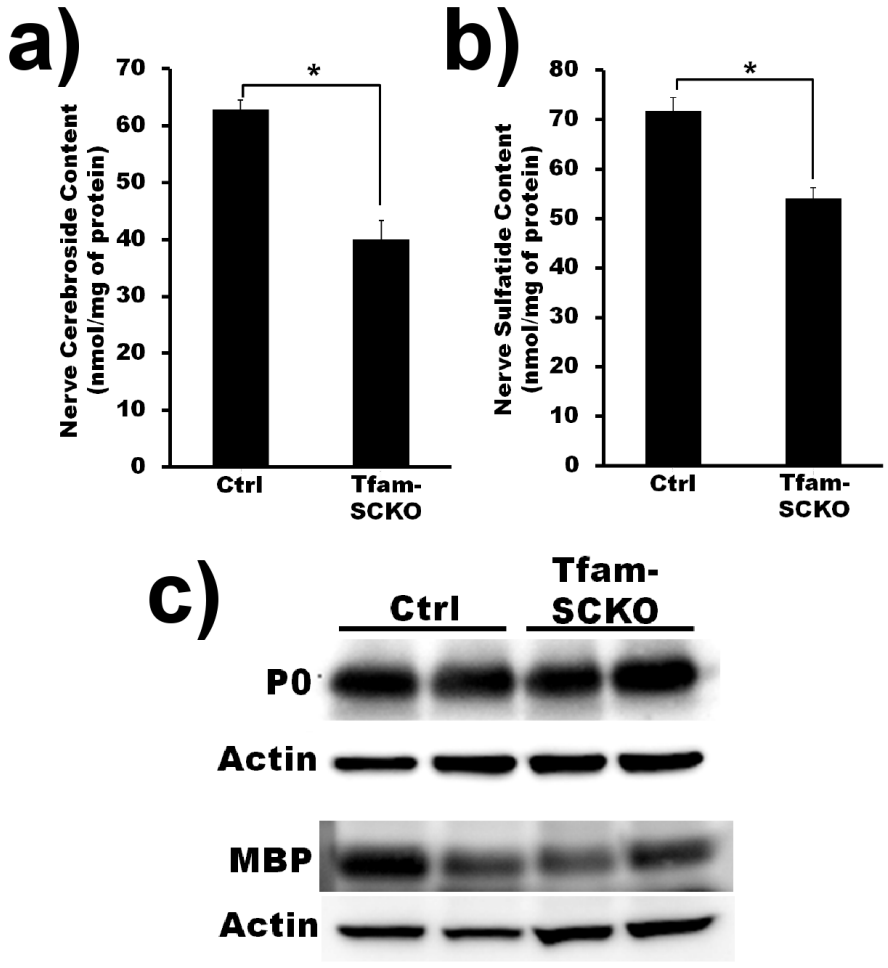

Figure 5: Abnormal lipid metabolism secondary to mitochondrial dysfunction causes severe accumulation of acylcarnitine fatty acid β-oxidation intermediates in Tfam-SCKO nerves *a, b*) Lipidomic analysis shows a significant accumulation of long-chain acylcarnitines (total, a) that affects most long-chain molecular species (b) in Tfam-SCKO vs. Ctrl nerves. Error bars, SEM. n=5 mice per genotype. *P<0.05. ***c*)** Diagram depicting fatty acid β-oxidation in the mitochondria. Long-chain fatty acids are converted to acylcarnitines to be shuttled into the mitochondrial matrix, the site of β-oxidation, where they are oxidized through repeated cycles of four enzymatic reactions. Red text indicates the altered ratio of $NAD/NADH^{+}$ in Tfam-SCKO nerves. Red stars indicate lipid intermediates accumulating in Tfam-SCKO nerves following mitochondrial dysfunction. Cpt1 and Cpt2: carnitine palmitoyltransferase 1 and 2; T outer: long-chain fatty acid transporter; T inner: carnitine-acylcarnitine translocase; Co-Ash: coenzyme A. ***d*)** Lipidomic analysis also shows the accumulation of hydroxy-acylcarnitine species (derived from 3-hydroxy acyl CoA) in Tfam-SCKO nerves, indicative of inhibition of the β-oxidation reaction catalyzed by 3-hydroxyacyl CoA dehydrogenase. Error bars, SEM. n=5 mice per genotype. *P<0.05. ***e*)** Reduced NAD+/NADH ratio in Tfam-SCKO nerves. Error bars, SEM. n=6 mice per genotype. *P<0.05.

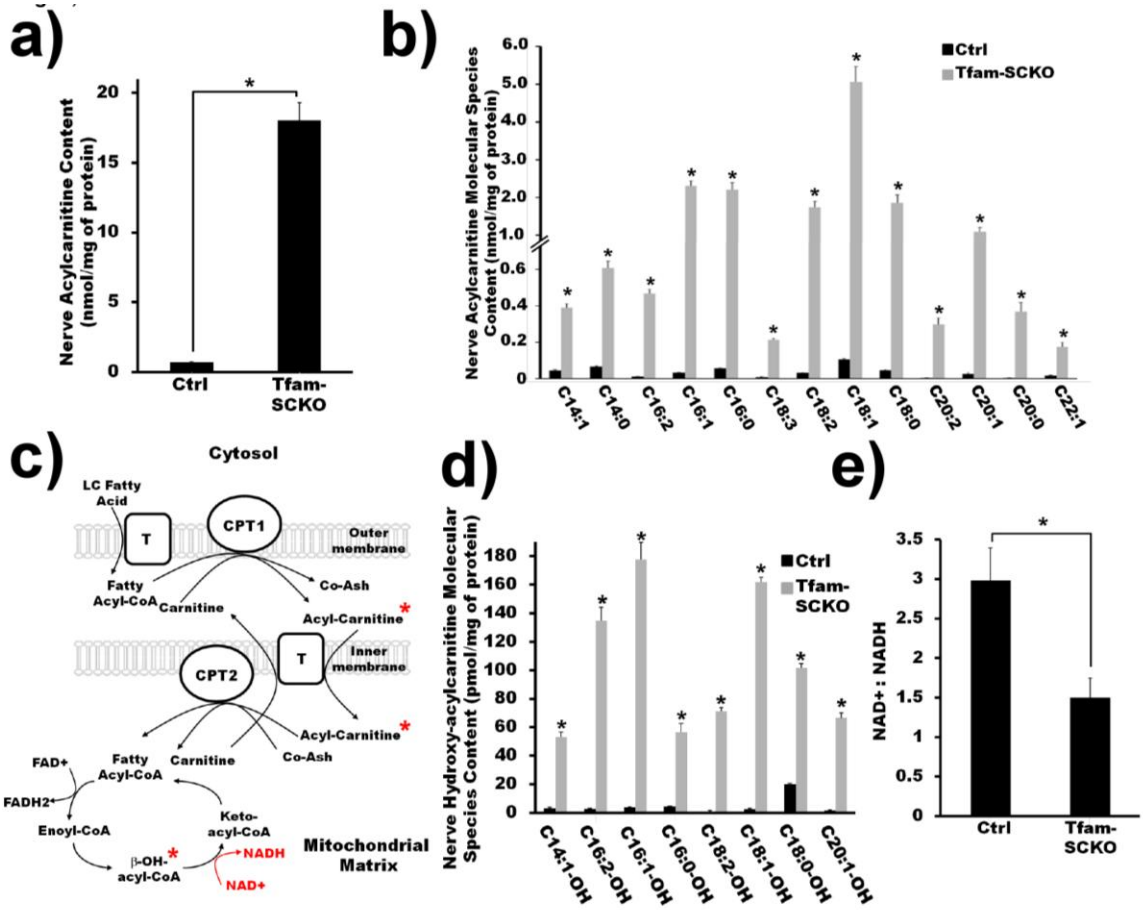
a)
Nerve Acylcarnitine Content (nmol/mg of protein)
Ctrl
Tfam-SCKO
b)
Nerve Acylcarnitine Molecular Species Content (nmol/mg of protein)
Ctrl
Tfam-SCKO
C14:1
C14:0
C16:2
C16:1
C16:0
C18:3
C18:2
C18:1
C18:0
C20:2
C20:1
C20:0
C22:1
c)
Cytosol
LC Fatty Acid
T
CPT1
Outer membrane
Fatty Acyl-CoA
Carnitine
Co-Ash
Acyl-Carnitine
CPT2
Inner membrane
FAD+
FADH2
Enoyl-CoA
Keto-acyl-CoA
β-OH-acyl-CoA
NADH
NAD+
Mitochondrial Matrix
d)
Nerve Hydroxy-acylcarnitine Molecular Species Content (pmol/mg of protein)
Ctrl
Tfam-SCKO
C14:1-OH
C16:2-OH
C16:1-OH
C16:0-OH
C18:2-OH
C18:1-OH
C18:0-OH
C20:1-OH
e)
NAD+ : NADH
Ctrl
Tfam-SCKO

Figure 6: Long-chain acylcarnitines are secreted from SCs and alter axonal calcium homeostasis and stability. a) Explanted Tfam-SCKO nerves but not Ctrl nerves release long-chain acylcarnitines into surrounding culture media as measured by mass spectrometry. Error bars, SEM. n=6 mice per genotype. *P<0.05 ***b)*** Images depicting increased fluorescence intensity of the Ca^{2+} dye Fluo-4 after acute (30 min) application of palmitoyl-carnitine (PC), an acylcarnitine species highly increased in Tfam-SCKO nerves, shows that this lipid intermediate can disrupt axonal calcium homeostasis. Note that similar changes were not seen when the corresponding free fatty acid (Palmitate, P) was applied. Scale bar, 100 μm ***c, d)*** Quantification of the effect of palmitoyl-carnitine on Fluo-4 intenstiy (c) and Ca^{2+} blebbing (d) shows that the effect of this lipid intermediate on axonal calcium is dose-dependent, and specific to acylcarnitines; application of the corresponding free fatty acid at the same concentrations exerted no comparable effect. Error bars, SEM. n=triplicate wells from 1 out of 3 representative experiments. *P<0.05. ***e)*** Images depicting a progressive increase in axonal degeneration following chronic application of 25 μM palmitoyl-carnitine (PC) after 9 days of treatment. Scale bar, 100 μm ***f)*** quantification of the effect on axonal degeneration of chronic treatment with 25 μM palmitoyl-carnitine (PC) shows a significant, progressive increase in the axon degeneration index. Error bars, SEM. n=6 wells from 1 out of 2 representative experiments. *P<0.05.

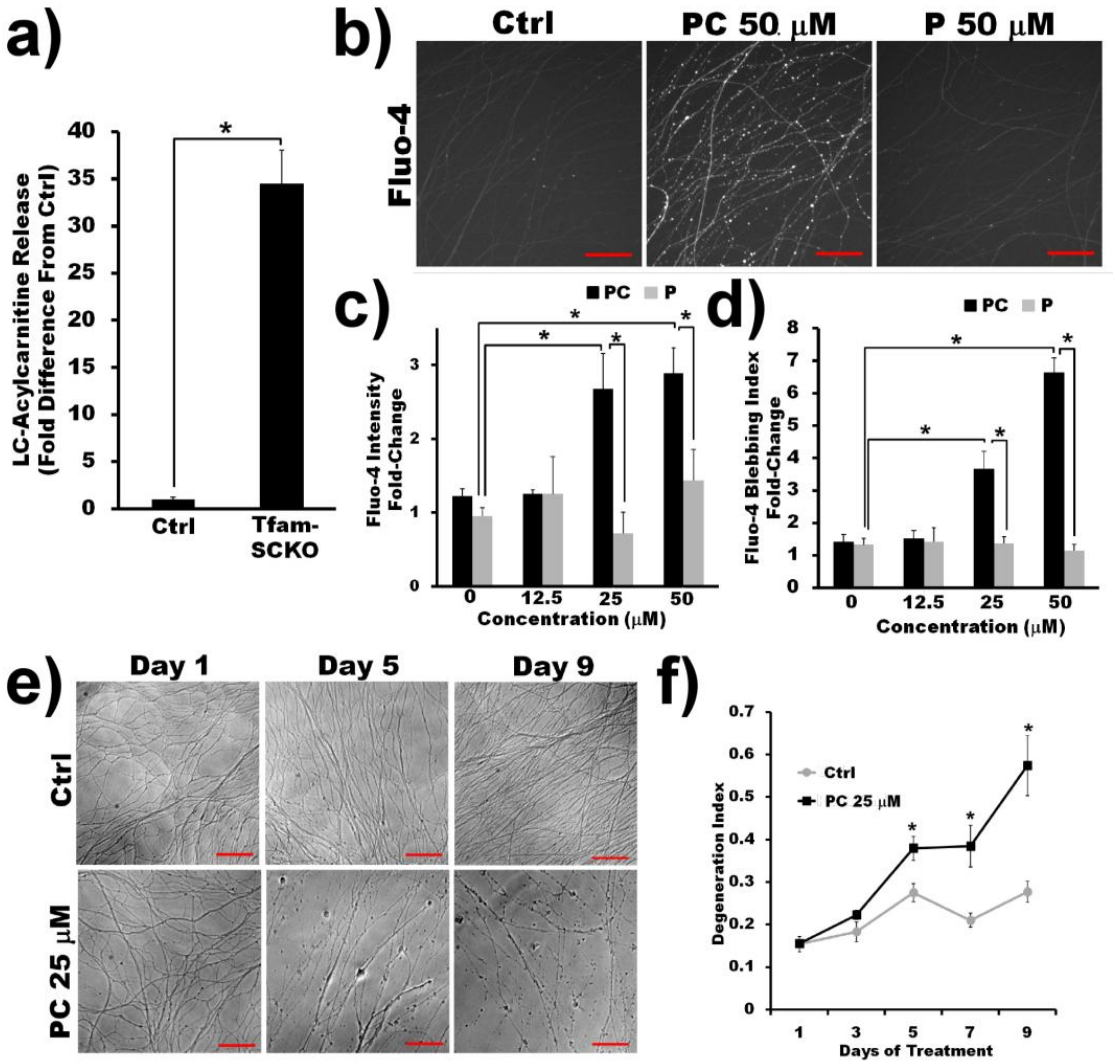
a)
LC-Acylcarnitine Release (Fold Difference From Ctrl)
Ctrl
Tfam-SCKO
b)
Ctrl
PC 50 μM
P 50 μM
Fluo-4
c)
PC
P
Fluo-4 Intensity Fold-Change
Concentration (μM)
d)
Fluo-4 Blebbing Index Fold-Change
e)
Day 1
Day 5
Day 9
Ctrl
PC 25 μM
f)
Degeneration Index
Ctrl
PC 25 μM
Days of Treatment

Figure 7: Altered SC lipid metabolism accompanied by the toxic accumulation of lipid intermediates induces axonal degeneration and demyelination in mitochondria-related peripheral neuropathies. Diagram describing the proposed model for how a shift in lipid metabolism away from lipid synthesis and towards lipid oxidation secondary to SC mitochondrial dysfunction may contribute to the pathology in peripheral neuropathies. CB: cerebrosides; ST: sulfatides; AC: acylcarnitine

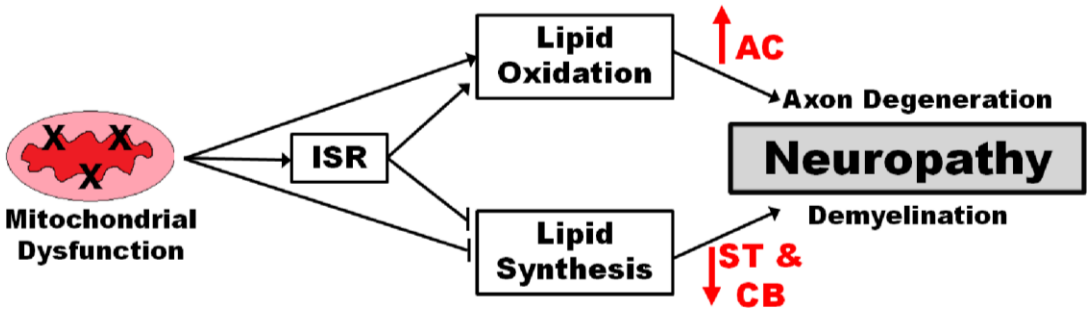

Supplementary Figure 1: Increased mitochondrial content and glycolysis help maintain cellular energy levels in Tfam-deficient SCs. *a*) Immunoblot analysis and quantification of band intensity (OD, optical density; b) of porin, a mitochondrial membrane protein that serves as a reliable marker of mitochondrial content, shows a 3-fold increase in Tfam-SCKO vs Ctrl nerves. Error bars, SEM. n=3 mice per genotype. *P<0.05. ***b*)** Increased ratio of maximum complex IV activity per mg of tissue vs maximum complex IV activity per mg of mitochondria for Tfam-SCKOs confirms a higher mitochondrial content in these mice. Error bars, SEM. n= complex IV activity measured from 5 whole nerves and from 4 nerve mitochondria preparations. *P<0.05. ***c*)** Lactate levels in Tfam-SCKO nerves are greater than in Ctrl nerves, suggesting increased glycolysis. Error bars, SEM. n=8 mice per genotype. *P<0.05.

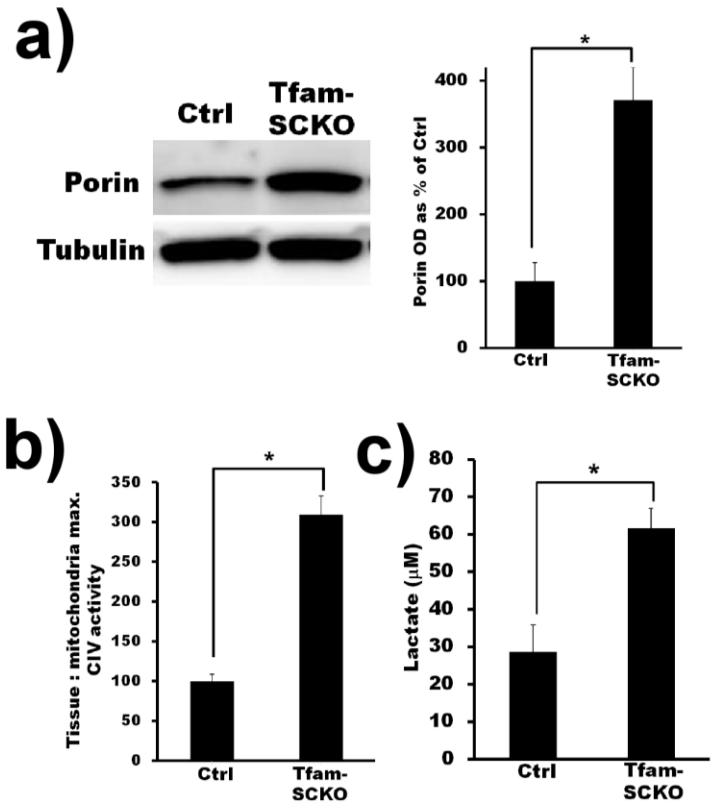

Supplementary Figure 2: Depletion of myelin lipid components and accumulation of acylcarnitine fatty acid β-oxidation intermediates in Tfam-SCKO nerves *a*) Representative spectrum of sulfatide species detected in Ctrl and Tfam-SCKO nerves shows depletion of this lipid class in SCs following mitochondrial dysfunction. Asterisk marks one of the more depleted sulfatide species, m/z = 888.6, d18:1, N24:1. IS, internal standard. ***b*)** Representative spectrum of acylcarnitine species detected in Ctrl and Tfam-SCKO nerves depicts the dramatic accumulation of this lipid class in SCs following mitochondrial dysfunction. Asterisks mark two of the more increased acylcarnitines species m/z = 398.3, C16:1; m/z = 426.3, C18:1. IS, internal standard.

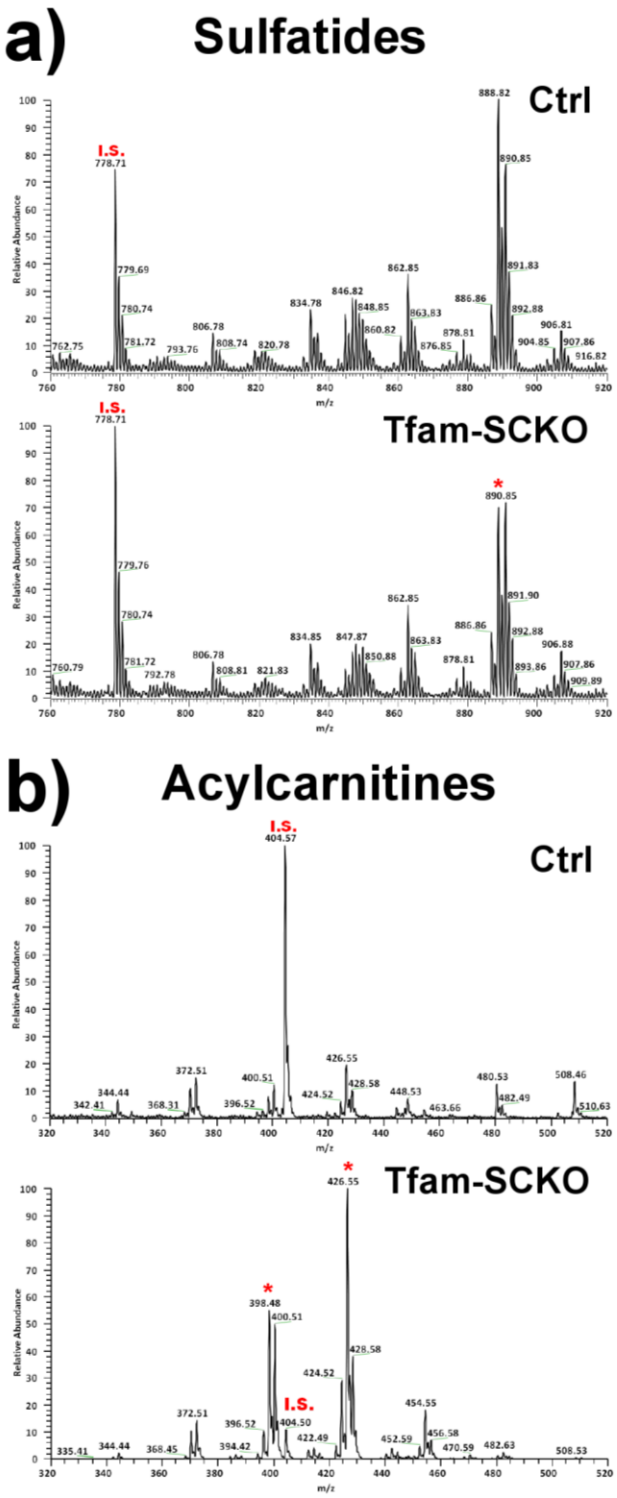
a)
Sulfatides
Ctrl
I.S.
778.71
888.82
890.85
779.69
780.74
781.72
762.75
793.76
806.78
808.74
820.78
834.78
846.82
848.85
860.82
862.85
863.83
876.85
878.81
886.86
891.83
892.88
904.85
906.81
907.86
916.82
Relative Abundance
m/z
Tfam-SCKO
I.S.
778.71
890.85
779.76
780.74
781.72
760.79
792.78
806.78
808.81
821.83
834.85
847.87
850.88
862.85
863.83
878.81
886.86
891.90
892.88
893.86
906.88
907.86
909.89
b)
Acylcarnitines
Ctrl
I.S.
404.57
342.41
344.44
368.31
372.51
396.52
400.51
424.52
426.55
428.58
448.53
463.66
480.53
482.49
508.46
510.63
Tfam-SCKO
426.55
398.48
400.51
428.58
424.52
I.S.
404.50
372.51
396.52
335.41
344.44
368.45
394.42
422.49
452.59
454.55
456.58
470.59
482.63
508.53

CHAPTER 4:

Differential Regional and Subtype-Specific Vulnerability of Enteric Neurons to Mitochondrial Dysfunction

Adapted from: Viader A, Wright-Jin EC, Vohra BPS, Heuckeroth RO, Milbrandt J (2011) Differential regional and subtype-specific vulnerability of enteric neurons to mitochondrial dysfunction. *PlosOne,*6(11):e27727.

Abstract

Mitochondrial dysfunction is a central mediator of disease progression in diverse neurodegenerative diseases that often present with prominent gastrointestinal abnormalities. Gastrointestinal dysfunction in these disorders is related, at least in part, to defects in the enteric nervous system (ENS). The role of mitochondrial deficits in ENS neurodegeneration and their relative contribution to gastrointestinal dysfunction, however, are unclear. To better understand how mitochondrial abnormalities in the ENS influence enteric neurodegeneration and affect intestinal function, we generated mice (Tfam-ENSKOs) with impaired mitochondrial metabolism in enteric neurons and glia through the targeted deletion of the mitochondrial transcription factor A gene (Tfam). Tfam-ENSKO mice were initially viable but, at an early age, they developed severe gastrointestinal motility problems characterized by intestinal pseudo-obstruction resulting in premature death. This gastrointestinal dysfunction was caused by extensive, progressive neurodegeneration of the ENS involving both neurons and glia. Interestingly, mitochondrial defects differentially affected specific subpopulations of enteric neurons and regions of the gastrointestinal tract. Mitochondrial deficiency-related neuronal and glial loss was most prominent in the proximal small intestine, but the first affected neurons, nitrergic inhibitory neurons, had the greatest losses in the distal small intestine. This regional and subtype-specific variability in susceptibility to mitochondrial defects resulted in an imbalance of inhibitory and excitatory neurons that likely accounts for the observed phenotype in Tfam-ENSKO mice. Mitochondrial dysfunction, therefore, is likely to be an important driving force of neurodegeneration in the ENS and contribute to gastrointestinal symptoms in people with neurodegenerative disorders.

Introduction

Gastrointestinal dysfunction is a prevalent symptom in neurologic and systemic diseases associated with neurodegeneration. Constipation, for example, is the most widely recognized non-motor symptom in people with Parkinson's disease (PD), the second most common neurodegenerative disorder in industrialized countries [1,2]. Decreased frequency of bowel movements is in fact one of the earliest signs of PD, predating the development of the classic motor symptoms, sometimes by many years [3-5]. In addition, impaired gastric emptying is estimated to affect the majority of patients with PD and complicates treatment by interfering with levodopa absorption, which can only be absorbed once it reaches the small intestine (SI) [1,6,7]. Similarly, up to 75% people with diabetes mellitus, a systemic metabolic disease associated with progressive neuronal damage [8], experience a variety of gastrointestinal symptoms ranging from diarrhea to severe gastroparesis and constipation [9]. Gastrointestinal dysfunction in these neurodegenerative disorders is related, at least in part, to abnormalities and cell loss in the enteric nervous system (ENS) [9-11], the complex network of neurons and glia that innervates the gut and controls intestinal function. A better understanding of the pathophysiology of neurodegeneration within the ENS could therefore be relevant to the treatment of patients with diseases characterized by neuron loss with prominent gastrointestinal symptoms.

Mitochondria are now thought to be critical mediators of disease progression in diverse disorders such as PD and diabetes. Studies primarily focusing on the central nervous system (CNS) have established that mitochondrial dysfunction is involved in both the initiation and propagation of disease processes that eventually result in neuron

death [12,13]. A growing body of evidence indicates that mitochondrial defects may similarly contribute to neurodegeneration in the ENS. Consistent with this notion, rodent models of PD induced by mitochondrial toxins are characterized by ENS pathology and cell loss, even at doses below those necessary to cause CNS pathology [14-17]. Indeed, the ENS appears to be particularly susceptible to mitochondrial dysfunction compared to other tissues. This is best exemplified by the fact that primary inherited mitochondrial disorders, a heterogeneous group of complex multisystem diseases, commonly include gastrointestinal symptoms. As is the case in PD, symptoms of gastrointestinal dysfunction can precede other presentations of mitochondrial deficits and, in some cases (e.g. mitochondrial neurogastrointestinal encephalomyopathy, or MNGIE) may be the most prominent manifestation of the disease [18]. The role of mitochondrial abnormalities in ENS neurodegeneration and its relative contribution to gastrointestinal dysfunction, however, remain poorly understood.

With the goal of elucidating how mitochondrial abnormalities in the ENS contribute to enteric neurodegeneration and affect gastrointestinal function, we generated mice with impaired mitochondrial metabolism in neurons and glia of the ENS. These Tfam-ENSKO mice were generated by tissue-specific deletion of the gene encoding mitochondrial transcription factor A (*Tfam*), which is required for mitochondrial DNA (mtDNA) transcription and replication [19]. We show that normal mitochondrial function in the ENS is essential for the survival of both enteric neurons and glia as well as for maintenance of normal gastrointestinal motility. Interestingly, we found that mitochondrial dysfunction differentially affected specific subpopulations of enteric neurons and, most surprisingly, specific regions of the gastrointestinal tract.

Mitochondrial deficiency-related neuronal and glial loss was most prominent in the proximal SI, but nitrergic, inhibitory neurons were less severely affected in this region and, instead, were most affected in the distal SI. Interestingly, this regional and subtype variability of enteric neurons appears to directly correlate to the phenotype observed in Tfam-ENSKO mice, with dilation in the proximal SI and relative constriction in the distal SI. Mitochondrial dysfunction in the ENS and the regional- and subtype-specific vulnerabilities of enteric neurons are likely contributors to the gastrointestinal symptoms of patients suffering from some neurodegenerative disorders.

Results

Cre-mediated deletion of Tfam results in mitochondrial abnormalities in the ENS:

To study how mitochondrial dysfunction in the ENS affects gastrointestinal function and contributes to enteric neurodegeneration, we generated mice with disrupted mitochondrial metabolism in both enteric neurons and glia (Tfam-ENSKOs). For this purpose we used a previously developed mouse with *loxP*-flanked *Tfam* alleles ($Tfam^{loxP}$) [19]. Tfam is a mitochondrial protein encoded by nuclear DNA that is essential for mtDNA maintenance, copy number regulation and transcription [19,20]. Previous studies have shown that *cre*-mediated deletion of *Tfam* in $Tfam^{loxP}$ homozygous mice results in severe tissue-specific mtDNA depletion and mitochondrial respiratory chain deficiency [19,21-25]. The tissue-specific deletion of *Tfam* is, therefore, an effective way to induce mitochondrial dysfunction in a selected population of cells.

We mated $Tfam^{loxP}$ mice to mice expressing *cre*-recombinase under the control of the C*np1* promoter (CNP-Cre) [26]. *Cnp1* encodes the enzyme 2′, 3′-cyclic nucleotide 3′-

phosphodiesterase (CNP), a commonly used marker for myelin-forming glia. However, we inadvertently discovered that the *Cnp1* promoter also drives the expression of *cre*-recombinase in the ENS and thereby induces recombination in the majority of enteric neurons and glia. Consistent with this fortuitous observation, CNP has been reported to be highly expressed in gut neural crest stem cells [27]. Indeed, when we crossed CNP-Cre mice with Cre-inducible Rosa26-YFP reporter animals, YFP fluorescence was visible in over 90% of enteric neurons and glia throughout the gut (Fig. 1a and b).

Crossing of Tfam-ENSKO mice to Cre-inducible Rosa26-YFP reporter animals (YFP/Tfam-ENSKOs) showed that *Tfam* was efficiently excised in all enteric neurons and glia in which we observed *Cnp1*-mediated expression of *cre*-recombinase (as visualized by YFP fluorescence). When we isolated YFP-positive enteric neurons and glia from 7 week old YFP/Tfam-ENSKO mice, we could not detect the *Tfam* allele by RT-PCR analysis (Fig. 1c). Given the extent and high efficiency of the *Cnp1* promoter-driven expression of *cre*-recombinase, we conclude that the mating of $Tfam^{loxP}$ to CNP-Cre mice resulted in animals that lacked Tfam in the majority of enteric neurons and glia.

To determine the functional effect of deleting *Tfam* in the ENS, we next assessed mtDNA copy number in YFP-positive enteric neurons and glia from 7 week old YFP/Tfam-ENSKO and YFP/control mice. Tfam has an essential role in the maintenance and replication of mtDNA [19,20] and previous reports have described severe mtDNA depletion following tissue-specific excision of Tfam from a cell of interest [19,21-25]. Consistent with this, we found an 80% reduction in total mtDNA content in enteric neurons and glia isolated from different regions throughout the gut of YFP/Tfam-ENSKO mice (Fig. 1d).

In previous studies using *Tfam*^{loxP} mice, the depletion of mtDNA following *Tfam* excision has been shown to induce severe respiratory chain deficiency, since the mitochondrial genome encodes 13 subunits that are essential components of the electron transport chain. In addition, Tfam deficiency-induced mitochondrial dysfunction is accompanied by abnormalities in mitochondrial morphology [19,21-25,28]. Therefore, to further confirm the enteric neuron- and glia-specific disruption of mitochondria in Tfam-ENSKO mice we examined the enteric nervous system by electron microscopy. Abundant abnormal and enlarged mitochondria with distorted cristae were found specifically within enteric neurons and glia of Tfam-ENSKOs but not of control littermates (Fig. 1e). Together, our results confirm that by deleting *Tfam* in enteric neurons and glia we were able to generate mice with disrupted mitochondria in the ENS.

Tfam-ENSKOs develop progressive gastrointestinal dysfunction characterized by intestinal pseudo-obstruction

Tfam-ENSKO mice were viable and born at the expected Mendelian ratios and, for the first 2 weeks of life, they were indistinguishable from their control littermates. After 2 weeks of age, however, Tfam-ENSKO mice displayed signs of poor growth and, by 4 weeks of age, they were significantly smaller than their control littermates (Fig. 2a). In addition, Tfam-ENSKO mice developed abdominal distention at about 6-8 weeks of age, which, together with poor growth, suggests gastrointestinal dysfunction. After 8 weeks of age, the health of Tfam-ENSKO mice deteriorated rapidly and the majority of the animals died by 12 weeks of age (Fig. 2b).

Dissection of late stage (i.e. 10-12 weeks old) Tfam-ENSKO mice consistently revealed massive dilation within the proximal small bowel along with relative contraction of the distal small bowel (Fig. 2c). The region of transition from dilated proximal small bowel to the narrower distal small bowel was consistently located within the mid-small bowel, with variable accumulation of luminal contents in the proximal small bowel and stomach. No stenosis or mechanical cause of the obstruction could be found and the mice did not have malrotation or other anatomic explanations for the obstruction. Proximal to the transition zone, in the region of dilation, the bowel was filled with dark-colored luminal contents and the bowel wall appeared to be stretched thinner than in controls (Fig. 2c). Luminal contents were absent distally and no stool pellets could be found in the colon or rectum. The distal small intestine and colon in Tfam-ENSKOs generally appeared to have a smaller diameter than in control mice. Therefore, we conclude that disrupted mitochondrial metabolism in enteric neurons and glia in Tfam-ENSKO mice results in significant gastrointestinal dysfunction and dysmotility.

Tfam-ENSKO mice develop progressive neuronal degeneration with distinct regional vulnerabilities

To test the hypothesis that ENS defects underlie the bowel abnormalities and early death observed in Tfam-ENSKO mice, we used whole mount immunohistochemical methods to evaluate ENS structure. We initially examined total myenteric neuron density using immunohistochemistry for HuC/HuD, a widely used pan-neuronal marker that labels the cell body of all neurons within the myenteric plexus [29]. 2 week old Tfam-ENSKO mice had a lower mean neuron density in all regions examined compared to WT

animals, but these differences were not statistically significant ($p>0.1$ in all cases, Fig. 3b and Table 1). This is consistent with the healthy appearance of Tfam-ENSKOs at this age and suggests that the ENS develops normally in these animals.

We next examined the myenteric plexus of 7 week old Tfam-ENSKO and control mice. At this age, Tfam-ENSKO mice begin to show subtle phenotypic abnormalities (i.e. poor growth) but appear healthy, do not display signs of gastrointestinal obstruction, and lack intestinal dilation (Fig. 2a and b). Despite their healthy appearance, at 7 weeks of age Tfam-ENSKO mice had a 68% decrease in myenteric neuron density in the proximal SI, and a 41% decrease in the distal SI (Fig. 3a and b and Table 1). Surprisingly, even though the extent of *Tfam* excision appeared equal in all regions analyzed at 7 weeks of age (Fig. 1), we found no difference in colon total neuron density between Tfam-ENSKOs and control littermates at this age (Fig. 3a and b and Table 1). In fact, enteric neuron density in the colon of Tfam-ENSKOs remained normal even at late pathological stages (e.g. 10-12 weeks old), when enteric neurodegeneration in more proximal regions was profound (data not shown). Thus, mitochondrial dysfunction in the ENS results in a progressive neurodegeneration with marked differences in regional vulnerability to neuronal loss.

Glial degeneration parallels that of neurons in Tfam-ENSKOs

A growing body of literature now implicates glial dysfunction in many neurodegenerative diseases traditionally thought to be neuron autonomous. In animal models of amyotrophic lateral sclerosis, PD, and Huntington's disease among others, glia-specific abnormalities alter disease onset and progression (for a review see [30]). To

address the role of enteric glia in the mitochondria-related gastrointestinal dysfunction of Tfam-ENSKO mice, we assessed the effect of Tfam-depletion on enteric glia using Sox-10 immunohistochemistry. We first examined glial density in the myenteric plexus of 2 week old mice and observed very little difference between Tfam-ENSKOs and littermate controls except in the distal SI (Fig. 3c and Table 1). By 7 weeks of age, however, Tfam-ENSKO mice had significantly reduced glial cell density in both the proximal and distal SI (Fig. 3a and 3c and Table 1). However, as is the case for HuC/HuD^{+} neurons, the glial cell density in the colon of Tfam-ENSKO mice remained normal at 7 weeks of age (Fig. 3a and 3c and Table 1).

The changes in glial cell density in Tfam-ENSKO mice, therefore, seemed to parallel that of neurons, involving the same regions and a similar proportion of cells. We examined this in more detail by comparing the ratio of neurons to glia in control and Tfam-ENSKO mice. As expected from the absence of either neuron or glial cell loss in 2 week old Tfam-ENSKOs, we found no difference in the neuron to glia ratio in any of the regions examined compared to control animals (Fig. 3d and Table 1). Interestingly, despite extensive neuron and glia loss in 7 week old Tfam-ENSKOs, the ratio of neurons to glia in all regions examined remained comparable to that of control littermates (Fig. 3d and Table 1). These results suggest that enteric neurons and glia are equally susceptible to mitochondrial defects in Tfam-ENSKO mice.

Early and differential loss of nitrergic inhibitory neurons in Tfam-ENSKO mice

Intestinal motility and peristalsis depend on the balance between ENS excitatory and inhibitory inputs which together produce the rhythmic coordination of contraction

and relaxation necessary to propel luminal contents [31]. The apparent constriction observed in the distal bowel of Tfam-ENSKO mice, as well as the dilation proximal to this point (Fig. 2c), suggested the possibility of an imbalance between these inputs. To address how enteric neuron loss in Tfam-ENSKO mice affects the balance between inhibitory and excitatory inputs, we examined the number and proportion of nitric oxide (NO)-producing inhibitory neurons in the myenteric plexus by NADPH diaphorase (NADPH-d) staining [32]. The proportion of NADPH-d^+ neurons in different gut regions is normally within a narrow range that maintains the balance between ENS excitatory and inhibitory inputs and allows for normal intestinal motility. As early as 2 weeks of age, the NADPH-d^+ neuron density in the proximal and distal SI in Tfam-ENSKO mice was significantly lower than in controls (Fig. 4b and Table 1). These data suggest early preferential loss of nitrergic inhibitory neurons relative to other neuronal subtypes.

As the pathologic changes in the ENS of Tfam-ENSKO mice progressed, the loss of NADPH-d^+ neurons became more pronounced and, moreover, by 7 weeks of age the percentage of NADPH-d^+ neurons varied quite dramatically between different regions of the gut. NADPH-d^+ neuron loss was greatest in the distal SI with a 60% decrease, but significant decreases were also found in the proximal SI and colon (33% and 25%, respectively; Fig. 4a and b and Table 1). Interestingly, the observed loss of nitrergic neurons did not parallel the loss of total neurons in each region (Fig. 3a and b), causing significant differences in the relative proportion of NADPH-d^+ neurons to total neurons (i.e. changes in inhibitory input) throughout the bowel (Fig. 4c and Table 1). In 7 week old Tfam-ENSKOs, NADPH-d^+ neurons accounted for 75% of total neurons in the proximal SI compared to 36% in controls (Fig. 4c and Table 1). In contrast, in the distal

SI, the proportion of NADPH-d$^+$ inhibitory neurons was lower than in control animals, (19% in Tfam-ENSKOs, 28% in controls; Fig. 4c and Table 1). In the colon, there was no significant difference in the ratio of nitrergic to total neurons between control and Tfam-ENSKO mice (Fig. 4c and Table 1). This concurrent increase in relative abundance of inhibitory inputs in the proximal SI along with the decrease in the ratio of NADPH-d$^+$ to total neurons in the distal SI of Tfam-ENSKOs may thus account for the proximal dilation and distal constriction observed in the late pathology of these mice (Fig. 4d).

Axonal degeneration is a key feature of enteric neuron loss in Tfam-ENSKOs and may precede cell body loss

During our examination of NADPH-d$^+$ neurons, we observed extensive and prominent blebbing in neuronal projections in the myenteric plexus of Tfam-ENSKO mice (Fig. 5a). In the CNS and PNS, axon blebbing has been recognized as a sign of axonal degeneration, a central component of many neurodegenerative diseases, which can precede and sometimes cause neuronal death [33]. To assess the role of axon degeneration in the neuron loss observed in Tfam-ENSKOs we first examined the neuronal projections, or neurites, extending into the villi in the proximal and distal SI. As early as two weeks of age, Tfam-ENSKO mice displayed signs of neurite loss within intestinal villi, although at this age neurite degeneration was limited to the proximal SI (Fig. 5c and Table 2). Neurite loss worsened over time, and by 7 weeks of age the number of neurites in the villi of Tfam-ENSKO mice was significantly reduced in both the proximal and distal SI (Fig. 5b and c and Table 2) suggesting that loss of neuronal projections could contribute to subsequent neuron loss.

Because we are unable to easily identify the cell of origin for neurites in the villi, we also quantified neuronal fiber density for NADPH-d^+ fibers in the myenteric plexus of 7 week old mice. We found no difference in the density of large fiber bundles (i.e., primary fibers; [34]) in any region examined between Tfam-ENSKOs and controls (Table 3). In contrast, small fiber density (i.e., secondary and tertiary fibers; [34]) was significantly lower (44%) in the proximal SI of Tfam-ENSKOs mice, but was similar to controls in the distal SI and colon (Table 3). Note, however, that what we count as "small fibers" or "large fiber bundles" are actually one or more tightly fasciculated neurites. In Tfam-ENSKO mice both "small fibers" and "large fiber bundles" appear significantly thinner than in control animals at 7 weeks of age (Fig. 4a and 5a), suggesting that our counting method for NADPH-d+ neuronal projections significantly underestimates neurite loss in the mutant mice. Because of these limitations, we devised an alternate method to evaluate the effect of mitochondrial dysfunction on enteric neuron and neurite degeneration *in vitro*.

E12.5 enteric neurons were cultured from control mouse gut and exposed to different inhibitors of the mitochondrial electron transport chain (e.g. rotenone and antimycin). Disrupting mitochondrial respiration induced significant neurite degeneration within 24 hours, yet did not initially affect neuron viability as measured by ethidium homodimer staining (Fig. 5d and e and Table 4). Moreover, even though extended exposure to mitochondrial inhibitors eventually induced enteric neuron death, the proportion of cells showing axonal degeneration remained larger at every time point examined (Table 4). Together, these results suggest that axonal degeneration precedes enteric neuron cell body loss induced by mitochondrial defects.

Discussion

The current understanding of how mitochondrial deficits affect enteric neurons and contribute to ENS neurodegeneration and gastrointestinal dysfunction has been hindered by a lack of animal models. Here we describe a new mouse model with disrupted mitochondrial function in enteric neurons and glia. We show that abnormal mitochondrial metabolism in the ENS causes widespread enteric neurodegeneration and results in severe intestinal pseudo-obstruction, the likely cause of premature death in Tfam-ENSKO mice. Remarkably, mitochondrial dysfunction differentially affected specific subpopulations of enteric neurons and regions of the gastrointestinal tract. This regional and subtype-specific variability resulted in an imbalance of inhibitory and excitatory enteric neurons that likely accounts for the observed phenotype in Tfam-ENSKO mice. Our observations support the hypothesis that damage to the ENS resulting from defects in mitochondrial function may underlie some of the pathophysiology involved in gastrointestinal abnormalities in many human neurodegenerative diseases.

Mitochondria are thought to be critical mediators of neuron loss in diverse neurodegenerative disorders such as PD or diabetes. We show that mitochondrial defects in the ENS cause both neuron and glia cell loss as well as severe intestinal dysmotility. Strikingly, not all regions of the gut were equally affected. The proximal SI suffered the most extensive neuron and glial loss whereas the colon was largely spared (Fig. 3). Furthermore, we observed differential vulnerability among distinct subtypes of enteric neurons. Nitrergic neurons, which are predominantly inhibitory in nature, were lost earliest in the progression of the disease in Tfam-ENSKOs (Fig. 4). These findings cannot be explained by variations in the efficiency of *Tfam* excision or in the resulting

effect on mitochondria. *Cnp1*-mediated expression of *cre*-recombinase (as visualized by YFP fluorescence) and mtDNA depletion were comparable throughout the bowel of Tfam-ENSKO mice (Fig. 1). The observed variability in sensitivity to mitochondrial defects suggests, therefore, that there are regional and cell type specific differences in metabolic needs for individual enteric neuron populations.

In the CNS, regional- and subtype-specific differences in the vulnerability of neurons to mitochondrial dysfunction are well established; such differences are thought to underlie the preferential loss of striatal neurons in PD or Huntington's disease [35]. Early preferential loss of nitrergic neurons has also been reported in a streptozotocin-induced rat model of diabetic autonomic neuropathy [36]. Similar differences in vulnerability to metabolic insults among enteric neurons had been suggested by an earlier study using a rotenone-induced rat model of PD [16]. The enteric nervous system abnormalities observed in Tfam-ENSKO mice suggest that regional- and subtype-specific differences in the susceptibility of neurons to mitochondrial defects are also present in the ENS and may explain the gastrointestinal presentations of neurodegenerative diseases.

While the mitochondrial dysfunction in Tfam-ENSKO mice is caused by the loss of Tfam, the way in which these mice recapitulate gastrointestinal pathological features often seen in neurodegenerative disorders indicates that there may be broader implications of this work for understanding the bowel dysfunction that accompanies both rare and common human disease. For example, Tfam-ENSKO mice consistently developed intestinal pseudo-obstruction with dilated proximal small bowel and contracted distal bowel reminiscent of that seen in the human mitochondrial disease MNGIE. Our results indicate that this pseudo-obstruction could occur because of an

imbalance in the ratio of inhibitory to excitatory inputs in the ENS. In Tfam-ENSKOs such an imbalance arises from a relative preservation of nitrergic inhibitory neurons in the proximal SI and preferential loss of these same neurons in the distal SI of these mice. This is of particular interest, because the severe intestinal pseudo-obstruction resulting in cachexia and death in MNGIE patients has traditionally been attributed to smooth muscle abnormalities, even though mtDNA depletion is also found within enteric neurons in the SI of MNGIE patients [37]. Our results demonstrating that mitochondrial dysfunction in enteric neurons and glia alone is capable of producing very similar pathology, however, suggest that the ENS may play a more prominent role in this mitochondrial disease than previously thought.

While MNGIE is a rare disease, mitochondrial dysfunction is thought to be a common underlying mechanism in both normal human aging [38] as well as in many common diseases such as type 2 diabetes [39]. Defects in gastrointestinal motility frequently cause serious problems in the elderly and in patients with diabetes [9,40]. These motility defects, similar to what we observed in Tfam-ENSKO mice, have been attributed to enteric neurodegeneration [9,40]. Moreover, enteric neurodegeneration in models of aging, PD and diabetes have been associated with imbalances in inhibitory and excitatory neurons [40]. As such, understanding the ENS abnormalities in Tfam-ENSKO mice could provide valuable insight into the pathophysiology responsible for gastrointestinal motility disorders involved in numerous disease processes and affecting a large number of people.

In summary, Tfam-ENSKO mice are the first genetic model of enteric nervous system-specific mitochondrial dysfunction and interestingly recapitulate a number of

pathological features often seen in human neurodegenerative diseases with prominent gastrointestinal presentations, such as MNGIE, PD or diabetes mellitus. Enteric mitochondrial dysfunction in these diseases is therefore likely to contribute to their gastrointestinal pathology. Moreover, Tfam-ENSKOs revealed a remarkable region- and subtype-specific differential vulnerability of enteric neurons to defects in mitochondrial metabolism. Appropriate management of gastrointestinal dysfunction in patients with neurodegenerative diseases might thus be facilitated by devising therapeutic strategies that improve ENS mitochondrial function and address the differential vulnerability of specific enteric neuron populations.

Materials and Methods

Ethics: All studies were reviewed and approved by the Washington University Animal Studies Committee, protocol approval # 20110071 (J.M.) and # 20090190 (ROH).

Matings of transgenic animals: *Tfam*$^{loxP/loxP}$ mice [19] and CNP-Cre mice [26] in pure C57Bl/6 backgrounds were crossed to generate Tfam-ENSKO mice (*CNP-Cre*$^{+/-}$, *Tfam*$^{loxP/loxP}$) and their control littermates (*CNP-Cre*$^{-/-}$, *Tfam*$^{loxP/loxP}$ or *CNP-Cre*$^{-/-}$, *Tfam*$^{+/loxP}$). For experiments involving YFP fluorescence-based FACS sorting or imaging of enteric neurons and glia, Tfam-ENSKO mice were crossed to Rosa26-YFP reporter mice [41] to generate YFP/Tfam-ENSKO mice (*Rosa26-YFP*$^{+/-}$, *CNP-Cre*$^{+/-}$, *Tfam*$^{loxP/loxP}$). Mice with transgenic *Rosa26-YFP* and *CNP-Cre* alleles, but with wild type Tfam alleles (YFP/control: *Rosa26-YFP*$^{+/-}$, *CNP-Cre*$^{+/-}$, *Tfam*$^{+/+}$), were used as controls in

these experiments. Tfam$^{loxP/loxP}$, CNP-Cre and Rosa26-YFP genotyping were carried out as previously described [19,26,41].

Quantitative ENS analysis: Mice were euthanized by carbon dioxide asphyxiation followed by cervical dislocation. The gastrointestinal tract was removed and enteric whole-mount samples were prepared. Intestines were flushed with ice cold PBS, then opened by cutting along the mesenteric border, flattened and pinned mucosal side down, and fixed using 4% paraformaldehyde for 30 minutes. After fixation, samples were washed with ice cold PBS before isolating the myenteric plexus by peeling off the muscle layers of the intestine. A 6 cm-long intestinal sample was isolated from the proximal SI (measured from the pylorus), distal SI (measured from the ileocecal junction), and distal colon (measured from the anus). In the 2-week-old mice, 3-4 cm long samples were obtained from the same regions as described above. Samples were then cut into 1 to 2 cm segments before storing in 50% glycerol/PBS at -20˚C until staining and analysis.

In the 7-week-old mice, sequential 1 cm-long samples of myenteric plexus were stained with NADPH-d [42], biotinylated-HuC/HuD (1:250; Invitrogen A21272) and Sox-10 (1:250; Santa Cruz). In the 2-week-old mice, sequential 1-1.5 cm long samples of myenteric plexus were stained with NADPH-d or biotinylated-HuC/HuD and Sox-10, again using the order described above. For the biotinylated-HuC/HuD and Sox-10 double labeling, samples were first labeled by HuC/HuD immunohistochemistry (1:250; Invitrogen A21272) and then labeled by Sox-10 immunohistochemistry (1:250; Santa Cruz).

Quantification of neuron or glial cell density was done by counting all cells present within the borders of a 0.5 x 0.5 mm grid (20x objective lens). For instances in which the cellular density was very high, counts were done using a 40x objective lens (within the borders of a 0.25 x 0.25mm grid). An attempt was made to stretch all segments evenly and equally for all samples. All analyses used three to six animals, and counting was done without knowledge of the mouse genotype. Twenty (20) randomly selected fields were counted for each region and data are presented as neurons/mm^2. Averages for each animal were used to calculate the mean, standard deviation and standard error for each genotype. Neuron-to-glia ratio was determined by dividing the number of neurons by the number of glia present within a single field.

Villus neurite quantification: Villus preparations were made by cutting along single rows of intestinal villi from full-thickness, pinned samples of proximal and distal small intestine in 70% ethanol. These were then labeled by TuJ1 (1:10,000; Covance) immunohistochemistry. Villus neurite quantification was determined by counting all $TuJ1^+$ projections that crossed a perpendicular line drawn through the middle of each villus. Twenty (20) randomly selected villi were counted for each region and averaged for each animal. At least 3 mice were used to calculate the mean, standard deviation and standard error for each genotype.

FACS isolation of enteric neurons and glia: Rosa26-YFP^+ cells were sorted by flow cytometry after isolating and digesting unfixed myenteric plexus from 7-week-old YFP/control and YFP/Tfam-ENSKO mice. A modified version of the protocol published

by Schafer et al. [43] was used to isolate adult mouse ENS neurons and glia. Briefly, muscle layers of the bowel containing the myenteric plexus were isolated by dissection as described above, but were not fixed. Samples from the proximal SI, distal SI and colon were cut into 1 mm^2 pieces in ice-cold PBS, then treated with collagenase (1 mg/ml in DMEM; 37^oC, 45 min). After collagenase treatment, tissues were centrifuged at 4,500 rpm for 2 min and collagenase solution was replaced with 0.25% Trypsin in DMEM. Samples were rotated (37^oC, 20-30 min) and triturated by pipetting before centrifugation (4,500 rpm for 2 min) to remove supernatant. Cells were diluted in 300 μL FACS buffer (0.002% BSA, 0.001% Sodium Azide, 1 mM EDTA in PBS) and filtered through 70 micron MACS separation filters. Cells were then sorted for YFP expression on a MoFlo Cell Sorter (Beckman Coulter Corp., Fullerton, CA), using 15 p.s.i. and a 120 μm sorting nozzle. YFP fluorescence was captured with a 525/40 optical filter in the cytometer's FL 1 channel. Samples were taken from three mice of each genotype (YFP/Ctrl: *Rosa26-YFP*$^{+/-}$, *CNP-Cre*$^{+/-}$, *Tfam*$^{+/+}$; YFP/Tfam-ENSKO: *Rosa26-YFP*$^{+/-}$, *CNP-Cre*$^{+/-}$, *Tfam*$^{loxP/loxP}$) and a non-YFP$^+$ littermate (*Rosa26-YFP*$^{-/-}$, *CNP-Cre*$^{+/-}$, *Tfam*$^{+/+}$ or *Rosa26-YFP*$^{-/-}$, *CNP-Cre*$^{+/-}$, *Tfam*$^{loxP/loxP}$) was used for standardization.

RNA and DNA preparation and quantitative real-time PCR (qRT-PCR): RNA and DNA were isolated from FACS sorted enteric neurons and glia from YFP/Tfam-ENSKO mice and YFP/Ctrl littermates. For RNA isolation, cells were lysed in Trizol reagent (Invitrogen) and total RNA prepared according to the manufacturer's protocol. For DNA isolation, cells were digested and DNA isolated using DNeasy Blood and Tissue Kit

(Qiagen) according to the manufacturer's protocol. DNA and RNA concentration were quantified using an ND-1000 spectrophotometer (Nanodrop Technologies).

For RT-PCR, cDNA was reverse transcribed from total RNA using M-MLV reverse transcriptase (Invitrogen) and Tfam or GAPDH mRNA were amplified using the following primers (5'-3'): Tfam: F, CAGGAGGCAAAGGATGATTC; R, ATGTCTCCGGATCGTTTCAC; GAPDH: F, TGCCCCCATGTTTGTGATG; R, TGTGGTCATGAGCCCTTCC. mtDNA content was quantified by qRT-PCR using a SYBR green-based detection system on a 7700 Sequence Detector instrument (Applied Biosystems) as described previously [44]. Instead of cDNA, however, 15 ng of total DNA were used per reaction. Primers that recognize a region unique to the mitochondrial genome were used to determine mtDNA content normalized to nuclear DNA content, as determined by a set of primers directed to the genomic locus of Smrt1. The primers used were as follows: mtDNA: F, AAGTCGTAACAAGGTAAGCA; R, ATATTTGTGTAGGGCTAGGG. Nuc.DNA: F, GGGTATATTTTTGATACCTTCAATGAGTTA; R, TCTGAAACAGTAGGTAGAGACCAAAGC

Cell culture: Enteric neural crest cells were immunoselected from embryonic day 12.5 (E12.5) CD1 mice small bowel and colon using $p75^{NTR}$ antibody (Millipore). Bowel was dissociated with collagenase (1 mg/ml) and dispase (1 mg/ml) to yield a single cell suspension. After $p75^{NTR}$ antibody incubation (Millipore, 1:1000, 1 h, 4°C) in B27 (Invitrogen) supplemented Neurobasal medium, cells were incubated with goat anti-rabbit coupled paramagnetic beads (1:50, 1 h, 4°C; Miltenyi Biotec, Bergisch Gladbach,

Germany) before separating neural crest-derived cells from unselected cells with a positive selection column (MACS separation columns; Miltenyi Biotec). Immunoselected crest-derived cells were plated at a density of 500 cells per well on poly-d-lysine/laminin-coated 24-well plates in B27 supplemented Neurobasal medium plus 50 ng/ml glial cell line-derived neurotrophic factor (GDNF). In all experiments, inhibitors were added to the medium 24 h after plating using 2.5 μm antimycin (Complex III inhibitor) or 2.5 μm rotenone (Complex I inhibitor). Control wells were treated with DMSO vehicle. All experiments were performed in triplicate. All analyses were performed blinded.

Neuronal cell body death assay and Immunohistochemistry: Neurons were treated with inhibitors or vehicle control and monitored for cell body damage by ethidium homodimer exclusion (Biotium, Hayward, CA). Ethidium homodimer was added to the cultures at a final concentration of 100 nM and after 30 minutes of incubation cells were washed with PBS and fixed 4% paraformaldehyde. After fixation, cells were washed with PBS and blocked with 5% normal donkey serum in TBST (Tris-buffered saline plus 0.1% Triton X-100) (1 h, 37°C). Cells were incubated in rabbit polyclonal Tuj1 antibody (1:1000 at 4°C overnight) and antibody binding was visualized with Alexa Fluor 488 conjugated anti-rabbit secondary antibodies (Jackson Immunoresearch Laboratory, 1:500, 25°C, 1 h).

Electron Microscopy: Samples for transmission electron microscopy were obtained from 7 week old mice by intracardiac perfusion of Modified Karnovsky's Fixative (2.5% glutaraldehyde, 2% paraformaldehyde in 0.1 mmol/liter cacodylate buffer), followed by

isolation of whole mount samples as described above, omitting peeling. Gut samples were pinned in modified Karnovsky's Fixative and postifixed in 2% OsO_4 (in 0.1 mmol/L cacodylate buffer). Samples were then dehydrated and embedded in PolyBed 812 (Polysciences Inc., Warrington, PA). 100 nm sections were cut with a Diatome diamond knife and stained with uranyl acetate in 50% methanol and Venable's lead citrate. Transmission EM was performed on a JEOL JEM 1200-EX microscope with AMT Advantage HR (Advanced Microscopy Techniques Corp., Danvers MA) high-speed, wide-angle 1.3 megapixel TEM digital camera.

Light Microscopy and quantification: Samples were counted using a 10 x 10 grid counting eyepiece on an Olympus Optical Bx60 microscope or Zeiss Axioskop and an Axiocam digital camera and AxioVision imaging software (Zeiss, Germany). Photoshop 7.0 was used to uniformly adjust contrast and brightness so that digital images appear as they did when observed directly through the microscope.

Statistical analysis: All values are expressed as mean ± SEM. P values were determined by paired Student's t-test or Mann-Whitney rank sum test using Sigma Plot 11.0 (Systat Software, San Jose, CA). In all applicable figures, an asterisk (*) indicates statistical significance (p value < 0.05).

Acknowledgments

We thank Nina Panchenko, Karen Green, Aishwarya Kundu Roy, Ben Capoccia, Hongtao Wang, Meredith Hitch, and Jacqueline Hughes for experimental assistance; Dr. Robert Schmidt for help interpreting electron micrographs; Nils-Goran Larsson for the

Tfam^{loxP} mice; Klaus-Armin Nave for the CNP-Cre mice; members of the Milbrandt and Heuckeroth laboratories for their comments on the manuscript and helpful discussions.

References

1. Pfeiffer RF. (2011) Gastrointestinal dysfunction in parkinson's disease. Parkinsonism Relat Disord 17(1): 10-15. 10.1016/j.parkreldis.2010.08.003.

2. Nussbaum RL, Ellis CE. (2003) Alzheimer's disease and parkinson's disease. N Engl J Med 348(14): 1356-1364. 10.1056/NEJM2003ra020003.

3. Abbott RD, Petrovitch H, White LR, Masaki KH, Tanner CM, et al. (2001) Frequency of bowel movements and the future risk of parkinson's disease. Neurology 57(3): 456-462.

4. Abbott RD, Ross GW, Petrovitch H, Tanner CM, Davis DG, et al. (2007) Bowel movement frequency in late-life and incidental lewy bodies. Mov Disord 22(11): 1581-1586. 10.1002/mds.21560.

5. Ashraf W, Pfeiffer RF, Park F, Lof J, Quigley EM. (1997) Constipation in parkinson's disease: Objective assessment and response to psyllium. Mov Disord 12(6): 946-951. 10.1002/mds.870120617.

6. Goetze O, Nikodem AB, Wiezcorek J, Banasch M, Przuntek H, et al. (2006) Predictors of gastric emptying in parkinson's disease. Neurogastroenterol Motil 18(5): 369-375. 10.1111/j.1365-2982.2006.00780.x.

7. Kurlan R, Rothfield KP, Woodward WR, Nutt JG, Miller C, et al. (1988) Erratic gastric emptying of levodopa may cause "random" fluctuations of parkinsonian mobility. Neurology 38(3): 419-421.

8. Tomlinson DR, Gardiner NJ. (2008) Glucose neurotoxicity Nat Rev Neurosci 9(1): 36-45. 10.1038/nrn2294.

9. Chandrasekharan B, Srinivasan S. (2007) Diabetes and the enteric nervous system Neurogastroenterol Motil 19(12): 951-960. 10.1111/j.1365-2982.2007.01023.x.

10. Braak H, de Vos RA, Bohl J, Del Tredici K. (2006) Gastric alpha-synuclein immunoreactive inclusions in meissner's and auerbach's plexuses in cases staged for parkinson's disease-related brain pathology Neurosci Lett 396(1): 67-72. 10.1016/j.neulet.2005.11.012.

11. Wakabayashi K, Takahashi H, Ohama E, Takeda S, Ikuta F. (1993) Lewy bodies in the visceral autonomic nervous system in parkinson's disease. Adv Neurol 60: 609-612.

12. Gibson GE, Starkov A, Blass JP, Ratan RR, Beal MF. (2010) Cause and consequence: Mitochondrial dysfunction initiates and propagates neuronal dysfunction, neuronal death and behavioral abnormalities in age-associated neurodegenerative diseases. Biochim Biophys Acta 1802(1): 122-134. 10.1016/j.bbadis.2009.08.010.

13. Ekstrand MI, Terzioglu M, Galter D, Zhu S, Hofstetter C, et al. (2007) Progressive parkinsonism in mice with respiratory-chain-deficient dopamine neurons. Proc Natl Acad Sci U S A 104(4): 1325-1330. 10.1073/pnas.0605208103.

14. Anderson G, Noorian AR, Taylor G, Anitha M, Bernhard D, et al. (2007) Loss of enteric dopaminergic neurons and associated changes in colon motility in an MPTP mouse model of parkinson's disease. Exp Neurol 207(1): 4-12. 10.1016/j.expneurol.2007.05.010.

15. Drolet RE, Cannon JR, Montero L, Greenamyre JT. (2009) Chronic rotenone exposure reproduces parkinson's disease gastrointestinal neuropathology. Neurobiol Dis 36(1): 96-102. 10.1016/j.nbd.2009.06.017.

16. Greene JG, Noorian AR, Srinivasan S. (2009) Delayed gastric emptying and enteric nervous system dysfunction in the rotenone model of parkinson's disease. Exp Neurol 218(1): 154-161. 10.1016/j.expneurol.2009.04.023.

17. Tian YM, Chen X, Luo DZ, Zhang XH, Xue H, et al. (2008) Alteration of dopaminergic markers in gastrointestinal tract of different rodent models of parkinson's disease. Neuroscience 153(3): 634-644. 10.1016/j.neuroscience.2008.02.033.

18. Hom XB, Lavine JE. (2004) Gastrointestinal complications of mitochondrial disease. Mitochondrion 4(5-6): 601-607. 10.1016/j.mito.2004.07.014.

19. Larsson NG, Wang J, Wilhelmsson H, Oldfors A, Rustin P, et al. (1998) Mitochondrial transcription factor A is necessary for mtDNA maintenance and embryogenesis in mice. Nat Genet 18(3): 231-236. 10.1038/ng0398-231.

20. Ekstrand MI, Falkenberg M, Rantanen A, Park CB, Gaspari M, et al. (2004) Mitochondrial transcription factor A regulates mtDNA copy number in mammals. Hum Mol Genet 13(9): 935-944. 10.1093/hmg/ddh109.

21. Sorensen L, Ekstrand M, Silva JP, Lindqvist E, Xu B, et al. (2001) Late-onset corticohippocampal neurodepletion attributable to catastrophic failure of oxidative phosphorylation in MILON mice. J Neurosci 21(20): 8082-8090.

22. Silva JP, Kohler M, Graff C, Oldfors A, Magnuson MA, et al. (2000) Impaired insulin secretion and beta-cell loss in tissue-specific knockout mice with mitochondrial diabetes. Nat Genet 26(3): 336-340. 10.1038/81649.

23. Wang J, Wilhelmsson H, Graff C, Li H, Oldfors A, et al. (1999) Dilated cardiomyopathy and atrioventricular conduction blocks induced by heart-specific inactivation of mitochondrial DNA gene expression. Nat Genet 21(1): 133-137. 10.1038/5089.

24. Wredenberg A, Wibom R, Wilhelmsson H, Graff C, Wiener HH, et al. (2002) Increased mitochondrial mass in mitochondrial myopathy mice. Proc Natl Acad Sci U S A 99(23): 15066-15071. 10.1073/pnas.232591499.

25. Viader A, Golden JP, Baloh RH, Schmidt RE, Hunter DA, et al. (2011) Schwann cell mitochondrial metabolism supports long-term axonal survival and peripheral nerve function. J Neurosci 31(28): 10128-10140. 10.1523/JNEUROSCI.0884-11.2011.

26. Lappe-Siefke C, Goebbels S, Gravel M, Nicksch E, Lee J, et al. (2003) Disruption of Cnp1 uncouples oligodendroglial functions in axonal support and myelination. Nat Genet 33(3): 366-374. 10.1038/ng1095.

27. Iwashita T, Kruger GM, Pardal R, Kiel MJ, Morrison SJ. (2003) Hirschsprung disease is linked to defects in neural crest stem cell function. Science 301(5635): 972-976. 10.1126/science.1085649.

28. Wang J, Silva JP, Gustafsson CM, Rustin P, Larsson NG. (2001) Increased in vivo apoptosis in cells lacking mitochondrial DNA gene expression. Proc Natl Acad Sci U S A 98(7): 4038-4043. 10.1073/pnas.061038798.

29. Phillips RJ, Hargrave SL, Rhodes BS, Zopf DA, Powley TL. (2004) Quantification of neurons in the myenteric plexus: An evaluation of putative pan-neuronal markers. J Neurosci Methods 133(1-2): 99-107.

30. Ilieva H, Polymenidou M, Cleveland DW. (2009) Non-cell autonomous toxicity in neurodegenerative disorders: ALS and beyond. J Cell Biol 187(6): 761-772. 10.1083/jcb.200908164.

31. Wood JD, Alpers DH, Andrews PL. (1999) Fundamentals of neurogastroenterology. Gut 45 Suppl 2: II6-II16.

32. Sang Q, Young HM. (1996) Chemical coding of neurons in the myenteric plexus and external muscle of the small and large intestine of the mouse Cell Tissue Res 284(1): 39-53.

33. Coleman M. (2005) Axon degeneration mechanisms: Commonality amid diversity. Nat Rev Neurosci 6(11): 889-898. 10.1038/nrn1788.

34. Furness JB. (2006) The enteric nervous system. Massachussetts: Wiley-Blackwell.

35. Pickrell AM, Fukui H, Wang X, Pinto M, Moraes CT. (2011) The striatum is highly susceptible to mitochondrial oxidative phosphorylation dysfunctions. J Neurosci 31(27): 9895-9904. 10.1523/JNEUROSCI.6223-10.2011.

36. Cellek S, Foxwell NA, Moncada S. (2003) Two phases of nitrergic neuropathy in streptozotocin-induced diabetic rats. Diabetes 52(9): 2353-2362.

37. Hao MM, Moore RE, Roberts RR, Nguyen T, Furness JB, et al. (2010) The role of neural activity in the migration and differentiation of enteric neuron precursors. Neurogastroenterol Motil 22(5): e127-37. 10.1111/j.1365-2982.2009.01462.x.

38. Dufour E, Terzioglu M, Sterky FH, Sorensen L, Galter D, et al. (2008) Age-associated mosaic respiratory chain deficiency causes trans-neuronal degeneration. Hum Mol Genet 17(10): 1418-1426. 10.1093/hmg/ddn030.

39. Lowell BB, Shulman GI. (2005) Mitochondrial dysfunction and type 2 diabetes. Science 307(5708): 384-387. 10.1126/science.1104343.

40. Wiskur B, Greenwood-Van Meerveld B. (2010) The aging colon: The role of enteric neurodegeneration in constipation. Curr Gastroenterol Rep 12(6): 507-512. 10.1007/s11894-010-0139-7.

41. Srinivas S, Watanabe T, Lin CS, William CM, Tanabe Y, et al. (2001) Cre reporter strains produced by targeted insertion of EYFP and ECFP into the ROSA26 locus BMC Dev Biol 1: 4.

42. Neuhuber WL, Worl J, Berthoud HR, Conte B. (1994) NADPH-diaphorase-positive nerve fibers associated with motor endplates in the rat esophagus: New evidence for co-innervation of striated muscle by enteric neurons. Cell Tissue Res 276(1): 23-30.

43. Schafer KH, Klotz M, Mergner D, Mestres P, Schimrigk K, et al. (2000) IgG-mediated cytotoxicity to myenteric plexus cultures in patients with paraneoplastic neurological syndromes. J Autoimmun 15(4): 479-484. 10.1006/jaut.2000.0454.

44. Nagarajan R, Svaren J, Le N, Araki T, Watson M, et al. (2001) EGR2 mutations in inherited neuropathies dominant-negatively inhibit myelin gene expression. Neuron 30(2): 355-368.

Figures

Figure 1. CNP-Cre excises Tfam in enteric neurons and glia and disrupts ENS mitochondria in Tfam-ENSKO mice. ***a)*** YFP fluorescence in 2-day-old Rosa26-YFP/CNP-Cre mice overlaps (merge) with enteric neurons (HuC/HuD$^+$ cells, Hu, red) and glia (Sox-10$^+$ cells, Sox, blue). Excision-dependent YFP fluorescence is visible in the majority of enteric neurons and glia in all gut regions. Asterisks indicate the occasional non-recombined, non-YFP$^+$ cell. Scale bars: 30 μm. ***b)*** Quantification of the percent of YFP$^+$ neurons (% of HuC/HuD$^+$ and YFP$^+$ cells/total HuC/HuD$^+$ cells) and glia (% of Sox-10$^+$ and YFP$^+$ cells/total Sox-10$^+$ cells) in different gut regions confirms high efficiency of CNP-Cre mediated recombination in the ENS. n=3 mice per genotype. ***c)*** RT-PCR of Tfam transcript demonstrates the complete excision of *Tfam* in YFP$^+$ FACS selected myenteric neurons and glia in YFP/Tfam-ENSKO mice at 7 weeks of age. n=3 mice per genotype. ***d)*** qRT-PCR results show depletion of mtDNA content in YFP$^+$ FACS-selected myenteric neurons and glia in 7 week old YFP/Tfam-ENSKO mice. mtDNA content was significantly reduced in YFP/Tfam-ENSKO mice in all regions examined at this age (*, $p<0.01$). Reported values are normalized to nuclear DNA content and ratio of mtDNA to nuclear DNA in control animals was set at 100; n=3 mice per genotype. ***e)*** Electron micrographs of myenteric plexus mitochondria (arrowheads) in 7 week old control and Tfam-ENSKO mice. Tfam-ENSKO myenteric neurons and glia contain abundant abnormal, enlarged mitochondria with dilated and distorted cristae. Scale bars, 500 nm.

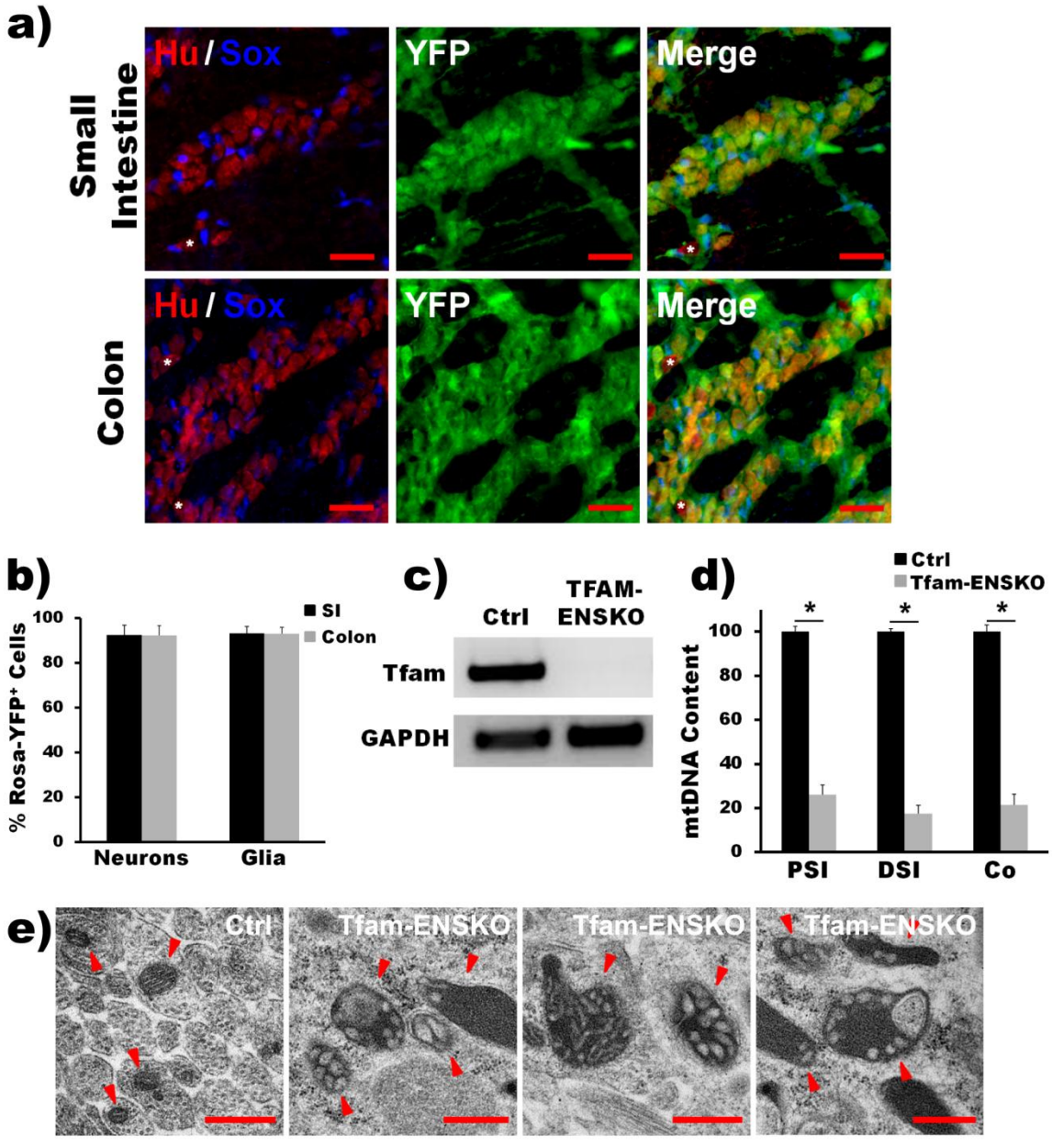
a)
Small Intestine
Colon
Hu / Sox
YFP
Merge
b)
% Rosa-YFP+ Cells
SI
Colon
Neurons
Glia
c)
Ctrl
TFAM-ENSKO
Tfam
GAPDH
d)
Ctrl
Tfam-ENSKO
mtDNA Content
PSI
DSI
Co
e)
Ctrl
Tfam-ENSKO
Tfam-ENSKO
Tfam-ENSKO

Figure 2. Tfam-ENSKOs develop progressive GI dysfunction characterized by intestinal pseudo-obstruction *a)* Growth curve of Tfam-ENSKO mice and control littermates. Tfam-ENSKOs are initially indistinguishable from control mice, but begin to exhibit poor growth at 4 weeks of age ($n \geq 10$ mice per genotype at each time point). ***b)*** Survival curve of Tfam-ENSKO mice and control littermates. Tfam-ENSKO mice die prematurely beginning at 60 days old. By 90 days, nearly all Tfam-ENSKO mice are dead. n=47 mice. ***c)*** Photograph of gastrointestinal tract of 11-12 week old control and Tfam-ENSKO mice depicts their typical appearance. Arrowheads indicate regions of dilation and accumulation of luminal contents. St: stomach, SI: small intestine, Co: colon.

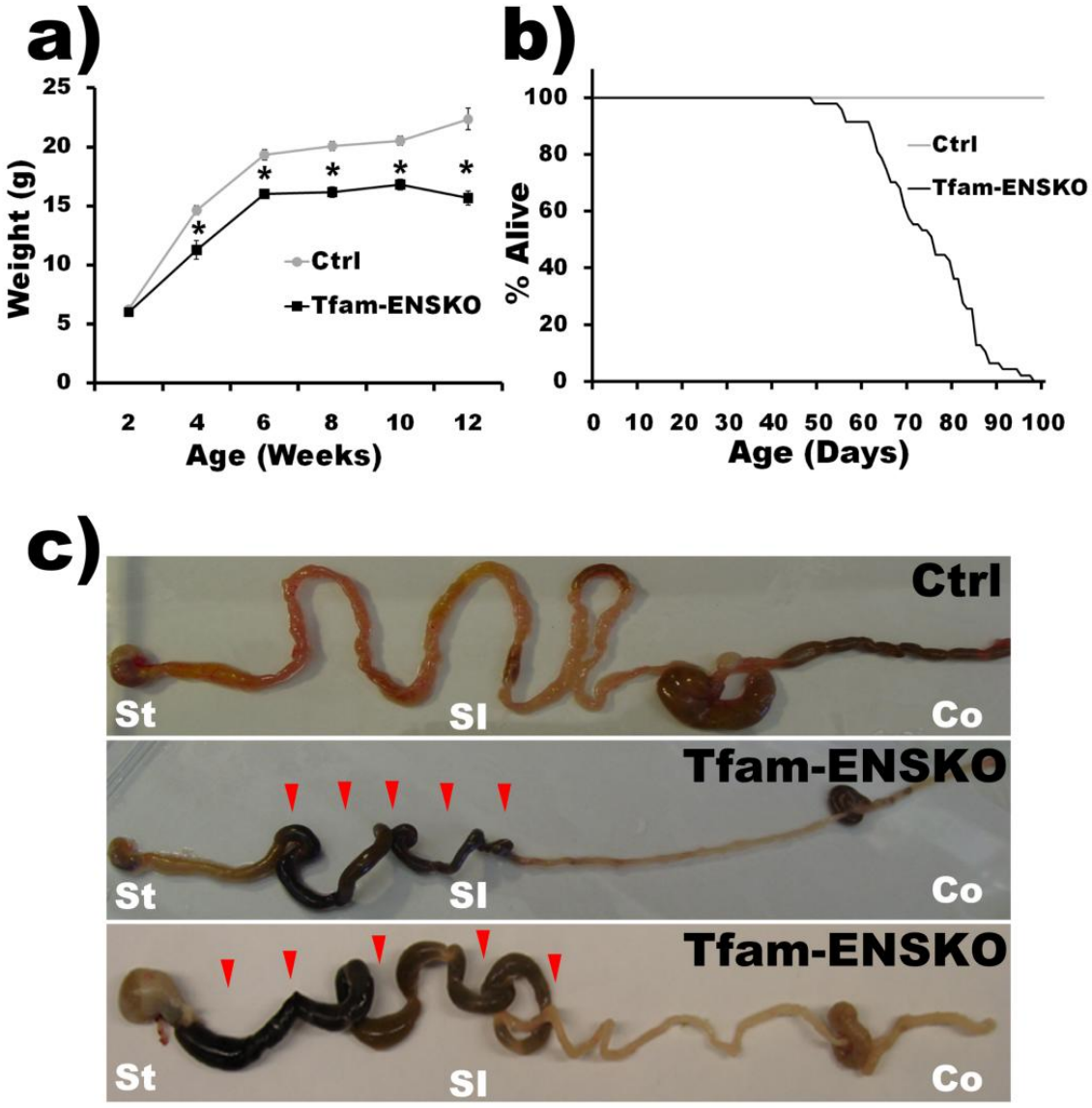
a)
Weight (g)
25
20
15
10
5
0
2
4
6
8
10
12
Age (Weeks)
Ctrl
Tfam-ENSKO
*
b)
% Alive
100
80
60
40
20
0
0 10 20 30 40 50 60 70 80 90 100
Age (Days)
Ctrl
Tfam-ENSKO
c)
Ctrl
St
SI
Co
Tfam-ENSKO
St
SI
Co
Tfam-ENSKO
St
SI
Co

Figure 3. Tfam-ENSKO mice display progressive degeneration of neurons and glia with distinct regional vulnerabilities. ***a)*** Representative images of HuC/HuD (neurons, red) and Sox-10 (glia, green) immunohistochemistry in three regions of myenteric plexus of 7 week old control and Tfam-ENSKO mice. Loss of both HuC/HuD^{+} neurons and Sox-10^{+} glia is apparent in Tfam-ENSKOs at this age. Scale bars, 100 μm. ***b)*** Quantification of total myenteric neuron density in Tfam-ENSKOs expressed relative to control littermates at 2 and 7 weeks of age. For 2 weeks old, n=6 (Ctrl) and n=4 (Tfam-ENSKO). For 7 weeks old, n=3 for each genotype. ***c)*** Quantification of glial density in Tfam-ENSKOs expressed relative to control littermates at 2 and 7 weeks of age. For 2 weeks old, n=6 (Ctrl) and n=4 (Tfam-ENSKO). For 7 weeks old, n=3 for each genotype. ***d)*** Neuron-to-glia ratio in ENS of Tfam-ENSKOs and control littermates at 2 and 7 weeks of age demonstrates that relative cell loss is equivalent for both neurons and glia. For 2 weeks old, n=6 (Ctrl) and n=4 (Tfam-ENSKO). For 7 weeks old, n=3 for each genotype. PSI: proximal small intestine, DSI: distal small intestine, Co: colon.

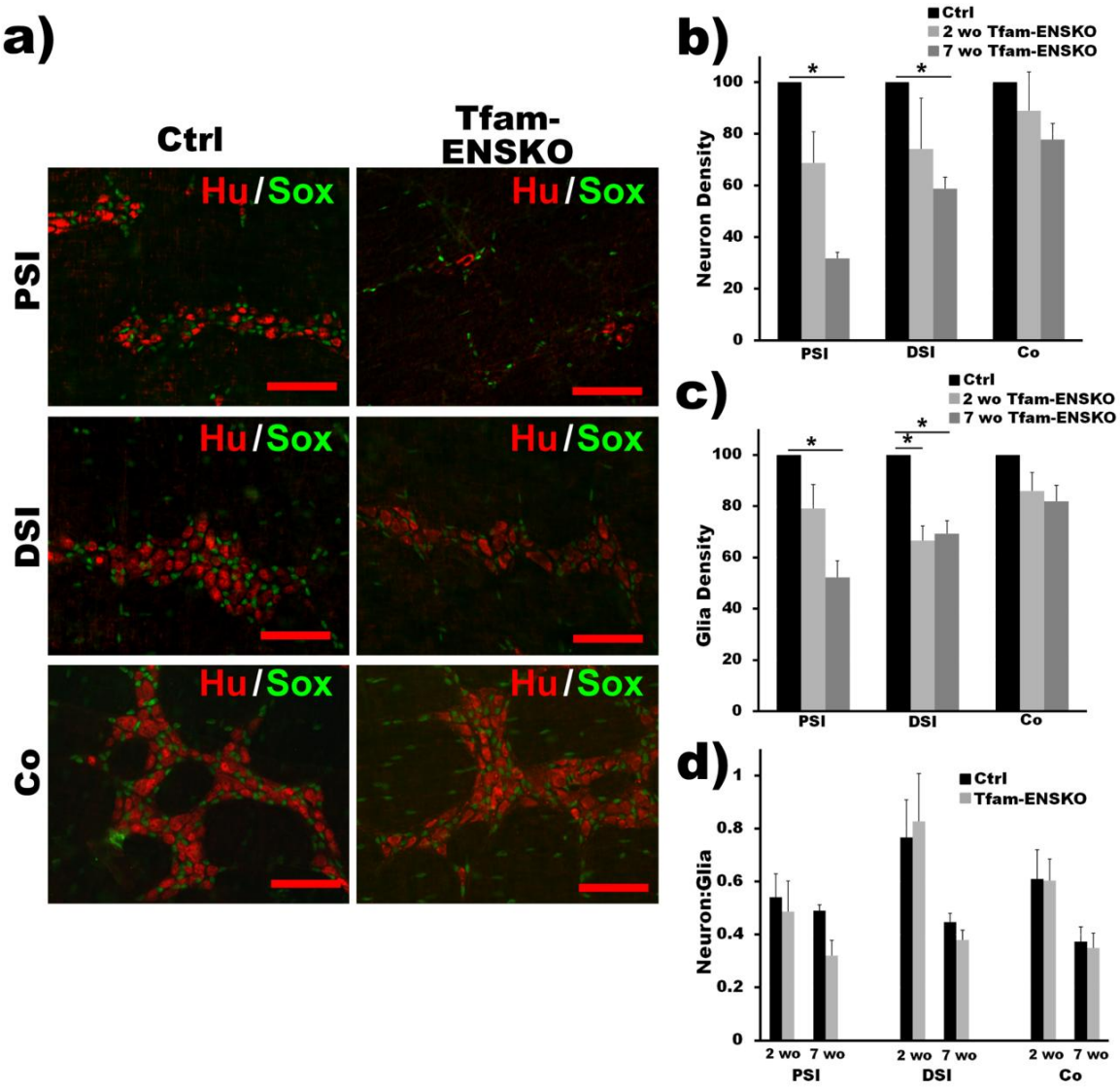
a)
Ctrl
Tfam-ENSKO
PSI
DSI
Co
Hu/Sox
b)
Ctrl
2 wo Tfam-ENSKO
7 wo Tfam-ENSKO
Neuron Density
PSI
DSI
Co
c)
Glia Density
d)
Tfam-ENSKO
Neuron:Glia
2 wo
7 wo

Figure 4. Early and differential loss of nitrergic inhibitory neurons in Tfam-ENSKO mice. ***a)*** Representative images of NADPH-d stained myenteric plexus show inhibitory neurons in the proximal SI and distal SI in 7 week old Tfam-ENSKO mice. Scale bar, 150 μm. ***b)*** Quantitative analysis of NADPH-d^+ neuron density in Tfam-ENSKOs relative to control littermates at 2 and 7 weeks of age. n=3 for each genotype at each age. ***c)*** Ratio of nitrergic neurons to total neurons in 7 week old Tfam-ENSKO and control mice. n=3 for each genotype. PSI: proximal small intestine, DSI: distal small intestine, Co: colon. ***d)*** Diagram depicting how the imbalance of inhibitory neurons to excitatory neurons in each region in Tfam-ENSKOs could produce the observed proximal SI dilation and distal SI constriction. In Tfam-ENSKO mice, greater total neuron loss (Tfam-ENSKO top panel) relative to NADPH-d^+ neuron loss (Tfam- ENSKO middle panel) would result in increased inhibitory input and dilation of the proximal SI (Tfam-ENSKO bottom panel). Greater NADPH-d^+ neuron loss (Tfam-ENSKO middle panel) relative to total neuron loss (Tfam-ENSKO top panel) would result in decreased inhibitory input and constriction (and pseudoobstruction) of the distal SI of Tfam-ENSKO mice (bottom panel). Color intensity represents neuronal density with WT density set as the most intense color in all regions of the bowel.

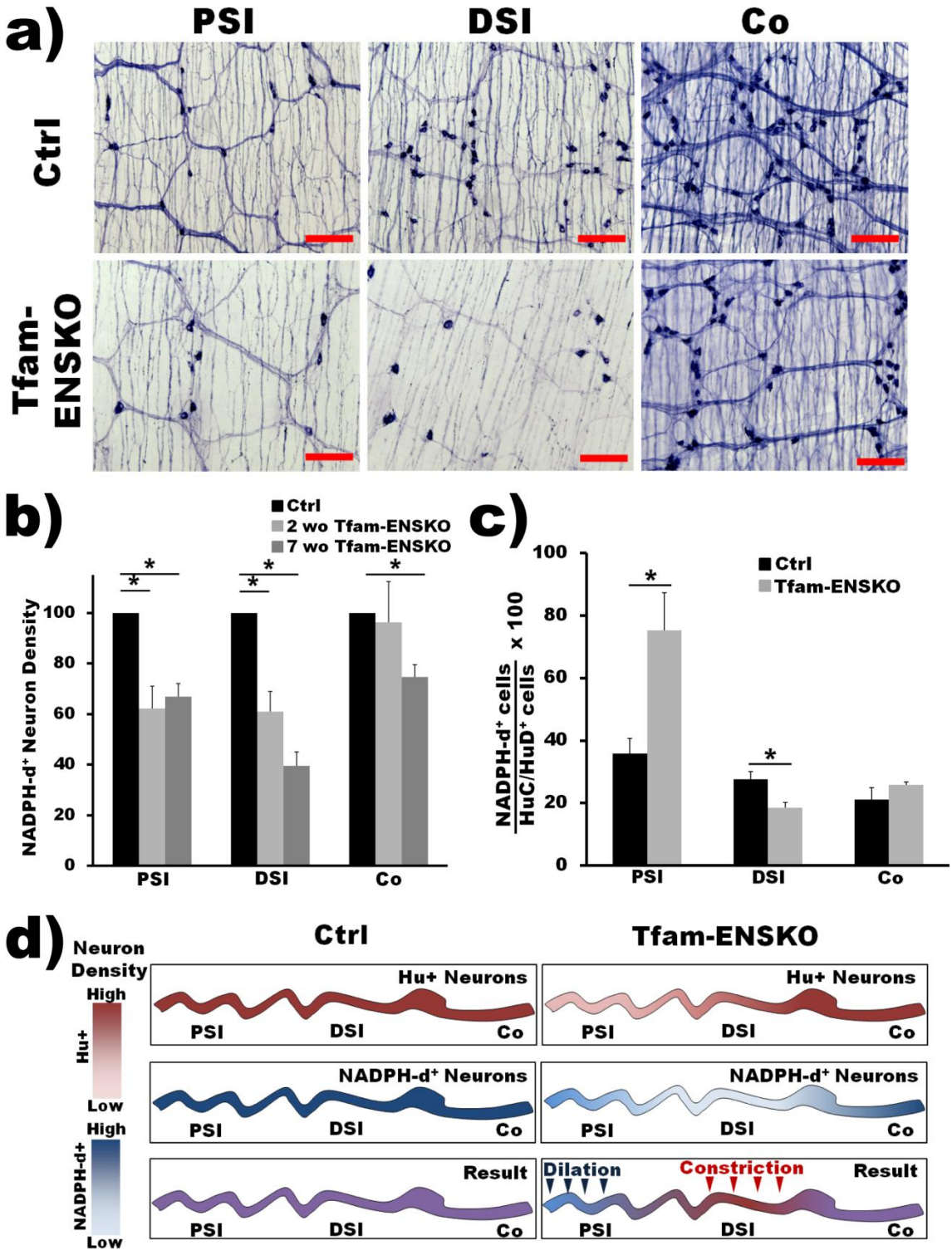
a)
PSI
DSI
Co
Ctrl
Tfam-ENSKO
b)
Ctrl
2 wo Tfam-ENSKO
7 wo Tfam-ENSKO
NADPH-d+ Neuron Density
100
80
60
40
20
0
PSI
DSI
Co
c)
Ctrl
Tfam-ENSKO
NADPH-d+ cells / HuC/HuD+ cells x 100
100
80
60
40
20
0
PSI
DSI
Co
d)
Neuron Density
High
Hu+
Low
High
NADPH-d+
Low
Ctrl
Tfam-ENSKO
Hu+ Neurons
NADPH-d+ Neurons
Result
Dilation
Constriction
PSI
DSI
Co

Figure 5. Axonal degeneration is present in Tfam-ENSKO mice and may precede enteric neuron loss. ***a)*** Tfam-ENSKO mice show noticeable neurite blebbing (arrowheads) in the proximal and distal SI at 7 weeks of age. Scale bars, 25 μm. ***b, c)*** Representative images (b) and quantification (c) of $TuJ1^+$ neurites extending into SI villi of 7 week old control and Tfam-ENSKO mice. n=3 for each genotype. Scale bars, 40 μm. ***d, e)*** Representative images (d) and quantification (e) of axonal fragmentation (TuJ1, green) and cell body loss (ethidium homodimer, staining not shown) in cultured enteric neurons after treatment with the mitochondrial inhibitors rotenone or antimycin. Images correspond to untreated or rotenone-treated enteric neurons. n= duplicate wells for each condition from 3 independent assays. Scale bars, 100 μm.

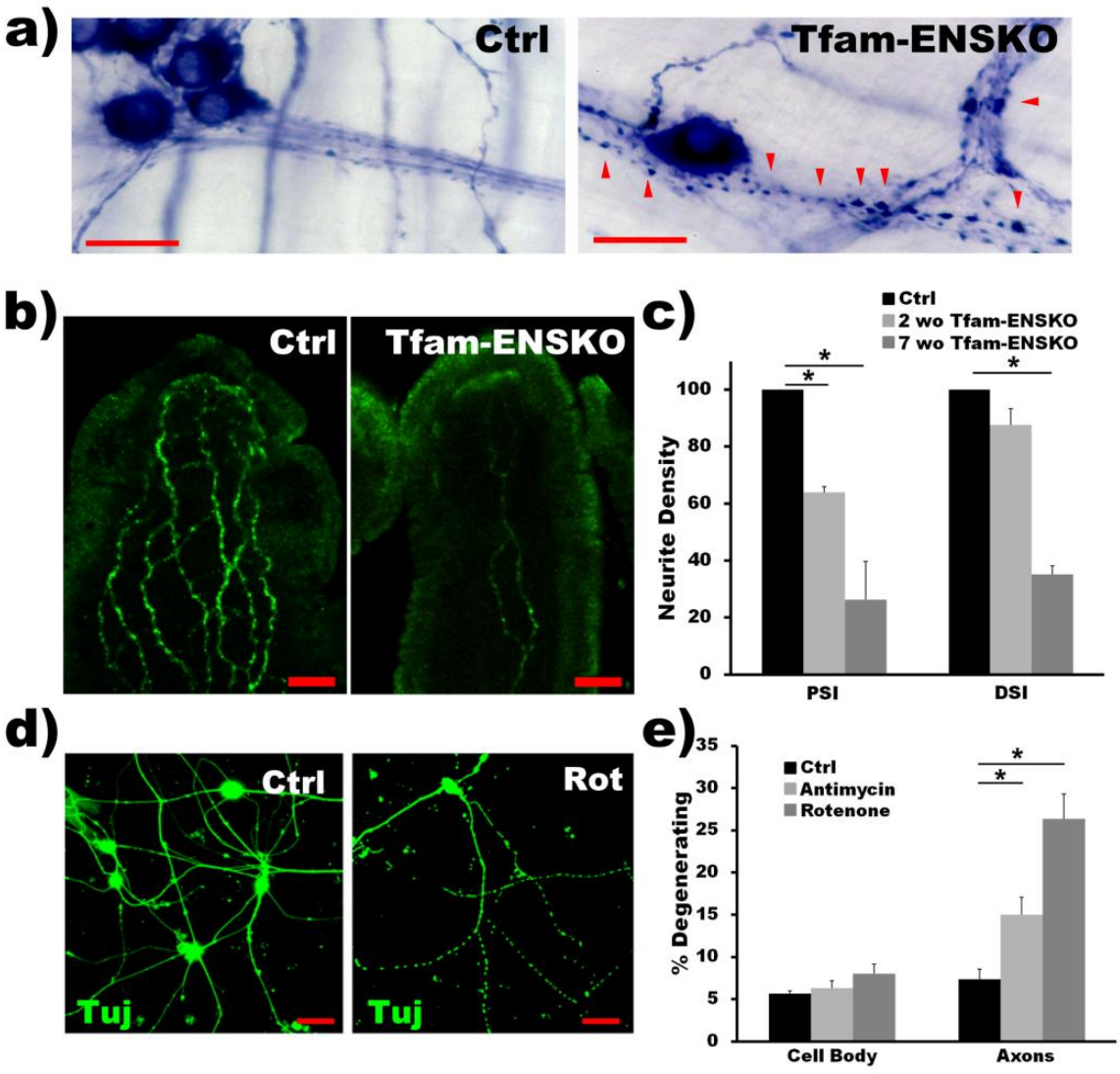
a)
Ctrl
Tfam-ENSKO
b)
Ctrl
Tfam-ENSKO
c)
Ctrl
2 wo Tfam-ENSKO
7 wo Tfam-ENSKO
Neurite Density
100
80
60
40
20
0
PSI
DSI
d)
Ctrl
Rot
Tuj
Tuj
e)
Ctrl
Antimycin
Rotenone
% Degenerating
35
30
25
20
15
10
5
0
Cell Body
Axons

Tables

Table 1. Myenteric Plexus Cell Density

Region	Age (weeks)	Total neuron density (Cells/mm^2)				Glial cell density (Cells/mm^2)				Neuron-to-Glia Ratio (Neurons/Glia)				NADPH-d+ Neuron Density (Cells/mm^2)				% of total neurons that are NADPH-d$^+$			
		Ctrl	*Tfam-ENSKO*	*% of Ctrl*	*p value*	*Ctrl*	*Tfam-ENSKO*	*% of Ctrl*	*p value*	*Ctrl*	*Tfam-ENSKO*	*% of Ctrl*	*p value*	*Ctrl*	*Tfam-ENSKO*	*% of Ctrl*	*p value*	*Ctrl*	*Tfam-ENSKO*	*% of Ctrl*	*p value*
PSI	2	1221 ± 156	839 ± 148		0.133	2316 ± 126	1831 ± 216		0.071	0.54 ± 0.09	0.49 ± 0.12		0.706	303 ± 24	188 ± 26	62%	0.030	25	22		
DSI	2	2355 ± 381	1747 ± 461		0.339	3142 ± 239	2094 ± 176	67%	0.012	0.77 ± 0.14	0.83 ± 0.18		0.794	574 ± 28	350 ± 46	61%	0.014	24	20		
Co	2	2113 ± 286	1879 ± 317		0.607	3633 ± 372	3117 ± 268		0.343	0.61 ± 0.11	0.60 ± 0.08		0.961	578 ± 73	557 ± 93		0.860	27	30		
PSI	7	235 ± 23	74 ± 5	31%	0.003	479 ± 31	250 ± 31	52%	0.007	0.49 ± 0.02	0.32 ± 0.06		0.054	82 ± 6	55 ± 4	67%	0.021	36 ± 5	75 ± 12	208%	0.038
D SI	7	329 ± 18	194 ± 14	59%	0.004	744 ± 55	515 ± 38	69%	0.027	0.45 ± 0.03	0.38 ± 0.04		0.400	91 ± 9	36 ± 5	40%	0.007	28 ± 2	19 ± 2	68%	0.035
Co	7	548 ± 85	426 ± 33		0.258	1409 ± 48	1153 ± 87		0.062	0.37 ± 0.06	0.35 ± 0.06		0.782	147 ± 8	110 ± 7	75%	0.027	21 ± 4	26 ± 1		0.288

Table 1. Myenteric Plexus Cell Density. Myenteric plexus neuron and glial cell density and ratios in 2 and 7-week-old Tfam-ENSKO and control mice. n= 3 for each genotype for all analyses of 7 week old mice. For 2 week old mice, n=6 (Ctrl) or 4 (Tfam-ENSKO) for total neuron density, glial density, and neuron to glia ratio and n=3 for NADPH-d$^+$ neuron density. N/A, not applicable; due to small size of tissue samples at 2 weeks of age, staining for both HuC/HuD$^+$ (total) and NADPH-d$^+$ (nitrergic) could not be performed on a single animal and therefore statistical analysis of the proportion of total neurons that are NADPH-d$^+$ was not possible. PSI: proximal small intestine, DSI: distal small intestine, Co: colon.

Table 2. Villus Neurite Density

Region	Age (weeks)	Neurites/villus			
		Ctrl	***Tfam-ENSKO***	***% of Ctrl***	***p value***
PSI	2	4.25 ± 0.18	2.72 ± 0.09	64%	0.002
DSI	2	3.63 ± 0.25	3.18 ± 0.2		0.235
PSI	7	10 ± 1.3	2.6 ± 0.23	26%	0.006
DSI	7	12 ± 1.6	4.1 ± 0.35	34%	0.011

Table 2. Villus Neurite Density. Density of neuronal projections in intestinal villi in 2 and 7 week old Tfam-ENSKO and control mice. n= 3 for each genotype and age. PSI: proximal small intestine, DSI: distal small intestine, Co: colon.

Table 3. Nitrergic Fiber Density

Region	Age (weeks)	NADPH-d^+ Bundles/mm^2				NADPH-d^+ Fibers/mm^2				NADPH-d^+ Fibers/neuron			
		Ctrl	***Tfam-ENSKO***	***% of Ctrl***	***p value***	***Ctrl***	***Tfam-ENSKO***	***% of Ctrl***	***p value***	***Ctrl***	***Tfam-ENSKO***	***% of Ctrl***	***p value***
PSI	7	19 ± 0.5	14 ± 2		0.073	312 ± 18	174 ± 32	56%	0.020	3.9 ± 0.6	3.1 ± 0.5		0.208
DSI	7	22 ± 3	19 ± 0.5		0.700	298 ± 25	233 ± 6		0.100	3.4 ± 1.4	6.8 ± 4.8		0.098
Co	7	25 ± 1	25 ± 1		0.844	583 ± 56	527 ± 5		0.378	4.0 ± 0.7	4.8 ± 0.2		0.099

Table 3. Nitrergic Fiber Density. Myenteric NADPH-d^+ fiber density and number of NADPH-d^+ fibers per neuron in 7 week old Tfam-ENSKO and control mice. n= 3 for each genotype. PSI: proximal small intestine, DSI: distal small intestine, Co: colon.

Table 4. *In vitro* Mitochondrial Inhibitor Assay Results

Time	Neurons with fragmented axons (%/well)			% of Control		*p* value		Et_2D^+ (dead) Neurons (%/well)			% of Control		*p* value	
	Veh	***Rot***	***Antim***	***Rot***	***Antim***	***Rot***	***Antim***	***Veh***	***Rot***	***Antim***	***Rot***	***Antim***	***Rot***	***Antim***
24 hrs	7.3 ± 1.2	26.3 ± 3	15 ± 3.6	360%	205%	0.004	0.03	5.7 ± 0.3	8 ± 1.15	6.3 ± 1.5			0.124	0.5
48 hrs	6.7 ± 1.2	51.7 ± 6.7	12 ± 1	772%	179%	0.003	0.01	6.7 ± 0.3	31 ± 3.6	12 ± 2.6	463%	179%	0.002	0.01
72 hrs	7.7 ± 1.2	83.7 ± 4.7	32 ± 6.8	1087%	416%	<0.001	0.003	7 ± 0.6	58.7 ± 5.2	19.3 ± 3.2	839%	276%	<0.001	0.003

Table 4. *In vitro* Mitochondrial Inhibitor Assay Results. *In vitro* mitochondrial inhibitor assay results from cultured E12.5 immunoselected enteric neurons. n= duplicate wells for each condition from 3 independent assays. Veh=Vehicle; Rot=Rotenone; Antim=Antimycin

CHAPTER 5

microRNAs modulate Schwann Cell response to nerve injury by reinforcing transcriptional silencing of dedifferentiation-related genes

Adapted from: Viader A, Chang LW, Fahrner T, Nagarajan R, Milbrandt J. (2011) miRNAs modulate Schwann Cell response to nerve injury by reinforcing transcriptional silencing of dedifferentiation-related genes. Schwann cell mitochondrial metabolism supports long-term axonal survival and peripheral nerve function. *Journal of Neuroscience.* 31(48):17358-69.

Abstract

In the peripheral nervous system, Schwann cells (SCs) surrounding damaged axons undergo an injury response that is driven by an intricate transcriptional program and is critical for nerve regeneration. To examine whether these injury-induced changes in SCs are also regulated post-transcriptionally by miRNAs, we performed miRNA expression profiling of mouse sciatic nerve distal segment after crush injury. We also characterized the SC injury response in mice containing SCs with disrupted miRNA processing due to loss of Dicer. We identified 87 miRNAs that were expressed in mouse adult peripheral nerve, 48 of which were dynamically regulated after nerve injury. Most of these injury-regulated SC miRNAs were computationally predicted to inhibit drivers of SC dedifferentiation/proliferation and thereby re-enforce the transcriptional program driving SC re-myelination. SCs deficient in miRNAs manifested a delay in the transition between the distinct differentiation states required to support peripheral nerve regeneration. Among the miRNAs expressed in adult mouse SCs, miR-34a and miR-140 were identified as functional regulators of SC dedifferentiation/proliferation and re-myelination, respectively. We found that miR-34a interacted with positive regulators of dedifferentiation and proliferation such as Notch1 and Ccnd1 to control cell cycle dynamics in SCs. miR-140 targeted the transcription factor Egr2, a master regulator of myelination, and modulated myelination in DRG/SC co-cultures. Together, these results demonstrate that SC miRNAs are important modulators of the SC regenerative response after nerve damage.

Introduction

Neuronal regeneration in adult vertebrates is largely limited to the peripheral nervous system (PNS). Unlike neurons in the central nervous system (CNS), PNS neurons are capable of long-distance axonal regeneration. Central to the differential plasticity of peripheral neurons are Schwann cells (SCs), the glial cells of the PNS. SCs have the striking ability to dedifferentiate and revert back to an immature-like state following axonal loss (Jessen and Mirsky, 2008). After a transient phase of proliferation, dedifferentiated SCs help support axonal regeneration by clearing myelin debris, forming tubular structures known as bands of Bungner, and upregulating the synthesis of a number of neurotrophic factors. As peripheral axons regenerate, SCs re-differentiate to form mature Remak bundles or new myelin sheaths, helping to restore, in this way, peripheral nerve function (Geuna et al., 2009). Greater insight into this highly orchestrated process of SC-mediated support of axonal regeneration could be harnessed to improve the treatment of peripheral and central neurodegenerative diseases characterized by axonopathy, including diabetic neuropathy and amyotrophic lateral sclerosis (Coleman, 2005).

Micro-RNAs (miRNAs) are small (around 22 nucleotides) non-coding RNAs capable of postrancriptionally regulating protein expression. miRNAs have emerged as ubiquitous regulators of developmental timing and cellular differentiation (Flynt and Lai, 2008). The central role of miRNAs in cell fate determination suggests that they could modulate the transcriptional program responsible for the dedifferentiation and redifferentiation of SCs following nerve injury (Jessen and Mirsky, 2008). This idea is supported by zebrafish studies implicating miRNAs in the regulation of tissue

regeneration (Thatcher et al., 2008; Yin et al., 2008; Ramachandran et al., 2010). Moreover, miRNAs are essential for the normal development of SCs, as miRNA-deficient SCs are unable to differentiate past an immature state (Bremer et al., 2010; Pereira et al., 2010; Yun et al., 2010). The behavior, identity, and potential role of miRNAs in the regenerative response of adult SCs after nerve injury, however, remain unexplored.

In this study we examined the dynamics of miRNA expression in mouse sciatic nerve following crush-induced axonal loss. We identified 87 miRNAs consistently expressed in adult peripheral nerve. Most of these SC miRNAs were computationally predicted to inhibit drivers of SC dedifferentiation/proliferation and their expression was dynamically regulated after injury to potentially re-enforce the transcriptional program driving the SC regenerative response. Accordingly, miRNA-deficient SCs had delayed transitions between the distinct differentiation states involved in the SC injury response. Among the miRNAs consistently expressed in SCs, miR-34a and miR-140 were characterized as functional regulators of two distinct processes carried out by SCs following peripheral nerve damage: proliferation and myelination. Together, our results demonstrate that miRNAs are important modulators of the SC regenerative response after nerve damage.

Results

Dynamics of SC miRNA expression after injury are consistent with a modulatory role in the SC regenerative response

To study the potential regulatory role of miRNAs in the SC regenerative response after peripheral nerve injury, we carried out miRNA microarray expression profiling of mouse sciatic nerves after crush-induced axonal degeneration. In previous work examining mRNA expression profiles during the SC injury response (Nagarajan et al., 2002; Araki et al., 2001; Bosse et al., 2006), we and others found that expression of regulators of SC dedifferentiation/proliferation and myelination peaks 4 (C4) and 14 (C14) days after nerve crush, respectively. In the present study we therefore profiled miRNA expression in the distal stump of injured nerves at C4 and C14, as miRNAs that are differentially expressed at these two time points are likely to be involved in the regulation of the SC regenerative response.

We identified 87 miRNAs that were reproducibly detected in the adult peripheral nerve (Fig. 1a). Given that SCs constitute greater than 80% of the cells in mouse sciatic nerves (King RH, 2005), the detected miRNAs primarily represent the microRNAome of these glia. Indeed, over one third of the miRNAs detected by our microarray analysis were previously found to be expressed in cultured isolated SCs (Verrier et al., 2009). Moreover, several of the most highly expressed miRNAs identified, including let-7f, miR-138, miR-145, and miR-16, have been previously related to the postnatal development of SCs (Bremer et al., 2010; Yun et al., 2010; Verrier et al., 2010). Remarkably, the expression of over half of the detected miRNAs was up- or down-regulated in the distal nerve segment following crush injury (48 of 87; C4 vs. Ctrl

$p<0.05$), suggesting that miRNAs may indeed play a role in modulating the processes of SC dedifferentiation and remyelination after injury.

Genes involved in the dedifferentiation/proliferation and remyelination of SCs following crush-induced axonal degeneration are dynamically regulated and have reciprocal patterns of expression (Nagarajan et al., 2002). We reasoned that miRNAs involved in the SC injury response would be dynamically regulated in a manner similar to genes known to be important for the regulation of this process. We applied k-means clustering to our previous SC mRNA expression profiling datasets (see Methods), and identified gene clusters containing known regulators of SC dedifferentiation/proliferation (proliferation profile) or differentiation/myelination (myelination profile) after injury (Fig. 2a) (Nagarajan et al., 2002). Of the 48 miRNAs differentially regulated following nerve crush injury, 31 of them were expressed in a pattern that was highly correlated with either the myelination or proliferation profile (with a Pearson's correlation coefficient>0.8). Interestingly, 21 of these miRNAs were regulated similarly to genes in the myelination cluster; their expression was inhibited immediately after injury and increased as remyelination ensued (Fig. 2a). The expression of a significant portion of SC miRNAs, therefore, is dynamically regulated after crush injury in a manner consistent with them playing a critical role in modulating the SC regenerative response.

Target bias analysis suggests that SC miRNAs modulate the injury response by repressing positive regulators of SC dedifferentiation/proliferation

miRNAs often act in concert with transcriptional control to regulate target gene expression more efficiently (Hornstein and Shomron, 2006). For this reason, biologically

relevant miRNAs tend to be either co-expressed (positive target bias) or negatively correlated (negative target bias) with their predicted targets to either fine-tune or inhibit their activity, respectively (Tsang et al., 2007). We hypothesized that miRNAs could modulate the SC injury response in a similar manner by cooperating with the transcriptional regulatory program that controls this process. A miRNA whose expression profile is correlated with that of myelination-associated genes (Fig. 2a) could thus reinforce the transcriptional program driving remyelination by inhibiting positive regulators of SC dedifferentiation/proliferation (demonstrating a negative target bias) or by modulating myelination-associated genes (demonstrating a positive target bias). Conversely, a miRNA whose expression is correlated with that of proliferation/dedifferentiation-associated genes could coordinate with the transcriptional regulatory program by inhibiting drivers of myelination (negative target bias) or by fine-tuning proliferation-related genes (positive target bias). To begin to address the biological function of SC miRNAs in modulating the injury response we therefore studied their target bias as well as examined their correlation with the proliferation and myelination expression profiles.

We first used the TargetScanS algorithm (Grimson et al., 2007) to identify SC expressed genes that were predicted targets of the 87 miRNAs we detected in SCs. We found that 59 of the 87 miRNAs detected by our microarray analysis had predicted targets among the ~8000 transcripts detected in our previous SC mRNA expression profiling datasets (Nagarajan et al., 2002 and unpublished data). TargetScanS is a relatively stringent miRNA target prediction algorithm, which requires an exact match between the miRNA seed sequence and any predicted sites. The 59 miRNAs we

identified (subset 1) therefore represent a high-confidence set of modulators of the SC injury response and were further examined in our functional analysis.

We then used a Mann-Whitney U-test to determine if the expression of each miRNA in subset 1 had a higher positive or negative correlation with the expression of its predicted targets than with that of predicted non-target genes (indicative of a target bias, see Methods). We found that 25 miRNAs in subset 1 had a significant target bias. Remarkably, 23 out of these 25 miRNAs had a negative target bias, meaning that when the expression of a given miRNA was high the mRNA level of its putative targets tended to be low and vice versa. This prevalence of a negative target bias is in agreement with previous studies (Farh et al., 2005; Lau et al., 2008), and suggests that the majority of SC miRNAs reinforce rather than fine-tune the concurrent transcriptional regulatory processes (Tsang et al., 2007).

Finally, the extent of target bias for each miRNA in subset 1 (measured by a Mann-Whitney z-score, See Methods) was plotted against the correlation of its expression with the myelination or proliferation profile (measured by ΔCC, the difference in correlation coefficients with the proliferation profile and the myelination profile). Interestingly, when plotted in this manner, the majority of SC miRNAs clustered in the top left quadrant of the graph, indicative of a negative target bias and an expression pattern that correlated with that of genes in the myelination cluster (Fig. 2b). Only six miRNAs had a negative target bias and a high correlation with the expression pattern of genes in the proliferation cluster. Similarly, very few miRNAs showed a positive target bias (Fig 2b). Importantly, these results suggest that SC miRNAs are likely to modulate

the injury response primarily through their inhibition of positive regulators of SC dedifferentiation/proliferation.

To further validate this conclusion we carried out gene ontology enrichment analysis for the putative targets of miRNAs that were: 1) differentially regulated after injury (C4 vs. Ctrl $p<0.05$); 2) demonstrated a statistically significant target bias; and, 3) had a high correlation with the myelination or proliferation clusters ($\Delta CC>1.6$). We reasoned that miRNAs that met these three criteria were more likely to be direct regulators of the SC injury response. Using these rigorous criteria, six miRNAs were identified. Interestingly, these miRNAs all had a negative target bias and an expression pattern that correlated with the myelination profile (Fig. 2c). Gene ontology enrichment analysis showed that the predicted targets of these miRNAs were enriched for genes involved in cellular processes that are normally more active in immature or proliferating SCs. These processes included cell cycle regulation, cell migration, and regulation of transcription or chromatin organization (Fig. 2d), and genes such as SC mitogens (e.g. fibroblast growth factor), oncogenes (e.g. Kras) or cyclins (e.g. cyclin E2). These results indicate that SC miRNAs regulate the injury response primarily by inhibiting positive regulators of SC dedifferentiation/proliferation, and reinforce the transcriptional program that keeps these dedifferentiation/proliferation genes quiescent in mature or differentiating SCs. This reinforcement likely facilitates rapid and robust transitions between the distinct differentiation states involved in the SC injury response (Farh et al., 2005; Stark et al., 2005).

SCs with disrupted miRNA processing show delays in cycling between differentiation states after peripheral nerve injury

The results described above suggest that miRNAs work in concert with transcriptional controls in order to ensure the correct extent and timing of the SC dedifferentiation and subsequent remyelination following nerve injury. To more directly examine this idea, we carried out nerve lesion studies on mice in which mature miRNA synthesis was disrupted in SCs through the targeted deletion of *Dicer1*¸ a gene encoding an essential enzyme in miRNA biosynthesis (Bartel and Chen, 2004). Mice harboring *loxP*-flanked *Dicer1* alleles (Cobb et al., 2005) were crossed to mice expressing a tamoxifen-inducible form of Cre-recombinase in both myelinating and non-myelinating SCs under the control of the proteolipid protein promoter (PLP-CreER$_T$) (Doerflinger et al., 2003). The resulting PLP-CreER$_T$:Dicer fl/fl mice were aged to 1 month and then injected daily with either 100 □g/g of tamoxifen (Dicer-SCKOs) or vehicle (Ctrl) for 10 consecutive days (see Methods). Eight weeks after exposure to tamoxifen, a majority of SC nuclei (82% +/- 5.1%, identified morphologically) in PLP-CreER$_T$ mice carrying a copy of a Cre-inducible Rosa26-YFP reporter exhibited YFP fluorescence (Fig. 3a). Accordingly, Dicer mRNA levels as well as the basal levels of a number of highly expressed miRNAs were significantly reduced in the sciatic nerves of Dicer-SCKO vs. Ctrl mice (Fig. 3b and data not shown). However, at 8 weeks and for as long as 14 weeks after tamoxifen treatment, nerves from Dicer-SCKO mice showed no apparent pathology and were indistinguishable from Ctrl nerves, indicating that disruption of miRNA processing in SCs after peripheral nerve myelination was fully completed was well tolerated (Fig. 3g and h and data not shown).

To determine whether miRNA deficiency led to deficits in the SC injury response and re-myelination, sciatic nerves of Dicer-SCKO and Ctrl littermates were crushed 8 weeks after tamoxifen administration. We first examined the response of SCs to axonal degeneration by assessing changes in SC proliferation and in their ability to break down existing myelin (Geuna et al., 2009). The rate of myelin loss, a measure of SC dedifferentiation, was similar between Dicer-SCKO and Ctrl mice, with no differences observed in the amount of myelin debris (Fig. 3c) or of myelin basic protein (MBP) immunofluorescence in the nerves after injury (data not shown). Similarly, immunostaining of the nerve distal stump 4 days after injury using an antibody against the proliferation marker phospho-histone 3 (PH3) showed that, following axonal loss, miRNA-deficient SCs were able to re-enter the cell cycle to the same extent as Ctrl SCs (% of PH3 positive cells Ctrl= 12.37 +/- 0.47; Dicer-SCKO= 13.12 +/- 0.69; Fig. 3d and e). Depletion of miRNAs, therefore, did not interfere with the ability of SCs to dedifferentiate and proliferate after injury.

We next studied the late phase of the SC-injury response, during which these glia exit the cell cycle and redifferentiate to restore peripheral nerve function. PH3 immunostaining was initially used to assess the proportion of proliferating SCs 14 days after crush, a time when SCs have normally exited cell cycle and are actively differentiating. Interestingly, PH3 immunoreactivity showed that while the number of proliferating SCs in Ctrl nerves had returned to pre-injury levels, significantly more SCs in Dicer-SCKO nerves were still actively proliferating at this time (% of PH3 positive cells Ctrl= 0.93 +/- 0.08; Dicer-SCKO= 4.47 +/- 0.32; $p<0.001$; Fig. 3d and e). Consistent with the reduced ability of miRNA-deficient SCs to exit cell cycle in a timely

manner, nerves from Dicer-SCKO mice showed reduced remyelination compared to nerves from Ctrl mice, as indicated by a decrease in the total number of myelinated axons 14 days after injury (Fig. 3g and h). Note that this difference in remyelination after injury in Dicer-SCKO mice was not due to changes in the overall number of SCs (SC number/50K μm^2: Ctrl=183.4 +/- 33.7; Dicer-SCKO=203.5 +/- 18.9; p=0.6). An examination of electron micrographs of injured sciatic nerves from Ctrl and Dicer-SCKO mice revealed equivalent total numbers of regenerated axons (remyelinated and non-remyelinated, axons/10K μm^2: Ctrl=525 +/- 46.2; Dicer-SCKO=576.9 +/- 2.5; p=0.3) (Fig. 3f). Interestingly, 28 days after nerve injury the total number of myelinated axons in nerves from Dicer-SCKO and Ctrl mice were similar (Fig. 3g and h), but the axons in Dicer-SCKO nerves remained more thinly myelinated (G-ratio (axon area/fiber area) Ctrl= 0.41 +/- 0.016; Dicer-SCKO= 0.46 +/- 0.012; p=0.05; Fig. 3h). Together these results support that SC miRNAs modulate the injury response by cooperating with transcriptional controls to ensure the correct extent and timing of SC dedifferentiation, cell cycle re-entry/exit, and subsequent differentiation and re-myelination after nerve injury.

miR-34a is a potential regulator of SC dedifferentiation and proliferation after peripheral nerve injury

Cellular differentiation is tightly linked to exit from the cell cycle. Therefore, the influence of miRNAs on cell fate decisions is often linked to their ability to modulate cell cycle regulators (Ivey and Srivastava, 2010). Given that SCs need to dedifferentiate and temporarily re-enter the cell cycle in order to support axonal regrowth after injury (Geuna

et al., 2009), we hypothesized that the regulation of SC cell cycle entry/exit by miRNAs could underlie their influence on the injury response. Among the miRNAs identified as most likely play a role in the SC injury response (Fig. 2c), we identified miR-34a as a particularly good candidate to regulate the competency of SCs to proliferate or differentiate. miR-34a is a tumor suppressor gene whose ectopic expression can induce cell cycle arrest (Hermeking, 2010). Moreover, Notch1 and cyclin D1 (Ccnd1), two important mediators of SC dedifferentiation, proliferation, and cell cycle entry/exit, after peripheral nerve injury (Woodhoo et al., 2009; Kim et al., 2001) are targets of miR-34a in cancer cells (Pang et al., 2010; Sun et al, 2008). In addition, we identified a negative target bias for miR-34a in SCs for genes in the proliferation cluster (Fig. 2c), suggesting that miR-34a is a modulator of cell cycle regulators in SCs.

To verify a potential role of miR-34a in the regulation of cell cycle entry in SCs we first examined the expression of this miRNA in more detail. Quantitative RT-PCR confirmed that miR-34a is highly expressed in adult peripheral nerves (Ctrl) but that its expression level drops sharply after nerve crush (C4) or transection (Trx14) when SCs dedifferentiate and re-enter the cell cycle. miR-34a expression, however, is restored to pre-injury levels as SCs exit the cell cycle and redifferentiation ensues (C7, C14) (Fig. 4a). The expression pattern of miR-34a before and after injury is consistent with a role in the modulation of cell cycle regulators in SCs.

We next assessed the effect of the differential expression of miR-34a after nerve injury on Notch1 and Ccnd1, two putative targets relevant to SC dedifferentiation/proliferation and the injury response (Woodhoo et al., 2009; Kim et al., 2001; Atanasoski et al., 2001). We overexpressed miR-34a in HEK293T cells together

with a luciferase construct containing the 3'-UTR of either Notch1 or Ccnd1 and confirmed that, as previously reported (Pang et al., 2010; Sun et al., 2008), miR-34a directly recognized and interacted with the transcripts of these two genes (Figure 4b). Consistent with direct targeting of Notch1 and Ccnd1 by miR-34a, the expression pattern of these two genes was reciprocally correlated with that of miR-34a following axonal degeneration (i.e., miR-34a expression decreased after injury as Notch1 and Ccnd1 expression increased). The converse expression pattern was observed as SC redifferentiation took place (Fig. 4c). Furthermore, when miR-34a was overexpressed in isolated SCs, Ccnd1 and Notch1 were downregulated at both the transcript and protein levels (Fig 4d and e). In SCs, therefore, miR-34a directly targets at least two positive regulators of SC dedifferentiation and proliferation (Notch1 and Ccnd1). In addition to Notch1 and Cnd1, other potentially relevant targets to SC dedifferentiation and remyelination (e.g. YY1) could also mediate some of the effects of miR-34a on the injury response (Chen et al., 2011; He et al., 2010)

Finally, to directly determine whether miR-34a regulates cell cycle entry and exit in SCs we assessed the effect of overexpressing this miRNA on the axon-induced proliferation of SCs *in vitro*. When isolated SCs are cultured in the presence of dorsal root ganglion (DRG) neurons, contact with axons initially induces SCs to enter the cell cycle and proliferate. We found that ectopic expression of miR-34a did not affect SC health and viability, but severely inhibited DRG axon-induced proliferation of SCs *in vitro* (Fig. 4f). Together our results indicate that mir-34 can directly interact with positive regulators of dedifferentiation and proliferation in SCs to control cell cycle dynamics in these peripheral glial cells, thus providing a mechanism by which miRNAs

could modulate proper cycling of SCs between the distinct differentiation states that support nerve regeneration after injury.

miR-140 targets Egr2, a master regulator of myelination, to help modulate SC redifferentiation after nerve injury

The differentiation status of SCs after injury is determined by the balance between signaling systems that drive SC maturation/myelination vs. those that induce SC dedifferentiation/proliferation (Jessen and Mirsky, 2008). While we initially found that most SC miRNAs interact with targets involved in SC dedifferentiation/proliferation (see above), we also searched for miRNAs that targeted positive regulators of myelination. To this end, we focused on identifying miRNAs that interact with Egr2, a transcription factor that is required for the formation and maintenance of myelin and that is often mutated in patients with peripheral myelinopathies (Svaren and Meijer, 2008).

In silico analysis using PicTar (Krek et al., 2005), TargetScanS (Grimson et al., 2007) and miRanda (John et al., 2004) algorithms identified a putative binding site for miR-140 in the 3'-UTR of Egr2 (Fig. 5a). This binding site has an exact match to the 2-8bp seed sequence of mouse miR-140 (AGUGGUU), which is highly conserved in human, rat, dog and horse, and thus this miRNA was selected for further testing. Although our microarray analysis detected expression of miR-140* (which originates from the opposite arm of the pre-miRNA for mir-140) rather than miR-140 in nerve samples (Fig. 1), qRT-PCR confirmed that miR-140 is also expressed in adult peripheral nerve. Moreover, we found that miR-140 expression was dynamically regulated after peripheral nerve injury, i.e. its expression level was significantly decreased immediately

after nerve crush (C4) and remained low until at least C7 (Fig. 5b). miR-140 expression was restored to pre-injury levels once SC redifferentiation ensued (C14) (Fig. 5b). Interestingly, the identified expression pattern of miR-140 after peripheral nerve injury is positively correlated with that of its putative target Egr2 (Fig. 5c), suggesting that miR-140 influences the injury response by fine-tuning the steady-state level of Egr2 in SCs that are actively forming or maintaining myelin (Tsang et al., 2007).

The dynamic regulation of miR-140 during active myelin remodeling prompted us to further examine this miRNA in SCs. To confirm that Egr2 is a target of miR-140, we first co-transfected HEK293T cells with plasmids encoding either pre-mir-140 or a control pre-miRNA together with a luciferase reporter construct carrying the 3'UTR of *Egr2*. Co-expression of this reporter plasmid with miR-140 decreased luciferase activity in these cells, indicating that miR-140 can directly recognize and interact with the *Egr2* 3'UTR (Fig. 5d). This interaction was dependent on the computationally predicted miR-140 binding site in this region, as a 3'UTR fragment containing a mutant site was no longer responsive to co-expression of pre-mir-140 (Fig. 5d). Consistent with results from these luciferase reporter assays, Egr2 protein levels were reduced 2.8-fold in cultured SCs overexpressing miR-140 (Fig. 5e). These results identify Egr2 as a new target of miR-140 and indicate that this miRNA directly interacts with Egr2 via a highly conserved site in its 3'UTR to regulate the expression of this transcription factor in SCs.

Finally, we examined whether miR-140 affected the ability of SCs to differentiate and myelinate *in vitro.* In the absence of neurons, prolonged exposure to cAMP-stimulating agents can promote SC growth arrest and differentiation and induce expression of genes typically associated with myelinating SCs (e.g. Mpz and Pmp22)

(Jessen et al., 1991; Monje et al., 2009). Using this system, we evaluated the effect of miR-140 overexpression on SC differentiation. Consistent with the down-regulation of Egr2 protein by mir-140 in SCs (Fig. 5e), cAMP-induced, Egr2-mediated upregulation of myelin markers in cultured SCs was inhibited in the presence of this miRNA (cAMP-induced gene expression fold induction, *MPZ:* Ctrl miR= 4.7 +/- 0.51; miR-140= 2.09 +/- 0.35; $p<0.05$; *PMP22*: Ctrl miR= 1.5 +/- 0.06; miR-140= 0.9 +/- 0.06; $p<0.05$)

When SCs are cultured together with dorsal root ganglion neurons (DRGs) in the presence of ascorbic acid, DRG axons will support the differentiation of SCs and the formation of myelin (Wood et al., 1990). Myelination can be monitored in this system by using myelin basic protein (MBP) immunostaining as a marker. We found that overexpression of miR-140 in SCs co-cultured with DRGs inhibited the expression of Egr2 as well as a number of myelination markers (Fig. 5f). Most importantly, miR-140 overexpression inhibited myelination in this *in vitro* assay as evidenced by the decreased number of myelin segments detected by MBP immunostaining (Fig. 5g). Together, our results indicate that miR-140 can directly interact with Egr2 and modulate the level of this transcription factor to regulate myelination. This suggests another mechanism by which miRNAs may modulate the injury-induced regenerative process of SCs in peripheral nerves.

Discussion

Following axonal loss, SCs mount a regenerative response involving coordinated dedifferentiation, proliferation and redifferentiation that helps restore peripheral nerve function. Extensive work has established that this SC injury response is driven by an

intricate transcriptional program controlling the balance between positive and negative regulators of SC differentiation (Jessen and Mirsky, 2008). The present study describes a new regulatory layer of the SC injury response involving post-transcriptional regulation by miRNAs. We show that SC miRNAs modulate the injury response by targeting primarily positive regulators of SC dedifferentiation/proliferation, cooperating with transcriptional controls to ensure rapid and robust transitions between the distinct differentiation states that support nerve regeneration. Moreover, we also identify miR-34a and miR-140 as important functional regulators of SC proliferation and myelination, two central processes of the SC regenerative response after injury. miRNAs therefore appear to be important modulators of the SC regenerative response after peripheral nerve injury.

miRNAs are thought to have evolved to canalize the genetic network and confer robustness to gene expression programs (Hornstein and Shomron, 2006). miRNAs achieve this by integrating into the pre-existing genetic network in two ways. On the one hand, miRNAs can wire into coherent feed-forward loops (FFLs) such that high expression of a given miRNA is induced at a time or location when the transcription of its predicted targets is repressed (negative target bias) (Hornstein and Shomron, 2006; Tsang et al., 2007). This type of network motif functions as a post-transcriptional failsafe and results in mutually exclusive expression domains for the miRNA and its putative targets (Stark et al., 2005; Mansfield et al., 2004). On the other hand, miRNAs can wire into incoherent FFLs, which would promote high expression of a given miRNA at a time or location where its predicted targets are also abundant (positive target bias) (Hornstein and Shomron, 2006; Tsang et al., 2007). Biological examples of incoherent FFLs (Karres et al., 2007) have shown that in this type of network motif miRNAs have a fine-tuning

action and keep protein levels in the correct functional range. Our work demonstrates that SC miRNAs show a prevalence of negative target biases during the SC injury response. This indicates that SC miRNAs primarily participate in coherent FFLs. Moreover, the expression of most SC miRNAs after injury was negatively correlated with that of positive regulator of SC dedifferentiation/proliferation. Interestingly, we also found that predicted targets of SC miRNAs are enriched for genes active in immature or proliferating SCs that are quiescent in adult, differentiated SCs. Together these observations indicate that SC miRNAs regulate the injury response primarily by inhibiting positive regulators of SC dedifferentiation/proliferation and thereby reinforcing a preexisting transcriptional silencing mechanism that keeps dedifferentiation/proliferation-related genes quiescent in differentiated SCs yet allows their induction following axonal degeneration.

The above results imply that the majority of miRNAs expressed in mature SCs are involved in maintaining the differentiated state. In accordance, we found that immediately after injury most SC miRNAs are down-regulated, which allows for the transcriptionally driven dedifferentiation of SCs. We also observed that, similar to what has been reported for SC postnatal development (Bremer et al., 2010; Pereira et al., 2010; Yun et al., 2010), the expression of most SC miRNAs is up-regulated once again shortly after axonal regrowth. Because most SC miRNAs target positive regulators of SC dedifferentiation/proliferation that must be repressed for proper SC differentiation to occur (Le et al., 2005), this serves to facilitate redifferentiation and stabilization of the mature SC phenotype. This observation is consistent with studies showing that miRNAs are generally expressed at lower levels in immature or dedifferentiated tissues than in

differentiated ones (Wienholds et al., 2005; Lu et al., 2005), and with the idea that miRNAs are largely involved in promoting, inducing, and stabilizing differentiated phenotypes (Wienholds and Plasterk, 2005). It is possible that manipulation of SC miRNAs could be used therapeutically to facilitate SC differentiation after injury or reverse the effects of neuropathy.

The therapeutic modulation of SC miRNAs, however, requires the identification of specific miRNAs playing critical roles in the establishment and maintenance of SC differentiation as well as in the modulation of the SC injury response. We identify miR-34a as one such candidate. We found that miR-34 was able to critically regulate SC cell cycle exit by directly interacting with Ccnd1 transcripts and impinging on Notch signaling, a central modulator of SC dedifferentiation after injury (Woodhoo et al., 2009). Other miRNAs are likely to play similar roles; for example, let-7 family members enhance differentiation and inhibit stem-cell self-renewance (Melton et al., 2010). Moreover, this family of miRNAs participates in regenerative processes in zebrafish (Ramachandran et al., 2010). Intriguingly, our microarray analysis found that several members of the let-7 family were differentially regulated in SCs after peripheral nerve injury.

While our work shows that most SC miRNAs interact with targets involved in SC dedifferentiation/proliferation, we also identified miR-140 as a potential regulator of Egr-2. Egr2 is an essential transcription factor for myelinogenesis and is often mutated in patients with peripheral myelinopathy (Svaren and Meijer, 2008). Accordingly, we found that overexpression of miR-140 in SCs impaired their ability to form myelin *in vitro.* Interestingly, the expression pattern of miR-140 and *Egr2* indicates the presence of an

incoherent FFL (Hornstein and Shomron, 2006; Tsang et al., 2007) in which both transcript and miRNA are co-expressed at the same time in SCs. This suggests that miR-140 may act to maintain Egr2 expression within precise functional levels. This is particularly interesting because myelin formation and maintenance is very sensitive to gene dosage effects. In fact, both abnormally low or high levels of specific myelin proteins can cause peripheral neuropathy in humans (Meyer zu Horste et al., 2006). Regulation of expression thresholds could therefore be a second mechanism, together with reinforcement of transcriptional silencing, by which SC miRNAs modulate the injury response of these glia and promote regeneration of peripheral nerves.

In summary, through miRNA expression profiling after nerve damage and examination of the effects of impaired miRNA processing on the SC injury response, the present study establishes a critical role for miRNAs in the modulation of the SC regenerative response in peripheral nerves. We demonstrate that SC miRNAs ensure rapid and robust transitions between the distinct differentiation states necessary to support nerve regeneration by reinforcing the transcriptional silencing of dedifferentiation and proliferation-related genes. Modulation of SC miRNAs could offer therefore a new therapeutic avenue to enhance nerve regeneration and improve the treatment of neurodegenerative diseases characterized by axonopathy

Materials and Methods

Animals and matings: All animal experiments were carried out in compliance with institutional animal protocols. For all nerve lesion studies, except those involving mice lacking *Dicer* specifically in SCs (Dicer-SCKOs), C57Bl6 mice of either gender were

used. Dicer-SCKO mice were generated by crossing *Dicer* $^{loxP/loxP}$ mice (Cobb et al., 2005) to *PLP-CreER*$_T^{+/-}$ mice (Doerflinger et al., 2003). Compound heterozytoges (*PLP-CreER*$_T^{+/-}$, *Dicer*$^{+/loxP}$) were then backcrossed to homozygous *Dicer* $^{loxP/loxP}$ to generate *PLP-CreER*$_T^{+/-}$, *Dicer*$^{loxP/loxP}$ mice. One-month-old *PLP-CreER*$_T^{+/-}$, *Dicer*$^{loxP/loxP}$ mice of either gender were injected daily with 100 μg/g of tamoxifen (10 mg/ml stock dissolved in a 10:1 peanut oil/ethanol mixture) for a total of 10 days (with a 2 day break after day 5) to generate Dicer-SCKOs. Ctrl mice were injected in the same way with vehicle alone (10:1 peanut oil/ethanol mixture). *PLP-CreER*$_T^{+/-}$ were also crossed to *Rosa26-YFP*$^{+/-}$ mice to generate *PLP-CreER*$_T^{+/-}$, *Rosa26-YFP*$^{+/-}$ mice, which were treated with tamoxifen in an analogous manner.

Surgical procedures: For lesion studies, adult mice (2-3 months of age) were anaesthetized by intraperitoneal injection of avertin. The sciatic nerve was exposed at the hip and either crushed using #5 jeweler's forceps for 30 sec or transected using small scissors. In the case of transection, the distal stump was deflected onto an adjacent muscle to prevent regeneration. When necessary, the site of injury was marked with a single 10-0 nylon epineural suture. Nerve lesions were produced on the right side and the intact contralateral nerve served as the uninjured control. At the appropriate time points nerves were harvested and processed for histology or immediately frozen in liquid nitrogen for subsequent extraction of RNA.

RNA preparation, and quantitative real-time PCR: Total RNA was isolated after homogenization (for sciatic nerves) or lysis (for cultured SCs) in Qiazol lysis reagent (Qiagen) using a miRNeasy Minikit (Qiagen) according to the manufacturer's protocol.

RNA concentration was quantified using an ND-1000 spectrophotometer (Nanodrop Technologies). mRNA was reverse transcribed from 100 ng of total RNA using qScript cDNA SuperMix (Quanta Biosciences) while miRNA was reverse transcribed from 100 ng of total RNA using NCode Vilo miRNA cDNA Synthesis kit (Invitrogen). mRNA qRT-PCR was performed using a SYBR green-based detection system on a 7900 HT Sequence Detector instrument (Applied Biosystems) as described previously (Nagarajan et al., 2001). GAPDH expression was used to normalize samples and obtain relative expression values that were used to calculate percent changes. miRNA qRT-PCR was carried out in an analogous manner but cycling conditions were adapted as per NCode Vilo miRNA qRT-PCR kit (Invitrogen) recommendations. U6 snRNA was used for normalization. The sequences of the qRT-PCR primers used are as follows (5'-3'): Dicer: F, AATTGGCTTCCTCCTGGTTAT; R, GTCAGGTCCTCCTCCTCCTC. mir-34a: F, GGCAGTGTCTTAGCTGG TTGT. mir-26a: F, GATTTCAAGTAATCCAGGATAGGCT. mir-140: CAGTGGTTTTACCC TATGGTAG. All miRs R, NCode Vilo Universal Primer. Egr-2: F, CATGGGCAAATTCTCCATTGA; R, TTGCAAGATGCCCGCAC. MPZ: F, CCCTGGCCATTGTGGTTTAC; R, CCATTCACTGGACCAGAAGGAG. MBP: F, CCAGTAGTCCATTTCTTCAAGAACATT; R, AGCTAAATCTGCTGAGGGACAGG. Ccnd1: F, GCGTACCCTGACACCAATCT; R, GAACCGGTCCAGGTAGTT CA; Notch1: F, TGACCTGCTCACTCTCACAGA GTAC; R, CGACAGATGTATGAAGACT CAAAGG.

Microarray and computational analysis: SC microarray gene expression profiling experiments were performed in previous studies using Affymetrix MU74v2 chips (Nagarajan et al., 2002). Expression data were processed and normalized using Affymetrix MAS5 algorithm. A SC expressed gene was defined as one that was called present in at least one time point during SC regeneration. k-means clustering was used to cluster genes based on their expression profiles, and gene clusters that had an expression pattern similar to the previously identified myelination or proliferation profile (Nagarajan et al., 2002) based on the Pearson correlation coefficient were identified and merged. The average expression profile, i.e. the centroid, was calculated as the final myelination or proliferation profile.

For miRNA expression profiling, total RNA samples were prepared by isolating and pooling RNA from at least 3 different mice at the appropriate times after nerve crush. Replicates were prepared entirely independently from two separate pools of at least three animals each. 2 replicates were used for hybridization onto HTG Molecular qNPA miRNA microarrays (HTG Molecular) according to the manufacturer's protocol, and microarray images were obtained and background substracted as per HTG Molecular recommendations. Scanned miRNA microarray expression data were first processed using the software provided by the manufacturer of the array. This microarray platform includes duplicate probesets for 1046 miRNAs. miRNA expression data were further filtered using the following criteria: 1) the average of the expression of control miRNA probesets on the array was used as a cutoff to remove miRNAs that have low or no expression, and 2) miRNAs for which the expression of one duplicate probeset at all time points are significantly higher than that of the other duplicate probeset were also removed

for further analysis, based on a Mann-Whitney U test. Expression data were then Z-score normalized for each miRNA, and at each time point the average expression of the two duplicate probesets was calculated. These miRNA expression profiles were compared to the previously identified myelination or proliferation profiles in the following target bias analysis.

TargetScanS, PicTar, and miRanda algorithms were used to predict potential miRNA regulatory targets. miRNA targets predicted by these programs were downloaded from the program websites. miRNA target bias analysis was performed as follows: for each miRNA, SC expressed genes that have a miRNA seed sequence match in the 3'UTR were identified using TargetScanS. The Pearson's correlation coefficient of gene and miRNA expression profiles was calculated for each target and non-target. The Mann-Whitney test P-value was calculated to test if miRNA target genes tend to have higher expression correlations with miRNA than non-target genes, i.e. a positive target bias.

Immunohistochemistry: The following primary and secondary antibodies were used: chicken anti-GFP (1:1000, Aves), rabbit anti-βIII tubulin (1:1000, Covance), rabbit anti-phospho histone 3 (1:200, Millipore), rat anti-MBP (1:100, Millipore), anti-rabbit Cy3 (1:500, Jackson ImmunoResearch Laboratories), anti-rat Cy3 (1:500, Jackson ImmunoResearch Laboratories), and anti-chicken Alexa 488 (1:500, Jackson ImmunoResearch Laboratories).

For immunohistochemical analysis of sciatic nerves, nerves were dissected, immersion fixed in 4% paraformaldehyde for 2 h, rinsed with PBS, and cryoprotected in 30% sucrose. Sciatic nerves were then embedded in Tissue-Tek OCT Compound (Sakura

Finetek) and sectioned at 6 μm. All frozen sections were immunostained by post-fixing in ice-cold acetone at -20°C for 10 min and blocking in 5% fish skin gelatin in PBS-0.2% Triton for 1 h at room temperature. Sections were then incubated with primary antibody diluted in blocking buffer overnight at 4°C. Secondary antibody incubation was performed at room temperature for 1 h also in blocking buffer. After all stainings, sections were mounted with Vectashield Mounting Medium with DAPI (Vector Laboratories) for microscopic visualization. Images were captured using an upright microscope equipped for epifluorescence microscopy (Nikon 80i; CoolSnapES camera) and were processed using MetaMorph, Image-J and Gimp software using global adjustments in brightness and contrast. All cell number quantifications were carried out by counting the cells of interest in 4 randomly selected regions in longitudinal nerve sections from each animal assessed (at least 3 mice per genotype at each time point) at a 20x magnification. The area covered by MBP immunostaining was determined using Image-J after automated background adjustment and binarization (Sasaki et al., 2009), from 4 randomly selected fields at a 20x magnification in longitudinal nerve sections. MBP area was normalized to total nerve area and results represent the average of at least 3 mice per genotype.

Nerve light and electron microscopy and morphometry: Sciatic nerve segments from Dicer-SCKO or Ctrl mice were dissected at the appropriate times after injury and placed in 3% glutaraldehyde overnight. The isolated nerve segments were approximately 15 mm in length and, in the case of crush-injured nerves, included the distal regenerated stump. After washing with phosphate buffer, nerves were postfixed in 1% osmium tetraoxide in

phosphate buffer overnight at 4°C. Specimens were then dehydrated in graded alcohols and embedded in 100% epoxy (Araldite 502). One-micrometer-thick plastic embedded sections were prepared and stained with toluidene blue for light microscopy. For electron microscopy, thin sections were prepared, stained with uranyl acetate and lead citrate, and photographed with a JEOL (Akishima) 1200 electron microscope. All nerves underwent qualitative assessment of neural architecture followed by detailed histomorphometric analysis carried out in a blinded fashion as previously described (Hunter et al., 2007), using at least three mice per genotype at each time point. For injured nerves, histomorphometric analysis was carried out 5 mm distal to the crush site. Total regenerated axon counts were determined by counting both remyelinated and non-remyelinated axons in Ctrl and Dicer-SCKO nerves 14 days after injury from electron micrographs taken at 5000x magnification.

Plasmids: miRNAs were obtained by PCR amplifying individual miRNA precursors from genomic DNA. The resulting fragments were cloned between the BamHI and Nhe I sites in the miRNASelect pEP-MIR Cloning and Expression Vector (Cell Biolabs) using the InFusion HD cloning system (Clonetech) according to the manufacurer's recommendations. Pre-miRNAs included the miRNA stem loop and ~100 nt of flanking sequence on either side and were amplified using the following primers: pre-mir-34a: F, TAGTTCTCGAGGATCCCCAGCTGAATCCCGACTA GT; R, AAAAGCTCGAGCTAGCTCTCTTAGCCAGAAGTGCTC. pre-mir-140: F, TAGTTC TCGAGGATCCGCCTCTGACCCTGCTTGCTGGTGGTGTA; R,

AAAAGCTCGAGCTAGC CCAACACCCACCCAATAGACGCCT. pEP-mir Null Vector (Cell Biolabs) was used as Ctrl.

A lentiviral miRNA expression vector was made by PCR amplifying the pEP-MIR expression cassette (promoter, miR processing portion, and mCherry reporter; F, AGATCCAGTTTGGTTAATTAAGTGAGG CTCCGGTGCCCGTCA; R, TAGAG TCGCGGCCGCTTTACTTGTACAGCTCGTCCATGCCGCCGGTGGA) and subcloning it between the PacI and BsrgI sites of an FCIV lentiviral vector (Araki et al., 2004) using the InFusion HD cloning system (Clonetech) according to the manufacurer's recommendations. For luciferase assays, the 3'UTR regions of *Egr2, Notch1 and Ccnd1* were PCR amplified from genomic DNA using the following primers: *Ccnd1* 3'UTR: F, AAAGCTGCGCACTAGTGGG CCACCGGGCAGGCGGGAGCCA; R, ATCCTTTATTAAGCTTTGAGATTTTACCAATTT TATTT; *Notch1* 3'UTR: F, AAAGCTGCGCACTAGTACAGAGATGTGGGATGCAGGACC; R, ATCCTTTATTAAGCTTGTTTAGCAAAATGTGGACAACCA; *Egr2* 3'UTR: F, AAAGCT GCGCACTAGTGATGAAGCTCTGGCTGACACACCA; R, ATCCTTTATTAAGCTTACCA TAGTCAATAAGCCATCCAT. DNA fragments were cloned downstream of the luciferase gene between the HindIII and SpeI sites in the pMIR-REPORT miRNA Expression Reporter Vector (Ambion). The 3'UTR of *Egr2* lacking the miR-140 landing pad was cloned in an analogous manner using the following sets of overlapping primers: F1, AAAGCTGCGCACTAGTGATGAAGCTCTGGCTGACACACCA R1, ACAGCCATACTTA

AACCCAAGTCTCGAGCTCGCGGCGCCTCTAGAAAGGCATCCTGTACACATGC

A F2, TGCATGTGTACAGGATGCCTTTCTAGAGGCGCCGCGAGCTCGAGACTTGGGT TTAAGTATGGCTGT R2 AAAGATCCTTTATTAAGCTTACCATAGTCAATAAGCCATCCATTAT CTGAACTCCAGTTTCAAAGCTTGGCGCGCCAGAATAGATTGTTTCTCTCT. pRL-CMV Renilla Luciferase Reporter vector (promega) was used as a transfection control.

Lentivirus production: Lentiviruses expressing miR-34a, miR-140 or a Ctrl miRNA were produced in HEK293T cells as previously described (Sasaki et al., 2006).

Luciferase assays: HEK293T cells were seeded at a density of 50,000 cells/well in 24 well plates in DMEM media (Invitrogen) supplemented with 10% fetal bovine serum (FBS), 2 mM L-glutamine. Cell were transfected 24 h later, with either a pEP-MIR vector expressing a pre-miRNA or with the pEP-mir Null control and with the pMIR-REPORT luciferase reporter vector containing the appropriate 3'UTR linked to luciferase. pRL-CMV Renilla Luciferase Reporter vector (Promega) was used as a transfection control. A total of 200 ng of plasmid DNA/well were transfected at a ratio of 50:1:0.5 (miRNA : luciferase reporter : transfection Ctrl). Cells were harvested 48 h post-transfection and assayed using a Dual-Luciferase Reporter Assay System (Promega) according to the manufacturer's protocol.

Primary SC cultures and lentiviral infection: Primary rat SCs were cultured from postnatal day1 to day3 rat pups sciatic nerves as previously described (Nagarajan et al., 2001). Established SC cultures were then transduced at an early passage (<passage 3) with a lentiviral vector expressing miR-34a, miR-140 or a Ctrl miRNA. Efficiency of infection was confirmed by visualization of expression of mCherry fluorescent reporter in the pEP-MIR cassette in almost 100% cells.

SC in vitro proliferation, differentiation, or myelination assays: For SC *in vitro* differentiation assays, Ctrl or miR-140 overexpressing SCs were initially seeded onto collagen coated 24-well plates (~75,000 cells/well) in 10% FBS-DMEM media and 24 hours later cells were switched to 1% FBS-DMEM media for 2 days. SCs were then induced to differentiate by adding 1% FBS-DMEM media containing 250 μM 8-(4-Chlorophenylthio) adenosine-3',5' cyclic monophosphate (cpt-cAMP, Biolog). RNA was isolated 72 h later. Reported results are from duplicated wells from two independent assays. For SC proliferation and *in vitro* myelination assays, dorsal root ganglion neurons were dissected from E14 rat embryos, dissociated, and seeded onto Matrigel-coated (BD Biosciences) 4-well plates in Neurobasal media (Invitrogen) containing 2% B27 (Invitrogen) and 50 ng/ml NGF. Glia were eliminated by addition of 20 μM 5-fluoro-2-deoxyuridine (Sigma) and 20 μM uridine (Sigma) to the media for 4 days. Seven days after seeding DRGs were switched to F-12/DMEM media supplemented with 15% FBS, 2mM L-glutamine and 50 ng/ml NGF, and Ctrl or miR overexpressing SCs were added to each well. To examine SC proliferation, 25,000 Ctrl or miR-34a overexpressing SCs/well were plated onto DRG neurons and growth curves were generated by monitoring changes

in cell number over 5 days. mCherry positive cells expressing miR-34a were visualized at a 20x magnification and quantified from 5 randomly selected fields. Results are averages from triplicate wells from 2 independent assays. For *in vitro* myelination assays, 50,000 Ctrl of miR-140 overexpressing SCs/well were plated onto DRG neurons and allowed to proliferate and ensheath axons for 7 days. At this point, myelination was induced by adding 50 μg/ml of ascorbic acid. Myelination was allowed to proceed for 14 days and myelinated segments were visualized through MBP immunostaining at a 20x magnification as previously described (Ryu et al., 2008). The number of myelinated segments was quantified by averaging five different fields from triplicate wells in 3 independent assays.

Western Blotting: Ctrl and miRNA overexpressing SCs were lysed in 200 μl of buffer containing 150 mM sodium chloride, 50 mM Hepes, 1% NP-40, 1 mM EDTA, 1 mM sodium fluoride, 1 mM sodium orthovanodate, and complete protease inhibitor cocktail (Roche Applied Science). Lysates were clarified by centrifugation at 14,000 rpm for 10 min and quantified using the MicroBCAProtein Assay kit (Pierce). For Western blotting, the proteins were separated by SDS-PAGE and transferred to a PVDF membrane (Millipore). Membranes were blocked in 5% milk in 0.1% TBS-Tween and incubated overnight with the appropriate primary antibody. Following incubation with secondary antibodies conjugated to HRP (GE Healthcare), membranes were developed with SuperSignal West Dura substrate (Pierce). The primary antibodies used were mouse anti-Ccnd1 (1:1000, Cell Signaling), anti-Notch1 (1:1000, Cell Signaling) and rabbit anti-

Egr2 (1:1000, Covance). The secondary antibodies used were anti-mouse and anti-rabbit HRP (1:5000; Jackson ImmunoResearch Laboratories).

Statistical analysis: All values are expressed as mean ± SEM. If not stated otherwise, *p* values were determined by unpaired, two-tailed Student's *t* test. All statistical analyses were performed using Microsoft Excel 2007.

Acknowledgements

We thank Amy Strickland and Nina Panchenko for experimental assistance; Matthias Merkenschlager for the Dicer conditional knockout mice; members of the Milbrandt laboratory for their comments on the manuscript and helpful discussions. We thank the Genome Technology Access Center (GTAC) in the Department of Genetics for help with genomic analysis. We also thank the Alvin J. Siteman Cancer Center at Washington University School of Medicine and Barnes-Jewish Hospital in St. Louis, Mo., for the use of the Biomedical Informatics Core (BMC), which provided the in silico analysis service. Both GTAC and BMC are partially supported by NCI Cancer Center Support Grant #P30 CA91842 to the Siteman Cancer Center and by ICTS/CTSA Grant# UL1RR024992 from the National Center for Research Resources (NCRR), a component of the National Institutes of Health (NIH), and NIH Roadmap for Medical Research. This work was also supported by NIH Neuroscience Blueprint Center Core Grant P30 NS057105 to Washington University, the HOPE Center for Neurological Disorders, National Institutes of Health Grants NS040745 (J.M.), AG13730 (J.M.). LC is supported by a NIH Pathway to Independence Award LM010824.

References

Araki T, Sasaki Y, Milbrandt J (2004) Increased nuclear NAD biosynthesis and SIRT1 activation prevent axonal degeneration. Science, 305:1010-1013.

Araki T, Nagarajan R, Milbrandt J (2001) Identification of genes induced in peripheral nerve after injury. expression profiling and novel gene discovery. J Biol Chem, 276:34131-34141.

Atanasoski S, Shumas S, Dickson C, Scherer SS, Suter U (2001) Differential cyclin D1 requirements of proliferating schwann cells during development and after injury. Mol Cell Neurosci, 18:581-592.

Bartel DP, Chen CZ (2004) Micromanagers of gene expression: The potentially widespread influence of metazoan microRNAs. Nat Rev Genet, 5:396-400.

Bosse F, Hasenpusch-Theil K, Kury P, Muller HW (2006) Gene expression profiling reveals that peripheral nerve regeneration is a consequence of both novel injury-dependent and reactivated developmental processes. J Neurochem, 96:1441-1457.

Bremer J, O'Connor T, Tiberi C, Rehrauer H, Weis J, Aguzzi A (2010) Ablation of dicer from murine schwann cells increases their proliferation while blocking myelination. PLoS One, 5:e12450.

Chen QR, Yu LR, Tsang P, Wei JS, Song YK, Cheuk A, Chung JY, Hewitt SM, Veenstra TD, Khan J (2011) Systematic proteome analysis identifies transcription factor YY1 as a direct target of miR-34a. J Proteome Res, 10:479-487.

Cobb BS, Nesterova TB, Thompson E, Hertweck A, O'Connor E, Godwin J, Wilson CB, Brockdorff N, Fisher AG, Smale ST, Merkenschlager M (2005) T cell lineage choice and differentiation in the absence of the RNase III enzyme dicer. J Exp Med, 201:1367-1373.

Coleman M (2005) Axon degeneration mechanisms: Commonality amid diversity. Nat Rev Neurosci, 6:889-898.

Doerflinger NH, Macklin WB, Popko B (2003) Inducible site-specific recombination in myelinating cells. Genesis, 35:63-72.

Farh KK, Grimson A, Jan C, Lewis BP, Johnston WK, Lim LP, Burge CB, Bartel DP (2005) The widespread impact of mammalian MicroRNAs on mRNA repression and evolution. Science, 310:1817-1821.

Flynt AS, Lai EC (2008) Biological principles of microRNA-mediated regulation: Shared themes amid diversity. Nat Rev Genet, 9:831-842.

Geuna S, Raimondo S, Ronchi G, Di Scipio F, Tos P, Czaja K, Fornaro M (2009) Chapter 3: Histology of the peripheral nerve and changes occurring during nerve regeneration. Int Rev Neurobiol, 87:27-46.

Grimson A, Farh KK, Johnston WK, Garrett-Engele P, Lim LP, Bartel DP (2007) MicroRNA targeting specificity in mammals: Determinants beyond seed pairing. Mol Cell, 27:91-105.

He Y, Kim JY, Dupree J, Tewari A, Melendez-Vasquez C, Svaren J, Casaccia P (2010) Yy1 as a molecular link between neuregulin and transcriptional modulation of peripheral myelination. Nat Neurosci, 13:1472-1480.

Hermeking H (2010) The miR-34 family in cancer and apoptosis. Cell Death Differ, 17:193-199.

Hornstein E, Shomron N (2006) Canalization of development by microRNAs. Nat Genet, 38 Suppl:S20-4.

Hunter DA, Moradzadeh A, Whitlock EL, Brenner MJ, Myckatyn TM, Wei CH, Tung TH, Mackinnon SE (2007) Binary imaging analysis for comprehensive quantitative histomorphometry of peripheral nerve. J Neurosci Methods, 166:116-124.

Ivey KN, Srivastava D (2010) MicroRNAs as regulators of differentiation and cell fate decisions. Cell Stem Cell, 7:36-41.

Jessen KR, Mirsky R (2008) Negative regulation of myelination: Relevance for development, injury, and demyelinating disease. Glia, 56:1552-1565.

Jessen KR, Mirsky R, Morgan L (1991) Role of cyclic AMP and proliferation controls in schwann cell differentiation. Ann N Y Acad Sci, 633:78-89.

John B, Enright AJ, Aravin A, Tuschl T, Sander C, Marks DS (2004) Human MicroRNA targets. PLoS Biol, 2:e363.

Karres JS, Hilgers V, Carrera I, Treisman J, Cohen SM (2007) The conserved microRNA miR-8 tunes atrophin levels to prevent neurodegeneration in drosophila. Cell, 131:136-145.

Kim HA, Ratner N, Roberts TM, Stiles CD (2001) Schwann cell proliferative responses to cAMP and Nf1 are mediated by cyclin D1. J Neurosci, 21:1110-1116.

King RH (2005) Nerve trunks and spinal roots. In: Peripheral neuropathy.(Dyck PJ TP, ed), pp35. Philadelphia: Elsevier Saunders.

Krek A, Grun D, Poy MN, Wolf R, Rosenberg L, Epstein EJ, MacMenamin P, da Piedade I, Gunsalus KC, Stoffel M, Rajewsky N (2005) Combinatorial microRNA target predictions. Nat Genet, 37:495-500.

Lau P, Verrier JD, Nielsen JA, Johnson KR, Notterpek L, Hudson LD (2008) Identification of dynamically regulated microRNA and mRNA networks in developing oligodendrocytes. J Neurosci, 28:11720-11730.

Le N, Nagarajan R, Wang JY, Araki T, Schmidt RE, Milbrandt J (2005) Analysis of congenital hypomyelinating Egr2Lo/Lo nerves identifies Sox2 as an inhibitor of schwann cell differentiation and myelination. Proc Natl Acad Sci U S A, 102:2596-2601.

Lu J, Getz G, Miska EA, Alvarez-Saavedra E, Lamb J, Peck D, Sweet-Cordero A, Ebert BL, Mak RH, Ferrando AA, Downing JR, Jacks T, Horvitz HR, Golub TR (2005) MicroRNA expression profiles classify human cancers. Nature, 435:834-838.

Mansfield JH, Harfe BD, Nissen R, Obenauer J, Srineel J, Chaudhuri A, Farzan-Kashani R, Zuker M, Pasquinelli AE, Ruvkun G, Sharp PA, Tabin CJ, McManus MT (2004) MicroRNA-responsive 'sensor' transgenes uncover hox-like and other developmentally regulated patterns of vertebrate microRNA expression. Nat Genet, 36:1079-1083.

Melton C, Judson RL, Blelloch R (2010) Opposing microRNA families regulate self-renewal in mouse embryonic stem cells. Nature, 463:621-626.

Meyer zu Horste G, Prukop T, Nave KA, Sereda MW (2006) Myelin disorders: Causes and perspectives of charcot-marie-tooth neuropathy. J Mol Neurosci, 28:77-88.

Monje PV, Rendon S, Athauda G, Bates M, Wood PM, Bunge MB (2009) Non-antagonistic relationship between mitogenic factors and cAMP in adult schwann cell re-differentiation. Glia, 57:947-961.

Nagarajan R, Le N, Mahoney H, Araki T, Milbrandt J (2002) Deciphering peripheral nerve myelination by using schwann cell expression profiling. Proc Natl Acad Sci U S A, 99:8998-9003.

Nagarajan R, Svaren J, Le N, Araki T, Watson M, Milbrandt J (2001) EGR2 mutations in inherited neuropathies dominant-negatively inhibit myelin gene expression. Neuron, 30:355-368.

Pang RT, Leung CO, Ye TM, Liu W, Chiu PC, Lam KK, Lee KF, Yeung WS (2010) MicroRNA-34a suppresses invasion through downregulation of Notch1 and Jagged1 in cervical carcinoma and choriocarcinoma cells. Carcinogenesis, 31:1037-1044.

Pereira JA, Baumann R, Norrmen C, Somandin C, Miehe M, Jacob C, Luhmann T, Hall-Bozic H, Mantei N, Meijer D, Suter U (2010) Dicer in schwann cells is required for myelination and axonal integrity. J Neurosci, 30:6763-6775.

Ramachandran R, Fausett BV, Goldman D (2010) Ascl1a regulates muller glia dedifferentiation and retinal regeneration through a lin-28-dependent, let-7 microRNA signalling pathway. Nat Cell Biol, 12:1101-1107.

Ryu EJ, Yang M, Gustin JA, Chang LW, Freimuth RR, Nagarajan R, Milbrandt J (2008) Analysis of peripheral nerve expression profiles identifies a novel myelin glycoprotein, MP11. J Neurosci, 28:7563-7573.

Sasaki Y, Araki T, Milbrandt J (2006) Stimulation of nicotinamide adenine dinucleotide biosynthetic pathways delays axonal degeneration after axotomy. J Neurosci, 26:8484-8491.

Stark A, Brennecke J, Bushati N, Russell RB, Cohen SM (2005) Animal MicroRNAs confer robustness to gene expression and have a significant impact on 3'UTR evolution. Cell, 123:1133-1146.

Sun F, Fu H, Liu Q, Tie Y, Zhu J, Xing R, Sun Z, Zheng X (2008) Downregulation of CCND1 and CDK6 by miR-34a induces cell cycle arrest. FEBS Lett, 582:1564-1568.

Svaren J, Meijer D (2008) The molecular machinery of myelin gene transcription in schwann cells. Glia, 56:1541-1551.

Thatcher EJ, Paydar I, Anderson KK, Patton JG (2008) Regulation of zebrafish fin regeneration by microRNAs. Proc Natl Acad Sci U S A, 105:18384-18389.

Tsang J, Zhu J, van Oudenaarden A (2007) MicroRNA-mediated feedback and feedforward loops are recurrent network motifs in mammals. Mol Cell, 26:753-767.

Verrier JD, Semple-Rowland S, Madorsky I, Papin JE, Notterpek L (2010) Reduction of dicer impairs schwann cell differentiation and myelination. J Neurosci Res, 88:2558-2568.

Verrier JD, Lau P, Hudson L, Murashov AK, Renne R, Notterpek L (2009) Peripheral myelin protein 22 is regulated post-transcriptionally by miRNA-29a. Glia, 57:1265-1279.

Wienholds E, Plasterk RH (2005) MicroRNA function in animal development. FEBS Lett, 579:5911-5922.

Wienholds E, Kloosterman WP, Miska E, Alvarez-Saavedra E, Berezikov E, de Bruijn E, Horvitz HR, Kauppinen S, Plasterk RH (2005) MicroRNA expression in zebrafish embryonic development. Science, 309:310-311.

Wood P, Moya F, Eldridge C, Owens G, Ranscht B, Schachner M, Bunge M, Bunge R (1990) Studies of the initiation of myelination by schwann cells. Ann N Y Acad Sci, 605:1-14.

Woodhoo A, Alonso MB, Droggiti A, Turmaine M, D'Antonio M, Parkinson DB, Wilton DK, Al-Shawi R, Simons P, Shen J, Guillemot F, Radtke F, Meijer D, Feltri ML,

Wrabetz L, Mirsky R, Jessen KR (2009) Notch controls embryonic schwann cell differentiation, postnatal myelination and adult plasticity. Nat Neurosci, 12:839-847.

Yin VP, Thomson JM, Thummel R, Hyde DR, Hammond SM, Poss KD (2008) Fgf-dependent depletion of microRNA-133 promotes appendage regeneration in zebrafish. Genes Dev, 22:728-733.

Yun B, Anderegg A, Menichella D, Wrabetz L, Feltri ML, Awatramani R (2010) MicroRNA-deficient schwann cells display congenital hypomyelination. J Neurosci, 30:7722-7728.

Figures

Figure 1: Expression profiles of 87 miRNAs expressed in SC. ***a)*** Z-score normalized miRNA expression levels 4 days (C4) and 14 days (C14) after nerve crush injury as well as in uninjured nerves (Ctrl) are shown in a heatmap. Red indicates higher expression than the average across all samples while green indicates lower expression. mmu refers to the standard abbreviation used to designate miRNAs of mouse origin.

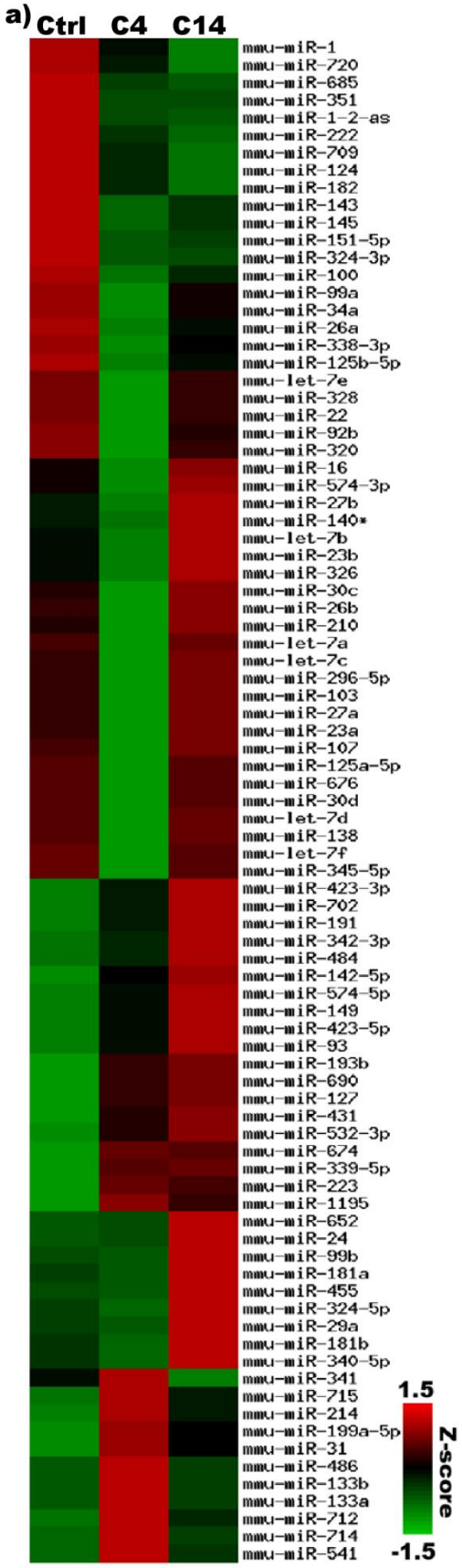
a)
Ctrl
C4
C14
mmu-miR-1
mmu-miR-720
mmu-miR-685
mmu-miR-351
mmu-miR-1-2-as
mmu-miR-222
mmu-miR-709
mmu-miR-124
mmu-miR-182
mmu-miR-143
mmu-miR-145
mmu-miR-151-5p
mmu-miR-324-3p
mmu-miR-100
mmu-miR-99a
mmu-miR-34a
mmu-miR-26a
mmu-miR-338-3p
mmu-miR-125b-5p
mmu-let-7e
mmu-miR-328
mmu-miR-22
mmu-miR-92b
mmu-miR-320
mmu-miR-16
mmu-miR-574-3p
mmu-miR-27b
mmu-miR-140*
mmu-let-7b
mmu-miR-23b
mmu-miR-326
mmu-miR-30c
mmu-miR-26b
mmu-miR-210
mmu-let-7a
mmu-let-7c
mmu-miR-296-5p
mmu-miR-103
mmu-miR-27a
mmu-miR-23a
mmu-miR-107
mmu-miR-125a-5p
mmu-miR-676
mmu-miR-30d
mmu-let-7d
mmu-miR-138
mmu-let-7f
mmu-miR-345-5p
mmu-miR-423-3p
mmu-miR-702
mmu-miR-191
mmu-miR-342-3p
mmu-miR-484
mmu-miR-142-5p
mmu-miR-574-5p
mmu-miR-149
mmu-miR-423-5p
mmu-miR-93
mmu-miR-193b
mmu-miR-690
mmu-miR-127
mmu-miR-431
mmu-miR-532-3p
mmu-miR-674
mmu-miR-339-5p
mmu-miR-223
mmu-miR-1195
mmu-miR-652
mmu-miR-24
mmu-miR-99b
mmu-miR-181a
mmu-miR-455
mmu-miR-324-5p
mmu-miR-29a
mmu-miR-181b
mmu-miR-340-5p
mmu-miR-341
mmu-miR-715
mmu-miR-214
mmu-miR-199a-5p
mmu-miR-31
mmu-miR-486
mmu-miR-133b
mmu-miR-133a
mmu-miR-712
mmu-miR-714
mmu-miR-541
1.5
Z-score
-1.5

Figure 2: Target bias analysis suggests that SC miRNAs modulate the injury response by repressing positive regulators of SC dedifferentiation/proliferation. ***a)*** mRNA expression profiles of gene clusters containing known regulators of SC dedifferentiation/proliferation (the proliferation profile) or differentiation/myelination (the myelination profile) after injury. ***b***) Graph plotting the target bias for each miRNA in subset 1 (measured by a Mann-Whitney z-score) against the correlation of its expression with the myelination or proliferation profile (measured by ΔCC, the difference in correlation coefficients with the proliferation profile and the myelination profile). Biological functions of miRNAs in regulating the SC injury response may be inferred from their correlation with the proliferation or myelination gene clusters and by their positive or negative target bias. The majority of SC miRNAs cluster in the top left quadrant of the graph (negative target bias, correlation with the myelination profile), suggesting that SC miRNAs are likely to modulate the injury response primarily through their inhibition of positive regulators of SC dedifferentiation/proliferation. Dotted and dashed lines represent statistical significance cutoffs. miRNAs differentially regulated after injury (C4 vs. Ctrl $p<0.05$), with a statistically significant target bias and a high correlation with the myelination or proliferation clusters ($\Delta CC>1.6$) are represented by triangles. Empty dots represent miRNAs that met statistical significance cutoffs for target bias and high correlation with the myelination or proliferation clusters, but were not differentially regulated after injury. ***c***) miRNAs likely to be direct regulators of the SC injury response (represented as triangles in *b*) based on their differential regulation after injury, significant target bias and a high correlation with the myelination or proliferation clusters. ***d)*** Predicted targets for miRNAs in *(c)* are enriched for genes

involved in cellular processes that are normally inhibited in adult or differentiating SCs but are active in immature or proliferating SCs.

a)

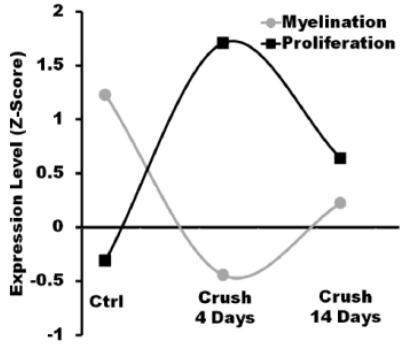

c)

miR ID	Injury Δ Expression		Target Bias		Correlation
	Fold Change	P-Value	Z-Score	P-Value	ΔCC
mmu-miR-34a	-3.60	0.008	-1.66	0.048	1.96
mmu-miR-30d	-1.83	0.004	-1.73	0.042	1.66
mmu-miR-22	-1.94	0.007	-1.77	0.038	1.84
mmu-miR-26a	-2.94	0.020	-1.81	0.035	1.99
mmu-miR-143	-2.92	0.002	-1.95	0.028	1.91
mmu-miR-92b	-1.99	0.0222	-2.54	0.005	1.91

b)

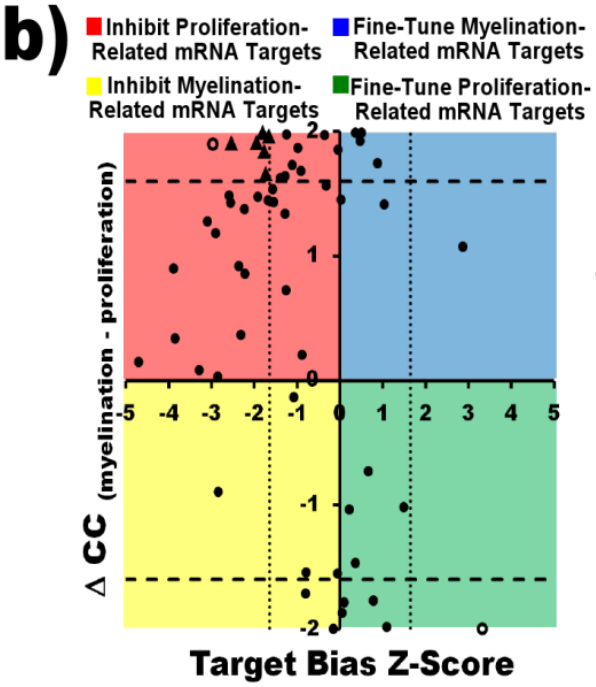

d)

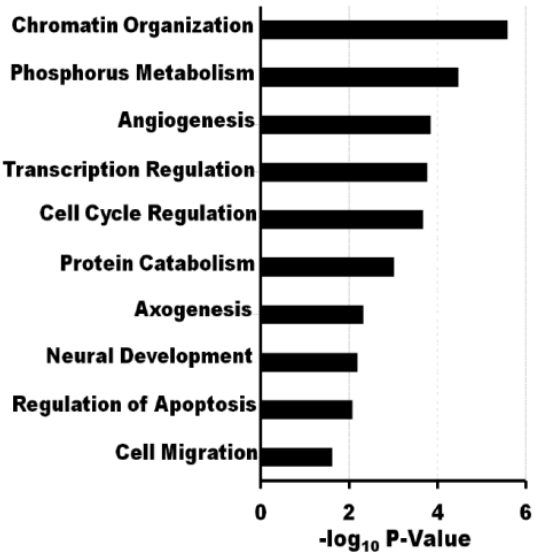

Figure 3: SCs with disrupted miRNA processing have delayed cycling between differentiation states after peripheral nerve injury. ***a)*** YFP fluorescence in SCs (arrowheads) of longitudinal sciatic nerve sections of Rosa26-YFP/ PLP-CreER$_T$ mice 8 weeks after injection with tamoxifen. PLP-CreER$_T$ induces specific and efficient recombination in most SCs and excision-dependent YFP fluorescence is localized to regions of SC cytoplasm but not to axons (Tuj1; note non-overlapping Tuj1 and YFP staining). Scale Bars: 50 μm. ***b)*** qRT-PCR results show efficient depletion of *Dicer1* mRNA and of mature miRNAs in Dicer-SCKO sciatic nerves 8 weeks after tamoxifen-induced recombination. Dicer mRNA levels and the levels of miR-34a and miR26a in the sciatic nerve of Dicer-SCKO mice at this time were decreased by over 60% ($p<0.001$ in all three cases, two-tailed Student's t-test) compared to Ctrl littermates. Reported values are normalized to *GAPDH* for mRNA and *U6* for miRNAs; error bars, SEM; n=5 mice per genotype. ***c)*** Quantification of the amount of myelin debris present in Ctrl and Dicer-SCKO nerves 14 days after crush injury shows no impairment in the ability of Tfam-deficient SCs to break down existing myelin. Error bars, SEM; n=3 mice per genotype. ***d and e)*** Pictures (*d*) and quantification (*e*) of phospho-histone 3 (PH3) immunostaining between sciatic nerves of Ctrl and Dicer-SCKO mice collected 4 (C4) or 14 (C14) days after crush injury. No difference in the number of proliferating SCs between Ctrl and Dicer-SCKO sciatic nerves was observed 4 days after crush injury. At C14, however, there were significantly more PH3 positive SCs in the sciatic nerves of Dicer-SCKO vs. Ctrl mice ($p<0.05$, two-tailed Student's t-test), indicating exit from cell-cycle was delayed in SCs with disrupted miRNA processing. Scale Bar: 25 μm. Error bars, SEM; n=3 mice per genotype. ***f)*** At C14, electron micrographs of sciatic nerves from Ctrl and

Dicer-SCKO mice show equivalent numbers of regenerated axons (remyelinated, arrows; non-remyelinated, arrow heads). Note the increased number of non-remyelinated axons (arrowheads) in Dicer-SCKO nerves. Scale Bar: 2 μm. ***g and h)*** Pictures (*h*) and quantification (*g*) of myelinated profiles in nerves from Ctrl and Dicer-SCKO mice before crush injury, or at C14 or C28. There is no difference in total number of myelinated axons in nerves from Dicer-SCKO vs. Ctrl mice before crush injury. However, examination of toluidene-blue stained plastic sections revealed a significant decrease ($p<0.05$, two-tailed Student's t-test) in the number of myelinated profiles at C14 in nerves from Dicer-SCKO mice. By C28 there is no longer a difference in total number of myelinated profiles between Dicer-SCKO and Ctrl nerves, however nerves in Dicer-SCKO mice are more thinly myelinated. Scale Bar: 25 μm. Error bars, SEM; n=3 or 4 mice per genotype at each time point.

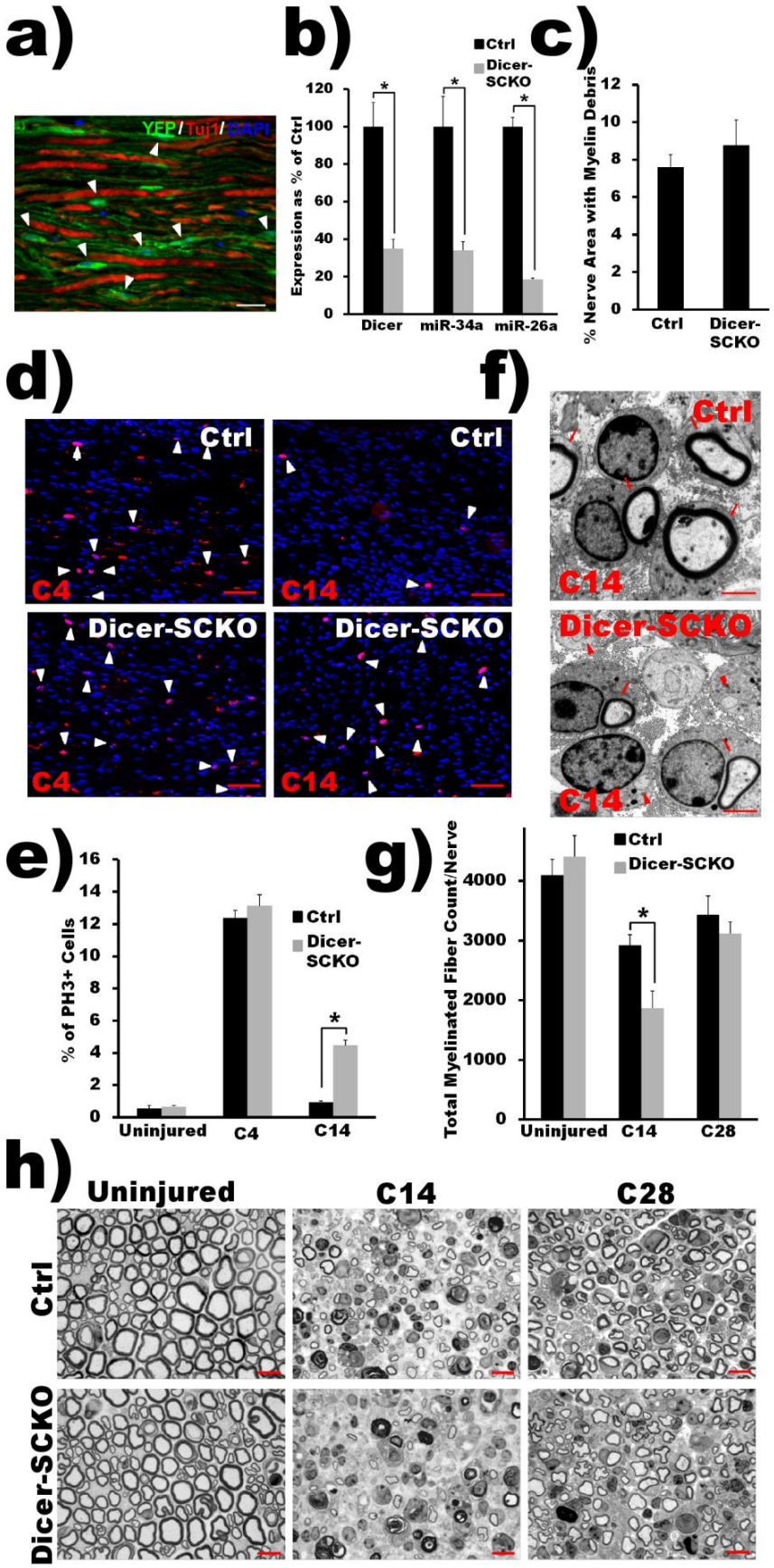
a)
YEP / Tuj1 / DAPI
b)
Ctrl
Dicer-SCKO
Expression as % of Ctrl
120
100
80
60
40
20
0
*
*
*
Dicer
miR-34a
miR-26a
c)
% Nerve Area with Myelin Debris
12
10
8
6
4
2
0
Ctrl
Dicer-SCKO
d)
Ctrl
C4
Ctrl
C14
Dicer-SCKO
C4
Dicer-SCKO
C14
f)
Ctrl
C14
Dicer-SCKO
C14
e)
% of PH3+ Cells
16
14
12
10
8
6
4
2
0
Ctrl
Dicer-SCKO
*
Uninjured
C4
C14
g)
Total Myelinated Fiber Count/Nerve
4000
3000
2000
1000
0
Ctrl
Dicer-SCKO
*
Uninjured
C14
C28
h)
Uninjured
C14
C28
Ctrl
Dicer-SCKO

Figure 4: miR-34a targets Notch-1 and Ccnd1 to regulate SC proliferation *in vitro*. ***a)*** The dynamic regulation of miR-34a expression in sciatic nerves after crush injury suggests a potential role in the modulation of cell cycle regulators. miR-34a levels are significantly decreased 4 days after crush injury ($p<0.01$, two-tailed Student's t-test) but recover as re-differentiation ensues (C14). After nerve transection (Trx), an injury paradigm in which remyelination does not occur, mir-34a levels remain low compared to uninjured nerves even 14 days after injury ($p<0.05$, two-tailed Student's t-test). Reported values are normalized to *U6*; error bars, SEM; n=3-6 mice at each time point. ***b)*** miR-34a directly interacts with the 3'UTRs of *Ccnd1* (top) and *Notch1* (bottom). Overexpression of miR-34a but not of a Ctrl miRNA in HEK293T cells expressing a luciferase reporter construct carrying the 3'UTR of either *Notch1 or Ccnd1* results in significantly decreased luciferase activity ($p<0.01$ in both cases, two-tailed Student's t-test). Error bars, SEM; n=3 independent assays ***c)*** qRT-PCR measurements show that the expression pattern of *Ccnd1* (top) and *Notch1* (bottom) after injury is inversely correlated with that of miR-34a, suggesting a direct targeting of these transcripts by miR-34a. Reported values are normalized to *GAPDH* for mRNA and *U6* for miRNAs; error bars, SEM; n=3-6 mice at each time point. ***d, e)*** Lentivirus-mediated mir-34a overexpression (≈ 3-fold) in cultured SCs significantly reduces Notch1 and Ccnd1 mRNA (d; $p<0.05$, in both cases, two-tailed Student's t-test) and protein levels (*e*, ≈ 2.5-fold decrease; Notch FL, Full-length; Notch NTM, cleaved transmembrane/intracellular region). qRT-PCR reported values are normalized to *GAPDH*; error bars, SEM; n=duplicate wells from three independent assays. ***f)*** Lentivirus-mediated mir-34a overexpression (≈ 3-fold) impairs the ability of SCs to proliferate in the presence of DRG axons. miR-34a expressing SCs have a

significantly decreased axon-induced proliferation *in vitro* compared to control SCs (no significant difference at day 1; $p<0.01$ at days 3 and 5; two-tailed Student's t-test). Error bars, SEM; n=triplicate wells from two independent assays.

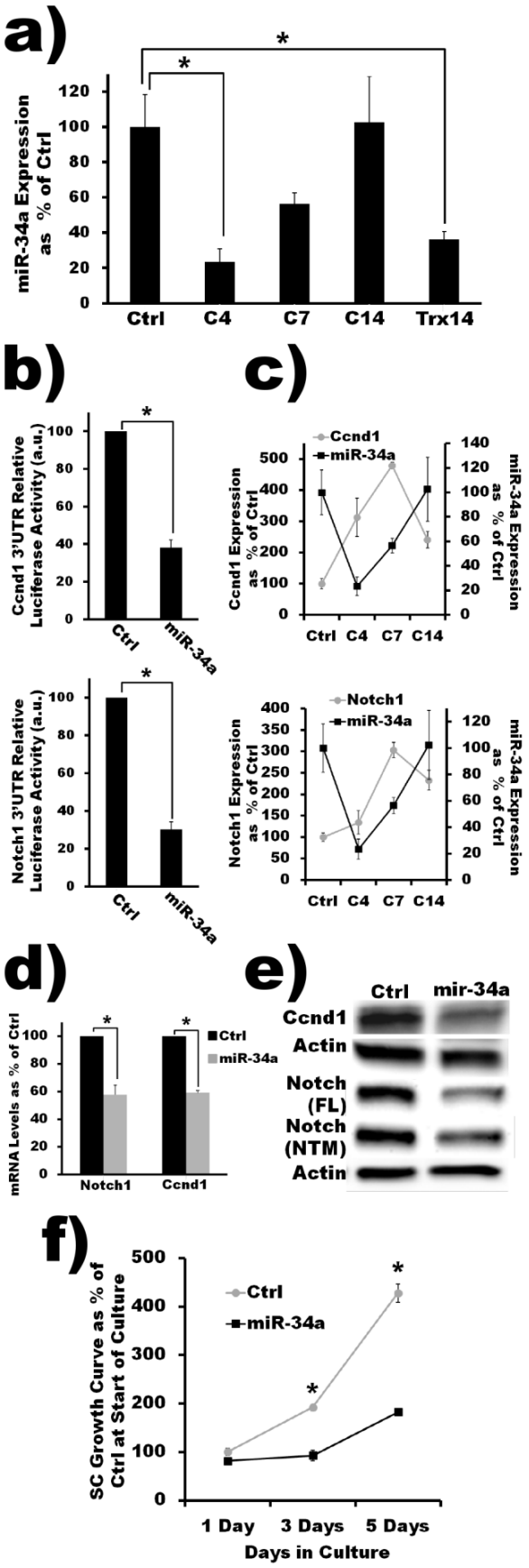
a)
miR-34a Expression as % of Ctrl
Ctrl
C4
C7
C14
Trx14
b)
Ccnd1 3'UTR Relative Luciferase Activity (a.u.)
Notch1 3'UTR Relative Luciferase Activity (a.u.)
Ctrl
miR-34a
c)
Ccnd1
miR-34a
Ccnd1 Expression as % of Ctrl
miR-34a Expression as % of Ctrl
Notch1
Notch1 Expression as % of Ctrl
d)
mRNA Levels as % of Ctrl
Notch1
Ccnd1
e)
Ctrl
mir-34a
Ccnd1
Actin
Notch (FL)
Notch (NTM)
Actin
f)
SC Growth Curve as % of Ctrl at Start of Culture
1 Day
3 Days
5 Days
Days in Culture

Figure 5: miR-140 directly interacts with Egr2 to regulate SC myelination *in vitro*. ***a)*** PicTar, TargetScanS, and miRanda algorithms all identify a putative binding site for miR-140 in the 3'-UTR of Egr2. ***b)*** qRT-PCR results show that miR-140 is expressed in mouse sciatic nerves and that its expression is dynamically regulated after injury. miR-140 expression is significantly decreased after injury (C4 and C7 $p<0.05$; two-tailed Student's t-test) but recovers as re-differentiation ensues (C14 no significant difference). Reported values are normalized to *U6*; error bars, SEM; n=3-6 mice at each time point. **c)** qRT-PCR measurements show that the expression pattern of *Egr2* is correlated with that of miR-140. Reported values are normalized to *GAPDH* for mRNA and *U6* for miRNAs; error bars, SEM; n=3-6 mice at each time point. ***d)*** Luciferase assays confirm a direct interaction between miR-140 and the 3'-UTR of *Egr2.* Overexpression of miR-140 but not of a Ctrl miRNA in HEK293T cells expressing a luciferase reporter construct carrying the 3'-UTR of *Egr2* results in significantly decreased luciferase activity ($p<0.05$, two-tailed Student's t-test). Mutating the predicted landing pad for miR-140 in the 3'-UTR of *Egr2* disrupts the interaction between miR-140 and the Egr2 3'-UTR luciferase construct and restores luciferase activity. ***e)*** Western blot analysis shows that overexpression of miR-140 in cultured SCs reduces the levels of Egr-2 protein ≈ 2.8 fold. ***f)*** Overexpression of miR-140 in SCs significantly decreases the levels of *Egr2* as well as of a number of myelin markers when these cells are co-cultured with DRGs and induced to myelinate (in all cases $p<0.05$, two-tailed Student's t-test). Reported values are normalized to *GAPDH*; error bars, SEM; n=duplicate wells from two independent assays. ***g)*** Similarly, miR-140 overexpression significantly inhibits the ability of SCs to form myelin *in vitro* in co-cultures with DRG neurons as visualized by MBP immunostaining

($p<0.05$, two-tailed Student's t-test). Error bars, SEM; n=triplicate wells from three independent assays.

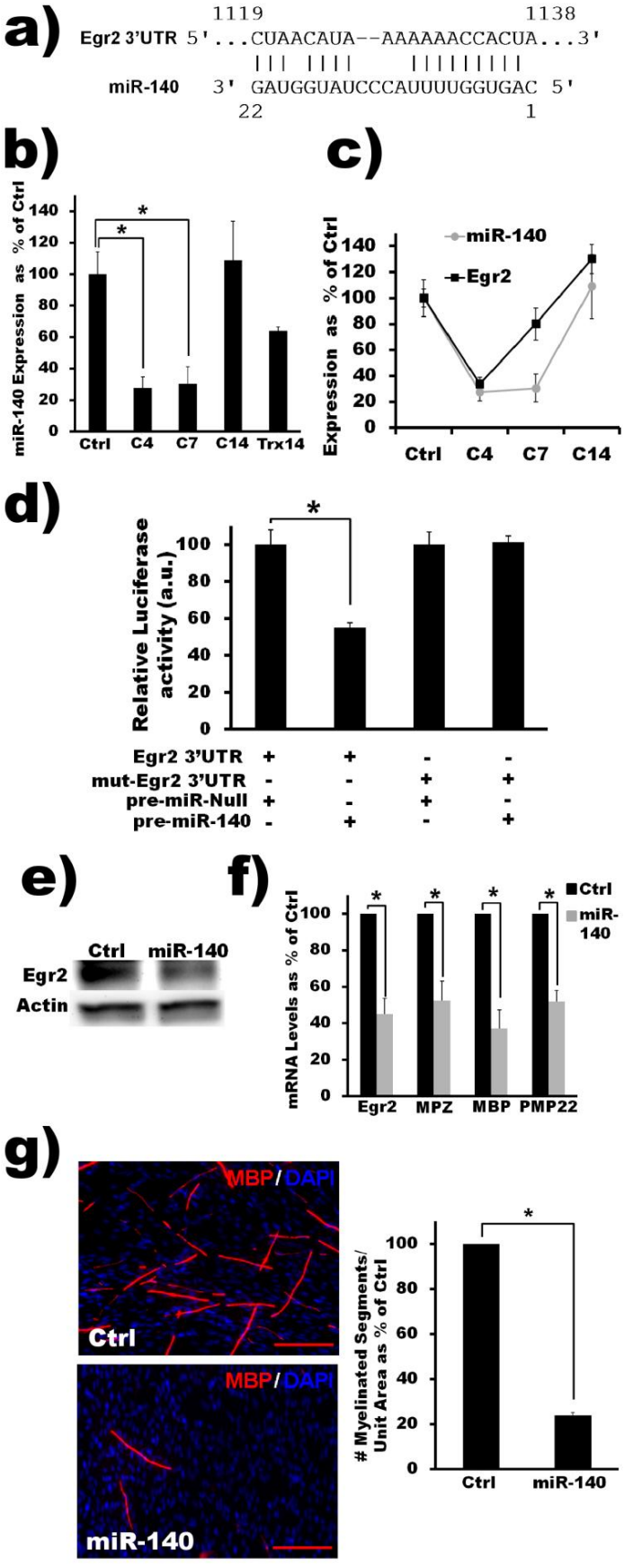
a)
1119
1138
Egr2 3'UTR 5'...CUAACAUA--AAAAAACCACUA...3'
miR-140 3' GAUGGUAUCCCAUUUUGGUGAC 5'
22
1
b)
miR-140 Expression as % of Ctrl
Ctrl
C4
C7
C14
Trx14
c)
Expression as % of Ctrl
miR-140
Egr2
Ctrl
C4
C7
C14
d)
Relative Luciferase activity (a.u.)
Egr2 3'UTR + + - -
mut-Egr2 3'UTR - - + +
pre-miR-Null + - + -
pre-miR-140 - + - +
e)
Ctrl
miR-140
Egr2
Actin
f)
mRNA Levels as % of Ctrl
Ctrl
miR-140
Egr2
MPZ
MBP
PMP22
g)
MBP / DAPI
Ctrl
MBP / DAPI
miR-140
Myelinated Segments/ Unit Area as % of Ctrl
Ctrl
miR-140

CHAPTER 6

An integrated approach to infer transcription factor and microRNA regulatory networks

Adapted from: Chang LW, Viader A, Payton JE, Varghese N, Milbrandt J, Nagarajan R. 2011. An integrated approach to infer transcription factor and microRNAs regulatory networks. Nucleic Acid Research. Submitted.

Abstract

Regulation of cell fate and developmental timing as well as maintenance of cellular and tissue homeostasis requires precise spatiotemporal control of gene expression, which is modulated by key transcription factors (TF) and microRNAs (miRNA) via a complex gene regulatory network. Elucidation of TF and miRNA regulatory networks is crucial to understand how normal gene regulatory mechanisms are disrupted in human disease. Computational methods have been developed to infer TF or miRNA mediated gene regulation, but few methods integrate these results to construct integrated TF and miRNA gene regulatory networks. In this study we present a systematic approach, IntegraNet, which combines mRNA and miRNA expression data, chromatin immunoprecipitation with sequencing (ChIP-Seq) data and computation TF and miRNA target prediction to build integrated TF and miRNA gene regulatory networks. We applied IntegraNet to expand a previously published miRNA-mRNA regulatory network as well as to infer the TF and miRNA regulatory network involved in Schwann cell (SC) response to nerve injury. Further analysis of regulatory network motifs in this SC injury response network provided insight on cooperative regulation of this process by TFs and miRNAs. This work demonstrates a systematic method for gene regulatory network inference that may be used to gain new insights on local and global features of gene regulation by TFs and miRNAs.

Introduction

Regulation of cell fate and developmental timing as well as maintenance of cellular and tissue homeostasis requires precise spatiotemporal control of gene expression. It is now apparent that such intricate control mechanisms are regulated by transcription factors (TFs) and microRNAs (miRNAs), which organize into exquisitely coordinated gene regulatory networks (Tsang et al. 2007; Martinez and Walhout 2009; Shalgi et al. 2009). Alteration or disruption of these regulatory networks often results in disease, including cancer and developmental disorders (Tenen 2003; Villard 2004; Zeng et al. 2010). Comprehensive delineations of how TFs and miRNAs cooperate in specific genetic programs are thus critical to understanding physiological and pathological processes.

Systematically inferring TF and miRNA regulatory networks is difficult to achieve by experimental methods and has motivated development of computational approaches. Thus, computational tools have been created to construct TF and miRNA regulatory networks using information such as gene expression profiling, miRNA expression profiling, and predicted TF and miRNA binding sites (Joung et al. 2007; Bandyopadhyay and Bhattacharyya 2009; Lionetti et al. 2009; Peng et al. 2009; Wang et al. 2009). Few studies, however, have combined all of these data to infer an integrated network of TFs and miRNAs. Particularly, transcriptional regulation of miRNAs is often excluded in these analyses due to the challenge in reliable prediction of miRNA promoters (Shalgi et al. 2007; Guo et al. 2010). In addition, chromatin immunoprecipitation with sequencing (ChIP-Seq) data for TFs, which experimentally characterizes TF regulatory targets and provides critical information for understanding

gene regulation, is seldom incorporated. These limitations highlight the need for new tools for gene regulatory network construction.

In this study we developed a novel approach (IntegraNet) to inferring human or mouse gene regulatory networks, which include TF-mRNA, TF-miRNA and miRNA-mRNA interactions. This method integrates mRNA and miRNA expression data, ChIP-Seq data, and computational TF and miRNA target predictions. Starting with a set of genes or miRNAs obtained from expression profiling analysis, our approach initially constructs a network by using TF targets identified from ChIP-Seq experiments. This network is then expanded to include additional regulatory targets of TFs and miRNAs by using genome-wide target prediction. To demonstrate the utility of our approach, we first applied IntegraNet to expand a published miRNA regulatory network involved in Hepatitis C Virus (HCV) infection (Peng et al. 2009). In addition, we used IntegraNet to construct the regulatory network involved in Schwann cell (SC) response to injury, a process driven by TFs and modulated by miRNAs. Using this network, we study cooperative TF/miRNA regulation in this regenerative process. This work demonstrates a systematic approach to infer TF and miRNA regulatory networks, which may be used to better understand coordinated gene regulation by TFs and miRNAs in complex biological systems.

Results

Overview of TF and miRNA regulatory network inference

We developed a systematic approach for TF and miRNA regulatory network inference. This approach, termed IntegraNet, integrates mRNA and miRNA expression

profiling data, chromatin immuneprecipitation with sequencing (ChIP-Seq) data, and computational TF and miRNA target predictions (Fig. 1). Two major applications of gene expression profiling analysis (including microarrays or RNA-Seq experiments) in order to understand gene regulation involve identification of differentially expressed genes between two conditions (e.g., disease vs. normal and mutant vs. wild type) or characterization of gene clusters that share a specific expression profile (over a time course or across multiple samples). Therefore, our approach for regulatory network inference starts with sets of coherently expressed or differentially expressed genes (termed core gene clusters, CGCs) and/or miRNAs (termed core miRNA clusters, CMCs) (Step 0). TF genes in CGCs and miRNAs in CMCs constitute the initial set of potential regulators in the gene regulatory network. In the first step, ChIP-Seq data is used to identify regulatory interactions between TFs and CGC mRNAs and between TFs and CMC miRNAs (Step 1). Additional mRNAs and miRNAs regulated by these TFs, as well as other TFs without ChIP-Seq data, are identified by genome-wide analysis of TFBS enrichment (Step 2). Next, genes in CGCs that may be regulated by miRNAs in CMCs are identified using computational miRNA target prediction (Step 3). The resulting regulatory network is further expanded to include TFs that, although not included in CGCs in the initial expression data analysis, are master regulators of genes in CGCs or miRNAs in CMCs (Step 4). Similarly, miRNAs that are not included in CMCs in the expression analysis but whose predicted targets are enriched in CGCs are identified (Step 5). Finally, upstream or downstream regulatory interactions of additional TFs and miRNAs added in Steps 4 and 5 are identified using ChIP-Seq data (as described in Step 1) and computational predictions (as described in Step 2) (Step 6). This final step

completes the regulatory network inference. In these steps, we have compiled and precalculated datasets of experimentally characterized and computationally predicted TF-mRNA, TF-miRNA, and miRNA-mRNA interactions, which are available as supplementary files and may be queried by an API to our in-house database upon request. Each step of IntegraNet is described in detail as follows.

Step 1: Identification of TF targets using ChIP-Seq data

To find TF-mRNA interactions among CGCs genes, IntegraNet first used experimentally validated TF targets characterized by ChIP-Seq results. We compiled a compendium of publicly available TF ChIP-Seq data, which included 47 independent datasets on 78 TFs (24 human TFs and 54 mouse TFs) (Supplementary Table 1). To use this dataset to identify TF targets conserved between human and mouse, we mapped the identified ChIP-Seq peak locations across the human and mouse genomes (see Methods). To assemble a high-confidence and high-quality TF target dataset and to reduce false-positive targets introduced by this mapping, we only used ChIP-Seq peaks that contained at least one match to one the TF's position weight matrix binding models. Additionally, we only included peaks that were located between -10kb and +5kb from the transcription start sites (TSSs) of annotated genes. After this filtering, 19.9% of the original ChIP-Seq peaks were retained in the list of high confidence TF target list, which consists of a total of 71,346 mouse and 64,367 human TF-mRNA interactions (Supplementary Files 1 and 2).

In addition to TF-mRNA interactions, the genome-wide mapped reads of ChIP-Seq data may be used to identify TF-miRNA interactions. Performance of such analysis

depends on accurate characterization of pri-miRNA promoters. Several studies have developed computational methods to predict pri-miRNA TSSs using several promoter features (Marson et al. 2008; Ozsolak et al. 2008; Saini et al. 2008; Corcoran et al. 2009). However, given that many of these methods rely on limited experimental datasets, they tend to only predict TSSs for a subset of miRNAs. To address this limitation we developed a new voting algorithm (TSSvote) for predicting human and mouse miRNA TSSs, which uses a comprehensive set of transcription-related sequence features (Fig. 2A, see Methods). These included mapping of known transcripts/ESTs, CpG islands, CAGE tags, H3K4me3 marks, and evolutionary conservation. Using TSSvote's predicted pri-miRNA TSSs, we defined the promoter sequences of miRNAs as the genomic region between -5kb and +1kb from the predicted TSS. We then identified ChiP-Seq peaks of TFs located within these predicted miRNA promoters. Only peaks that contained at least one sequence match to the TF's binding model were retained, so as to obtain high confidence TF target predictions. This analysis generated a high quality list of 1,183 mouse and 1,511 human TF-miRNA interactions (Supplementary Files 3 and 4).

Note, that the performance of TSSvote was tested by a compiled benchmark set of 21 experimentally determined human and mouse miRNA TSSs (Supplementary Table 2). TSSvote predicted 52% of these test TSSs within 500bp and 81% of them within 2500bp, outperforming all other currently available methods tested (as measured by the number of miRNA TSSs predicted within a given error range; Fig. 2B). The predictions of TSSvote were further supported by the fact that a large proportion of miRNAs (63% of intergenic and 45% of intragenic miRNAs in mouse) were located within 10kb from the pre-miRNA sequence (Fig. 2C, Supplementary Table 3). Furthermore, the miRNA promoter

sequences (as defined above) were more conserved than randomly selected intergenic sequences of the same length (Chi-square P-value=1.45E-51) (Fig. 2D) and contained significantly more TF binding sites than random sequences (Chi-square P-value=1.28E-34) (Fig. 2E).

Step 2: TF target prediction using genome-wide TFBS enrichment analysis

Although ChIP-Seq data of TFs allowed the extraction of experimentally characterized TF-target interactions, this information was only available for a subset of TFs. Moreover, because ChIP-Seq experiments might have been performed under different conditions, some transcriptional regulatory interactions critical to the CGCs under study might not be identified. To address this shortcoming our IntegraNet algorithm included computationally predicted genome-wide TF regulatory interactions based on an improved version of a previously developed statistical model for TF binding site (TFBS) enrichment (Chang et al. 2008). This approach calculated a binding probability score for a TF-gene pair using conserved TF binding sites in proximal promoters and evaluated a P-value using TFBS permutation (See Methods, Supplementary Fig. 1). In this study, the model was improved by using a phylogenetic tree-based scoring function to incorporate evolutionary conservation information from more species. Using this model, we predicted 108,204 mouse and 132,516 human TF-mRNA interactions (Supplementary Files 5 and 6). By applying this model to the miRNA promoters predicted by TSSvote (Supplementary Fig. 1) we also predicted a total of 2,658 mouse and 5,395 human TF-miRNA interactions (Supplementary Files 7 and 8).

We validated this computational model using the compendium of ChIP-Seq datasets for 78 TFs described earlier. In this validation, we tested if the target genes identified by ChIP-Seq tended to have significantly higher scores for binding among all the genes in the genome, based on a Mann-Whitney U-test (Fig. 3A). We found that ChIP-Seq identified mouse and human mRNA targets had significantly higher scores in 94% and 93% of the ChIP-Seq datasets, and ChIP-Seq identified mouse and human miRNA targets had significantly higher scores in 55% and 64% of the datasets (Fig. 3B). This analysis showed that our computational TF-target prediction was consistent with experimental results, for both TF-mRNA and TF-miRNA regulation.

Step 3: Identification of miRNA targets using computational prediction

The previous ChIP-Seq data analysis and genome-wide TF target prediction identified TF-mRNA and TF-miRNA interactions. To identify miRNA-mRNA interactions we performed computational miRNA target prediction. A recent study showed that better performance of miRNA target prediction may be achieved by combining multiple currently available algorithms in order to reach reasonable specificity while minimizing loss of sensitivity (Sethupathy et al. 2006). Therefore we chose to combine TargetscanS (Lewis et al. 2005) and pictar (Krek et al. 2005), which provides higher specificity, with miRanda (John et al. 2004), which provide higher sensitivity, to identify targets of miRNAs. Only targets of miRNAs predicted by at least two of these three methods were included in the network construction. Using this approach, we identified 57,980 mouse and 75,570 human miRNA-mRNA interactions (Supplementary Files 9 and 10). The average number of targets is 250 genes per miRNA, respectively,

which is close to the speculated number of targets per miRNA (Martinez and Walhout 2009).

Step 4: Expanding networks by adding master TF regulators of CGC and CMC genes

Up to this step, TFs included in the regulatory network were identified either by their correlation with expression profiles of interest or by their differential expression. However, master regulators of genes in the CGCs may share a coherent expression profile but with a lag time (hence not being identified by cluster analysis of expression data). Alternatively, they may be modulated by mechanisms other than transcriptional control and have similarly expression under two experimental conditions (hence not being identified by differential expression). These TFs could be identified by computational tools such as PAP (Chang et al. 2006), oPOSSUM (Ho Sui et al. 2007), and ToppGene (Chen et al. 2009), which predict common regulators of gene sets based on enriched TBFS in proximal promoters. To ensure that the final regulatory networks contain all important TFs, the IntegraNet algorithm incorporated the PAP algorithm.

Step 5: Expanding networks by adding master miRNA regulators of CGC genes

Similar to TFs, common miRNA regulators of genes in the CGCs may not have expression profiles that are tightly correlated/anti-correlated with their mRNA targets or may not have significant differential expression. Therefore, to ensure that the regulatory networks inferred by IntegraNet contain all critical miRNAs, we identified miRNAs whose predicted targets were enriched among CGC genes using a hypergeometric

distribution (see Methods). This target enrichment analysis may also identify miRNA regulators whose expression is not accurately measured on microarray.

Step 6: Identifying regulatory interactions for master TF and miRNA regulators

After additional TF and miRNA regulators found in Steps 4 and 5 were added to the network, additional TF-mRNA, TF-miRNA, and miRNA-mRNA interactions were characterized using ChIP-Seq data of TFs (Step 1) and computational predictions (Steps 2 and 3). This final step completed the regulatory network construction.

Application of IntegraNet to expand a previously identified miRNA regulatory network

To demonstrate the utility of IntegraNet, we first applied our approach to analyze a published dataset of mRNA and miRNA expression profiling data from Hepatitis C Virus (HCV) negative or positive human liver biopsy samples (Peng et al. 2009). The goal of this study was to identify miRNA regulatory networks that were associated with HCV infection. The authors found that 54 miRNAs were differentially expressed between HCV positive and negative samples. The study then constructed a miRNA-target regulatory network using computationally predicted miRNA-mRNA interactions. We expanded this network by applying IntegraNet to add TF-mRNA and TF-miRNA interactions.

Using the 54 differentially expressed miRNAs as the CMC, we found 773 genes whose expression was correlated or anti-correlated with CMC miRNAs (based on a cutoff of CC=0.65). These genes were defined as the CGC. These 773 genes contain 5

TFs with available ChIP-Seq data and 18 TFs with available binding profiles. Using enrichment of TFBS, we identified 14 additional TFs as master regulators of the CGC or CMC. Using enrichment of miRNA targets in the CGC, we added 5 miRNAs to the network (using a hypergeometric P-value cutoff of 0.01). Overall, we identified 32 TFs and 5 additional miRNAs as important regulators of the previously characterized miRNA regulatory network. We identified and predicted a total of 55 TF-TF and 45 TF-miRNA regulatory interactions (Supplementary Fig. 2, Supplementary Table 4). This analysis demonstrated that IntegraNet can be adopted to extract additional biological information using previously collected genomic profiling datasets.

Application of IntegraNet to identify TF and miRNA regulation networks involved in Schwann cell response to peripheral nerve injury

In the peripheral nervous system (PNS), Schwann cells (SCs) surrounding damaged axons undergo an injury response that is critical for nerve regeneration. This regenerative process relies on the unique ability of SCs to dedifferentiate/proliferate to support axonal re-growth and to subsequently re-differentiate to restore peripheral nerve function (Geuna et al. 2009). The cycling between the different SC differentiation states after injury are controlled by an intricate regulatory program that involves TFs and miRNAs (Jessen and Mirsky 2008; Bremer et al. 2010; Pereira et al. 2010; Yun et al. 2010), but the interactions between them are unknown. Therefore, we applied IntegraNet to study the TF and miRNA regulatory networks governing the SC injury response.

Identification of important TFs and miRNAs in the SC injury response network

To identify important regulators involved in SC response to injury, we first reanalyzed a published gene expression profiling dataset on a mouse nerve injury model (Nagarajan et al. 2002). Using unsupervised k-means clustering, we identified co-expressed gene clusters that were differentially expressed after nerve injury and that contained known myelination genes (see Methods). Four coexpressed core gene clusters for injury response (CGCIR) were identified (Supplementary Table 5). Two of the clusters included genes that were downregulated immediately after crush and returned to pre-injury levels as the nerve regenertated (CGCIRs 1 and 2), while the other two displayed the reciprocal expression pattern (CGCIRs 3 and 4) (Supplementary Fig. 3A). Gene Ontology analysis showed that CGCIRs 1 and 2 contain genes related to myelination and CGCIRs 3 and 4 were enriched for proliferation related genes (Supplementary Fig. 3B). In total, these CGCIRs contained 35 TFs.

Next, we identified core miRNA clusters for SC injury response (CMCIRs) by profiling nerve miRNA expression before and after crush injury (A Viader, L Chang, T Fahrner, R Nagarajan, J Milbrandt, in press). We focused on miRNAs whose expression was correlated or anti-correlated with one of the four CGCIRs. Overall, this analysis identified 30 miRNAs that were expressed similar to genes in CGCIRs 1 and 2 and identified 6 miRNAs that were expressed similar to genes in CGCIRs 3 and 4 (Supplementary Table 6, Supplementary Fig. 3C).

Applying IntegraNet, we first identified 37 TF-TF and 15 TF-miRNA regulatory interactions for 8 TFs from the compiled ChIP-Seq datasets (Step 1). We then used computational TF target predictions and expanded the network to include 79 TF-TF and

70 TF-miRNA interactions (Step 2). Using miRNA target prediction we next added 43 miRNA-TF interactions (Step 3). Furthermore, using the Promoter Analysis Pipeline (PAP) (Chang et al. 2006), we identified 12 and 1 TFBS significantly enriched in CGCIRs and CMCIRs, respectively (Step 4). We also identified 7 miRNAs with significantly enriched targets in CGCIRs (Step 5). Overall, the final TF and miRNA network for SC injury response included 146 TF-TF, 117 TF-miRNA, and 71 miRNA-TF interactions, connecting 48 TFs and 32 miRNAs (Fig. 4, Supplementary Table 7).

Regulatory network for SC injury response inferred by IntegraNet is consistent with current knowledge

The regulatory network constructed above provided a global view of TF and miRNA mediated gene regulation in SC injury response. When we organized the SC injury response regulatory network to show its cluster structures (using the "organic layout" in Cytoscape (Shannon et al. 2003)), one of the nodes in the center of the network was Egr2, the early growth response 2 (Egr2/Krox-20) transcription factor. Egr2 is required for peripheral nerve myelin formation and maintenance and it is often mutated in patients with peripheral myelinopathies (Svaren and Meijer 2008). Five TFs were predicted to regulate the expression of Egr2 (Fig. 5A), two of which (Nfkb1 and Fos) have been previously associated with SC myelination (Nickols et al. 2003) and dedifferentiation (Stevens and Fields 2000; Parkinson et al. 2008). In addition to TFs, two miRNAs, miR-140 and miR-124, were found to target Egr2. Additional experimental studies confirmed these interactions and showed that these two miRNAs contribute to the modulation of the expression of Egr2 (Supplementary Fig. 4, A Viader, L Chang, T

Fahrner, R Nagarajan, J Milbrandt, in press). Egr2 was in turn predicted to directly regulate the expression of the TF Hic1 and 3 miRNAs (let-7f, let-7a, and miR-22) (Fig. 5A). The tumor suppressor miR-22 has been shown to target the 3'UTR of Pten and modulate Akt signaling, which critically determines the extent of SC myelination (Ogata et al. 2004; Cotter et al. 2010). These results showed that our method to delineate the genetic networks driving the SC injury response elucidated Egr2 regulatory pathways that were consistent with current knowledge on the regulation of SC differentiation.

TF and miRNA feedforward loops in the SC injury response network

The importance of transcriptional and post-transcriptional control in the SC injury response as well as the reciprocal nature of the genetic programs driving this process make SC recovery after injury an ideal system for studying the cooperation of TF and miRNA mediated gene regulation. TFs and miRNAs form cooperative regulatory network motifs to reinforce (via coherent loops) or modulate (via incoherent loops) the expression of target genes (Tsang et al. 2007; Martinez and Walhout 2009; Shalgi et al. 2009). In the regulation of SC injury response, an incoherent or coherent feedforward loop may target genes that are correlated with the expression of differentiation/myelination genes (i.e., genes in CGCIRs 1 and 2) or with the expression of proliferation genes (i.e., genes in CGCIRs 3 and 4), with the participating miRNA acting as a reinforcer or modulator (Fig. 5B). Thus, to understand the coordinated regulation of TFs and miRNAs we examined the regulatory network inferred by IntegraNet for the presence of coherent and incoherent loops (Supplementary Table 8). When we categorized all the regulatory loops based on the target gene's expression and

the type of the feedforward loop, we found a significantly higher frequency of myelination genes in the incoherent loops than in the coherent loops (Fig. 5B, I1 as opposed to C1). In contrast, there was a significantly higher frequency of proliferation genes in the coherent loops than in the incoherent loops (Fig. 5B, C2 as opposed to I2). These results suggest that in SC injury response, regulation of myelination gene expression tends to be modulated or carefully controlled by miRNAs in incoherent feedforward loops, whereas regulation of proliferation gene expression tends to be reinforced by miRNAs in coherent feedforward loops. This analysis demonstrated that the gene regulatory networks inferred by IntegraNet may provide new insights on the cooperative gene regulation by TF and miRNA in complex biological systems.

Discussion

In this study, we developed the IntegraNet algorithm for TF and miRNA regulatory network inference that integrates expression profiling data of mRNAs and miRNAs, TF regulatory targets derived from ChIP-Seq data, and computational TF and miRNA target prediction. IntegraNet takes a step-wise, bottom-up approach that starts with clusters of dynamically regulated or differentially expressed genes or miRNAs as the basic network node set and sequentially adds TFs and miRNAs and their regulatory interactions to the network. We applied IntegraNet to reanalyze a published dataset of mRNA and miRNA expression profiling and expanded a previously identified miRNA regulatory network to include TF regulation. By applying IntegraNet to comprehensively delineate the gene regulatory network underlying the Schwann cell response to nerve injury, we showed that IntegraNet allows integrated inference of gene regulation by TFs

and miRNAs in complex biological settings. Our method was able to provide valuable new insights into fundamental aspects of the SC regenerative response, indicating its potential to help elucidate the complexities of biological processes governed by intricate networks of TFs and miRNAs.

Importantly, the design of IntegraNet took into account the confidence level of multiple types of gene regulation information. For example, experimentally identified transcriptional regulatory interactions derived from ChIP-Seq datasets were added before the regulatory interactions for correlated or anti-correlated regulators, which are followed by interactions for regulators with enriched binding sequences but without observed coordinated expression (Fig. 1). To further ensure the quality of the network construction, the computational predictions used in our method were tested and verified in several ways. The computational model for TF target prediction was previously validated using ChIP-chip data (Chang et al. 2006). This model was further validated in this study using a much larger set of ChIP-Seq experiment data for 70 TFs. When we applied IntegraNet to study the gene regulatory network involved in SC response to nerve injury, we compared the inferred subnetwork around Egr2, a well-known transcription regulator of myelination, to current knowledge of gene regulation in SC and found high consistency. Finally, the post-transcriptional regulation of Egr2 by two miRNAs, miR-124 and miR-140, identified in our network were validated experimentally using luciferase assays (Supplementary Fig. 4, A Viader, L Chang, T Fahrner, R Nagarajan, J Milbrandt, in press). These results suggest that our method produced an informative and reliable regulatory network for SC injury response.

An important step in our approach was to use available Chip-Seq data to derive mRNA and miRNA targets of TFs. While a significant number of transcription factor ChIP-Seq data has been accumulated, only few studies have combined these datasets and used this resource to study transcriptional regulation of mRNAs (Hannah et al. 2011), and no studies have co-analyzed these datasets to infer transcriptional regulation of miRNAs. This is partly due to the lack of reliable prediction of miRNA promoters. By developing a new miRNA TSS prediction algorithm, TSSvote, we were able to circumvent this problem. Our prediction algorithm incorporates several sequence features that imply TSS and our method does not rely on experimental data that probe promoter usage, which may be dependent on the experimental conditions. Testing our algorithm using experimentally validated miRNA TSS sites showed that the accuracy of our prediction was within 2500bp in 81% of the cases and the performance was better than current methods (Fig. 2B). These predicted miRNA TSS allowed for the identification of ChIP-Seq peaks that were located within miRNA promoters. The identified miRNA promoters also allowed for the computational prediction of TFs that regulate miRNAs (Supplementary Fig. 1). Our computational predictions are expected to be more accurate than previously reported methods (Shalgi et al. 2007; Guo et al. 2010) due to the more accurate miRNA promoter annotation and a more robust TF binding site analysis model.

A notable strength of our methods is that while it integrates multiple types of experimental and computational data, it is also modular in its design. Thus, individual components of the network inference pipeline may be improved or replaced separately, and additional information about TF or miRNA regulation may be added to the prediction model. For example, the computational prediction of TF targets may be further improved

by incorporating epigenetic information (Ramsey et al. 2010). Also, additional regulatory mechanisms, such as regulation by non-coding RNAs and by RNA binding proteins (Viswanathan et al. 2008), may be added into the network once experimental data or computational prediction become available for these interactions.

miRNAs and TFs tend to cooperate in coherent or incoherent feed-forward loops, in which miRNAs may function as either a reinforcer or a modulator, to control the expression of a target gene (Tsang et al. 2007; Martinez and Walhout 2009; Shalgi et al. 2009). In our analysis of network motifs in the SC injury response network, we found that genes involved in proliferation tend to be regulated by coherent loops, where their repression during SC injury response is reinforced by miRNAs. Genes involved in myelination, on the other hand, tend to be regulated by incoherent loops, where their activation during SC injury response is "fine-tuned" by miRNAs (Fig. 5B). This suggests that fast and precise timing of the activation/inactivation of genes associated with the immature state of SCs is most critical for the dedifferentiation of these glia after nerve injury. In contrast, proper remyelination seems not to require as carefully controlled timing of gene expression, but instead depend mostly on achieving precise functional levels of myelin-related proteins. This is particularly interesting because myelin formation and maintenance is very sensitive to gene dosage effects. In fact, both abnormally low or high levels of specific myelin proteins can cause peripheral neuropathy in humans (Meyer zu Horste et al. 2006).

To conclude, we present in this work a new algorithm, IntegraNet, for TF and miRNA regulatory network inference. Our approach systematically integrates multiple types of experimental data and computational prediction on gene regulation and thus

produces more reliable gene regulatory networks. Applying our approach to the SC injury response dataset demonstrates that our method may be used to gain new insight on the local and global features of gene regulation by TFs and miRNAs.

Methods

Analysis of ChIP-Seq datasets: Publicly available ChIP-Seq datasets for human and mouse transcription factors were compiled and collected from literature search. Peak locations identified in the original studies were used if they are available. When peak locations were not available, Partek Genomic Suite with default parameters was used to identify peaks using raw alignment data. All peak locations were converted to genomic coordinates of human genome build hg18 or mouse genome build mm9. Peak locations of human datasets were then mapped to the mouse genome using UCSC's liftover tool and vice versa. ChIP-Seq peaks that contained binding sites of a TF were identified using the position weight matrix models of TFs available in the TRANSFAC, JASPAR and UniPROBE databases (Newburger and Bulyk 2009). Peaks that were located near mRNAs or miRNAs were identified using NCBI's gene annotation for mRNAs and computationally predicted miRNA TSS (see below).

Computational prediction of miRNA TSS: To predict miRNA TSS, all human and mouse miRNAs were categorized as intergenic or intragenic miRNAs. Intragenic miRNAs were defined as miRNAs located between the start and end of a protein coding gene that is on the same strand (termed the host gene). miRNAs that are not intragenic were defined as intergenic. For intergenic miRNAs, the TSS search range was defined as

the genomic sequence between the end of the upstream gene and the start of the pre-miRNA. For intragenic miRNAs, the TSS search range was defined as the genomic sequence between the start of the host gene and the start of the pre-miRNA. To predict miRNA TSS, a new algorithm, TSSvote, was developed to score each 100bp window within the TSS search range based on transcription related sequence features. Mapping locations of known transcripts or ESTs and CpG islands were downloaded from the UCSC genome browser. CAGE tags were downloaded from the FANTOM project (Severin et al. 2009). H3K4me3 histon modification marks were collected from a compiled set of H3K4me3 ChIP-Seq studies (Barski et al. 2007; Mikkelsen et al. 2007; Pan et al. 2007; Zhao et al. 2007; Robertson et al. 2008; Araki et al. 2009; Wei et al. 2009; Cheung et al. 2010; Guenther et al. 2010). Conservation score was calculated as the number of aligned species in the 100bp sequence window divided by the number of species in which the pre-miRNA was conserved. Using these sequence features, TSSvote calculated the score of each sequence window by $score = 2\delta_{transcript/EST} + \delta_{CpG} + \delta_{CAGE} + \delta_{H3K4me3} + conservation$ where $\delta_{feature}$equals one if a given feature is located within the sequence window. Otherwise, $\delta_{feature}$equals zero. For each miRNA, the sequence window within the TSS search range that had the highest score was predicted as the miRNA TSS. When multiple sequence windows had the same score, the sequence window closest to the miRNA was assigned as the predicted TSS.

Computational prediction of TF regulatory targets: To predict TF regulatory targets, we applied a previously developed computational model of transcription factor binding site (TFBS) enrichment to the mouse genome (Chang et al. 2008). This approach

calculated a binding probability score for a TF-gene pair using all the TF binding sites in the proximal promoters of protein coding genes. In this study, we improved this model by including 10 mammalian species, whose genomes were completely sequenced with a good coverage (>6x). Using NCBI's mouse genome annotation (build 37.1), for each mouse gene the multiple alignments of genomic sequence (downloaded from the UCSC genome browser site) from -100kb of the TSS to the end of the gene itself were extracted. Within this range, the sequence between -10kb and +5kb of the TSS and the sequence regions that have a regulatory potential (RP) score (Kolbe et al. 2004) larger than 0.1 were identified and collected as the TFBS search space. To search for TFBS, a total of 867 vertebrate position weight matrix models (PWMs) of TFs were compiled from the TRANSFAC, JASPAR, and UniProbe (Newburger and Bulyk 2009) databases. Using these PWMs, putative TFBS were identified in the TFBS search space, and the evolutionary conservation of each site was determined using multiple sequence alignments.

The original PAP model only considered TFBS conserved in human, mouse and rat. Therefore, transcriptional regulation based on non-conserved sites was not accurately modeled, and the regulation of non-conserved genes was neglected. To overcome these limitations of the original model, we developed a phylogenetic tree-based scoring function to weight the contribution of each TFBS by the total tree branch length of all the species in which the TFBS is conserved. Thus, TFBS that are conserved in a distantly related species will gain a higher weight than those conserved in a closely related species.

Using this scoring model, for each TF-gene pair, the probability score for binding and the P-value were calculated based on all the identified TFBSs. Regulatory targets of

TFs were identified using a P-value cutoff of 0.005, which was determined by comparing the number of computationally predicted targets to the number of ChIP-Seq identified targets for available TFs. The same analysis was applied to identify TFs that regulate miRNAs using miRNA promoters, which were defined as the sequence between -5kb and +1kb of the miRNA TSS predicted by TSSvote.

Identification of master TF regulators CGC mRNAs or CMC miRNAs: Common TF regulators of coexpressed mRNAs were identified by the previously developed Promoter Analysis Pipeline tool (Chang et al. 2006), which searches for the enriched TF binding sites in the promoter sequences of coexpressed mRNAs or miRNAs. Briefly, an R-score was calculated for each gene in the mouse genome based on the ranking of the probability score for binding. Genes that are more likely to be regulated by a TF will have a higher R-score for that TF. For a set of coexpressed genes, the average of the R-scores of the member genes were calculated for each TF. The P-value for a given R-score was then calculated by using randomly selected gene clusters of the same size. A Bonferroni corrected P-value cutoff of 0.05 was used to identify TFs that had significantly higher average R-scores as common regulators. The same analysis was applied to identify common TF regulators of coexpressed miRNAs based on miRNA R-scores, which were calculated using the probability score for binding for miRNAs.

Identification of master miRNA regulators of CGC mRNAs: Common miRNA regulators of coexpressed mRNA genes were identified by the enrichment of miRNA targets in the coexpresed genes. The hypergeometric P-value for enrichment was

calculated for a miRNA using the total number of nerve expressed genes that were predicted as targets of any miRNA (population size), the number of coexpressed mRNA genes (sample size), the number of nerve expressed genes that were predicted as targets of the miRNA (number of successes in population), and the number of coexpressed genes that were predicted as targets of the miRNA (number of successes in sample). Common miRNA regulators were identified using a hypergeometric P-value cutoff of 0.05.

Analysis of the mRNA and miRNA expression profiling data in HCV infection: Raw data of mRNA and miRNA expression profiling data were downloaded from GEO (GSE15387). For miRNA microarray data, the total gene signal was used. The expression data was normalized across arrays using median centered approach and log2-transformed, as described in the original study (Peng et al. 2009). For mRNA microarray data, log-transformed signal ratios from replicates of the same sample were averaged and used as the expression level of the sample. Processed expression data were used to calculate the correlation coefficients between the expression profiles of mRNAs and miRNAs.

Identification of core gene clusters for SC injury response (CGCIRs): SC mRNA expression profiling before and after crush and transection injury were performed using Affymetrix MU74Av2 chips in a previous study (Nagarajan et al., 2002). Gene expression levels were measured for uninjured nerves, on days 4, 7 and 10 after crush injury, and on days 1, 4, 7, and 10 after transection injury. Mouse gene expression profiling data during SC development were collected from an independent study (Verheijen et al. 2003). This dataset profiled mRNA expression on days 0, 2, 4, and 10

after birth. Expression data were processed and normalized using Affymetrix MAS5 algorithm. k-means clustering was used to cluster genes based on the combined expression profiles of injury response and development. Gene clusters that contained known myelin genes and that were differentially expressed before and after crush injury based on a t-test were identified. Clusters with similar expression profiles based on the Pearson correlation coefficient were identified and merged. The average expression profile, i.e. the centroid, was calculated for each cluster. Nerve-expressed genes that were correlated with the centroids based on a Pearson correlation coefficient cutoff of 0.8 were identified as the final CGCIRs.

Identification of core miRNA clusters for SC injury response (CMCIRs): SC miRNA expression profiling before and after crush injury were performed using HTG Molecular qNPA miRNA microarrays in a previous study (A Viader, L Chang, T Fahrner, R Nagarajan, J Milbrandt, unpublished). Expression of 1046 miRNAs was profiled using this microarray platform on days 0, 4 and 14 after crush injury. miRNA expression data were filtered using the following criteria: miRNAs that had an expression level lower than the average expression of the control miRNA probesets were removed from further analysis. miRNAs for which the expression of one duplicate probeset at all time points were significantly higher than that of the other duplicate probeset based on a Mann-Whitney U test were also removed from further analysis. After this filtering procedure, the average expression of the two duplicate probesets at each time point was used as the expression at that time point. miRNAs that were correlated or anti-correlated with the

expression of one of the four CGCIRs were identified as CMCIRs using crush injury mRNA expression data on days 0, 4, and 10.

Experimental validation: Plasmids: pre-mir-124 was obtained through PCR amplification from genomic DNA. The resulting fragment was cloned between the BamHI and Nhe I sites in the miRNASelect pEP-MIR Cloning and Expression Vector (Cell Biolabs) using the InFusion HD cloning system (Clonetech) according to the manufacurer's recommendations. Pre-mir-124 included the miRNA stem loop and ~100 nt of flanking sequence on either side. For luciferase assays, the 3'UTR region of *Egr2* was PCR amplified from genomic DNA using the following primers: *Egr2* 3'UTR: F, AAAGCT GCGCACTAGTGATGAAGCTCTGGCTGACACACCA; R, ATCCTTTATTAAGCTTACCA TAGTCAATAAGCCATCCAT. DNA fragments were cloned downstream of the luciferase gene between the HindIII and SpeI sites in the pMIR-REPORT miRNA Expression Reporter Vector (Ambion). The 3'UTR of *Egr2* lacking the miR-124 pad was cloned in an analogous manner. pRL-CMV Renilla Luciferase Reporter vector (promega) was used as a transfection control.

Luciferase assays: HEK293T cells were seeded at a density of 50,000 cells/well in 24 well plates in DMEM media (Invitrogen) supplemented with 10% fetal bovine serum (FBS), 2 mM L-glutamine. Cell were transfected 24 h later, with either a pEP-MIR vector expressing a pre-miRNA or with the pEP-mir Null control and with the pMIR-REPORT luciferase reporter vector containing the appropriate 3'UTR linked to luciferase. pRL-CMV Renilla Luciferase Reporter vector (Promega) was used as a transfection control. A total of 200 ng of plasmid DNA/well were transfected at a ratio of 50:1:0.5 (miRNA :

luciferase reporter : transfection Ctrl). Cells were harvested 48 h post-transfection and assayed using a Dual-Luciferase Reporter Assay System (Promega) according to the manufacturer's protocol.

Acknowledgements

We thank the Center for Biomedical Informatics (CBMI), which provided the in silico analysis service. The CBMI is partially supported by NCI Cancer Center Support Grant P30 CA91842 to the Alvin J. Siteman Cancer Center and by ICTS/CTSA Grant UL1RR024992 from the National Center for Research Resources (NCRR), a component of the National Institutes of Health (NIH), and NIH Roadmap for Medical Research. This work is also supported by NIH Neuroscience Blueprint Center Core Grant P30NS057105 to Washington University, the HOPE Center for Neurological Disorders, National Institutes of Health Grants NS040745 (JM), AG13730 (JM). LC is supported by an NIH Pathway to Independence Award K99LM010824.

References

Araki Y, Wang Z, Zang C, Wood WH, 3rd, Schones D, Cui K, Roh TY, Lhotsky B, Wersto RP, Peng W, et al. 2009. Genome-wide analysis of histone methylation reveals chromatin state-based regulation of gene transcription and function of memory CD8+ T cells. *Immunity* **30**(6): 912-925.

Bandyopadhyay S, Bhattacharyya M. 2009. Analyzing miRNA co-expression networks to explore TF-miRNA regulation. *BMC Bioinformatics* **10**: 163.

Barski A, Cuddapah S, Cui K, Roh TY, Schones DE, Wang Z, Wei G, Chepelev I, Zhao K. 2007. High-resolution profiling of histone methylations in the human genome. *Cell* **129**(4): 823-837.

Bremer J, O'Connor T, Tiberi C, Rehrauer H, Weis J, Aguzzi A. 2010. Ablation of Dicer from murine Schwann cells increases their proliferation while blocking myelination. *PLoS One* **5**(8): e12450.

Chang LW, Nagarajan R, Magee JA, Milbrandt J, Stormo GD. 2006. A systematic model to predict transcriptional regulatory mechanisms based on overrepresentation of transcription factor binding profiles. *Genome Res* **16**(3): 405-413.

Chang LW, Payton JE, Yuan W, Ley TJ, Nagarajan R, Stormo GD. 2008. Computational identification of the normal and perturbed genetic networks involved in myeloid differentiation and acute promyelocytic leukemia. *Genome Biol* **9**(2): R38.

Chen J, Bardes EE, Aronow BJ, Jegga AG. 2009. ToppGene Suite for gene list enrichment analysis and candidate gene prioritization. *Nucleic Acids Res* **37**(Web Server issue): W305-311.

Cheung I, Shulha HP, Jiang Y, Matevossian A, Wang J, Weng Z, Akbarian S. 2010. Developmental regulation and individual differences of neuronal H3K4me3 epigenomes in the prefrontal cortex. *Proc Natl Acad Sci U S A* **107**(19): 8824-8829.

Corcoran DL, Pandit KV, Gordon B, Bhattacharjee A, Kaminski N, Benos PV. 2009. Features of mammalian microRNA promoters emerge from polymerase II chromatin immunoprecipitation data. *PLoS One* **4**(4): e5279.

Cotter L, Ozcelik M, Jacob C, Pereira JA, Locher V, Baumann R, Relvas JB, Suter U, Tricaud N. 2010. Dlg1-PTEN interaction regulates myelin thickness to prevent damaging peripheral nerve overmyelination. *Science* **328**(5984): 1415-1418.

Geuna S, Raimondo S, Ronchi G, Di Scipio F, Tos P, Czaja K, Fornaro M. 2009. Chapter 3: Histology of the peripheral nerve and changes occurring during nerve regeneration. *Int Rev Neurobiol* **87**: 27-46.

Guenther MG, Frampton GM, Soldner F, Hockemeyer D, Mitalipova M, Jaenisch R, Young RA. 2010. Chromatin structure and gene expression programs of human embryonic and induced pluripotent stem cells. *Cell Stem Cell* **7**(2): 249-257.

Guo AY, Sun J, Jia P, Zhao Z. 2010. A novel microRNA and transcription factor mediated regulatory network in schizophrenia. *BMC Syst Biol* **4**: 10.

Hannah R, Joshi A, Wilson NK, Kinston S, Gottgens B. 2011. A compendium of genome-wide hematopoietic transcription factor maps supports the identification of gene regulatory control mechanisms. *Exp Hematol* **39**(5): 531-541.

Ho Sui SJ, Fulton DL, Arenillas DJ, Kwon AT, Wasserman WW. 2007. oPOSSUM: integrated tools for analysis of regulatory motif over-representation. *Nucleic Acids Res* **35**(Web Server issue): W245-252.

Jessen KR, Mirsky R. 2008. Negative regulation of myelination: relevance for development, injury, and demyelinating disease. *Glia* **56**(14): 1552-1565.

John B, Enright AJ, Aravin A, Tuschl T, Sander C, Marks DS. 2004. Human MicroRNA targets. *PLoS Biol* **2**(11): e363.

Joung JG, Hwang KB, Nam JW, Kim SJ, Zhang BT. 2007. Discovery of microRNA-mRNA modules via population-based probabilistic learning. *Bioinformatics* **23**(9): 1141-1147.

Kolbe D, Taylor J, Elnitski L, Eswara P, Li J, Miller W, Hardison R, Chiaromonte F. 2004. Regulatory potential scores from genome-wide three-way alignments of human, mouse, and rat. *Genome Res* **14**(4): 700-707.

Krek A, Grun D, Poy MN, Wolf R, Rosenberg L, Epstein EJ, MacMenamin P, da Piedade I, Gunsalus KC, Stoffel M, et al. 2005. Combinatorial microRNA target predictions. *Nat Genet* **37**(5): 495-500.

Lewis BP, Burge CB, Bartel DP. 2005. Conserved seed pairing, often flanked by adenosines, indicates that thousands of human genes are microRNA targets. *Cell* **120**(1): 15-20.

Lionetti M, Biasiolo M, Agnelli L, Todoerti K, Mosca L, Fabris S, Sales G, Deliliers GL, Bicciato S, Lombardi L, et al. 2009. Identification of microRNA expression patterns and definition of a microRNA/mRNA regulatory network in distinct molecular groups of multiple myeloma. *Blood* **114**(25): e20-26.

Marson A, Levine SS, Cole MF, Frampton GM, Brambrink T, Johnstone S, Guenther MG, Johnston WK, Wernig M, Newman J, et al. 2008. Connecting microRNA genes to

the core transcriptional regulatory circuitry of embryonic stem cells. *Cell* **134**(3): 521-533.

Martinez NJ, Walhout AJ. 2009. The interplay between transcription factors and microRNAs in genome-scale regulatory networks. *Bioessays* **31**(4): 435-445.

Meyer zu Horste G, Prukop T, Nave KA, Sereda MW. 2006. Myelin disorders: Causes and perspectives of Charcot-Marie-Tooth neuropathy. *J Mol Neurosci* **28**(1): 77-88.

Mikkelsen TS, Ku M, Jaffe DB, Issac B, Lieberman E, Giannoukos G, Alvarez P, Brockman W, Kim TK, Koche RP, et al. 2007. Genome-wide maps of chromatin state in pluripotent and lineage-committed cells. *Nature* **448**(7153): 553-560.

Nagarajan R, Le N, Mahoney H, Araki T, Milbrandt J. 2002. Deciphering peripheral nerve myelination by using Schwann cell expression profiling. *Proc Natl Acad Sci U S A* **99**(13): 8998-9003.

Newburger DE, Bulyk ML. 2009. UniPROBE: an online database of protein binding microarray data on protein-DNA interactions. *Nucleic Acids Res* **37**(Database issue): D77-82.

Nickols JC, Valentine W, Kanwal S, Carter BD. 2003. Activation of the transcription factor NF-kappaB in Schwann cells is required for peripheral myelin formation. *Nat Neurosci* **6**(2): 161-167.

Ogata T, Iijima S, Hoshikawa S, Miura T, Yamamoto S, Oda H, Nakamura K, Tanaka S. 2004. Opposing extracellular signal-regulated kinase and Akt pathways control Schwann cell myelination. *J Neurosci* **24**(30): 6724-6732.

Ozsolak F, Poling LL, Wang Z, Liu H, Liu XS, Roeder RG, Zhang X, Song JS, Fisher DE. 2008. Chromatin structure analyses identify miRNA promoters. *Genes Dev* **22**(22): 3172-3183.

Pan G, Tian S, Nie J, Yang C, Ruotti V, Wei H, Jonsdottir GA, Stewart R, Thomson JA. 2007. Whole-genome analysis of histone H3 lysine 4 and lysine 27 methylation in human embryonic stem cells. *Cell Stem Cell* **1**(3): 299-312.

Parkinson DB, Bhaskaran A, Arthur-Farraj P, Noon LA, Woodhoo A, Lloyd AC, Feltri ML, Wrabetz L, Behrens A, Mirsky R, et al. 2008. c-Jun is a negative regulator of myelination. *J Cell Biol* **181**(4): 625-637.

Peng X, Li Y, Walters KA, Rosenzweig ER, Lederer SL, Aicher LD, Proll S, Katze MG. 2009. Computational identification of hepatitis C virus associated microRNA-mRNA regulatory modules in human livers. *BMC Genomics* **10**: 373.

Pereira JA, Baumann R, Norrmen C, Somandin C, Miehe M, Jacob C, Luhmann T, Hall-Bozic H, Mantei N, Meijer D, et al. 2010. Dicer in Schwann cells is required for myelination and axonal integrity. *J Neurosci* **30**(19): 6763-6775.

Ramsey SA, Knijnenburg TA, Kennedy KA, Zak DE, Gilchrist M, Gold ES, Johnson CD, Lampano AE, Litvak V, Navarro G, et al. 2010. Genome-wide histone acetylation

data improve prediction of mammalian transcription factor binding sites. *Bioinformatics* **26**(17): 2071-2075.

Robertson AG, Bilenky M, Tam A, Zhao Y, Zeng T, Thiessen N, Cezard T, Fejes AP, Wederell ED, Cullum R, et al. 2008. Genome-wide relationship between histone H3 lysine 4 mono- and tri-methylation and transcription factor binding. *Genome Res* **18**(12): 1906-1917.

Saini HK, Enright AJ, Griffiths-Jones S. 2008. Annotation of mammalian primary microRNAs. *BMC Genomics* **9**: 564.

Sethupathy P, Megraw M, Hatzigeorgiou AG. 2006. A guide through present computational approaches for the identification of mammalian microRNA targets. *Nat Methods* **3**(11): 881-886.

Severin J, Waterhouse AM, Kawaji H, Lassmann T, van Nimwegen E, Balwierz PJ, de Hoon MJ, Hume DA, Carninci P, Hayashizaki Y, et al. 2009. FANTOM4 EdgeExpressDB: an integrated database of promoters, genes, microRNAs, expression dynamics and regulatory interactions. *Genome Biol* **10**(4): R39.

Shalgi R, Brosh R, Oren M, Pilpel Y, Rotter V. 2009. Coupling transcriptional and post-transcriptional miRNA regulation in the control of cell fate. *Aging (Albany NY)* **1**(9): 762-770.

Shalgi R, Lieber D, Oren M, Pilpel Y. 2007. Global and local architecture of the mammalian microRNA-transcription factor regulatory network. *PLoS Comput Biol* **3**(7): e131.

Shannon P, Markiel A, Ozier O, Baliga NS, Wang JT, Ramage D, Amin N, Schwikowski B, Ideker T. 2003. Cytoscape: a software environment for integrated models of biomolecular interaction networks. *Genome Res* **13**(11): 2498-2504.

Stevens B, Fields RD. 2000. Response of Schwann cells to action potentials in development. *Science* **287**(5461): 2267-2271.

Svaren J, Meijer D. 2008. The molecular machinery of myelin gene transcription in Schwann cells. *Glia* **56**(14): 1541-1551.

Tenen DG. 2003. Disruption of differentiation in human cancer: AML shows the way. *Nat Rev Cancer* **3**(2): 89-101.

Tsang J, Zhu J, van Oudenaarden A. 2007. MicroRNA-mediated feedback and feedforward loops are recurrent network motifs in mammals. *Mol Cell* **26**(5): 753-767.

Verheijen MH, Chrast R, Burrola P, Lemke G. 2003. Local regulation of fat metabolism in peripheral nerves. *Genes Dev* **17**(19): 2450-2464.

Villard J. 2004. Transcription regulation and human diseases. *Swiss Med Wkly* **134**(39-40): 571-579.

Viswanathan SR, Daley GQ, Gregory RI. 2008. Selective blockade of microRNA processing by Lin28. *Science* **320**(5872): 97-100.

Wang L, Tang H, Thayanithy V, Subramanian S, Oberg AL, Cunningham JM, Cerhan JR, Steer CJ, Thibodeau SN. 2009. Gene networks and microRNAs implicated in aggressive prostate cancer. *Cancer Res* **69**(24): 9490-9497.

Wei G, Wei L, Zhu J, Zang C, Hu-Li J, Yao Z, Cui K, Kanno Y, Roh TY, Watford WT, et al. 2009. Global mapping of H3K4me3 and H3K27me3 reveals specificity and plasticity in lineage fate determination of differentiating CD4+ T cells. *Immunity* **30**(1): 155-167.

Yun B, Anderegg A, Menichella D, Wrabetz L, Feltri ML, Awatramani R. 2010. MicroRNA-deficient Schwann cells display congenital hypomyelination. *J Neurosci* **30**(22): 7722-7728.

Zeng C, Wang R, Li D, Lin XJ, Wei QK, Yuan Y, Wang Q, Chen W, Zhuang SM. 2010. A novel GSK-3 beta-C/EBP alpha-miR-122-insulin-like growth factor 1 receptor regulatory circuitry in human hepatocellular carcinoma. *Hepatology* **52**(5): 1702-1712.

Zhao XD, Han X, Chew JL, Liu J, Chiu KP, Choo A, Orlov YL, Sung WK, Shahab A, Kuznetsov VA, et al. 2007. Whole-genome mapping of histone H3 Lys4 and 27 trimethylations reveals distinct genomic compartments in human embryonic stem cells. *Cell Stem Cell* **1**(3): 286-298.

Figures

Figure 1. The IntegraNet algorithm for gene regulatory network construction. Starting with TFs and miRNAs that are correlated with particular expression profiles or differentially expressed between two conditions, IntegraNet takes sequential steps in this workflow to integrate multiple types of experimental and computational information. In each step, nodes and interactions identified from earlier steps are placed in the background. Circles: TFs. Hexagons: miRNAs. Blue or red nodes: TFs or miRNAs that are identified by expression analysis. Grey nodes: master TF or miRNA regulators identified by enrichment of binding sites or targets.

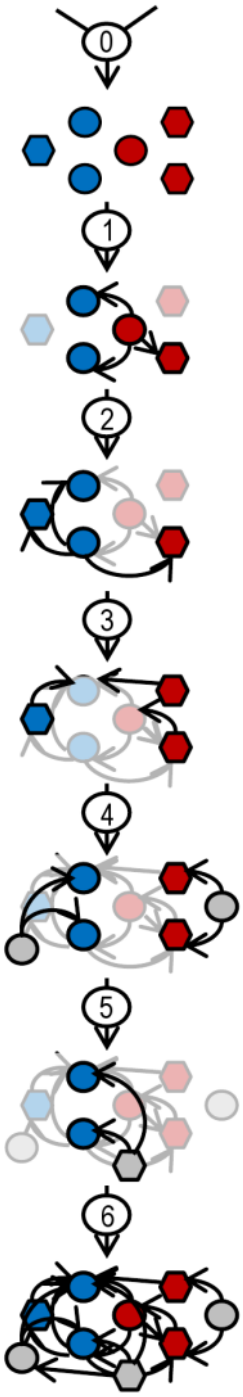

Step 0: Identify core gene clusters (CGCs) and core miRNA clusters (CMCs) that are coherently expressed or differentially expressed

Step 1: Identify TF-mRNA and TF-miRNA interactions using ChIP-Seq data

Step 2: Identify additional TF-mRNA and TF-miRNA interactions using computational TF target prediction

Step 3: Identify miRNA regulatory targets using computational prediction

Step 4: Expand network by adding master TF regulators of CGC mRNAs or CMC miRNAs

Step 5: Expand network by adding master miRNA regulators of CGC mRNAs

Step 6: Identify regulatory interactions for nodes added in Steps 4 and 5

Figure 2. A **new computational method, TSSvote, predicts the TSS of miRNAs reliably**. *(A)* Illustration of the TSSvote algorithm. For intergenic miRNAs (top sequence bar), the TSS search range is defined as the genomic sequence between the end of the upstream gene and the start of the pre-miRNA. For intragenic miRNAs (bottom sequence bar), the TSS search range is between the TSS of the host gene and the start of the pre-miRNA. TSSvote calculates a score for each 100bp sequence window within the TSS search range based on five supporting sequence features of TSS. The sequence window that is "voted" by the most features is predicted as the miRNA TSS. *(B)* Benchmarking computational methods for miRNA TSS prediction using a set of 21 experimentally validated miRNA TSS. For each method, the percentage of test cases where the distance between the predicted TSS and the true TSS is with a given distance is plotted. *(C)* The distribution of the distance between the predicted miRNA TSS and the pre-miRNA. *(D)* The distribution of the percentage of sequence conservation in predicted miRNA promoters versus random sequences. *(E)* The distribution of the number of TF binding sites found in predicted miRNA promoters versus random sequences. In *(C)*, *(D)*, and *(E)*, mouse data were used, while using human data produced similar results.

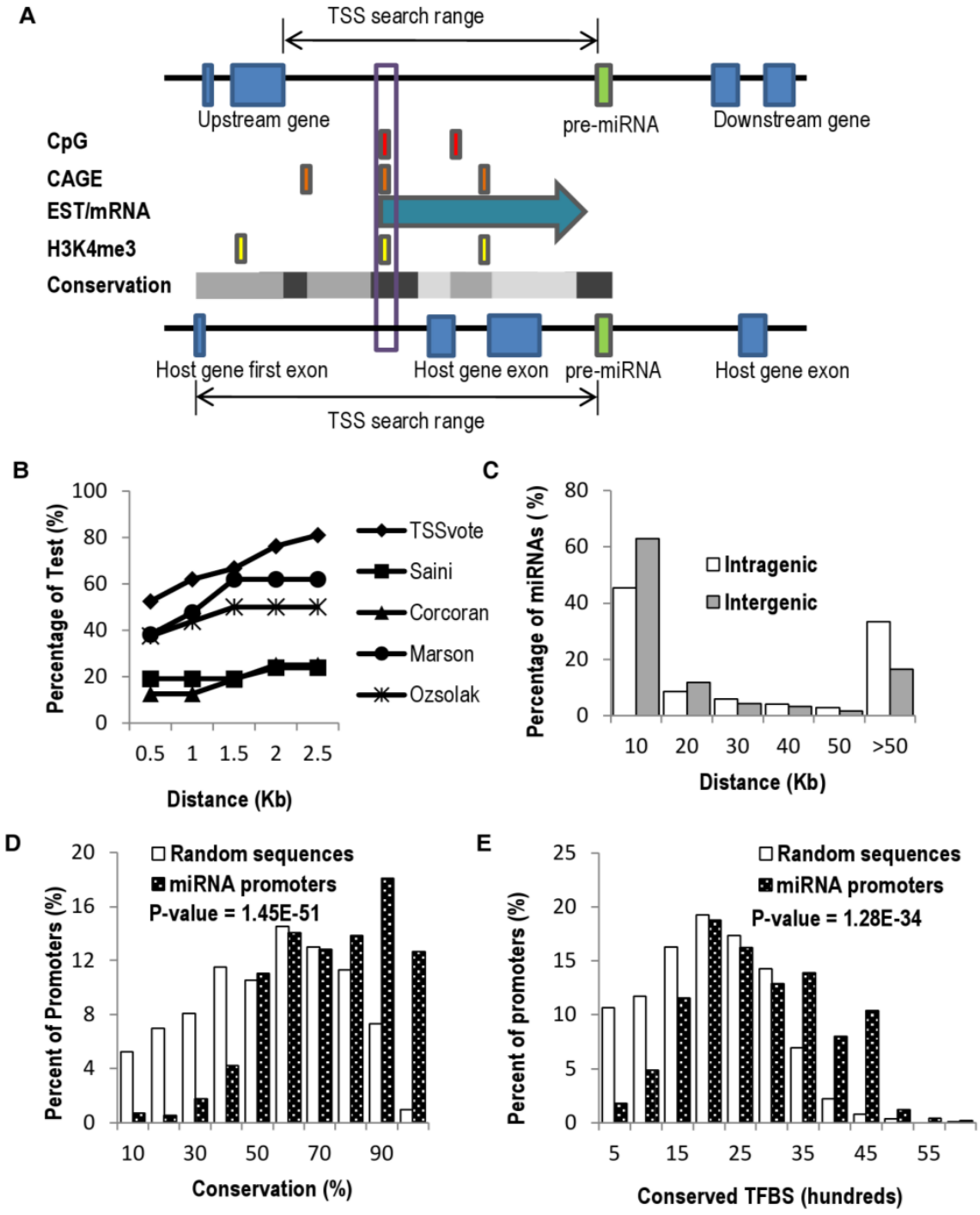
A
TSS search range
Upstream gene
pre-miRNA
Downstream gene
CpG
CAGE
EST/mRNA
H3K4me3
Conservation
Host gene first exon
Host gene exon
pre-miRNA
Host gene exon
TSS search range
B
Percentage of Test (%)
Distance (Kb)
TSSvote
Saini
Corcoran
Marson
Ozsolak
C
Percentage of miRNAs (%)
Intragenic
Intergenic
Distance (Kb)
D
Percent of Promoters (%)
Random sequences
miRNA promoters
P-value = 1.45E-51
Conservation (%)
E
Percent of promoters (%)
Random sequences
miRNA promoters
P-value = 1.28E-34
Conserved TFBS (hundreds)

Figure 3. Validating computational TF target prediction using the compendium of TF ChIP-Seq datasets. *(A)* ChIP-Seq identified TF binding locations (peaks) near annotated mRNA transcription start sites (TSS) or predicted miRNA TSS were identified. Peaks that also contained TF binding sites (TFBS) based on known TF binding profiles were used to identify regulatory targets of TFs. Mann-Whitney U test was used to test if identified targets have higher binding scores calculated by the computational model. *(B)* Percent of ChIP-Seq datasets that were consistent with computational TF target prediction when tested using mouse or human mRNAs or miRNAs.

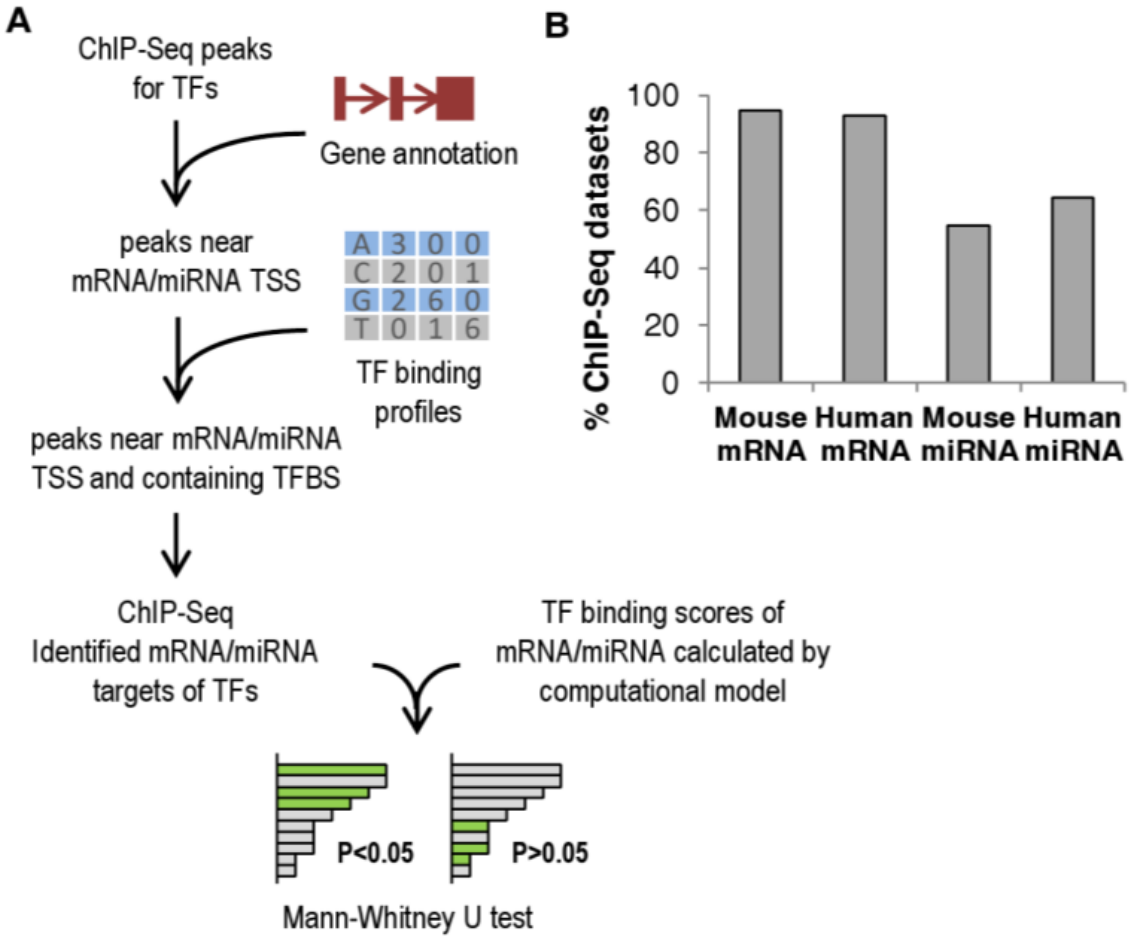
A
ChIP-Seq peaks for TFs
Gene annotation
peaks near mRNA/miRNA TSS
A 3 0 0
C 2 0 1
G 2 6 0
T 0 1 6
TF binding profiles
peaks near mRNA/miRNA TSS and containing TFBS
ChIP-Seq Identified mRNA/miRNA targets of TFs
TF binding scores of mRNA/miRNA calculated by computational model
P<0.05
P>0.05
Mann-Whitney U test
B
% ChIP-Seq datasets
100
80
60
40
20
0
Mouse mRNA
Human mRNA
Mouse miRNA
Human miRNA

Figure 4. The SC injury response regulatory network inferred by integrating experimental data and computational prediction. Circles: TFs. Hexagons: miRNAs. Blue nodes: TFs or miRNAs correlated with myelination gene clusters. Red nodes: TFs or miRNAs correlated with proliferation gene clusters. Grey nodes: master TF or miRNA regulators of coexpressed genes. Black edges: regulatory interactions derived from TF ChIP-Seq data. Grey edges: regulatory interactions inferred by computational prediction. Arrowed edges: activation by TFs. T-shaped edges: repression by TFs or miRNAs.

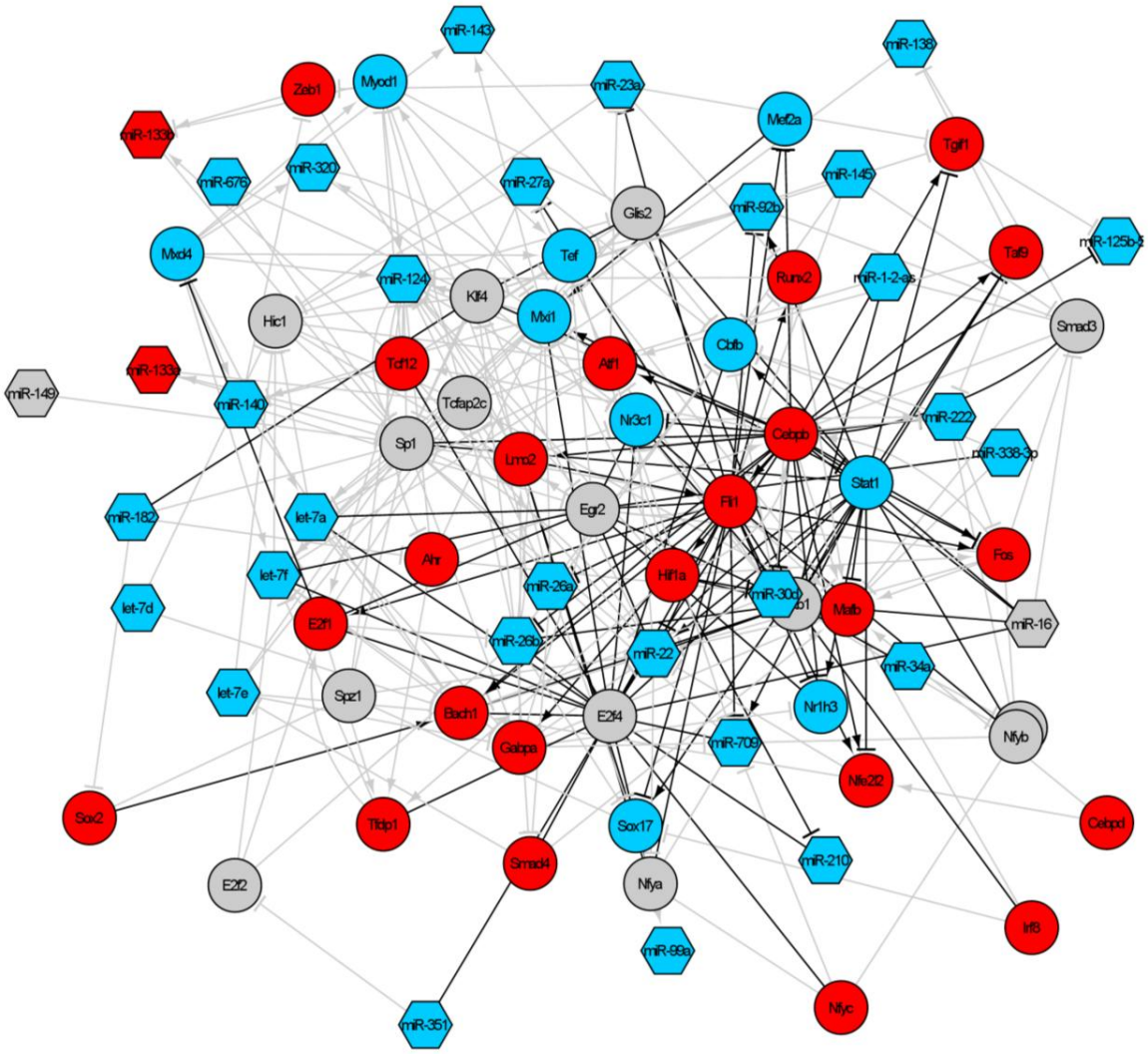
miR-143
miR-138
Zeb1
Myod1
miR-23a
Mef2a
miR-133b
Tgif1
miR-675
miR-320
miR-27a
miR-145
Gli3
miR-92b
Mxd4
Tef
Runx2
Taf9
miR-125b-5
miR-124
miR-1-2-as
Klf4
Mxi1
Hic1
Smad3
Cbfb
miR-133a
Tcf12
Atf1
miR-149
miR-140
Tcfap2c
Nr3c1
miR-222
Cebpb
Sp1
Lmo2
miR-338-3p
Stat1
Fli1
miR-182
Egr2
let-7a
Fos
Ahr
let-7f
Hif1a
miR-26a
miR-30d
Mafb
let-7d
E2f1
miR-16
miR-26b
miR-22
miR-34a
let-7e
Spz1
Nr1h3
Bach1
E2f4
Nfyb
Gabpa
miR-709
Nfe2l2
Sox2
Tfdp1
Sox17
Cebpd
Smad4
miR-210
E2f2
Nfya
Irf3
miR-99a
Nfyc
miR-351

Figure 5. Local and global analysis of the SC injury response regulatory network. *(A)* Upstream regulators and downstream targets of Egr2 and regulatory interactions among them. *(B)* Biased usage of incoherent and coherent feedforward loops in the SC injury response network. Feedforward loops are divided into four categories according to the expression pattern of its target gene: I1: an incoherent loop regulating myelination genes, I2: an incoherent loop regulating proliferation genes, C1: a coherent loop regulating myelination genes, and C2: a coherent loop regulating proliferation genes. For each category, the number of network motifs in the SC injury response network and the number of TFs, miRNAs, and targets that participate in those motifs are shown, with more prevalent network motifs highlighted in grey. Circles: TFs. Hexagons: miRNAs. Rectangles: target mRNAs. Blue nodes: TFs or miRNAs correlated with myelination gene clusters. Red nodes: TFs or miRNAs correlated with proliferation gene clusters. Grey nodes: master TF or miRNA regulators. White boxes: downstream target genes not included in the network. Arrowed edges: activation by TFs. T-shaped edges: repression by TFs or miRNAs.

A

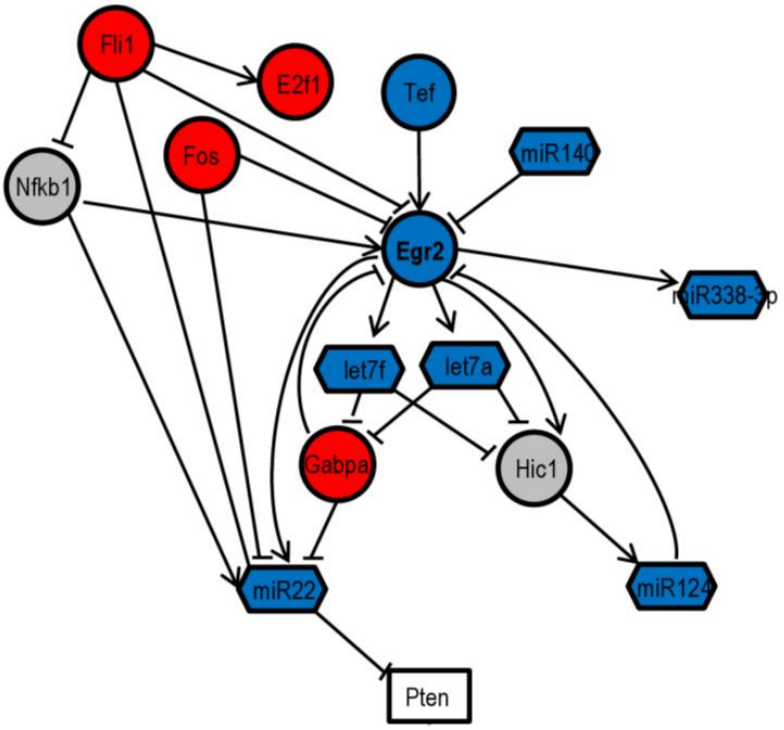

B

	Incoherent Feedforward Loop	Coherent Feedforward Loop
Targeting Myelination Genes (T)	I1 Motif 45 TF 16 miRNA 9 Target 25	C1 Motif 3 TF 2 miRNA 1 Target 3
Targeting Proliferation Genes (T)	I2 Motif 2 TF 2 miRNA 2 Target 1	C2 Motif 115 TF 21 miRNA 17 Target 25

Supplementary Figure 1. Workflow of the computational method for predicting TFs that regulate mRNAs, using NCBI's TSS annotation, or miRNAs, using computational TSS prediction.

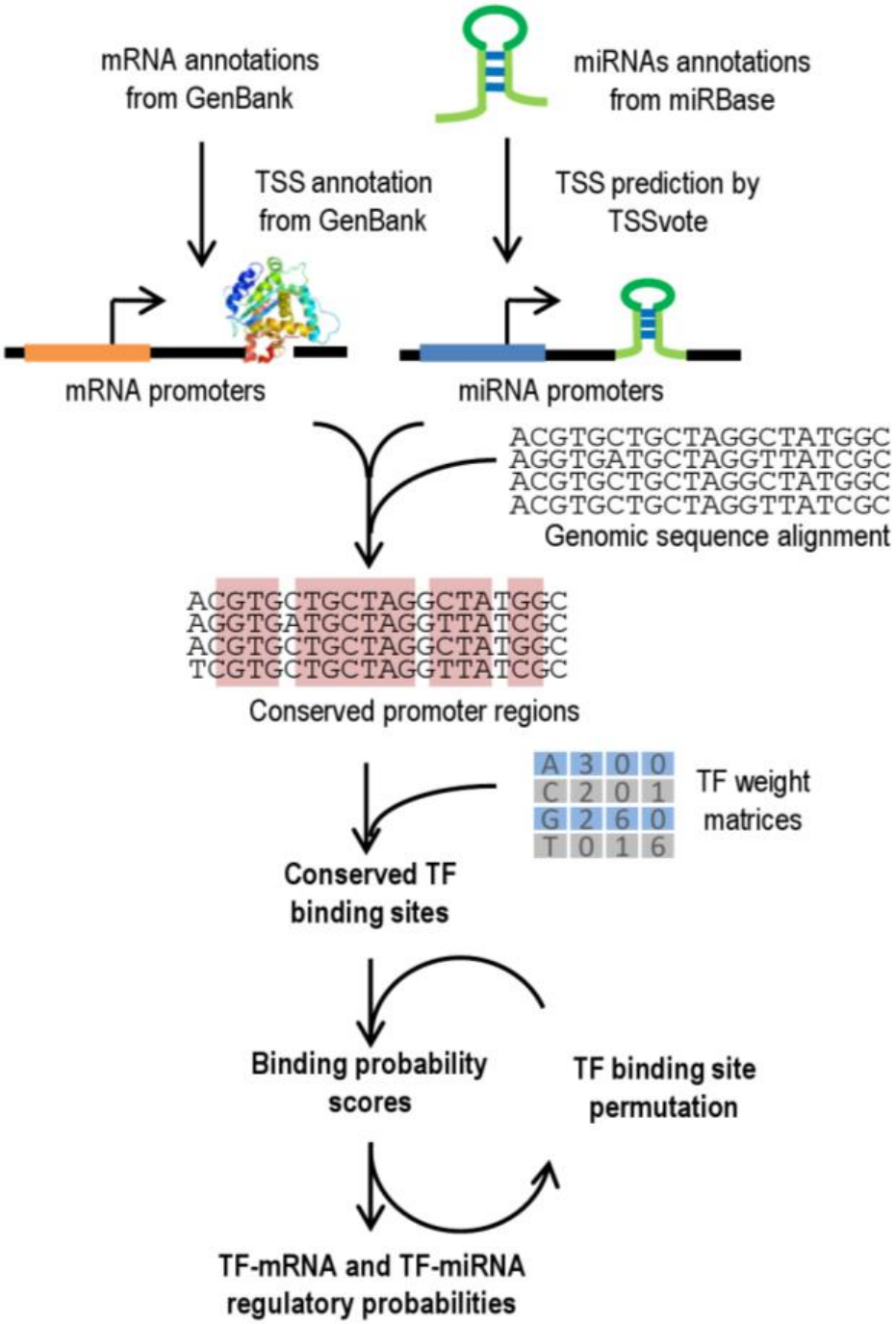

Supplementary Figure 2. The hepatitis C virus (HCV) associated gene regulatory network. Circles: TFs. Hexagons: miRNAs. Blue nodes: TFs or miRNAs over-expressed in HCV-positive samples. Red nodes: TFs or miRNAs over-expressed in HCV-negative samples. Grey nodes: master TF or miRNA regulators of differentially expressed genes. Black edges: regulatory interactions derived from TF ChIP-Seq data. Grey edges: regulatory interactions inferred by computational prediction. Arrowed edges: activation by TFs. T-shaped edges: repression by TFs or miRNAs.

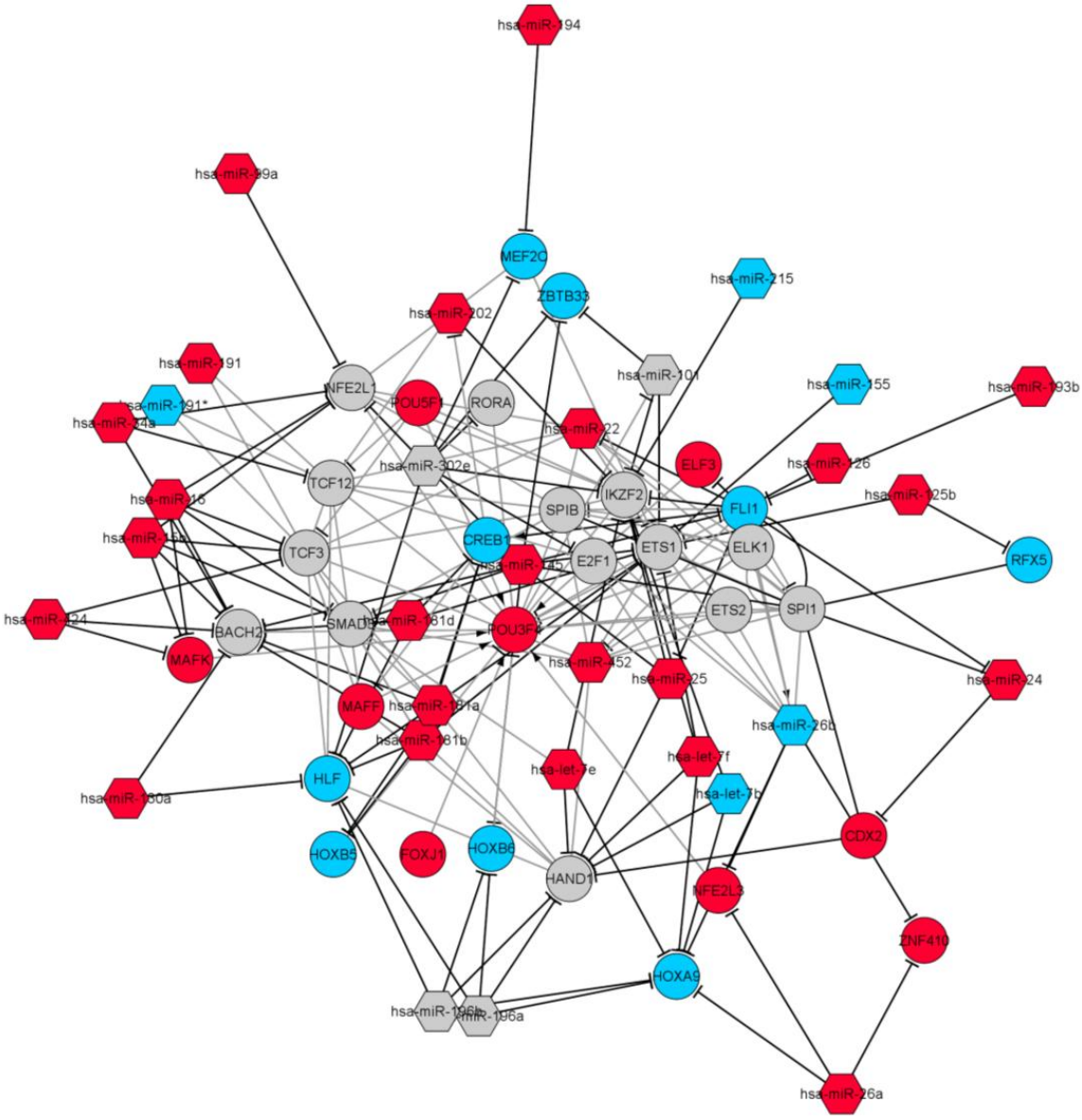
hsa-miR-194
hsa-miR-99a
MEF2C
ZBTB33
hsa-miR-215
hsa-miR-202
hsa-miR-191
NFE2L1
POU5F1
RORA
hsa-miR-101
hsa-miR-155
hsa-miR-193b
hsa-miR-191*
hsa-miR-22
ELF3
hsa-miR-126
TCF12
hsa-miR-302e
IKZF2
FLI1
hsa-miR-125b
SPIB
CREB1
ETS1
ELK1
RFX5
TCF3
E2F1
ETS2
SPI1
hsa-miR-424
BACH2
SMAD1
hsa-miR-181d
POU3F2
MAFK
hsa-miR-452
hsa-miR-125
hsa-miR-224
MAFF
hsa-miR-181a
hsa-miR-181b
hsa-miR-26b
hsa-let-7e
hsa-let-7f
HLF
hsa-let-7b
hsa-miR-130a
CDX2
HOXB5
FOXJ1
HOXB6
HAND1
NFE2L2
ZNF410
HOXA9
hsa-miR-196b
miR-196a
hsa-miR-26a

Supplementary Figure 3. CGCIRs and CMCIRs dynamically regulated in SC injury response. *(A)* Expression profiles of the four CGCIRs. *(B)* Gene Ontology terms enriched in each of the four CGCIRs. Color coding of bars matches that of the expression profiles shown in *(A)*. *(C)* Expression profiles of miRNAs that are correlated with CGCIRs 1 or 2 (blue) and miRNAs that are correlated with CGCIRs 3 or 4 (red).

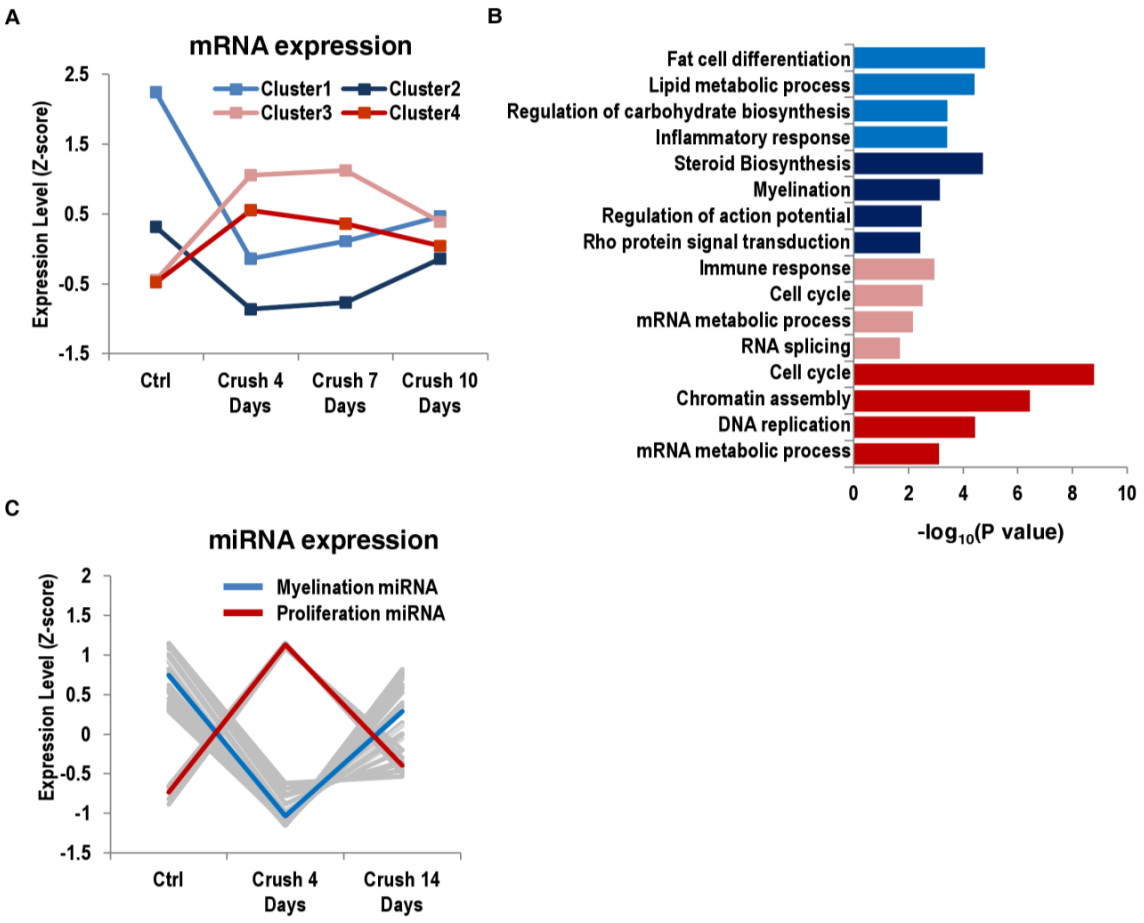

Supplementary Figure 4. Luciferase assays confirm a direct interaction between miR-124 and the 3'-UTR of Egr2. Overexpression of miR-124 but not of a Ctrl miRNA in HEK293T cells expressing a luciferase reporter construct carrying the 3'-UTR of Egr2 results in significantly decreased luciferase activity ($p<0.05$, two-tailed Student's t-test). Mutating the predicted landing pad for miR-124 in the 3'-UTR of Egr2 disrupts the interaction between miR-124 and the Egr2 3'-UTR luciferase construct and restores luciferase activity.

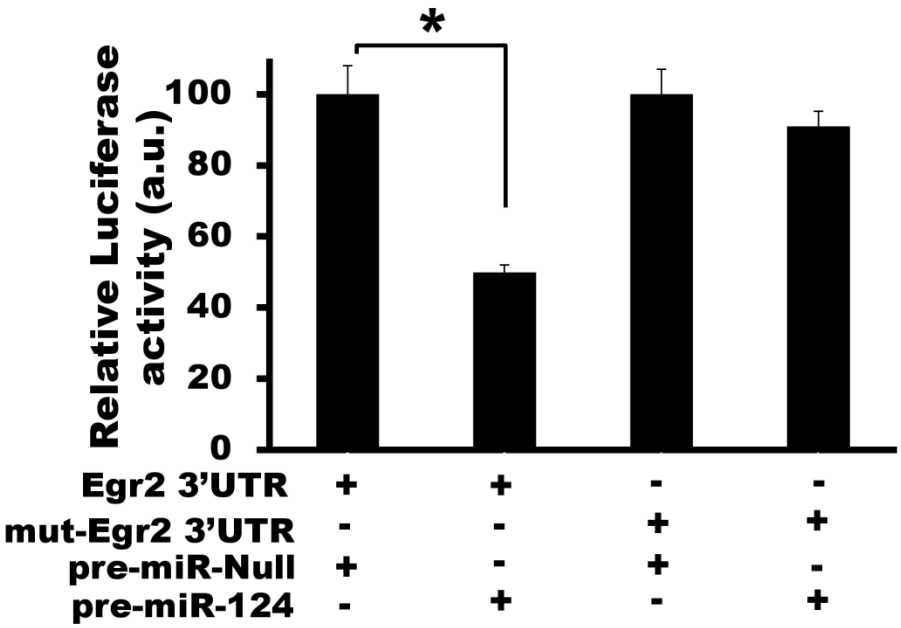

CHAPTER 7

Conclusions and Future Directions

Conclusions and Future Directions

Mitochondria are critical mediators of disease progression in peripheral neuropathies. Mitochondrial dysfunction, for example, is thought to be largely responsible for peripheral nerve diseases associated with systemic metabolic disorders such as diabetes (Fernyhough et al., 2010). Similarly, abnormalities in mitochondrial metabolism ultimately account for the presentation of some forms of CMT in which mitochondrial proteins are mutated (Niemann et al., 2006). With the hope of developing new therapies much effort is being devoted to understanding how mitochondrial deficiencies influence nerve function. To date, most work has focused on clarifying the role played by neuronal/axonal mitochondria (Baloh, 2008). The contribution of SC-specific mitochondrial deficits to the pathophysiology of peripheral neuropathy, however, has remained largely unexplored. Given that SCs intimately associate with and critically support all peripheral nerve axons (Chen et al., 2003; Meyer zu Horste et al., 2007; Reddy et al., 2003), greater insight into the biology and pathology of SC mitochondrial metabolism could be relevant to the treatment of peripheral neuropathies. In the present thesis we addressed the contribution of mitochondrial deficits specifically in SCs to disease progression in peripheral nerve disease. We also explored some of the mechanisms by which mitochondrial metabolism abnormalities in SCs may contribute to axonal degeneration and damage peripheral nerves. Finally, we examined the gene regulatory network that is important for peripheral nerve regeneration after injury and in disease states.

Mitochondrial derangements in SCs are underappreciated contributors to the pathology of peripheral neuropathies

With the goal of understanding whether SC mitochondrial abnormalities affect axonal survival and peripheral nerve function, we generated and characterized the first mouse model useful in directly interrogating the contribution of SC mitochondrial dysfunction to peripheral neuropathy (Chapter 2) (Viader et al., 2011). These mice (Tfam-SCKOs), were produced through the tissue-specific deletion of the mitochondrial transcription factor A gene (*Tfam*), which is required for mtDNA transcription and replication and when excised induces progressive defects in the mitochondrial electron transport chain (Larsson et al., 1998) Interestingly, we found that the induction of mitochondrial dysfunction specifically in SCs did not affect their survival; instead it resulted in a severe, progressive peripheral neuropathy characterized by extensive axonal degeneration. These results showed that disrupted mitochondrial function specifically in SCs can itself cause axonal degeneration and peripheral nerve disease. Moreover, these results highlighted that much of the pathology present in peripheral neuropathies may primarily reflect metabolic abnormalities in SCs. This is in agreement with previous work examining the role of the polyol pathway in diabetic neuropathy (Tomlinson and Gardiner, 2008), and emphasizes the potential of targeting metabolic abnormalities that affect SCs as a way to treat peripheral neuropathies.

Importantly, Tfam-SCKO mice generated in our study recapitulated a number of critical pathological features of human peripheral neuropathies. Disrupting mitochondrial metabolism specifically in SCs was sufficient to induce both axonal degeneration as well as demyelination. Tfam-SCKOs also displayed distal weakness and sensory deficits, two

common problems in human patients. Finally, Tfam-SCKOs suffered preferential early loss of unmyelinated C fibers followed by the degeneration of large-caliber myelinated axons. This was of particular interest because preferential loss of small-caliber unmyelinated fibers is characteristic of peripheral and optic neuropathies associated with systemic diseases such as diabetes or with exposure to environmental toxins (Kennedy et al., 1996; McArthur et al., 2005; Sadun, 2002). Together, our results indicated that key pathological features commonly encountered in human peripheral nerve disease can potentially be explained by SC-specific mitochondrial dysfunction. Moreover, our observations suggested that Tfam-SCKO mice may be particularly useful in understanding some of the pathophysiology of diabetic and other mitochondria-related neuropathies, as these mice are one of few metabolic mutants (Sullivan et al., 2007) that strongly recapitulate some of the pathology of human peripheral nerve diseases.

Role of SC mitochondrial metabolism in the biology of these glia and the metabolic support of axons

Unexpectedly, severe respiratory chain abnormalities in the SCs of Tfam-SCKO mice did not affect their survival. This observation suggested that SCs have an adaptable energy metabolism. In fact, we observed that following Tfam-depletion and inhibition of mitochondrial respiration SCs induced mitochondrial biogenesis and increased glycolysis. These two metabolic adaptations that often follow mitochondrial deficits (Chabi et al., 2005; Piao et al., 2010), likely account for the relative preservation of energy levels in Tfam-SCKO nerves as well as the limited or largely delayed death of SCs. Our current knowledge of the basic energy metabolism and requirements of SCs,

however, is still very rudimentary. SCs, for example, have been hypothesized to be largely glycolytic and rely on the non-oxidative catabolism of glucose to meet their energy needs (Pellerin and Magistretti, 2003). This idea is supported by the observation that in explant systems SCs take up a disproportionately large amount of glucose (Vega et al., 2003). The fact that disruption of mitochondrial energy metabolism in Tfam-SCKO mice did not affect SC survival and resulted in increased glycolysis provided indirect support for this hypothesis. At the same time, increased mitochondrial biogenesis in Tfam-deficient SCs suggested that these glia still depend on mitochondria to meet some of their metabolic needs. Future work aimed at understanding the basic metabolic requirements of SCs and the adaptations that follow disturbances of specific energy metabolism pathways (e.g. OXPHOS, glycolysis, fatty acid oxidation…) should provide valuable insight into both the biology and pathology of SCs.

One of the more intriguing aspects of the pathology in Tfam-SCKO nerves is that it may reflect a disruption of SC-mediated metabolic support of axons. SCs have a primary role in supporting axonal function and survival (Chen et al., 2003; Meyer zu Horste et al., 2007; Reddy et al., 2003), and metabolic support of axons by ensheathing glia is hypothesized to be critical to this function of SCs (Nave and Trapp, 2008). Similar to what happens in the CNS between neurons and astrocytes, SCs may support axons through the transfer of metabolites or by helping axons eliminate certain toxic species (Benarroch, 2005). Tfam-SCKO mice provide an *in vivo* system in which begin to address some of the details of the mechanisms behind the putative metabolic support of axons by SCs. Tfam-SCKO mice may be a particularly valuable model when combined with other systems designed to more directly examine the transfer of specific energy

metabolites likely to shuttle between SCs and neurons (e.g. lactate, glutamine, 2-oxoglutarate, malate) (Miller et al., 2002). In this context, the generation of new transgenic mice lacking certain metabolite transporters specifically in SCs or axons could prove especially informative (Voutsinos-Porche et al., 2003). Mechanistic inside derived from such studies will complement our basic observation of that SC mitochondria are essential for the SC-mediated support of axonal function and survival; it should also be important in identifying new potential therapeutic targets for peripheral neuropathy.

The integrated stress response as a common maladaptive mechanism in peripheral neuropathies

Having established the relevance of the characterization Tfam-SCKO mice to understanding and potentially treating peripheral neuropathies, chapter three in this thesis described our efforts aimed at discovering the mechanisms underlying the nerve pathology in these mice. Our examination of Tfam-SCKO mice uncovered the activation of the ISR in Tfam-deficient SCs secondary to mitochondrial dysfunction. The ISR is an evolutionarily conserved, "stress"-activated, gene expression program centered on phosphorylation of eIF2α. Activation of this program is meant to promote a cellular stress-resistant state by global attenuation of protein synthesis, which reduces the ER load and diverts amino acids from energetically costly protein synthesis to other metabolic pathways (Ron and Walter, 2007). Activation of this program in SCs, however, is particularly maladaptive and is thought to cause some of the pathology present in neuropathies associated with mutations to structural myelin proteins (Pennuto et al., 2008). In this context, induction of the ISR in SCs is associated with the accumulation of

mutant myelin proteins in the ER and an unfoled protein response (Lin and Popko, 2009). Activation of the ISR in Tfam-SCKO, mice, however, was not associated with ER stress or an unfolded protein response. The maladaptive induction of the ISR in SCs could therefore be a common pathological mechanism in different forms of peripheral neuropathy, including those associated with mutations to structural myelin as well as metabolic abnormalities.

While the idea that ISR activation may be a common pathological mechanism in peripheral neuropathies of diverse etiology is attractive, this hypothesis would be greatly strengthened by evidence that confirms the role of this pathway in the pathology of Tfam-SCKO mice. This evidence could come from the examination of nerve disease progression in Tfam-SCKOs that also lack the key downstream mediator of the ISR Chop, as previously done by Pennuto and colleages in another neuropathy model (Pennuto et al., 2008). Intriguingly, neuropathy-causing chemotherapy drugs have also been shown to activate the ISR in cell lines *in vitro* (Gately et al., 1996). Experiments that explore whether chemotherapy drugs activate the ISR in SCs would also provide further credit to our hypothesis.

A shift in SC lipid metabolism as a key driver of the pathology of Tfam-SCKO nerves

Lipids play a crucial role in the normal biology of SCs; they are required for myelin assembly and maintenance, regulate the differentiation status of these glia, and may also be important for SC-mediated metabolic support of axons (Chrast et al., 2010). Our work identified a shift in lipid metabolism early in the disease progression of Tfam-

SCKO nerves. This alteration in SC lipid metabolism was characterized by a decreased flux of fatty acids towards new lipid synthesis and a concomitant increase in lipid oxidation. Importantly, this shift in SC lipid metabolism secondary to mitochondrial dysfunction in Tfam-deficient SCs preceded much of the nerve pathology in Tfam-SCKOs and could thus ultimately account for the disease phenotype in these mice. Abnormalities in nerve lipid composition are present in a number of peripheral neuropathies in which mitochondrial dysfunction is known to occur (Chrast et al., 2010; Navarro et al., 2010; Niemann et al., 2006). Our results suggested therefore that alterations in SC lipid metabolism may be at the center of the pathology of mitochondrial-related neuropathies modeled in Tfam-SCKO nerves.

The shift in the lipid metabolism in Tfam-deficient SCs resulted in depletion of sulfatides and cerebrosides, key myelin lipid components that together represent almost 30% of all myelin lipid content (Garbay et al., 2000). The early reduction of these lipids likely accounted for the prominent demyelinating phenotype apparent in late stages of disease in Tfam-SCKO mice (Viader et al., 2011). Interestingly, sulfatides and cerebrosides also have an important role in maintaining axon-glial contact (Dupree et al., 1998; Hoshi et al., 2007). Depletion of these galactolipids could thus also drive some of the later axon loss in Tfam-SCKO nerves by disrupting the ability of SCs to properly associate with and support axons. As our understanding of SC-mediated metabolic support of axons expands it will be interesting to examine how this support is affected by depletion of sulfatides and cerebrosides and disruption normal axon-glial interactions.

We also observed a significant accumulation of acylcarnitines in Tfam-SKCO nerves. Our work provided initial evidence that such accumulation of fatty acid β-

oxidation intermediates in SCs following mitochondrial deficits could also be contributing to axonal degeneration in peripheral neuropathies. We found that long-chain acylcarnitines could be released from SCs, disrupt the membrane properties of axons, and induce their degeneration. These results are in agreement with the fact that neuropathy is among the long-term complications of genetic disorders leading to buildup of acylcarnitines (Schaefer et al Turnbull, 1996; Tyni & Pihko, 1999). To unequivocally link acylcarnitine accumulation to axonal degeneration in Tfam-SCKO nerves, however, one will need to assess the benefits of preventing the increase of these lipid intermediates in Tfam-SCKOs. Etomoxir treatment, an inhibitor of the acylcarnitine synthesizing enzyme Cpt1, could be useful in pursuing this line of investigation, particularly as etomoxir has shown therapeutic potential in the treatment of other neurodegenerative conditions (Shriver et al., 2011). Crossing Tfam-SCKOs to mice lacking malonyl-coA decarboxylase, an enzyme that degrades the natural CPT1 inhibitor malonyl-CoA, could provide an alternative genetic model to further asses the role of acylcarnitine accumulation in peripheral neuropathy. Intriguinly, malonyl-coA decarboxyalse deficient mice are protected against diet induced glucose-intolerance (Koves et al., 2008)

miRNAs modulate the ability of SCs to support peripheral nerve regeneration

To complement the work describe in the first part of this thesis, which aimed at understanding the basic pathological mechanism that drive peripheral nerve disease, we also examined the transcriptional and post-transcriptional gene regulatory networks that are responsible for the regenerative response of Schwann cells (chapters 5 and 6). Greater insight into this highly orchestrated process could be harnessed to help restore function in

peripheral and central neurodegenerative diseases characterized by axonopathy, including diabetic neuropathy and amyotrophic lateral sclerosis (Coleman, 2005). We explored whether injury-induced changes in SCs were orchestrated post-transcriptionally by microRNAs (miRNAs). Interestingly, we found that SC miRNAs modulated the injury response largely by targeting positive regulators of SC dedifferentiation/proliferation. SC miRNAs cooperated with transcriptional controls to promote rapid and robust transitions between the distinct differentiation states necessary to support nerve regeneration. Our results suggested, therefore, that that manipulation of SC miRNAs could be used therapeutically to facilitate SC differentiation after injury or reverse the effects of neuropathy.

The therapeutic modulation of SC miRNAs, however, requires the identification of specific miRNAs playing critical roles in the establishment and maintenance of SC differentiation as well as in the modulation of the SC injury response. We identified miR-34a and miR-140 as two such candidates that critically regulate SC proliferation and myelination, respectively. mir-34a and mir-140 deficient mice have been generated (Choi et al., 2011; Miyaki et al., 2010) and examination of the SC injury response in these mice could be especially useful in determining the therapeutic value of these two miRNAs. Future experiments that examine some of the other miRNAs identified in this thesis to be potentially important for the SC regenerative response (e.g. let-7 familiy members, mir-22, mir-26a…) could also be interesting.

In conclusion, the results described in the present thesis expand our understanding of how mitochondrial abnormalities specifically in SCs contribute to the clinical

impairment in patients afflicted with peripheral neuropathy. Our findings emphasize that future therapies for peripheral neuropathy will need to address metabolic abnormalities in SCs and not just in axons if they hope to effectively prevent disease progression. More importantly, our work identifies new potentially important therapeutic targets that may eventually enhance the quality of life of patients with peripheral nerve diseases.

References

Baloh, R.H. (2008). Mitochondrial dynamics and peripheral neuropathy. Neuroscientist 14, 12-18.

Benarroch, E.E. (2005). Neuron-astrocyte interactions: partnership for normal function and disease in the central nervous system. Mayo Clin. Proc. 80, 1326-1338.

Chabi, B., Adhihetty, P.J., Ljubicic, V., and Hood, D.A. (2005). How is mitochondrial biogenesis affected in mitochondrial disease? Med. Sci. Sports Exerc. 37, 2102-2110.

Chen, S., Rio, C., Ji, R.R., Dikkes, P., Coggeshall, R.E., Woolf, C.J., and Corfas, G. (2003). Disruption of ErbB receptor signaling in adult non-myelinating Schwann cells causes progressive sensory loss. Nat. Neurosci. 6, 1186-1193.

Choi, Y.J., Lin, C.P., Ho, J.J., He, X., Okada, N., Bu, P., Zhong, Y., Kim, S.Y., Bennett, M.J., Chen, C., *et al.* (2011). miR-34 miRNAs provide a barrier for somatic cell reprogramming. Nat. Cell Biol. 13, 1353-1360.

Chrast, R., Saher, G., Nave, K.A., and Verheijen, M.H. (2010). Lipid metabolism in myelinating glial cells: lessons from human inheriteddisorders and mouse models. J. Lipid Res.

Coleman, M. (2005). Axon degeneration mechanisms: commonality amid diversity. Nat. Rev. Neurosci. 6, 889-898.

Dupree, J.L., Coetzee, T., Suzuki, K., and Popko, B. (1998). Myelin abnormalities in mice deficient in galactocerebroside and sulfatide. J. Neurocytol. 27, 649-659.

Fernyhough, P., Roy Chowdhury, S.K., and Schmidt, R.E. (2010). Mitochondrial stress and the pathogenesis of diabetic neuropathy. Expert Rev. Endocrinol. Metab. 5, 39-49.

Garbay, B., Heape, A.M., Sargueil, F., and Cassagne, C. (2000). Myelin synthesis in the peripheral nervous system. Prog. Neurobiol. 61, 267-304.

Gately, D.P., Sharma, A., Christen, R.D., and Howell, S.B. (1996). Cisplatin and taxol activate different signal pathways regulating cellular injury-induced expression of GADD153. Br. J. Cancer 73, 18-23.

Hoshi, T., Suzuki, A., Hayashi, S., Tohyama, K., Hayashi, A., Yamaguchi, Y., Takeuchi, K., and Baba, H. (2007). Nodal protrusions, increased Schmidt-Lanterman incisures, and paranodal disorganization are characteristic features of sulfatide-deficient peripheral nerves. Glia 55, 584-594.

Kennedy, W.R., Wendelschafer-Crabb, G., and Johnson, T. (1996). Quantitation of epidermal nerves in diabetic neuropathy. Neurology 47, 1042-1048.

Koves, T.R., Ussher, J.R., Noland, R.C., Slentz, D., Mosedale, M., Ilkayeva, O., Bain, J., Stevens, R., Dyck, J.R., Newgard, C.B., Lopaschuk, G.D., and Muoio, D.M. (2008). Mitochondrial overload and incomplete fatty acid oxidation contribute to skeletal muscle insulin resistance. Cell. Metab. 7, 45-56.

Larsson, N.G., Wang, J., Wilhelmsson, H., Oldfors, A., Rustin, P., Lewandoski, M., Barsh, G.S., and Clayton, D.A. (1998). Mitochondrial transcription factor A is necessary for mtDNA maintenance and embryogenesis in mice. Nat. Genet. 18, 231-236.

Lin, W., and Popko, B. (2009). Endoplasmic reticulum stress in disorders of myelinating cells. Nat. Neurosci. 12, 379-385.

McArthur, J.C., Brew, B.J., and Nath, A. (2005). Neurological complications of HIV infection. Lancet Neurol. 4, 543-555.

Meyer zu Horste, G., Prukop, T., Liebetanz, D., Mobius, W., Nave, K.A., and Sereda, M.W. (2007). Antiprogesterone therapy uncouples axonal loss from demyelination in a transgenic rat model of CMT1A neuropathy. Ann. Neurol. 61, 61-72.

Miller, K.E., Richards, B.A., and Kriebel, R.M. (2002). Glutamine-, glutamine synthetase-, glutamate dehydrogenase- and pyruvate carboxylase-immunoreactivities in the rat dorsal root ganglion and peripheral nerve. Brain Res. 945, 202-211.

Miyaki, S., Sato, T., Inoue, A., Otsuki, S., Ito, Y., Yokoyama, S., Kato, Y., Takemoto, F., Nakasa, T., Yamashita, S., *et al.* (2010). MicroRNA-140 plays dual roles in both cartilage development and homeostasis. Genes Dev. 24, 1173-1185.

Navarro, J.A., Ohmann, E., Sanchez, D., Botella, J.A., Liebisch, G., Molto, M.D., Ganfornina, M.D., Schmitz, G., and Schneuwly, S. (2010). Altered lipid metabolism in a Drosophila model of Friedreich's ataxia. Hum. Mol. Genet. 19, 2828-2840.

Nave, K.A., and Trapp, B.D. (2008). Axon-glial signaling and the glial support of axon function. Annu. Rev. Neurosci. 31, 535-561.

Niemann, A., Berger, P., and Suter, U. (2006). Pathomechanisms of mutant proteins in Charcot-Marie-Tooth disease. Neuromolecular Med. 8, 217-242.

Pellerin, L., and Magistretti, P.J. (2003). How to balance the brain energy budget while spending glucose differently. J. Physiol. 546, 325.

Pennuto, M., Tinelli, E., Malaguti, M., Del Carro, U., D'Antonio, M., Ron, D., Quattrini, A., Feltri, M.L., and Wrabetz, L. (2008). Ablation of the UPR-mediator CHOP restores motor function and reduces demyelination in Charcot-Marie-Tooth 1B mice. Neuron 57, 393-405.

Piao, L., Marsboom, G., and Archer, S.L. (2010). Mitochondrial metabolic adaptation in right ventricular hypertrophy and failure. J. Mol. Med. (Berl) 88, 1011-1020.

Reddy, L.V., Koirala, S., Sugiura, Y., Herrera, A.A., and Ko, C.P. (2003). Glial cells maintain synaptic structure and function and promote development of the neuromuscular junction in vivo. Neuron 40, 563-580.

Ron, D., and Walter, P. (2007). Signal integration in the endoplasmic reticulum unfolded protein response. Nat. Rev. Mol. Cell Biol. 8, 519-529.

Sadun, A.A. (2002). Metabolic optic neuropathies. Semin. Ophthalmol. 17, 29-32.

Sullivan, K.A., Hayes, J.M., Wiggin, T.D., Backus, C., Su Oh, S., Lentz, S.I., Brosius, F.,3rd, and Feldman, E.L. (2007). Mouse models of diabetic neuropathy. Neurobiol. Dis. 28, 276-285.

Tomlinson, D.R., and Gardiner, N.J. (2008). Glucose neurotoxicity. Nat. Rev. Neurosci. 9, 36-45.

Vega, C., Martiel, J.L., Drouhault, D., Burckhart, M.F., and Coles, J.A. (2003). Uptake of locally applied deoxyglucose, glucose and lactate by axons and Schwann cells of rat vagus nerve. J. Physiol. 546, 551-564.

Viader, A., Golden, J.P., Baloh, R.H., Schmidt, R.E., Hunter, D.A., and Milbrandt, J. (2011). Schwann cell mitochondrial metabolism supports long-term axonal survival and peripheral nerve function. J. Neurosci. 31, 10128-10140.

Voutsinos-Porche, B., Bonvento, G., Tanaka, K., Steiner, P., Welker, E., Chatton, J.Y., Magistretti, P.J., and Pellerin, L. (2003). Glial glutamate transporters mediate a functional metabolic crosstalk between neurons and astrocytes in the mouse developing cortex. Neuron 37, 275-286.